Replicated microcellular aluminium structures for thermal management

THÈSE N^{O} 7497 (2017)

PRÉSENTÉE LE 24 MARS 2017

À LA FACULTÉ DES SCIENCES ET TECHNIQUES DE L'INGÉNIEUR
LABORATOIRE DE MÉTALLURGIE MÉCANIQUE
PROGRAMME DOCTORAL EN SCIENCE ET GÉNIE DES MATÉRIAUX

ÉCOLE POLYTECHNIQUE FÉDÉRALE DE LAUSANNE

POUR L'OBTENTION DU GRADE DE DOCTEUR ÈS SCIENCES

PAR

Alexandros ATHANASIOU-IOANNOU

acceptée sur proposition du jury:

Prof. H. Hofmann, président du jury
Dr L. Weber, Prof. A. Mortensen, directeurs de thèse
Dr F. Topin, rapporteur
Dr S. Mancin, rapporteur
Prof. J. R. Thome, rapporteur

ÉCOLE POLYTECHNIQUE
FÉDÉRALE DE LAUSANNE
Suisse
2017

When you set out for distant Ithaca,

fervently wish your journey may be long, —

full of adventures and with much to learn.

Of the Laestrygones and the Cyclopes,

of the angry god Poseidon, have no fear:

these you shall not encounter, if your thought

remains at all times lofty, — if select

emotion touches you in body and spirit.

Not the Laestrygones, not the Cyclopes,

nor yet the fierce Poseidon, shall you meet,

unless you carry them within your soul, —

unless your soul should raise them to confront you.

****

At every stage bear Ithaca in mind.

The arrival there is your appointed lot.

But hurry not the voyage in the least:

'twere better if you travelled many years

and reached your island home in your old age,

being rich in riches gathered on the way,

and not expecting more from Ithaca.

Ithaca gave you the delightful voyage:

without her you would never have set out:

and she has nothing else to give you now.

And though you should find her wanting, Ithaca

will not surprise you; for you will arrive

wise and experienced, having long since perceived

the unapparent sense in Ithacas..

C.P.Cavafy, Ithaca, translation by J.Cavafy

Acknowledgements

The present thesis could not had been fulfilled without the following people: Iro & Kostantinos, Electra, Aristidis, Sokratis & Angeliki, Giorgos, Polydefkis, Christina, Gabriele, Richard Parker & Elizabeth, Konstantinos & Danae, Spyros, Harry, Maria, Lida, Michalis, Callia, Angeliki, Aristotelis, Electra, Angelos, Maria & Lefteris, Gianni, Filippo, Claudia, Karel, Édy, Selmar, Gabriella, Ana, Marta, Jérôme, Suzanne, Lionel, Roberto, Arda, Alain, Carmen, Aparna, Vaclav, Martin, Goran, Cyril, Hamed, Léa, Maïté, Gionata, Lionel, José Miguel, Raphaël, Cyril, Willy, Marie, Fabienne, Jose Felix Vega Stavro, Pierre, Andreas, Jean-Marc, Tehrani, Éric, Yves, Werner, Pierre-André, Simone, Frédéric, Marek, Sofie, Vincent, Sandra, Jessica, Céline, Thibault, David, Ludger and Andreas.

A big *thank you* for your generous contribution!

Lausanne, le 6 février 2017

Abstract

Open-pore aluminium foams are of interest in thermal management of power electronics due to their large specific surface area, low weight and relatively high thermal conductivity. The replication process is a low-cost and simple foam manufacturing method that offers many opportunities for the investigation of the influence exerted by the microstructure (porosity, pore size) and geometry or their combination in the performance of metal foams in heat-exchange applications.

In this study, we explored replicated aluminium foams as a part of an integrated heat sink manufactured in one step that seamlessly combines metal and ceramic phases. Replicated aluminium foams were manufactured and tested first under natural and then under forced convection.

A dedicated test apparatus was built to test these samples under both natural and forced convection, using the guarding ring technique. In the case of natural convection, the aluminium foams had different pore sizes (125-180 μm, 400-450 μm and 5 mm), porosities (78 to 86%) and geometry (disk, cylinder and finned structures). In all cases, replicated aluminium foams were found to dissipate the same amount of heat as their bulk aluminium (alloy) equivalents.

The thermal heat exchange performance of replicated microcellular aluminium was also measured under forced convection. The test rig was modified to measure the pressure drop and volumetric air flow in a cylindrically symmetric jet impingement configuration. Foams of different pore size (125-180, 400-450 and 900-1300 μm), porosity (between 75 and 85 %), height (1 and 2.8 cm) and infiltrated at various pressures (between 2.7 and 70 bars) were manufactured for thermal testing, all having a hollow central channel, through which air is injected at a range of flow rates. The results show that within the covered parameter range foams of higher porosities, larger pore sizes and lower infiltration pressures dissipate more heat at lower cost in terms of pumping power. Shorter heights also dissipate more heat for a given volumetric flow but do so at the cost of an increased pressure drop and hence greater pumping power expenditure.

A numerical model, developed and written by Dr. D. Ingram, using the finite-volumes technique, was employed to elucidate how the various parameters influence the heat transfer. The model solves the Darcy-Forchheimer formulation of fluid flow in porous media, which is then coupled to a convective/conductive heat transfer model of the same structure. These simulations were used to perform parametric studies on the influence of height and pore size with regard to the thermal behaviour of replicated foams. Furthermore, the model was benchmarked against the experimental results; overall, despite some discrepancies with measured temperature profiles, the model captures data trends well, and provides insight on the physical phenomena that underlie the experimental data and observations. In particular, the presence and influence of recirculating air flow along the inner portion of the heat exchanger structures was identified.

Finally, we successfully fabricated the proposed integrated multimaterial structure and tested it under forced convection, using the same conditions as the replicated aluminium foams. Results demonstrate that this type of structures can be effectively used to cool power electronics.

Keywords

Aluminium foams, forced convection, air flow, pressure drop, heat transfer, thermofluids, porous media, fluid mechanics.

Résumé

Les mousses d'aluminium à cellules ouvertes sont d'un intérêt potentiel pour la gestion thermique des électroniques de puissance grâce à leur surface spécifique élevée, leur faible masse et leur conductivité thermique effective élevée. Le procédé de réplication fournit une approche simple et économique pour la production de telles structures et présente de plus l'opportunité d'étudier l'influence de la microstructure et de la géométrie ou leur combinaison sur le comportement et la performance thermiques de ces mousses pour l'évacuation de la chaleur.

Cette thèse explore les mousses d'aluminium, produites par le procédé de réplication, en vue de leur application dans les dissipateurs thermiques, au sein de structures fabriquées en une étape combinant sans discontinuité les phases métalliques et céramiques. En outre, la performance de structures en aluminium poreux produites par réplication est étudiée, premièrement sous convection naturelle et ensuite, sous convection forcée.

Nous avons développé à cette fin un appareil permettant de mesurer le coefficient de transfert de chaleur moyen de tels échantillons sous convection naturelle ou forcée, utilisant la technique dite du "guarding-ring". En convection naturelle, les mousses d'aluminium contenant des pores de taille 125-180 μm, 400-450 μm et 5 mm, et de porosité relative comprise entre 78% et 86%, ont une performance thermique égale à celle d'un bloc d'alliage d'aluminium ayant la même géométrie.

Le comportement thermique de ces structures a aussi été étudié sous convection forcée. L'appareil de mesure a été modifié afin de mesurer la baisse de pression et le débit d'air sous la configuration dite du "jet impingement". Des échantillons de mousses d'aluminium avec différentes tailles de pores (125-180, 400-450 et 900-1300 μm), ayant des porosités relatives entre 75 et 85%, de taille comprise entre 1 cm et 2.8 cm et infiltrées sous des pressions différentes, ont été produits pour avoir une forme cylindrique avec un canal creux au milieu. Les résultats indiquent que les mousses ayant une porosité élevée, des pores de grande taille et été infiltrées sous basse pression (dans les limites des variations de paramètres explorées), dissipent plus de chaleur tout en requiérant des pressions de pompage d'air inférieures. Les plus courts échantillons dissipent aussi plus de chaleur mais au détriment d'une augmentation de la pression requise pour le même débit d'air.

Un modèle de simulation numérique, conçu et écrit par le Dr. D. Ingram, a été utilisé pour élucider comment les paramètres de microstructure et de forme influencent le transfert de chaleur dans ces structures. Le modèle est basé sur la formulation de Darcy-Forchheimer d'un fluide incompressible filtrant au travers d'un milieu poreux et est lié à un modèle d'échange de chaleur par conduction et convection au sein de la même structure poreuse. Nous avons utilisé ces simulations pour étudier l'influence de taille des échantillons combinée avec leur

taille de pores sur le comportement thermique des mousses. Une comparaison des prédictions du modèle avec des mesures de la température du métal et du gaz sortant montrent un accord satisfaisant ; en outre le modèle permet l'interprétation physique des mesures, mettant notamment en évidence l'existence de la recirculation de l'air dans les structures ayant une hauteur excédant une certaine valeur.

Enfin, nous avons fabriqué avec succès la structure multi-matériel proposée et nous avons testé cette structure sous convection forcée, utilisant les mêmes conditions que pour les mousses d'aluminium fabriquées par réplication; les résultats indiquent que ce type de structure peut être utilisé pour refroidir efficacement les circuits électroniques de puissance.

Mots-clés

Mousses d'aluminium, convection forcée, débit d'air, baisse de pression, transfert de chaleur, thermo fluides, milieu poreux, mécanique des fluides.

Contents

Acknowledgements iv

Abstract v

Keywords vi

Résumé vii

Mots-clés viii

Contents 1

List of Figures xii

Chapter 1 Introduction 1

1.1 Introduction and motivation of the research 1

1.2 Statement of the problem and proposed approach 3

1.3. Objectives of this thesis and statement of the novelty of the proposed work 5

Chapter 2 Literature Review 6

2.1 Metal matrix composites in thermal management 6

2.2 Aluminium diamond composites in thermal management 7

2.3 Metal foams in thermal management 13

Chapter 3 Experimental Procedures 29

3.1 Aluminium foam processing by replications 29

3.2 Natural convection testing apparatus 33

3.3 Forced convection testing apparatus 45

3.4 Integrated heat-sink fabrication and forced convection testing thereof..... 60

Chapter 4 Experimental Results 65

4.1 Foams under natural convection 65

4.2 Foams under forced convection..... 71

4.3 Fluid flow through the foam 88

4.4 Temperature profiles..... 90

4.5 Integrated Structure 91

Chapter 5 Theoretical model and Results 93

5.1 Description of the air flow model..... 93

5.2 Description of the heat transfer model..... 96

5.4 Results 100

Chapter 6 Discussion 119

6.1 Thermal performance under natural convection 119

6.2 Thermal performance under forced convection..... 120

6.3 Fluid flow through the foam 125

6.4 Thermal performance of the foam 127

6.5 The theoretical model: confontration with experiment 129

6.6 The Integrated Structure..... 139

Chapter 7 Concluding Remarks..... 141

7.1 Summary of present work..... 141

7.2 Suggested Future Work 143

Chapter 8 Appendix 145

Appendix A: Estimation of the permeability and Forhheimer coefficients of Open-pore replicated foams 145

Appendix B: Electrical Insulating Properties of the IS before and after thermal cycling 149

Appendix C: Thermoelastic bending of the integrated structure..... 150

Appendix D: Thermal Resistance of the Thermal Interface Material 152

Appendix E: Selective compilation of forced convection results..... 153

Chapter 9 Bibliography..... 157

Curriculum Vitae..... 176

List of Figures

Figure 1.1: Evaluation of the need for high temperature electronics, primarily high temperature circuit boards stable above 140°C. As seen, after 2003 this trend towards high temperatures becomes even stronger [9]..... 2

Figure 1.2: Typical schematic of an IGBT Module Assembly [15]..... 4

Figure 1.3: Proposed solution, with yellow for the aluminium diamond composite, grey for the ceramic layer and orange with white circles for the aluminium foam. 5

Figure 2.1: Ashby plot of thermal properties for various thermal management materials, © Fraunhofer IFAM Dresden [52]..... 8

Figure 2.2: Thermal conductivity of composite samples with diamond as reinforcement with regard to their fabrication method [55]..... 10

Figure 2.3: Thermal conductivity of aluminium/diamond composites, along with the contact time for two infiltration temperatures: 760°C (empty circles) and 850°C (filled circles) [84]. 11

Figure 2.4: Evolution of scientific publication over time as categorised by Google Scholar using the following keywords: “metal foam”, “heat transfer” and “open-cell”[97]. 13

Figure 2.5: Schematic representation of the replication process for open-cell foam fabrication [98]..... 14

Figure 2.6: Schematic representation of forced convection in metal foams.From [99].... 16

Figure 2.7: Schematic representation of a typical experimental setup (”standard configuration”) for testing the performance of metal foam specimens [135]. 17

Figure 2.8: Different aluminium foam samples tested in [172]. (a) Single 5mm pore size sample, (b) Segmented sample with one third of the total sample length (vertical in the figure) having 1mm pore size and the remaining two thirds having 5mm pore size, and (c) Integrated sample equivalent to (b), produced via the replication process…… 20

Figure 2.9: Schematic representation of a typical by-pass testing configuration [173]. . 21

Figure 2.10: Schematic representation of a typical experimental setup for testing the performance of metal foam under oscillating flows [176]. 22

Figure 2.11: Wrapped metal foams around tubes of different thickness compared with their equivalent finned tube, used as a benchmark. From left to right: Aluminium foam covered tube (5 mm thick), Circular Finned Tube (center), aluminium foam covered tube (15 mm thick) [194]..... 23

Figure 2.12: Experimental apparatus for the measurement of heat transfer characteristics of aluminium-foam heat sinks in the impingement jet configuration [201]. 24

Figure 2.13: Experimental apparatus creating an L-shaped flow through metal foams [205]..... 26

Figure 3.1: a) Cold Isostatic pressing apparatus and b) Sketch of the process. From Ref. [220]..... 30

Figure 3.2: a) Schematic description and b) Photograph of the infiltration apparatus used. From [220]..... 31

Figure 3.3: a) Schematic description of the infiltration process and b) an infiltrated composite bar outcome. From Ref. [220]..... 32

Figure 3.4: Schematic representation of the natural convection testing apparatus. 34

Figure 3.5: Sensitivity analysis for the global heat transfer coefficient under natural convection, using the linear model..... 38

Figure 3.6: Sensitivity analysis for the global heat transfer coefficient under natural convection, using the parabolic model. 38

Figure 3.7: Schematic propagation of error in temperature measurement under a linear model. The distances between the thermocouples and the uncertainty assigned to T1, T2 and T3 are not in scale, to enhance the visibility of the phenomenon. 39

Figure 3.8: Schematic propagation of error in temperature measurement under a parabolic model. The distances between the thermocouples and the uncertainty assigned to T1, T2 and T3 are not in scale, to enhance the visibility of the phenomenon. 39

Figure 3.9: From left to right:Corevo™ 5mm pore size commercial aluminium foam, replicated 125-180 µm pore size aluminium, replicated aluminium 400-450 µm pore size. 42

Figure 3.10: Aluminium foam fins and their equivalent bulk parts that were tested under natural convection. 43

Figure 3.11: Schematic representation of the experimental apparatus illustrating how fins were mounted on the apparatus. 44

Figure 3.12: Schematic representation of the new set up, depicting relevant components. 46

Figure 3.13: Schematic representation of the apparatus calibration procedure. 47

Figure 3.14: Measured evolution of the temperature difference between the guarding ring and the upper part of the duct with the volumetric air flow. A temperature difference between 5 and 35°C, similar to the temperature gradient across the duct, explains the noticeably nonlinear temperature profile. 48

Figure 3.15: Evolution of the temperatures at the top of the duct $T_{topduct}$ and at the bottom of the sample T_{surf}, with heat flux for a 28 mm tall aluminium foam, with 125-180 µm pore size, 85% porous fraction and infiltrated at 70 bars. 50

Figure 3.16: Evolution of the global heat transfer coefficient with heat flux using different input temperatures (T_{surf} and $T_{topduct}$) for a 28 mm tall aluminium foam, with 125-180 µm pore size, 85% porous fraction and infiltrated at 70 bars. 50

Figure 3.17: Cumulative and binned frequency plot for the relative change of the global heat transfer coefficient under 400l/h, after a randomized change of parameters. The number of bins follows Rice's rule. 52

Figure 3.18: Cumulative and binned frequency plot for the relative change of the global heat transfer coefficient under 1400l/h, after a randomized change of parameters. The number of bins follows Rice's rule. 53

Figure 3.19: Cumulative and binned frequency plot for the relative change of the global heat transfer coefficient under 2400l/h, after a randomized change of parameters. The number of bins follows Rice's rule. 54

Figure 3.20: Samples after leaching. There is a ≈ 2 mm thick full metal skin at their bottom to improve thermal contact with the duct. 55

Figure 3.21: SEM pictures of pure Al replicated foams made out of similar salt preforms (porosity≈ 25%) infiltrated at various pressures P_{inf}: a) P_{inf} = 2 bars, b) P_{inf} = 5 bars, c) P_{inf} = 10 bars, c) P_{inf} = 155 bars. Figure reproduced from [100]. 56

Figure 3.22: Typical evolution of volumetric air flow with time in forced convection experiments 57

Figure 3.23: Mechanical drawing of the of the air flow bench, indicating its parts (image courtesy D. Ingram) 59

Figure 3.24: Trimetric projection of the air flow bench (image courtesy D. Ingram) 59

Figure 3.25: (a)Top and (b) side view of the integrated structure. 61

Figure 3.26: Cross sectional view of the graphite mould used for the fabrication of the integrated structure. 62

Figure 3.27: The infiltration set-up, with its infiltration box (yellow frame), having Plexiglas® walls. The infiltration chamber is attached at the pulley above the furnace and the gas and vacuum pipe are connected with a three-way valve. This apparatus was used and described in Ref.[240] 62

Figure 3.28: Photographs from a) to f), depict the different consecutive steps of the infiltration procedure described in the text. From Ref. [240]. 63

Figure 4.1: Global heat transfer coefficient of one of our samples, tested twice in two different days. The discrepancy is less than the maximum experimental error possible (8%). 65

Figure 4.2: Evolution of the global heat transfer coefficient of nearly flat samples versus the temperature at the top of the duct, $T_{topduct}$. The samples have a varying pore size 125-180 and 400-450 μm) and porosity (78 and 85%). 67

Figure 4.3: Evolution of the global heat transfer coefficient of 12 mm tall samples versus the temperature at the top of the duct, $T_{topduct.}$ The samples have a varying pore size (between 125-180 μm) and porosity (78 and 85%). 68

Figure 4.4: Evolution of the global heat transfer coefficient of a Corevo aluminium foam of 5 mm pore size, 80% V_p and 75 mm height versus the temperature at the top of the duct, $T_{topduct.}$ 69

Figure 4.5: Overall heat transfer coefficient for two different finned geometries made out of both aluminium foam and solid aluminium alloy. One geometry consists of 5 fins and one of 11 fins. In both geometries, fins have 7 mm height and are 1.2 mm apart. 70

Figure 4.6: Overall heat transfer coefficient for unleached, partially leached and fully leached aluminium foam sample. 71

Figure 4.7: Evolution of the global heat transfer coefficient h_{total} with volumetric flow for 28 mm tall samples of same pore size and porosity but infiltrated at different pressures. In the present geometry a flow rate of 2500l/h corresponds to roughly 1 m/s average inflow superficial velocity over the heat transfer footprint area, equal in the present experiments to $7.07*10^{-4}$ m^2 72

Figure 4.8: Evolution of the global heat transfer coefficient h_{total} with volumetric flow for 28 mm tall samples of same pore size and infiltrated at nearly the same pressure but of different porosity. In the present geometry a flow rate of 2500l/h corresponds to roughly 1 m/s average inflow superficial velocity over the heat transfer footprint area, equal in the present experiments to 7.07*10-4 m2. 72

Figure 4.9: Evolution of the global heat transfer coefficient h_{total} with volumetric flow for 10 mm tall samples of same pore size and porosity but infiltrated at different pressures. In the present geometry a flow rate of 2500l/h corresponds to roughly 1 m/s average inflow superficial velocity over the heat transfer footprint area, equal in the present experiments to $7.07*10^{-4}$ m^2. 73

Figure 4.10: Evolution of the global heat transfer coefficient h_{total} with volumetric flow for 10 mm tall samples of same pore size and infiltrated at the same pressure range but of different porosity. In the present geometry a flow rate of 2500l/h corresponds to roughly 1 m/s average inflow superficial velocity over the heat transfer footprint area, equal in the present experiments to $7.07*10^{-4}$ m^2 73

Figure 4.11: Evolution of the global heat transfer coefficient h_{total} with volumetric flow for samples of same pore size, porosity and infiltrated at the same pressure range but of different height. In the present geometry a flow rate of 2500l/h corresponds to roughly 1 m/s average inflow superficial velocity over the heat transfer footprint area, equal in the present experiments to $7.07*10^{-4}$ m^2. 74

Figure 4.12: Evolution of the global heat transfer coefficient h_{total} with volumeetric flow for 10 mm tall samples of same pore size and infiltrated at the same pressure range but of different porosity. In the present geometry a flow rate of 2500l/h corresponds to roughly 1 m/s average inflow superficial velocity over the heat transfer footprint area, equal in the present experiments to $7.07*10^{-4}$ m^2. 75

Figure 4.13: Evolution of the global heat transfer coefficient h_{total} with with volumetric flow for samples of same pore size, porosity and infiltrated at the same pressure range but of different height. In the present geometry a flow rate of 2500l/h corresponds to roughly 1 m/s average inflow superficial velocity over the heat transfer footprint area, equal in the present experiments to $7.07*10^{-4}$ m^2 75

Figure 4.14: Evolution of the global heat transfer coefficient h_{total} with volumetric flow for 10 mm tall samples of same porosity but of different pore size. In the present geometry

a flow rate of 2500l/h corresponds to roughly 1m/s average inflow superficial velocity over the heat transfer footprint area, equal in the present experiments to $7.07*10^{-4}$ m^2 ..... .76

Figure 4.15: Evolution of the global heat transfer coefficient h_{total} with volumetric flow for 28 mm tall samples of same porosity but of different pore size. In the present geometry a flow rate of 2500l/h corresponds to roughly 1m/s average inflow superficial velocity over the heat transfer footprint area,equal in the present experiments to $7.07*10^{-4}$ m^2 76

Figure 4.16: Evolution of the global heat transfer coefficient h_{total} with volumetric flow for samples of same pore size, porosity and infiltrated at the same pressure range but of different heights. In the present geometry a flow rate of 2500l/h corresponds to roughly 1 m/s average inflow superficial velocity over the heat transfer footprint area, equal in the present experiments to $7.07*10^{-4}$ m^2 77

Figure 4.17: Evolution of the global heat transfer coefficient h_{total} with volumetric flow for 10 mm tall samples of same porosity but of different pore size. In the present geometry a flow rate of 2500l/h corresponds to roughly 1m/s average inflow superficial velocity over the heat transfer footprint area,equal in the present experiments to $7.07*10^{-4}$ m^2 78

Figure 4.18: Evolution of the global heat transfer coefficient h_{total} with volumetric flow for different samples. In the present geometry a flow rate of 2500l/h corresponds to roughly 1 m/s average inflow superficial velocity over the heat transfer footprint area, equal in the present experiments to $7.07*10^{-4}$ m^2 79

Figure 4.19: Evolution of the global heat transfer coefficient h_{total} with ideal pumping power per footprint for 28 mm tall samples of same pore size and infiltrated at the same pressure range but of different porosity. 80

Figure 4.20: Evolution of the global heat transfer coefficient h_{total} with ideal pumping power per footprint for 28 mm tall samples of same pore size and porosity but infiltrated at different pressures. 80

Figure 4.21: Evolution of the global heat transfer coefficient h_{total} with ideal pumping power per footprint for 10 mm tall samples of same pore size and infiltrated at similar pressures but of different porosities. 81

Figure 4.22: Evolution of the global heat transfer coefficient h_{total} with ideal pumping power per footprint for 10 mm tall samples of same pore size and porosity but infiltrated at different pressures. 81

Figure 4.23: Evolution of global heat transfer coefficient h_{total} with ideal pumping power per footprint for samples of same pore size, porosity and infiltrated at the same pressures but of different height. 82

Figure 4.24: Evolution of the global heat transfer coefficient h_{total} with ideal pumping power per footprint for 10 mm tall samples of same pore size and infiltrated at the same pressures but of different porosities. 83

Figure 4.25: Evolution of the global heat transfer coefficient h_{total} with ideal pumping power per footprint for samples of the same pore size, porosity and infiltrated at the same pressures but of different heights. 83

Figure 4.26: Evolution of the global heat transfer coefficient h_{total} with ideal pumping power per footprint for samples of the same height (10 mm) and porosity but with different pore size and infiltration pressure. 83

Figure 4.27: Evolution of the global heat transfer coefficient h_{total} with ideal pumping power per footprint for samples of the same pore size, porosity and infiltrated at the same pressures but of different heights. 84

Figure 4.28: Evolution of the global heat transfer coefficient h_{total} with ideal pumping power per footprint for samples of the same height (10 mm) but with different pore size, porosity and infiltrated at different pressures. 85

Figure 4.29: Evolution of the global heat transfer coefficient h_{total} with ideal specific pumping power for different samples. 86

Figure 4.30 : Total pressure for one of our samples, tested twice in two different days. The discrepancy is around 9%. 87

Figure 4.31: Global heat transfer coefficient of one of our samples, tested twice in two different days. The discrepancy is less than the maximum estimated experimental error (10%)..... 87

Figure 4.32: Distribution of the static Pressure P_s for samples of 400-450 µm pore size, 85% V_p, infiltrated at 4.4 bar and of different heights, under a volumetric flow of 2520 l/h.....87
Figure 4.33: Distribution of the static Pressure P_s for samples of 400-450 µm pore size, 85% V_p, infiltrated at 4.4 bar and of different heights, under a volumetric flow of 1800 l/h..... 88

Figure 4.34: Distribution of the static Pressure P_s for samples of 400-450 µm pore size, 85% V_p, infiltrated at 4.4 bar and of different heights, under a volumetric flow of 1260 l/h.....88
Figure 4.35: Distribution of the static Pressure P_s for samples of 400-450 µm pore size, 85% V_p, infiltrated at 4.4 bar and of different heights, under a volumetric flow of 720 l/h.. 89

Figure 4.36: Distribution of the static pressure P_s for a sample of 900-1300 µm pore size, 85% V_p, infiltrated under 4 bars and of 28 mm height, under different volumetric flows.90

Figure 4.37: Evolution of the temperature of outflowing air and metal surface as a function of distance from the heated surface under different volumetric air flows. The sample has 400-450 µm pore size, 85% V_p and was infiltrated at 9.7 bars..... 91

Figure 4.38: Evolution of the surface temperature of the microcellular aluminium as a function of distance from the heated surface for different volumetric air flows. The sample has 900-1300 µm pore size, 85% V_p and was infiltrated at 3.4 bars. 91

Figure 4.39: Evolution of the global heat transfer coefficient h_{total} with volumetric flow for the integrated structure. In the present geometry a flow rate of 2500l/h corresponds to roughly 1m/s average inflow superficial velocity over the heat transfer footprint area,equal in the present experiments to $7.07*10^{-4}$ m^2..... 92

Figure 4.40: Evolution of the global heat transfer coefficient h_{total} with ideal pumping power per footprint for the integrated structure..... 92

Figure 5.1: Schematic representation of the fluid flow boundary conditions. 95

Figure 5.2: (a) Schematic representation of the boundary conditions for the solid phase (b) Schematic representation of the boundary conditions for the fluid phase 99

Figure 5.3 (a)-(d): Results of the model for a foamed sample of 28 mm height, 400 µm pore size and 85% V_p, under 2520 l/h. (a) Solid temperature field, (b) Fluid temperature field, (c) Pressure differential, (d)Velocity Vector Field. 101

Figure 5.3 (e)-(f) : Results of the model for a foamed sample of 28 mm height, 400 µm pore size and 85% V_p, under 2520 l/h. (e) Radial velocity field, (f) Vertical velocity field. 102

Figure 5.4 (a)-(b) : Results of the model for a foamed sample of 28 mm height, 400 µm pore size and 85% V_p, under 1800 l/h. (a) Solid temperature field, (b) Fluid temperature field..... 102

Figure 5.4 (c)-(f) : Results of the model for a foamed sample of 28 mm height, 400 µm pore size and 85% V_p, under 1800 l/h. (c) Pressure differential, (d)Velocity Vector Field, (e) Radial velocity field, (f) Vertical velocity field 104

Figure 5.5 (a)-(d) : Results of the model for a foamed sample of 28 mm height, 400 µm pore size and 85% V_p, under 1260 l/h. (a) Solid temperature field, (b) Fluid temperature field, (c) Pressure differential, (d)Velocity Vector Field..... 104

Figure 5.5 (e)-(f) : Results of the model for a foamed sample of 28 mm height, 400 µm pore size and 85% V_p, under 1260 l/h. (a) Solid temperature field, (b) Fluid temperature field.105

Figure 5.6 (a)-(b) : Results of the model for a foamed sample of 28 mm height, 400 µm pore size and 85% V_p, under 720 l/h. (a) Solid temperature field, (b) Fluid temperature field..... 105

Figure 5.6 (c)-(f) : Results of the model for a foamed sample of 28 mm height, 400 µm pore size and 85% V_p, under 720 l/h. (c) Pressure differential, (d)Velocity Vector Field, (e) Radial velocity field and (f) Vertical velocity field. 105

Figure 5.7 (a)-(d) : Results of the model for a foamed sample of 10 mm height, 400 µm pore size and 85% V_p, under 2520 l/h. (a) Solid temperature field, (b) Fluid temperature field, (c) Pressure differential, (d)Velocity Vector Field. 107

Figure 5.7 (e)-(f): Results of the model for a foamed sample of 10 mm height, 400 µm pore size and 85% V_p, under 2520 l/h. (e) Radial velocity field and (f) Vertical velocity field.108

Figure 5.8 (a)-(b): Results of the model for a foamed sample of 10 mm height, 400 µm pore size and 85% V_p, under 1800 l/h.(a) Solid temperature field, (b) Fluid temperature field. 108

Figure 5.8 (c)-(f): Results of the model for a foamed sample of 10 mm height, 400 µms pore size and 85% V_p, under 1800 l/h (c) Pressure differential, (d) Velocity Vector Field, (e) Radial velocity field and (f) Vertical velocity field. 110

Figure 5.9 (a)-(d): Results of the model for a foamed sample of 10 mm height, 400 µms pore size and 85% V_p, under 1260 l/h (a) Solid temperature field, (b) Fluid temperature field, (c) Pressure differential, (d) Velocity Vector Field. 110

Figure 5.9 (e)-(f) : Results of the model for a foamed sample of 10 mm height, 400 µm pore size and 85% V_p, under 1260 l/h (a) Radial velocity field and (f) Vertical velocity field.111

Figure 5.10 (a)-(b) : Results of the model for a foamed sample of 10 mm height, 400 µm pore size and 85% V_p, under 720 l/h (a) Solid temperature field, (b) Fluid temperature field. 111

Figure 5.10 (c)-(f) : Results of the model for a foamed sample of 28 mm height, 1100 µm pore size and 85% V_p, under 720 l/h. (c) Pressure differential, (d)Velocity Vector Field, (e) Radial velocity field and (f) Vertical velocity field. 113

Figure 5.11 (a)-(d) : Results of the model for a foamed sample of 28 mm height, 1100 µm pore size and 85% V_p, under 2520 l/h. (a) Solid temperature field, (b) Fluid temperature field, (c) Pressure differential, (d)Velocity Vector Field. 113

Figure 5.11 (e)-(f) : Results of the model for a foamed sample of 28 mm height, 1100 µm pore size and 85% V_p, under 2520 l/h. (e) Radial velocity field and (f) Vertical velocity field. 114

Figure 5.12 (a)-(b) : Results of the model for a foamed sample of 28 mm height, 1100 µm pore size and 85% V_p, under 1800 l/h. (a) Solid temperature field, (b) Fluid temperature field. 114

Figure 5.12 (c)-(f) : Results of the model for a foamed sample of 28 mm height, 1100 µm pore size and 85% V_p, under 1800 l/h. (c) Pressure differential, (d)Velocity Vector Field, (e) Radial velocity field and (f) Vertical velocity field. 116

Figure 5.13 (a)-(d) : Results of the model for a foamed sample of 28 mm height, 1100 µm pore size and 85% V_p, under 1260 l/h. (a) Solid temperature field, (b) Fluid temperature field, (c) Pressure differential, (d)Velocity Vector Field. 116

Figure 5.13 (e)-(f) : Results of the model for a foamed sample of 28 mm height, 1100 µm pore size and 85% V_p, under 1260 l/h. (e) Radial velocity field and (f) Vertical velocity field. 117

Figure 5.14 (a)-(b) : Results of the model for a foamed sample of 28 mm height, 1100 µm pore size and 85% V_p, under 720 l/h. (a) Solid temperature field, (b) Fluid temperature field. 117

Figure 5.14 (c)-(f) : Results of the model for a foamed sample of 28 mm height, 1100 µm pore size and 85% V_p, under 720 l/h. (c) Pressure differential, (d)Velocity Vector Field, (e) Radial velocity field and (f) Vertical velocity field. 117

Figure 6.1: SEM pictures of pure Al replicated foams made out of similar salt preforms (porosity≈ 25%) infiltrated at various pressures P_{inf}: a) P_{inf} = 2 bars, b) P_{inf} = 5 bars, c) P_{inf} = 10 bars, c) P_{inf} = 155 bars. Figure reproduced from [100]. It is the same image as *Fig.3.21*. 122

Figure 6.2: Thermal efficiency of 28 mm tall samples under three different volumetric flows: 400, 1400 and 2400 l/h 125

Figure 6.3: Thermal efficiency of 12 mm tall samples under three different volumetric air flows: 400. 1400 and 2400 l/h. 125

Figure 6.4: Schematic representation of the confined impingement box used in the experimental work of Ref. [247] 126

Figure 6.5: Velocity magnitude contours and Stokes streamlines obtained from the CFD results in the symmetry from Ref. [247] 126

Figure 6.6: Comparative presentation of other studies with regard to the global heat transfer coefficient of foams: silver colour stands for aluminium foams and orange for copper. [125],[133],[151], [158]. 128

Figure 6.7: Schematic representation of the testing configurations used in the work whose results are summarised in *Fig.5.4. a) description in* [158]*, b) description in* [125] *, c) description in* [133]*, d) description in* [151] 128

Figure 6.8: Evolution of the surface temperature of the aluminium foam (400-450 μm, 85% V_p) and the outflowing air under a 2520 l/h air flow rate as a function of the distance from the heated surface. 131

Figure 6.9: Evolution of the surface temperature of the aluminium foam (pore size 400-450 μm, 85% V_p) and the outflowing air under a 1800 l/h air flow rate as a function of the distance from the heated surface. 131

Figure 6.10: Evolution of the surface temperature of the replicated aluminium foam (400-450 μm, 85% V_p) and the outflowing air under 1260 l/h air flow rate as a function of the distance from the heated surface.mm 132

Figure 6.11: Evolution of the surface temperature of the aluminium foam (400-450 μm, 85% V_p) and the outflowing air under a 720 l/h air flow rate as a function of the distance from the heated surface. 132

Figure 6.12: Evolution of the global heat transfer coefficient of the replicated aluminium foam (400-450 μm, 85% V_p) under various air flow rates for both experimental and simulated results. 133

Figure 6.13: Evolution of the surface temperature of the aluminium foam (900-1300 μm sea salt, 85% V_p) and the outflowing air under a 2520 l/h air flow rate as a function of distance from the heated surface. 134

Figure 6.14: Evolution of the surface temperature of the aluminium foam (900-1300 μm sea salt, 85% V_p) and the outflowing air under a 1800 l/h air flow rate as a function of distance from the heated surface. 134

Figure 6.15: Evolution of the surface temperature of the aluminium foam (900-1300 μm sea salt, 85% V_p) and the outflowing air under a 1260 l/h air flow rate as a function of distance from the heated surface. 135

Figure 6.16: Evolution of the surface temperature of the aluminium foam (900-1300 μm sea salt, 85% V_p) and the outflowing air under a 720 l/h air flow rate as a function of distance from the heated surface. 135

Figure 6.17: Evolution of the global heat transfer coefficient of the replicated aluminium foam (900-1300 μm sea salt, 85% V_p) under various air flow rates for both experimental and simulated results. 136

Figure 6.18: Sensitivity analysis for the replicated aluminium foam (900-1300 μm sea salt, 85% V_p) under 2520 l/h air flow rate. The experimental error was added and subtracted to the measured static pressure values inside the central channel. 136

Figure 6.19: Sensitivity analysis for the replicated aluminium foam (400-450 μm, 85% V_p) under 2520 l/h air flow rate. The experimental error was added and subtracted to the measured static pressure values inside the central channel. 137

Figure 6.20: Temperature difference between the metal and air for a 28 mm tall replicated aluminium foam (400-450 μm, 85% V_p) under 2520 (left) and 720 l/h (right) air flow rate. 138

Figure 6.21: Temperature difference between the metal and air for a 10 mm tall replicated aluminium foam (400-450 μm, 85% V_p) under 2520 (left) and 720 l/h (right) air flow rate. 139

Figure 6.22: Temperature difference between the metal and air for a 28 mm tall replicated aluminium foam (900-1300 µm, 85% V_p) under 2520 (left) and 720 l/h (right) air flow rate..... 139

Figure 8.1: Comparison between the experimental and permeability values by the model for different pore sizes and volumetric porosities (Image courtesy of D. Ingram)..... 148

Figure 8.2 Comparison between the experimental and predicted Forchheimer coefficient values by the model for different pore sizes and volumetric porosities. (Image courtesy of D. Ingram)..... 148

Figure 8.3 Cross section of the setup of the thermal fatigue. The LN_2 dewar in which the nitrogen gas is cooled is not shown. 149

Figure 8.4: Temperature vs. time history obtained for a piece of aluminium foam inserted in the thermal cycle setup. The setup is controlled by a LabView program prepared in house that allows setting the minimum and maximum temperature as well as the hold times as T_{min} and T_{max}. 150

Figure 8.5: Schematic showing the Integrated Structure (IS) and the coordinate system.151

Figure 8.6*:* Influence of the thickness of the first (composite) and the last (porous aluminum) layer of the integrated structure on its warpage : the calculated warpage w is given as a function of the thickness of the aluminum-diamond layer (in blue) or the microcellular aluminum (in green), holding other parameters at the following values: thickness of the Aluminum Nitride t_1 = 500µm, AlN Young's modulus E_1 = 320GPa, diamond/Aluminum composite modulus E_s= 200 GPa (corresponding to roughly 55% diamond by volume) with its thickness t_s fixed at 1100µm when calculating the blue curve, microcellular aluminum modulus E_2=3GPa (corresponding to roughly 88% porosity in closed-pore Al foam or roughly 70% porosity in replicated open-pore microcellular aluminum such as that produced in our experiments) with its thickness t_2 fixed at 4 mm when calculating the green curve..... 152

Figure 8.7: Evolution of thermal resistance of the interface material versus time. As seen, the thermal resistance of the paste remains constant under a constant air flow, which keeps also the temperature constant. The amount of thermal paste or the way it is distributed in the contact do not seem to play a key role in this degradation..... 153

List of Tables

Table 1: Microstructural characteristics and geometry of the cylindrical specimens tested under natural convection..... 42

Table 2: Microstructural characteristics and geometry of the finned structures tested under natural convection..... 43

Table 3: List of tested samples and their properties..... 56

Table 4: Physical constants used by the model and their values. 100

Table 5 :Brief selection of key results under forced convection..... 154

Table 5 : Brief selection of key results under forced convection..... 155

Table 5 :Brief selection of key results under forced convection..... 156

Chapter 1 Introduction

The present thesis addresses heat transfer in metal foams, with focus on thermal management of power electronics. The proposal of the thesis at hand is the performance of aluminium foams as a part of an integrated heat sink that is manufactured in one step and combines thermal stress reduction, thermal spreading, electrical insulation and heat transfer through the aluminium foam to a fluid, in particular air. Main attention is laid here on how the geometrical characteristics of the foam, i.e. pore geometry, pore volume fraction and size, influence heat extraction efficiency.

1.1 Introduction and motivation of the research

The global electrical energy consumption of transportation is rising because of a steady increase in the use of electrical actuators and on-board electronic equipment [1][2]. Power electronics, *i.e.,* the technology of efficiently processing electric power, plays an essential part in this technical evolution.

One of the main challenges in packaging of power electronics is the evacuation of the rising amount of dissipated heat under the lowest possible power consumption and weight penalty; designs ought to be of high reliability and low cost [3]. In particular, the continuous demand for higher performance processors has led to a steady increase in power consumption and dissipated heat flux on the semiconductor level across all devices, such as laptops and mobile phones, as well as workstations and servers [4][5]. This growing demand for both electronics able to withstand higher temperatures and consequently, for cooling systems dissipating larger quantities of heat can be seen in *Fig.1.1*, where one can note that service temperatures are anticipated to become particularly high in the automotive sector. Moreover, as the market of electric and hybrid electric vehicles continues to grow. This trend will become more evident with the years, since the number of electric and hybrid vehicles in the transportation sector (e.g. aerospace, railway, etc.) rises.[6]

Rising power density and current in the microprocessors create several challenges in thermal management, which include the reduction of on-chip hotspots, or package and interconnection Joule heating [7]. If these are excessive, degradation or failure of the system might occur through several mechanisms, including, junction failure, resistor drift, metallization failure, corrosion, thermal runaway, or current assisted diffusion, i.e. electromigration [3][8]. Hence, it is crucial to keep local temperature values in an electronic package within acceptable limits.

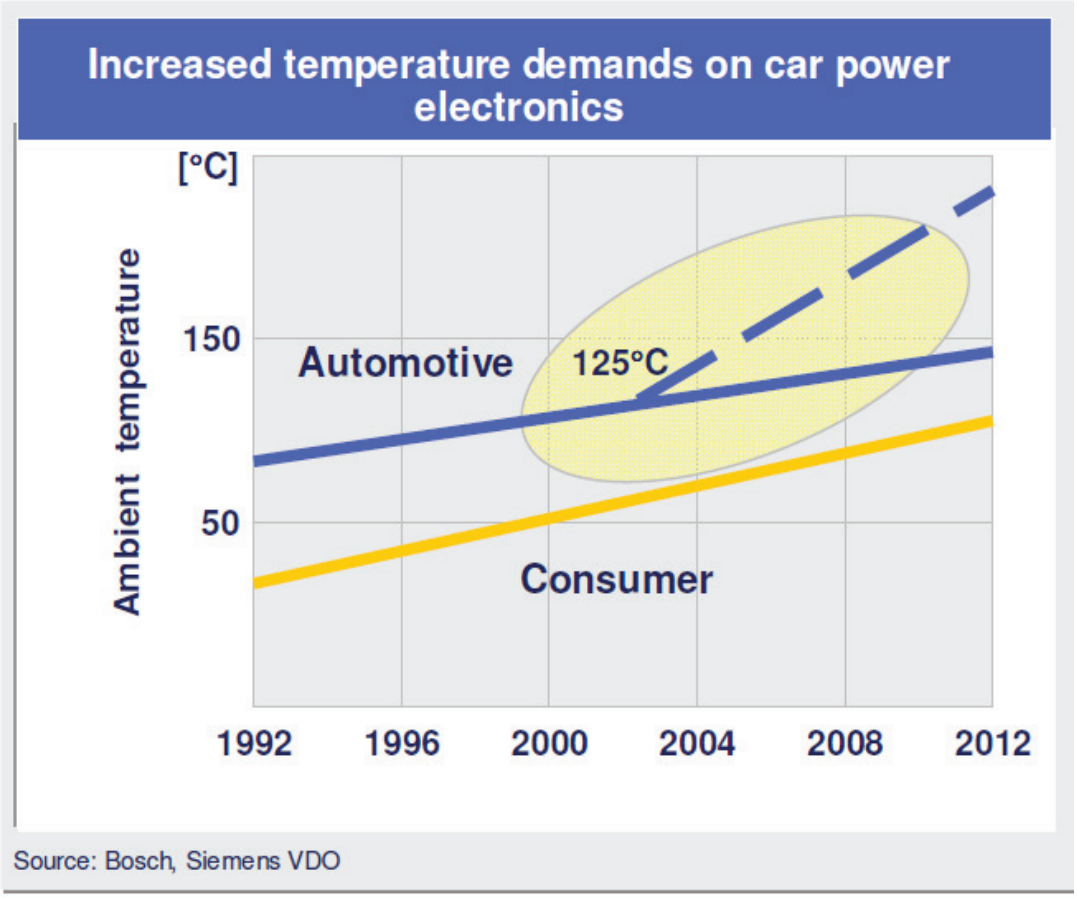

Figure 1.1: Evaluation of the need for high temperature electronics, primarily high temperature circuit boards stable above 140°C. As seen, after 2003 this trend towards high temperatures becomes even stronger [9].

Current challenges in thermal management can be viewed in terms of a set of different but interlinked problems [3][10] [11]:

(i) The chip temperature must be kept low despite a high local heat generation density. Losses in performance of some electric/electronic components are much greater in a hotter environment. The high heat loads extracted from the chip must be handled at the assembly or module level.

(ii) Catastrophic thermal failures, as a result of thermomechanical fracture of a mechanical element in an electronic package, should be prevented. The failure rate is documented to increase exponentially with the operating temperature [3].

(iii) While many of the modern active cooling strategies, such as phase change materials [12] or thermionics [13], may provide sufficient levels of heat extraction, these technologies are viewed as too complex for the transportation sector.

Thus, pushing the limits of highly efficient forced convection designs seems to be a viable strategy; this, however, requires breakthroughs in advanced cooling and system design at several levels [3]. The thermal engineering of electronics, the importance of which has increased significantly over the years [14], is likely to be an area of rapid progress, particularly in the transportation sector.

1.2 Statement of the problem and proposed approach

Three major objectives should be achieved through thermal management:

(i) Prevention of catastrophic failure by one-time overheating or by thermo-mechanical fatigue.

(ii) Improvement in the efficiency of the system.

(iii) Extension of the useful lifetime of the electronic device by reducing the amplitude of thermal cycles.

These objectives affect in particular the design of integrated Insulated Gate Bipolar Transistors (IGBT) modules. In recent years, the need to increase the reliability of high-power IGBT multichip modules has been one of the most powerful drivers for the design of new products in thermal management, especially among products intended for traction (railway and automotive), for power transmission, and for power distribution applications.

Heat sinks of high-power IGBT modules should fulfil requirements of (i) high thermal conductivity, (ii) high dielectric strength required for electrical insulation between semiconductor devices (IGBTs and diodes) and a device substrate (base plate), coupled with (iii) a low thermal expansion coefficient mismatch with the surroundings, notably with electronic components, in order to minimize thermo-mechanical stresses that would reduce the component lifetime. In classical designs, such as that illustrated in *Fig.1.2*, [15] power electronic devices are soldered onto metallised ceramic substrates of relatively high thermal conductivity (Al_2O_3 or AlN)[16][17], which provide electrical insulation, and then, the whole system is connected to a heat sink. Sometimes, a heat spreader is placed between the electrical ceramic insulation and the chip. However, these designs comprise many interfaces between different materials or subcomponents, which add extra thermal resistance, thus making the heat management of the IGBT more difficult. For instance, the thermal resistance of a commercial thermal grease can account for up to 26.9% of the overall thermal resistance of the heat sink in the Intel Core Duo™ [18][19], counting the latter from the junction to ambient air.

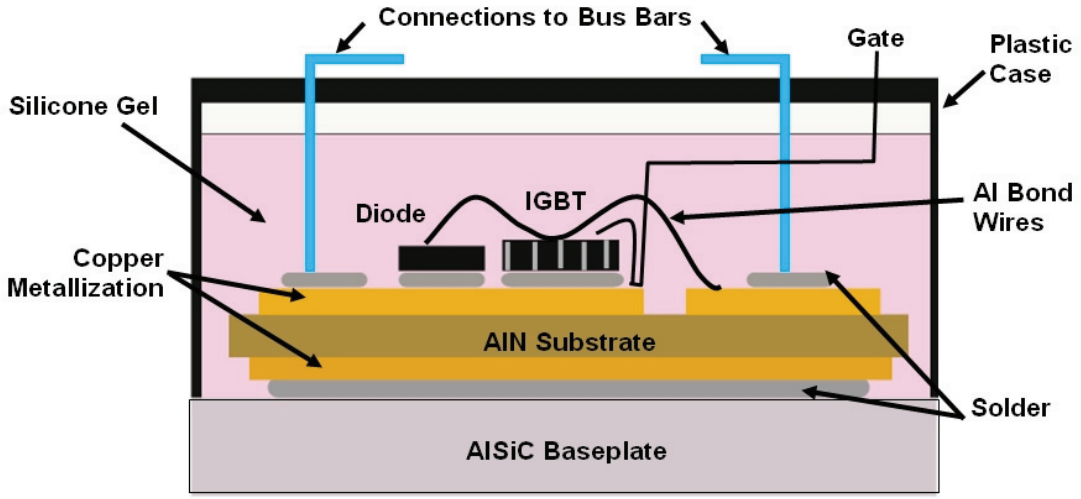

Figure 1.2: Typical schematic of an IGBT Module Assembly [15].

In the present thesis, the approach that is explored is the production of an integrated multimaterial composite substrate of metal and ceramic comprising three stacked layers, as illustrated in *Fig. 1.3* :

(i) A first layer to act as a heat spreader, made of an aluminium composite reinforced with diamond particles, of high thermal conductivity and electrical conductivity coupled with a tailored Coefficient of Thermal Expansion (CTE), onto which the IGBT is to be brazed. This layer is introduced to spread the heat given off by the chip, and also to minimize the level of thermal mismatch stress within the package by having a CTE near that of the electronic component.

(ii) A layer of a highly thermally conductive ceramic (Al_2O_3 or AlN) to create an electrical insulation barrier, in the present work we use plates of aluminium nitride (AlN).

(iii) A highly porous aluminium foam designed to allow air to efficiently extract heat out of the stack, as measured by a high overall heat transfer coefficient *h,* based on the footprint area of the device. Specifically, we explore here open-pore microcellular aluminium produced by the replication process.

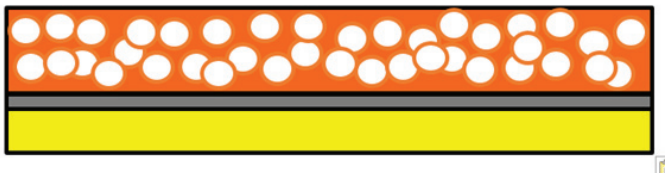

Figure 1.3: Proposed solution, with yellow for the aluminium diamond composite, grey for the ceramic layer and orange with white circles for the aluminium foam.

1.3. Objectives of this thesis and statement of the novelty of the proposed work

The present thesis' objective is twofold. A first objective is to explore the processing, design and performance of *integrated structures* as regular heat sinks under the jet impingement configuration, as opposed to layered bonded assemblies classically used in industry. These structures should

i) have the potential to sustain a heat flux of the order of 10W/cm^2 [3] across their thickness and spread it within their plane,
ii) be mechanically compatible with a chip that heats up by more than one hundred Kelvin above room temperature and has a coefficient of thermal expansion (CTE) of roughly 5 ppm/K,
iii) be electrically conductive along the interface with the chip while presenting an electrically insulating barrier to a voltage difference on the order of $\Delta V = 1$ kV across their thickness
iv) be capable for implementation in applications where there are limitations in terms of space, weight and complexity and
v) be able to operate within a temperature range from -40°C to 150°C [20].

The underlying logic is that integrated thermal management structures that seamlessly combine metal and ceramic phases can achieve far higher thermal performance than current assembled multilayer structures. The reason is that such structures reduce interfacial heat transfer barriers that strongly limit the performance of layered structures. Furthermore, the use of metal foam subjected to an air flow to actively cool the structure takes advantage of the qualities of metal foams for heat transfer, as discussed before, without decreasing its simplicity. Although there are various other possible solutions under research which can face current challenges in electronics thermal management, few have, to our knowledge, focused on elimination of interfaces [21] as is the focus of the thesis at hand. By the same token, the production of integrated structures in a single infiltration step would not only improve the homogeneity of the heat sink but also, the processing of these heat sinks might be simplified [22].

The second objective of this thesis, and its greatest focus, is to explore and quantify the performance of replicated aluminium foams as heat exchangers between a solid surface and air in the jet impingement configuration, exploring the influence of foam microstructural parameters (relative density, pore size, processing parameters notably the infiltration pressure) and macroscopic parameters (foam geometries and gas inlet) on the performance of the aluminium foam in active cooling.

Chapter 2 Literature Review

The chapter at hand presents the current state of the art in the use of metal matrix composites and metal foams for thermal applications. The latter category of materials is considered a special case of metal matrix composites, where the second phase is void (gas). Among this large amount of work, we will focus in the current review, on (i) the use of aluminium diamond composites in electronic packaging and (ii) metal foams used for single phase convective heat transfer. Other aspects of these materials, such as the thermal conductivity of metal foams or the general use of metal matrix composites will be shortly reviewed, for the sake of completeness.

2.1 Metal matrix composites in thermal management

It is well accepted that failure due to CTE-mismatch thermal stresses is a rather common problem in electronics [20], [23]–[26]. Due to the large thermomechanical mismatch between silicon substrates and metal thin films in general, electronic structures may also experience significant thermal stresses, causing structures to deform. This can lower the rate of heat transfer from the IGBT to the cooling body it is mechanically attached to [27][28]. Another CTE-mismatch-related main failure mechanism of power modules is associated with the thermomechanical fatigue of the solder alloy layers. In general, fatigue phenomena occur also in the solder between the silicon chip and ceramic substrate; these can be exacerbated by process-induced voids, which can both interact with the thermal flow and hasten crack initiation within the solder layer. Gross voids and extended fatigue-induced cracks can severely affect dissipating devices, increasing the peak junction temperature of an IGBT and thus accelerate the evolution of several failure mechanisms including bond wire lift off and solder fatigue [14][29].

To alleviate such CTE mismatch problems, Metal Matrix Composites (MMCs) have been explored and are now used in electronic substrates, as manufactured e.g. by CPS Technologies (Norton, Massachussetts, USA) [27]. Metal Matrix Composites (MMCs) are materials that have received considerable attention in the thermal management of high-power electronics for the last two decades and are now used in significant production applications [30][26], because of their capacity to combine high thermal conductivity, relatively low density, and a tailored coefficient of thermal expansion [3][30]. The latter can be exploited to match the CTE of materials used in power semiconductor assemblies such as silicon, gallium arsenide, or alumina. The optimal design of MMC components is based on careful selection of matrix materials, reinforcements, together with the geometry, volume fraction and distribution of the two phases.

Although other metals have been explored [3][30], aluminium is often preferred as a matrix material because of the combination of its low density, good thermal and electrical conductivities, adequate mechanical strength, and excellent resistance against corrosion. The application of such aluminium matrix composites in

electronics packaging market has thus been growing rapidly over the past two decades [1][8],[16–19].

Aluminium Matrix Composites (AMCs) were first developed to meet very high performance defence and aerospace needs. As material cost became a more significant consideration, the emphasis shifted from fibre- towards particulate reinforced materials, with the goal of a lower-cost, high-volume product that could be used in commercial applications, notably ones in sectors where low weight is important, such as transportation. AMCs reinforced with SiC have been used for years in thermal management, as a heat sink material in electronics. Other AMCs that have been explored for thermal applications include boron reinforced aluminium, continuous carbon fibre reinforced aluminium, discontinuous carbon fibre reinforced aluminium, carbon flake reinforced aluminium, silicon reinforced aluminium and diamond particle reinforced aluminium, to be used here [3][30]–[33].

The use of diamond is not new in heat management of electronics. It was proposed for various reasons as far back as 1968 [34] to serve as a heat spreader, ducting heat from the chip to another area from where it can be dissipated into the surroundings. The main driver for its use is its high heat conductivity (2000W/mK at room temperature, depending mainly on its nitrogen content) [35]–[37].

More recently, first in 1992 [38] and later in works of other groups [39][40][41], one finds reports of composite structures incorporating diamond layers that were fabricated as a solution for thermal management of electronics. Substrates produced based on this approach, namely Silicon On Diamond (SOD), show a strongly improved electrical and thermal performance compared with current Silicon on Insulator technologies, especially with the diminishing size of the substrate [42]. This technology is, however, feasible only for a specific geometry in IGBTs. Furthermore the CVD process involved in the manufacturing is inherently expensive.

2.2 Aluminium diamond composites in thermal management

By the same token, the use of diamond particles in MMCs is not new either. In 1991, a US patent [43] was awarded for the use of metal matrix composites with diamond particles as heat sinks for semiconductor devices. Since then, copper [44]–[47], aluminium [48], cobalt [49] and silver [50][51] have been examined as MMC matrices for heat sinks—with research still going on—so as to take advantage not only of the good thermal behaviour of diamond, but also to have a coefficient of thermal expansion (CTE) near that of silicon, as seen in *Fig.2.1* [52].

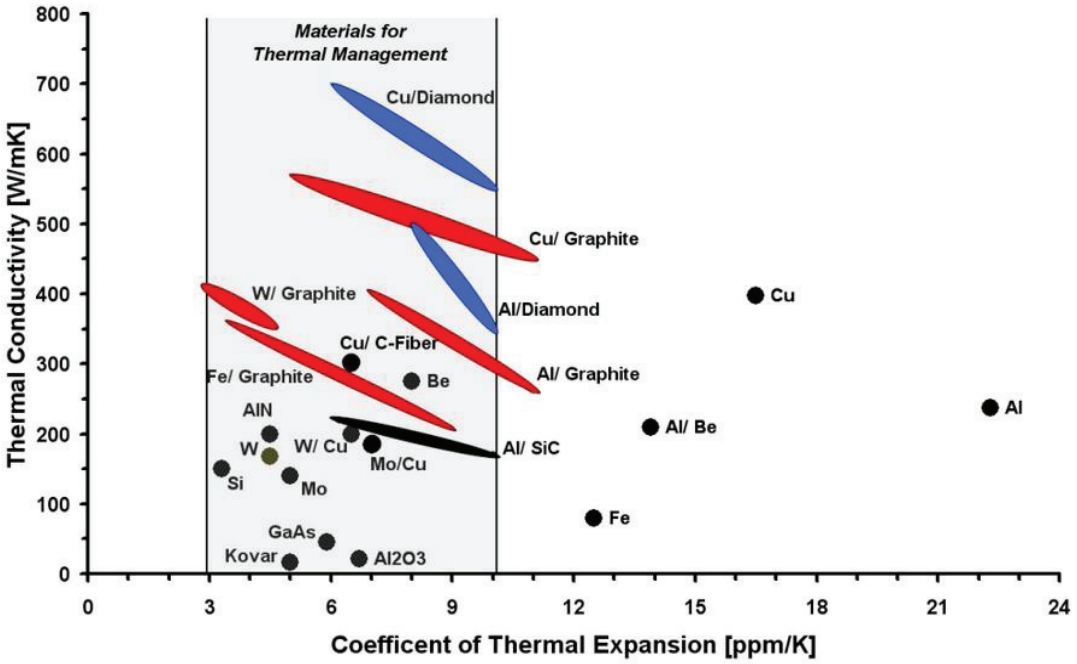

Figure 2.1: Ashby plot of thermal properties for various thermal management materials,© Fraunhofer IFAM Dresden [52].

Various groups have been working with aluminium/diamond composite materials. Initially, a group lead by W.B. Johnson, started to produce their own aluminium/diamond composites, with a view to applications as heat sinks for electronics [48]. Since then, several other groups have investigated various aspects of these materials [53]–[66].

Generally speaking, four methods have been used for the fabrication of metal matrix diamond composites: a) Liquid metal infiltration, b) Spark plasma sintering, c) High Pressure-High Temperature sintering method and d) Hot pressing. Most often, given the need for high volume fractions of ceramic, the technique used is infiltration of packed particle preforms of diamond; nonetheless, some groups have created aluminium diamond composites via sintering (hot press or plasma) [66], [67] of powder compacts or by other powder metallurgy techniques[68].

In the liquid metal infiltration process, aluminium is heated up to ~700-850°C and then is either let to spontaneously infiltrate the diamond preform or it is driven into the preform by applying pressure, using a piston (squeeze casting) or an inert gas (gas-driven pressure infiltration, using mainly Ar) [37][53]–[55], [58], [61], [62], [69]–[71]. In gas-pressure infiltration, the metal is often preheated around 100°C, above the aluminium melting point or liquidus (for alloys) before infiltration[37][69][70]. The infiltration process as such has an average duration of some minutes if aided by pressure. On the other hand, this step of the process lasted several hours when it was pressureless [48][57][59] as in the Lanxide process [72], [73], which can produce net or near-net shape composites.

Recently, there have been several papers on Al/diamond composites made by spark plasma sintering: aluminium-based powder is packed with diamond particles in a die and then is pressed up to 50-80MPa. Then, spark plasma sintering is performed at a temperature in the range of 818-878K. Results seem to indicate strong bonding between the diamond particles and the Al–matrix in the composite; however, such composites have thermophysical properties inferior to those obtained in composites made by infiltration or sintering [63]–[65], [67].

Finally, a group in China has succeeded in fabricating diamond/Al composites with 20–50 vol.% diamond via a classical powder metallurgy technique, namely vacuum hot pressing [68], [74], [75]. The composites exhibited a wide range of thermal conductivities of 320–567 W/mK, depending on both the diamond volume fraction and the diamond coating, making this fabrication route an attractive powder metallurgical alternative to spark plasma sintering.

I. Coefficient of Thermal Expansion

The volume fraction of reinforcement is important, since it dictates to a significant degree the intrinsic properties of the composite such as its thermal conductivity or its coefficient of thermal expansion (CTE). The CTE of the composite as a general rule diminishes when the diamond fraction rises [48][44–46],[50–54]; its value is usually measured experimentally using a dilatometer.

Aluminum metal matrix composites need a high diamond volume fraction in order to attain a low effective CTE since the aluminium matrix has a relatively high CTE of 23 ppm/K [76]. With regard to aluminium diamond composites, the diamond fraction should be close to 60% in order to have an effective CTE similar to silicon [70], meaning smaller than 10 ppm/K [76]. Various models exist to predict its value, such as the Turner model [57][58][67], the variational approach of Hashin and Shtrikman, extended by Shapery [77] and the Kerner model [58][63][77]. This last model coincides with one of the variational bounds and is generally appropriate for predicting the CTE of particulate aluminium diamond composites [77].

II. Thermal Conductivity

Bounds were proposed by Hashin and Shtrikman [77] for the thermal conductivity of isotropic composites. Maxwell developed a mean-field model [77]; this model does not take into account finite interface thermal conductance between particles and matrix. Hasselman and Johnson [56][60][67][70] gave an explicit formula taking into account a finite interface thermal conductance, for spherical reinforcements.

The Differential Effective Medium (DEM) model is prominent amongst the models being used, since it typically yields good agreement with experimental results and can account for the shape of the reinforcement particles [69][77]–[80]. Other models capable of taking non-spherical inclusions into account include the Maxwell model and the Hamilton–Crosser model [67], the latter being a modification of the first.

In principle, the larger the diameter of the diamond particle reinforcement, the better is the effective thermal conductivity of the composite; however, other factors are equally important, such as the volume fraction of diamond reinforcement, the fabrication method, the interface chemistry of diamond particles, the production process or the intrinsic thermal conductivity of the diamond particles. *Figure 2.2* from [55] shows clearly that no matter the matrix material (aluminium as in Cases A and C or AlSi as in Cases B and D) the thermal conductivity of samples fabricated by gas pressure infiltration is much higher than those of samples fabricated by squeeze casting.

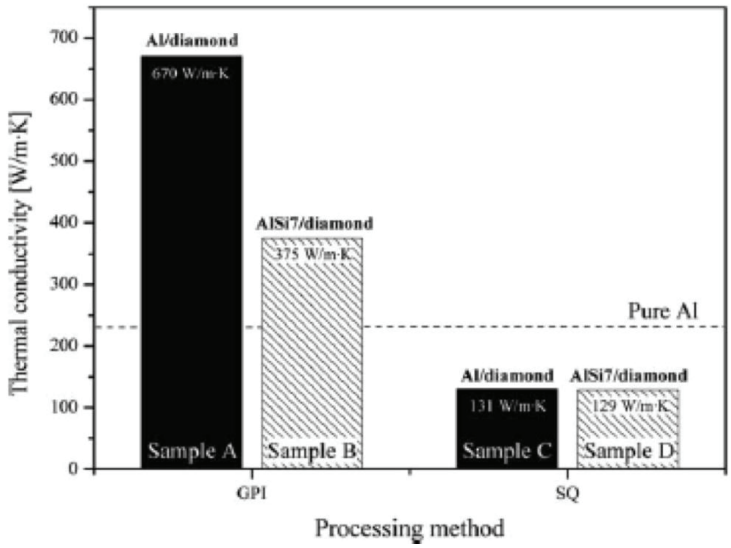

Figure 2.2: Thermal conductivity of composite samples with diamond as reinforcement with regard to their fabrication method [55].

The reason for this discrepancy lies on the reaction between aluminium and diamond to form Al_4C_3, since it advances rather slowly at the processing temperatures of 745/800 °C due to the strong covalent bond between carbon atoms in diamond. The formation of Al_4C_3 can be a predicament in two ways: firstly, it can be strongly deleterious to the thermal conductivity of the composite, potentially lowering its value below that of pure aluminium [48]; secondly, it tends to react with atmospheric moisture or water, resulting in the degradation of the composite[81]. Nevertheless, limited Al_4C_3 formation has been favoured by some authors [55], because limited aluminium carbide formation promotes stronger interfacial bonding and consequently, improved heat transfer across the interface; this explains why gas pressure driven infiltration has led to composites with higher thermal conductivities [37][55][69] in comparison with squeeze casting [70], where little or no Al_4C_3 is formed[54]. Some research teams have coated the diamond particles by Chemical Vapour Deposition (CVD) of a layer of SiC or Ti or W prior to composite fabrication. Their goal was to prevent the formation of Al_4C_3, which is expected from a thermodynamic standpoint upon contact of carbon with aluminium [48][58][61][62][71][81]. However, none of them reached the high thermal conductivities reported in [55], thus confirming the thesis that Al_4C_3 in improves the thermal conductivity of the composite.

Since the exposure time of diamond to the aluminium melt was much shorter in squeeze casting than that in gas pressure infiltration, the infiltration time is an important parameter, affecting the thermal conductivity of diamond composites. This was proven in [82]–[85], where the contact time in infiltration of diamond preforms with aluminium was found to have an optimum that depends on the temperature (*Fig.2.3*). In similar work, researchers varied the infiltration temperature and pressure to tailor the thermal conductance of the interface and consequently, the thermal conductivity of the composites. In order to overcome this limitation, researchers modified the squeeze casting process, achieving thermal conductivities close to the samples produced by gas pressure infiltration, by increasing the time of contact of particles with liquid aluminium, a parameter that was found to be of critical importance[86].

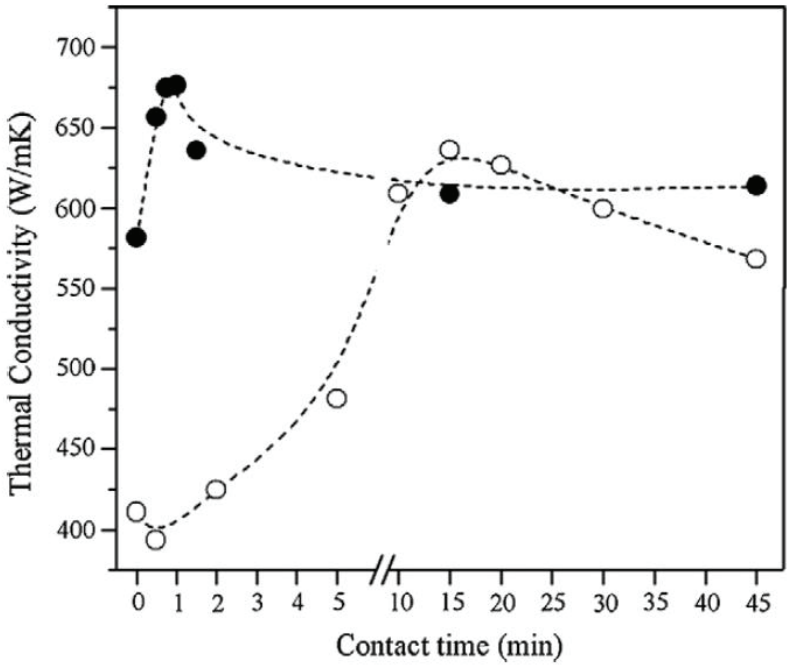

Figure 2.3: Thermal conductivity of aluminium/diamond composites, along with the contact time for two infiltration temperatures: 760°C (empty circles) and 850°C (filled circles) [84].

The formation of Al_4C_3 also improves the adhesion between the diamond particles and the aluminium matrix— this interface conductance between Al and diamonds was found to be a critical parameter for the effective conductivity of the composite [87]–[90].

On this basis, research teams with a goal to achieve the highest possible thermal conductivity in diamond-based composite materials, use relatively large diamond particles (in the range 90–450 μm), maximising the distance of phonon conduction without meeting an interface, since the tailoring of the latter is the key for an enhanced thermal conductivity in Al-diamond composites [91].

Furthermore, monocrystalline synthetic diamond particles appear to have a better surface contact with the matrix than polycrystalline synthetic diamond, thus diminishing the scattering of phonons through the interface [53]. Secondary treatments such as ageing or annealing have been found to be of small effect on the thermal conductivity of the composites[92].

Last but not least, another way of increasing the thermal conductivity of aluminium diamond composites is to increase the diamond volume fraction in the composite material. This can be achieved through the use of combinations of diamond particles of various sizes, of the same [37] or of another nature [69] (bimodal mixtures). With preforms combining diamonds of roughly 9:1 size ratios, thermal conductivities of 725 W/m K and 970 W/m K have been obtained for pure Al and Ag–3 wt.%Si matrices, respectively [37]. On the other hand, the use of a bimodal mixture of diamond and SiC particles of the same average size, can help achieving thermal conductivities at lower cost; values of 400 W/m K have been achieved with only 50–60% of diamond in the preform, the rest being low-cost SiC powder [69].

In summary, thermal conductivity is highly affected by the microstructure of the Al-diamond composite [93] with the highest cited values being above 750 W/mK, given in [37], [85] for a monomodal distribution of diamonds.

III. Microstructure

In infiltrated composites, micron-scale diamond particles are well embedded in the metallic matrix and uniformly distributed, while nanodiamonds tend to form strong agglomerates with an overall size ranging from 10 to 500 μm, before being infiltrated [54]. The interface between aluminium and diamond can be characterized as clean for composites made by squeeze-casting. Generally, if the pressure is sufficient, no evidence of either porosity or any other obvious defects is found in the materials. If the aluminium is pure, no other phases than diamond and Al are found, regardless of matrix chemistry for composites manufactured by squeeze casting [70]. Porosity does on the other hand exist in powder metallurgy composites, its amount increasing with increasing volume fraction of diamond [63], [64], [67].

In conclusion, gas pressure infiltration of synthetic diamond particles of diameter above 100 μm is able to yield material with roughly 60 vol. pct of diamond having a thermal conductivity of 600 W/mK and above. The CTE of such composite will be in the range of 6-8 ppm/K over the temperature range from ambient to 200°C. Such properties should be perfectly suited for the thermal management application in power electronics.

2.3 Metal foams in thermal management

I. Introduction

Microcellular metals, often called "metal foams", were firstly recorded in a French patent in 1926 by A. De Meller [94]; they combine metal with a high fraction of porosity, which makes them in some respects a composite of two phases: metal and void (or gas). The pores are either closed (as bubbles in a foam), or open, meaning interconnected and accessible to the outer surroundings through free surfaces of the microcellular metal (as in a sponge). The latter microstructure can explain why these materials can conduct heat comparatively well and have shown in trial experiments a very high performance in convective heat exchange [95], [96]. Consequently, the literature on this subject is quite voluminous (*Fig 2.4*), [97] indicating the growing interest in the field. For an overview of this research subject, extensive reviews on thermal transport through metal foams can be found in the literature [95], [97]–[99].

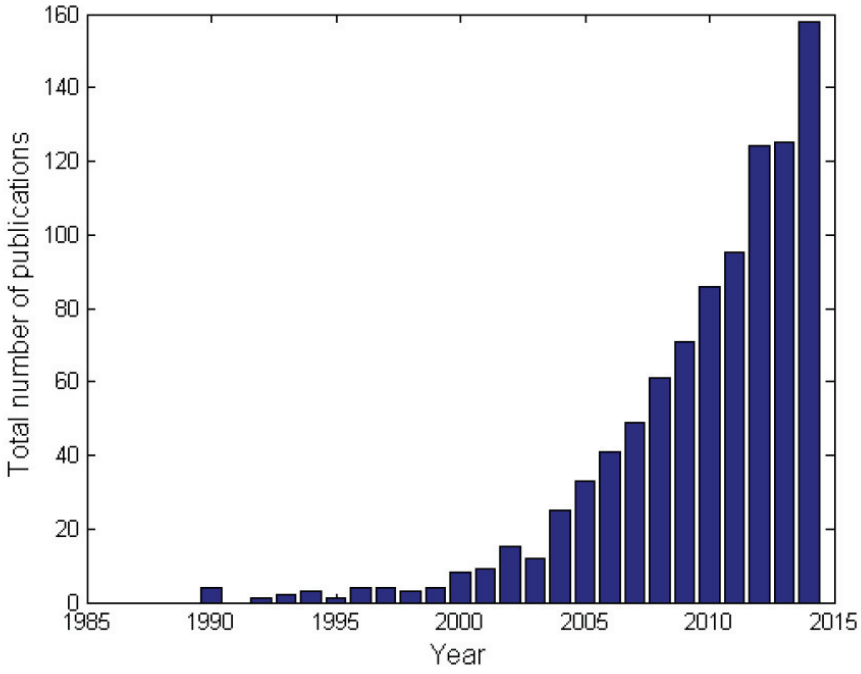

Figure 2.4: Evolution of scientific publication over time as categorised by Google Scholar using the following keywords: "metal foam", "heat transfer" and "open-cell"[97].

Metal foams can be manufactured essentially in three ways, which can be sorted according to the state of the metal making the foam during the process:

(i) *Solid state processes*, which involve primarily sintering of particles

(ii) *Liquid state processes*, in which molten metal is used, in combination either with a solid pattern to keep voids in the structure during solidification or with bubbles of gas that are sufficiently stable to remain in the solidified metal.

(iii) *Deposition processes*, in which the metal is deposited on a polymer template that is usually removed at a later stage [100].

From the above mentioned processes, replication processing, illustrated in *Figure 2.5*, in which an inert leachable pattern is infiltrated by molten metal and then leached in a solvent, is one of the most economical and flexible methods for mass production of metal foams. This process is particularly attractive with aluminium, as NaCl is a cost-effective material for the pattern (in a recent variant of the process designed for larger pore sizes [101], this process has been developed for industrialization by Constellium). Furthermore, the process has the advantage that pores can be made to have relatively regular and well-controlled characteristics (size, shape, volume fraction)[100]–[102].

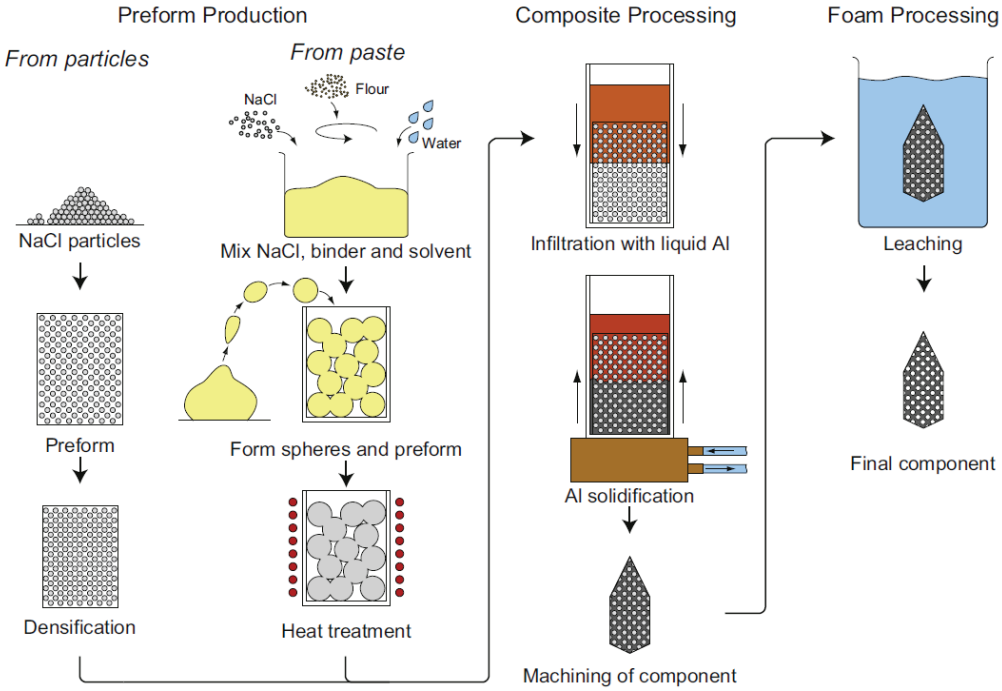

Figure 2.5: Schematic representation of the replication process for open-cell foam fabrication [98].

II. Thermal conductivity

The thermal conductivity of metal foams can be calculated using the same models as those for particulate composites assigning now a zero conductivity to the second phase that is combined with the metal. For the purposes of the present thesis, we will give only a brief summary of thermal conductivity models for metal foam; for a more extensive review collecting a large number of the correlations and models that have been proposed, see Ref. [103].

Despite the non-negligible contribution of thermal radiation to effective thermal conductivity at temperatures above 250°C [99], [104], at lower temperatures the previous assumptions can be considered sufficient—thus both the Maxwell model [105] or the DEM approximation [98] can *a priori* be used. Additional models have

also been proposed for metal foams, as that by Ashby *et al.* [106][107] or analytical models that are based on the strut geometry [108]–[110]. Comparison with data shows that the DEM model performs particularly well in the volume fraction range of interest here i.e. V_p = 0.6…0.9, if the pore shape is adapted to account for deviations from sphericity [106], [107], [111], [112]:

$$k_f = k_m V_m^n \tag{2.1}$$

where V_m is the relative density (or fraction metal, equal to one minus the fraction porosity) of the porous metal, k_m its conductivity (thermal or electric), k_f the conductivity of the foam and n, an exponent that depends on the shape of pores (n=1.5 for spherical pores) [107]. At very low fractions of solid (a few percent), on the other hand, Lemlich's law, which considers the relative conductivity as equal to that of the metal times the fraction metal and multiplied by one-third, gives a good approximation when the metal takes the foam of connected constant-section struts [107][113][114][115]:

$$k_f = k_m \frac{V_m}{3} \tag{2.2}$$

Since empirical or analytical models have been found to be both sufficient and efficient, the use of other approaches, such as trying to extract the effective thermal conductivity values of different open-cell foams using the microCT-CFD approach, is justified only when higher accuracy is required (i.e. in the calibration of simpler models), given the considerable investment of time and resources they require [103], [116].

As a conclusion, the thermal conductivity of the foam of a given material is related to two factors: first and foremost the porosity and secondly, the pore geometry (or in other words the metal architecture). Pore size on the other hand does not influence the conductivity in a significant way.

III. Convective thermal transport

From a heat transfer point of view, open-pore microcellular materials are another type of permeable porous media. The equations that govern the energy transfer through a solid porous stationary medium, saturated with a flowing fluid, assuming the solid phase to be rigid, are [98], [117]:

$$(\rho c_p)_f \left(V_f \frac{\partial T_f}{\partial t} + u \nabla T_f\right) = V_f \nabla (k_f \nabla T_f + k_D \nabla T_f) + h_{sf}(T_f - T_m) + V_f \dot{Q}_f \tag{2.3}$$

for the fluid phase and

$$(\rho c_p)_m V_m \frac{\partial T_m}{\partial t} = V_m \nabla (k_m \nabla T_m) - h_{sf}(T_f - T_m) + V_m \dot{Q}_m \tag{2.4}$$

for the solid phase, where T is the average temperature of each phase, (ρc_p) is volumetric heat capacity, h_{sf} is the average (volumetric) heat transfer coefficient between solid and fluid phases, Q is the volumetric heat generation rate inside each phase, k is the thermal conductivity with subscripts f and m denoting the

fluid and metal phase respectively, V_p =1-V_m is the pore (and therefore fluid) volume fraction, and k_D is an effective thermal conductivity expressing the role of dispersive heat transfer within the fluid.

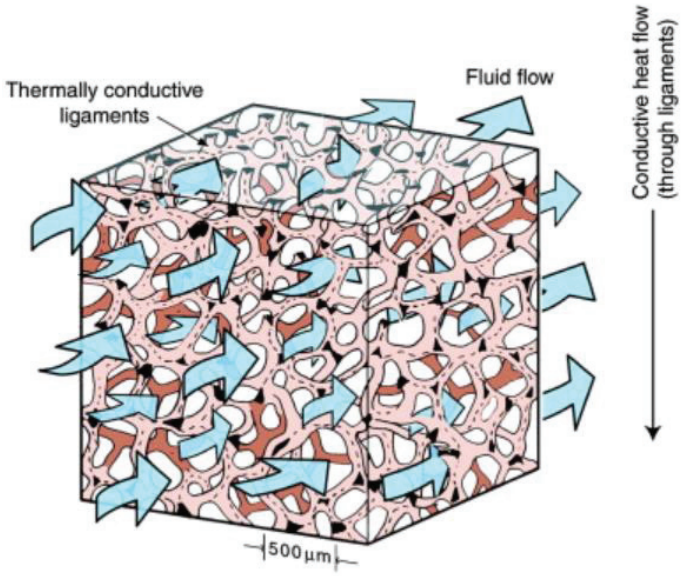

Figure 2.6: Schematic representation of forced convection in metal foams.From [99].

Convective heat exchange between a fluid and open-pore metal foams, illustrated in *Fig. 2.6,* has been investigated by several authors; the two main reasons for metal foams being so attractive as heat exchanger lie in their high surface area and their relatively good thermal conductivity. These properties, when inserted into analytical microstructure based models which practically treat foams as an extensive network of fins [118][119], show a significant impact in one of the most common performance evaluation criteria for heat exchangers, namely the area goodness factor, j/f , where j is the Colburn factor and f, is the Fanning friction factor [96]. Furthermore, foam filaments offer more boundary layer disruption and mixing [120], [121], resulting in significantly more heat transfer surface area, compared with wavy shaped fins [122]; this enhanced mixing capability of metal foams has been confirmed experimentally from Magnetic Resonance Velocimetry (MRV)[123] and from combined particle image velocimetry (PIV) and planar laser induced fluorescence (PLIF)[124] measurements. For an overview of the theoretical correlations that have been proposed for single phase flow and thermal transport through metal foams, one can consult Ref. [122].

Most of the experimental research was conducted placing the foam inside an air duct/wind tunnel, subjecting it to a homogeneous horizontal flow with either a constant heat flux or a constant temperature, imposed under steady state conditions [125]–[140]; the resulting boundary conditions can be symmetrical or not. This configuration, illustrated in *Fig. 2.7,* will be hereafter called the "standard configuration" for convective heat transfer experiments, for brevity purposes.

In all examined experimental cases, metal foam was found to be beneficial for heat transfer; the same conclusions have also been deduced by computational studies based on this "standard configuration" [141]–[144]. Microstructural properties, such as porosity, pore shape, the constituent material (which affects the thermal conductivity) and macrostrostructural parameters (height, thickness) were found to be critical for the thermophysical (heat transfer coefficient, thermal efficiency, heat extraction, pressure drop, etc.) performance of the foam as heat exchanger. Yet, the exact mechanism of these effects as of today is not fully elucidated; researchers have found contradictory results, which are quite often counterintuitive. For instance, the rate of heat transfer does not always increase monotonically with the pore density (number of pores per unit length)[125], [127], [128], [133], [139], [140] or the sample height [126], [127], even when samples keep all the other properties the same; both of these characteristics often appear to have an optimum when it comes to heat transfer enhancement. Another factor that might be playing a role is the exact testing configuration—one example is the different conclusions deduced regarding the role of pore density between a constant base temperature [137] and a constant average heat flux [125], [127], [128]. Mechanisms by which convective heat transfer takes place through metal foams is thus a complicated subject that needs to be further clarified. This need becomes even stronger since the characteristic dimension of metal foams has not been uniquely defined. This makes the unequivocal definition of Reynolds number difficult and consequently, deteriorates the entanglement around the heat transfer mechanism; the square root of the permeability of metal foams, "mean pore diameter", "strut diameter", "cubic representative unit cell", have all been used in literature [96], [122] .

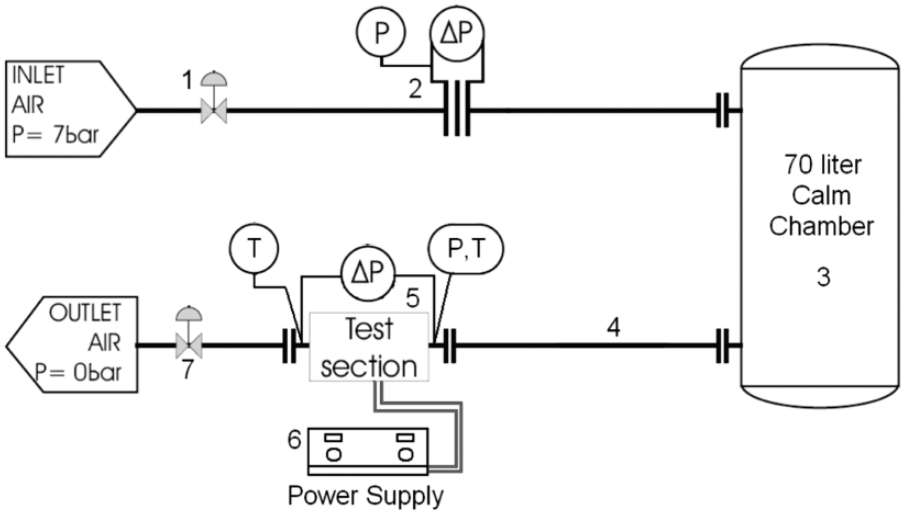

Figure 2.7: Schematic representation of a typical experimental setup ("standard configuration") for testing the performance of metal foam specimens [135].

One of the parameters most influenced by the microstructure is the induced pressure drop in the fluid passing through the foam. The pressure drop through foams has been found to be well described by the semi-empirical correlation of Darcy Forchheimer [124], [134]–[136], [145]–[156], presented in (*Eq.2.5*),

$$\frac{\Delta p}{L} = \frac{\mu_f}{K_d} u + \frac{\rho_f}{K_f} u^2 \tag{2.5}$$

where Δp is the pressure differential, L is the total length over which the pressure drop is taking place, μ_f and ρ_f are the viscosity and the density of the fluid respectively, u is the superficial velocity of the fluid and K_d, K_f are the permeability of the foam and the drag term, both dependent of the foam microstructure. Hence, the same law that governs single phase flow through other porous media, governs the flow through metal foams too, as long as the latter have a minimum length of at least 5 to 6 pore cells, in order to eliminate entrance and exit side effects [148][157].

The permeability of the foam is largely attributed to viscous friction losses within the fluid. Measured values of K_d for foams can vary by many orders of magnitude, with reported values ranging very roughly from 10^{-12} to 10^{-6} m^2. A somewhat smaller spread (one order of magnitude), is found for the values of the drag term, K_f [98]. A possible explanation for this variation lies in the strong dependency of these two characteristics on both the pore size and the relative density V_m of the foam, factors themselves strongly influenced by the fabrication method of the foam. Consequently, despite the plethora of models that connect the permeability and the drag term with the microstructure of foams [122], there is no generally applicable correlation able to straightforwardly predict either the K_d or K_f of a foam by just taking into account only basic microstructural parameters such as the average pore diameter and its metal fraction; factors such as its architecture also intervene and can exert a strong influence.

The previously discussed pressure drop for a fluid through a metal foam is of critical importance for the evaluation of the performance of metal foams as heat exchangers. Comparative studies between foamed and finned structures in the previously described set up [158]–[160] have shown that although foams can dissipate more heat than conventional designs such as finned structures, this is usually done at the expense of a higher pressure drop, something critical for the power consumption of the foam and for its operative cost. Ref. [159] suggests that in order for the foams to be competitive with louver-fin heat exchangers, the price of metal foam should be reduced to roughly \$16/kg (as opposed to ~\$466/kg in 2012). Preheating the working fluid through an economizer—in order to reduce energy consumption—or tailoring the fluid flow rate seem to have little impact on the overall performance of a metal-foam heat exchanger matching the performance of a louver-finned structure, according to Ref. [159]. Computational studies comparing foams with fins or microchannels [161], [162], have also shown similar results, calling for a careful optimization of the foam characteristics (microstructure and geometry).

Under this light and taking into account that the so called “standard configuration” has been studied thoroughly in the literature, variations of this configuration have been studied by researchers in an effort to improve the foam performance. Testing compacted metal foams as a way to decrease porosity has shown to alter significantly the performance of metal foams. On the one hand,

compaction increases the inertial term and decreases permeability of the samples[140], [151], [163], [164], on the other hand, it can increase their thermal conductivity for a given height [140]. The latter appears to be of significant importance where the working fluid is of high heat capacity, in particular water, leading to a decreased thermal resistance of the heat exchanger [151]. On the other hand, where the working fluid is of lower heat capacity [140], compressing foams did not improve their thermal performance. In all cases, since compressed foams induce an increased pressure drop to their working fluid, they are considered more efficient at low flow rates [134]. It should be noted here that compressing metal foams changes significantly the internal structure and so any conclusion regarding the influence of porosity may not apply to situations in which the internal structure does not remain unchanged as the porosity is varied.

Foams with implemented rigid metal blocks in their body, inserted so as to increase locally the thermal conductivity of the samples, have also been studied under the "standard configuration", both numerically [165]–[167] and experimentally [168], [169]. These rigid bodies can have the geometry of fins (plates [166], [168] or elliptic pins [165], [167]) or they can be solid cylindrical blocks [169]. In all numerical studies, results demonstrated that the introduction of fins, no matter their shape inside the foam, can significantly improve the thermal performance (increased heat transfer, more homogeneous temperature distribution) by decreasing the overall porosity of the structure; this however, occurs at the cost of a slight increase of the pressure drop. Still, experimental studies show scattered results. In the case of foams and plate fins, results show that metal foamed structures with inserted bulk metal blocks are beneficial to the overall heat transfer, with finned foam surpassing the thermal performance of single foamed samples or single finned structures. In the case of a solid copper cylinder inside an aluminium foam, the overall heat transfer was not improved but it did promote a more homogeneous spatial thermal regulation. As a special case of a non-homogeneous finned foamed structure [170], a study was carried out with foamed fins. Here, there is not a solid block occupying extra space inside the duct but, on the contrary, there is an empty space between the foamed fins. Experimental results show that the overall heat transfer rises with fins made out of high pore density, low porosity foams. The porous fins used in that study exhibit thermal performance similar to the conventional louvered fin but also inducing an increased pressure drop.

The "standard configuration" has also been used to test metal foams with graded pore sizes. This has been achieved by placing together two different foam samples with different pore sizes (but keeping all the other characteristics the same)[171] or by fabricating metal foams, [172] using the replication process described before, with graded pore size, as seen in *Fig. 2.8.* For both cases, the thermal performance of metal foams was found to be sensitive to the orientation of the sample; the heat transfer rate was enhanced when the fluid flowed first through the section with the larger pores. However, regarding the induced pressure drop to the traversing fluid, in both cases the orientation was found to have a minor effect and lead to mixed results.

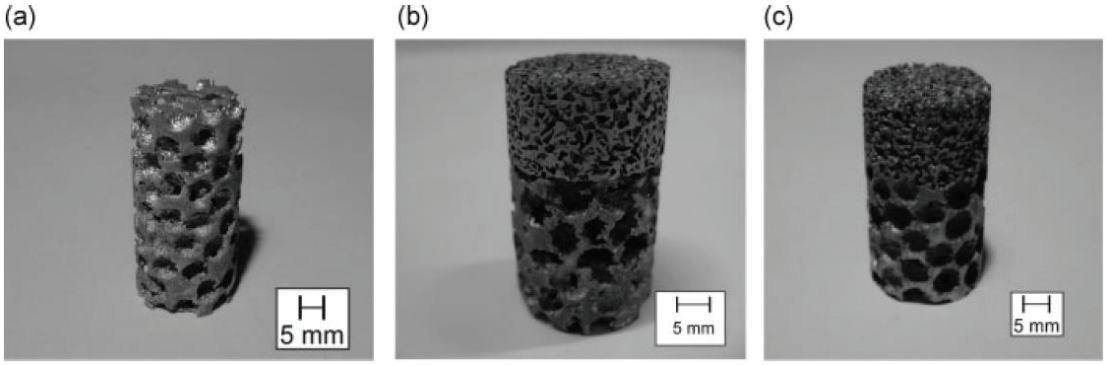

Figure 2.8: Different aluminium foam samples tested in [172]. (a) Single 5mm pore size sample, (b) Segmented sample with one third of the total sample length (vertical in the figure) having 1mm pore size and the remaining two thirds having 5mm pore size, and (c) Integrated sample equivalent to (b), produced via the replication process.

As another way of exploring the thermal performance of foams in the "standard configuration", foamed samples can have different dimensions than the elements in the fluid duct, disrupting the homogeneity of the flow; the goal is to create the so called bypass effect, where for a given pumping power consumption, the respective air fluxes into and around the heat sink are dependent on the relative sizes of the duct and the foam. Research groups have conducted experiments with foams having smaller dimensions than those of the air duct [173], [174]; a schematic representation illustrating a typical set up of this kind is illustrated in *Fig. 2.9* . In the first case [173], aluminium foam samples with a smaller height than that of the duct, high porosity (92%) and various pore diameters (10, 20, 40 pores per inch) were tested experimentally and were found to have a thermal resistance decreasing with increasing fluid velocity and simultaneously to outperform various parallel-plate structures. Separate computational studies investigated also aluminium foams of high porosity and of 5 mm strut thickness under the same scenario; additionally, researchers found an increasing heat removal capacity with air velocity, outperforming results from finned structures, thereby supporting the previous conclusions from the experimental studies. In the second reference [174], three different cases of the bypass effect were created; one with a top bypass, one with a side bypass and one with both top and side bypass. In the last two cases, the foam had also a copper cylindrical solid block implemented in its main body, as in the case described in the foams with integrated solid blocks part. For the same pumping power, the case where the bypass appeared on the sides of the foam (with a copper cylinder in its main body) presented the best thermal performance.

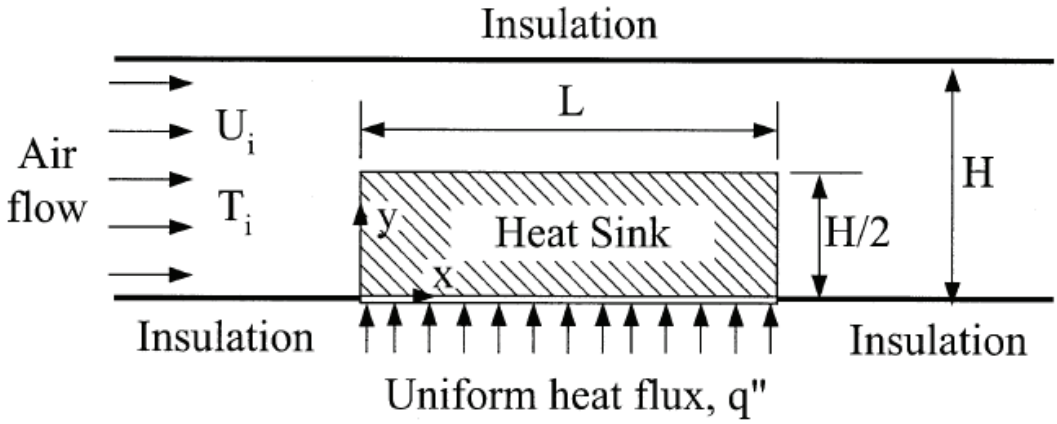

Figure 2.9: Schematic representation of a typical by-pass testing configuration [173].

Oscillating flows through metal foams in the "standard" configuration have also been studied[175]–[181]; a typical experimental set up of oscillating flow can be seen in *Fig. 2.10*. The motivation for this approach rises from the fact that one-directional flow through metal foams creates a relatively high temperature gradient along the flow direction; hence, the so called "hot spots" in electronics can appear and affect the overall reliability of the silicon chip. In these experiments, a sinusoidal oscillating fluid flow goes through the metal foam, under various maximum flow displacements and frequencies. Studies have shown that for a given metal foam, the wall temperature is in phase with flow velocity and no matter the properties of the flow, higher fluid displacements and frequencies produce more uniform and lower wall temperatures. These local surface temperatures are also much lower under an oscillating flow than in an empty channel. Moreover, the pressure drop, the heat transfer and the flow velocity increase with the increase of the kinetic Reynolds number and a dimensionless flow amplitude. Regarding the metal foam properties, the heat transfer rate was enhanced by an increase of the pore density at a constant flow rate; nonetheless, this increased heat transfer came with an increased pressure drop.

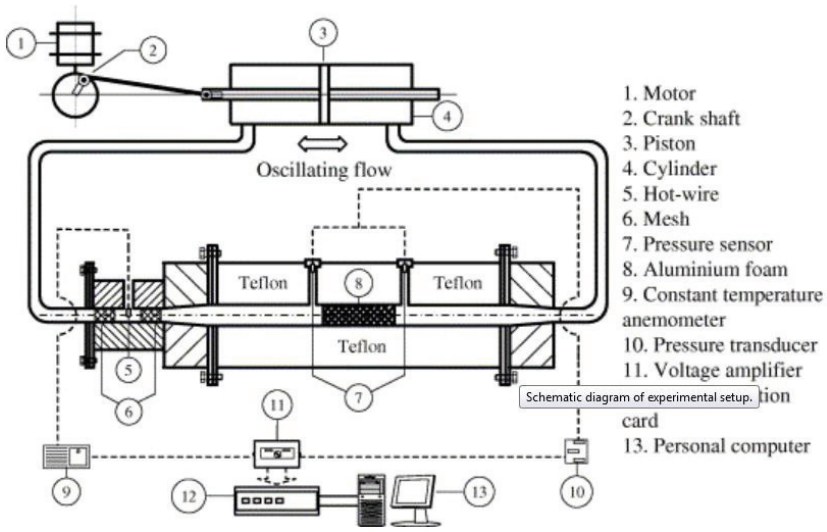

Figure 2.10: Schematic representation of a typical experimental setup for testing the performance of metal foam under oscillating flows [176].

The case of cylindrical pipes filled with foams was theoretically analysed [182], [183], targeting the implementation of metal foams in traditional heat exchanger designs, such as tube-in-tube heat exchangers [184]. Results have shown that higher metal fraction and higher pore density have a beneficial effect for heat transfer but a detrimental effect on pressure drop. Researchers propose using higher porosity foams, made out of high conductivity metals. Compared to plain tubes, the use of metal foams can increase significantly heat transfer (up to 40 times for the same volumetric flow) and compared to finned channels (spiral or longitudinal fins), a metal-foam filled annular channel has superior heat transfer properties, by up to one order of magnitude. Experimental studies [185] of such configurations have verified the enhancement of heat transfer (up to 10 times) of pipes filled with foams, as compared with the case of a single plain tube.

Using the "standard configuration", transient measurements using the single blow technique have also been conducted to test the thermal performance of foams [186]–[189]. The name "single-blow" means that the experiment uses only one fluid stream and heat transfer occurs only between the fluid and the solid surface along which the fluid passes. The heat transfer surface of the test core to be measured is usually a uniformly distributed porous matrix. With this widely used transient technique one can directly obtain the convective heat transfer coefficient between the solid surface and the fluid. Using this method, researchers testing FeCrAlloy, copper [188] and aluminium [186], [187], [189] foams, confirmed previous studies about the beneficial behaviour of foams to heat transfer, with aluminium foams found able to outperform a grilled aluminium structure (depending on their pore geometry and volume fraction) as heat exchangers [186] and steel ball bearings as regenerators [187].

Following the research on metal foams inside pipes for conventional heat exchangers, the case of wrapped metal foam around a tube has also been numerically studied [190]–[193]; this new configuration aims to integrate metal foams into wrapped tube bundles for conventional heat exchangers, as seen in *Fig. 2.11*. The presence of metal foams was shown to be beneficial for heat transfer as compared to bare tube bundle (up to an order of magnitude) and superior to that of conventional finned tube heat exchangers; nevertheless, this enhancement came at the cost of a higher pressure drop. The exact characteristics of the foam (thickness, porosity, thermal conductivity and pore size) have been found to influence significantly the thermal performance of this configuration. The presence of more than one tube in the tube bundle [194] (like in the existence of tube banks) did not alter the previous conclusions.

Figure 2.11: Wrapped metal foams around tubes of different thickness compared with their equivalent finned tube, used as a benchmark. From left to right: Aluminium foam covered tube (5 mm thick), Circular Finned Tube (center), aluminium foam covered tube (15 mm thick) [194].

In all previous cases, with metal foams tested in the standard configuration [195], inside tubes [185] or around foams [196], [197] or even integrated into finned structures [198], the thermal contact resistance between the foam and the solid surface merits consideration. The method of cutting the foam as well as the type of contact (epoxy, brazing, pressed or simple mechanical contact) can influence the thermal performance of metal foams used as heat exchangers. Depending on the type of contact, the configuration and the level of heat dissipation, the thermal contact resistance can vary by two orders of magnitude, i.e. from 10^{-6} to 10^{-4} m^2K/W [195], [198]; consequently this can alter the thermal performance of foam by one-third of the global value [196], [198].

A different configuration than the “standard configuration” that has also been used for testing the thermal performance of foams in single phase flow is

impinging jet flow testing. The advantages of a typical impingement jet configuration are i) the potential for a better thermal performance over the parallel flow condition (10-20% for a fin-pin array [199]), ii) ease of implementation where there is little space available, since it does not demand any flow guiding channels around the heat sink and iii) it retains lower pressure drop and a smaller temperature difference of the cooling flow within the heat sink [200]. In this configuration, illustrated in *Fig. 2.12,* steady state experiments can be performed, with the bottom of the metal (aluminium or copper) foam subjected to a constant heat flux and to a homogeneous fluid flow (namely air), perpendicular to the dissipating/heat generating surface, with the same cross section as that of tested samples. Compared with the standard configuration, where the thermal performance of the structure was mainly based on the foam characteristics, here the exact geometry of the jet impingement can also significantly influence the thermal performance of metal foams as heat exchangers. Characteristics such as the type of the flow source, its cross section (especially when compared with the overall cross section of the foam), its distance from the sample or its relative position to it, all can significantly alter how metal foams exchange heat with the working fluid. The plethora of factors that affect the thermal performance in this configuration unfortunately does not allow for the deduction of unequivocal conclusions.

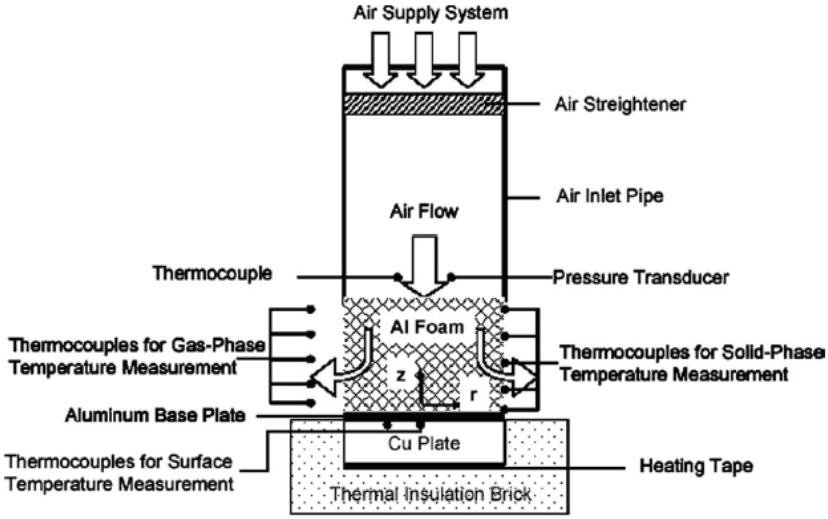

Figure 2.12: Experimental apparatus for the measurement of heat transfer characteristics of aluminium-foam heat sinks in the impingement jet configuration [201].

Researchers have tested this configuration both having the outlet of the fluid flow freely, as in [201]–[203] or confined, as in [204]; In all cases, they have found that the presence of a metal foam is beneficial to heat transfer, the latter increasing with the velocity of the flow. Regarding the foam properties (pore geometry, porosity, thickness and/or height) and the setup geometry (height of the flow restrictor), all have been found to influence the result. Increasing pore density increases the heat transfer, whether the outlet of the fluid flow is confined or not. On the contrary, increased porosity seems to affect negatively the thermal

performance of the metal foam when the flow outlet is confined and positively when not. Furthermore, for unconfined flows, the height of the sample, for a given cross section, was found to strongly affect the thermal properties of the foam and not always monotonically. The heat transfer rate appears to increase for smaller heights, for a given diameter—this is a global trend independent of the foam properties. Whether it has an optimum (at shorter heights) and where that optimum is situated, seems to be influenced by the microstructural properties of the foam (porosity, pore geometry). When the outlet of the flow was confined [204] through a flow-restricting mask at the upper part of a 20 pores per inch foam (forcing the flow to leave the foam at different heights), researchers found that the thermal performance of the foam was improved; the lower the air leaves from underneath the foam (and thus, the closer it is to the hot surface), the better the thermal performance of the sample, with the effect of the confined flow, for a given flow velocity, being stronger than that of the height or pore density. Finally, heat transfer was found to decrease with the thickness of the foam when the flow was confined, no matter the height of the flow outlet.

A plausible explanation of why the increased height (for a given cross section), in the impingement jet configuration, has a detrimental effect on the heat extraction might lie in the flow pattern through the foam; when the height decreases, a higher percentage of the cooling fluid reaches the lower hotter surface of the sample (which is an outcome of the reduced flow resistance). However, at the same time, there is a reduced heat-exchanging area between the cooling air and the solid phase of the aluminium-foam heat sink. With the existence of a restricted flow mask around the foam, this effect is lost, since air is forced to flow to the lower and hotter part of the sample. Therefore, geometrical characteristics or other ways of assuring that the air is flowing until the lower end of the impingement jet are of critical importance.

As with the “standard configuration”, other versions of the impingement jet have also been tested. One of these has the nozzle (a slot jet) placed at the one end of the rectangular aluminium foam [205]; the same end is also isolated, forcing the air to circulate through aluminium foams (of 93% porosity and with 10 or 40 pores per inch) in an L-shape fluid pattern, as seen in *Fig. 2.13*. In this experiment, any effect on the heat transfer from the foam properties (namely, the pore density) or from the cross section of the nozzle, becomes negligible at a fixed volumetric flow; only an increased volumetric flow has a positive effect on the heat transfer rate, at the expense of an increased pressure drop. Nonetheless, this increased pressure drop can be counterbalanced by increasing the pore diameter or the nozzle cross section, since both characteristics have a positive effect, by reducing the pressure drop. Additionally, comparing this configuration to the “standard” configuration, the latter has a slightly better heat transfer rate at higher volumetric flows, at the cost of a higher pumping power. At lower volumetric flows, the impingement jet (with the slot jet place at one end of the sample) produces a better heat exchanging rate, while also requiring a lower pumping power.

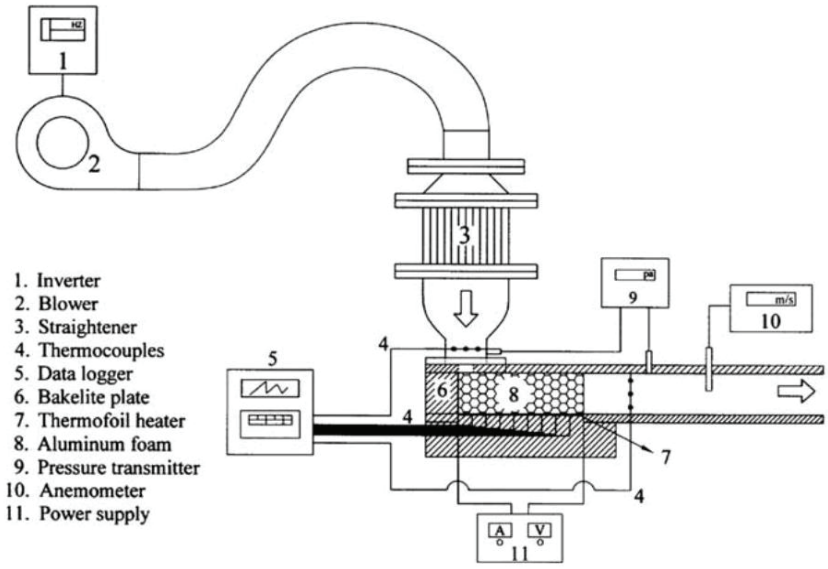

Figure 2.13: Experimental apparatus creating an L-shaped flow through metal foams [205].

Numerical studies [206] have been performed for another version of the impingement jet configuration, where a slot jet was placed in the middle of a metal foam, the latter having a variable height. The slot jet had a cross section smaller than that of the foam (20 times) and the metal foam fixed microstructural characteristics (10 pores per inch, 93% porosity). Varying the volumetric flow, reveals recirculation (and consequently, stagnation) at higher air flow rates. This has opposite effects on average and on maximum local heat transfer coefficient, increasing the former and reducing the latter. Shorter foams, as in the case of impingement jet with a confined outlet, were also found to have a better thermal performance. This configuration, when optimized, showed an increased heat transfer coefficient for metal foams when compared with a flat surface (up to 3 times) and a 30% higher heat transfer coefficient when compared with plate fin heat sinks. Additional numerical studies of the general case of a porous medium subjected to the impingement jet configuration [207] indicate recirculation phenomena too, under the form of vortices inside the porous medium. Assuming a mixed convection regime inside the porous medium (meaning that heat transfer through the foam is the result of combined effect forced and natural convection), showed that higher porosities and the use of fluids of higher thermal conductivity increase heat transfer.

Finally, versions of the previous configuration where the air source lies at a distance from the foam also exist—the nozzle can have the form of a slot jet [208], [209] or of a fan [210]. In all cases, heat transfer increases with the rate of volumetric air flow, as one would expect. For the case of a fan symmetrically placed above a copper foam (produced via the sintered metal powder route) with 8 pores per inch and 97% V_p, it was found that the best thermal performance of the tested copper foam was achieved when the fan was placed closer to the foam. Comparison of the foam with conventional plate fin heat sinks shows that, for the same heat dissipating performance, foams are 10% and 30% lighter than copper and aluminium plate fins and also take up less than 50% of the space.

The detrimental effect of a large distance between the air source and the foam is also confirmed for the case of the slot jet nozzle [208] above a 10 pores per inch aluminium foam with 93% porosity, at a given pressure drop; nevertheless, the overall influence of the distance of the nozzle on the heat exchange was much weaker than in the case of the foam. Moreover, decreasing the width of the jet nozzle, for a given height, affects positively the heat transfer coefficient, at the cost of a higher pressure drop; if the system operates at fixed pumping power, heat transfer is increased when the width of the jet nozzle increases.

When it comes to foam characteristics, such as pore density [209], (for a 92% porosity), metal foams, at a fixed distance from the slot jet, perform better when they have small pore density (10 pores per inch versus 20 or 40 pores per inch), at a given volumetric flow. Under the same configuration, foams have a better heat extraction capacity when compared with conventional plate fin heat sinks (8-33%, depending on the foam properties). With multiple slot jets, a high distance between the jets is not recommended; at a given height, the closer the jets are, the better the thermal performance of the metal foam as the volumetric flow rate rises. The use of multiple slot jets at small distance between each other, at the same distance from the sample as with the single jet, does not change conclusions regarding the microstructure of the foam and its influence; low pore density foams perform better than high pore density foams and all of them perform better than the conventional plate fin heat sink (2-29%). A comparison between multi jet and single jet configurations, reveals a better performance of the single jet at lower volumetric flows, no matter the distance between the multi jets.

Numerical studies combining the nozzle at a distance from the foam and the L-shaped flow pattern [211] have shown that the performance of metal foams increases with the volumetric flow rate since proportionally more air flows through the foam than around it. Foams with relatively smaller porosity (91%) perform better than those of higher porosity (97%), for the same material, while both foam samples perform better than a pin-fin heat sink of the same porosity, size and material.

As a final examination of impingement jet configuration, foams integrated into finned structures have been also studied (numerically and experimentally) under the jet impingement configuration [203], [212]. There are indications that for a given cross section of the finned foam, there might be an optimum height of the structure, at which the heat exchange is maximized. When compared with finned structures (plate fins), optimized finned foam structures have a better thermal performance for the same pumping power, even when bare fins are also optimized. Moreover, in order for the fins to dissipate the same amount of heat with foams, they have to be three times heavier (if made of the same metal).

Last but not least, despite the fact that natural convection using foams as a version of fins has also been studied, it has nevertheless received significantly less attention than forced flow. The reason is its lower potential for heat transfer, although this heat exchange takes place at virtually zero functional cost, since no power is required to pump the fluid through the foam. Then again, natural

convection is not negligible; the effective thermal conductivity of high porosity foams decreased more than 50% under vacuum conditions when compared with atmospheric pressure [213]. Experimental studies of high porosity foams (above 85%) under free convection are divided: there are studies that have demonstrated a minor beneficial effect of increasing pore density in metal foams [22], [214] by about 10%; on the other hand, other references [215]–[217] find a significant effect of foam pore density, with higher pore density having a detrimental effect on the thermal performance of the foam. Therefore, it is likely that secondary factors such as the fabrication process of the foam or the exact testing configuration influence the results: for example, investment casting foams perform better with a porosity close to 0.96 whereas sintered foams [217] dissipate more heat, when their porosity is close to 0.9, all other properties held constant for each type of foam. Nevertheless, all studies find an increased heat exchange rate when using foamed extended surfaces compared with a smooth flat surface, even when the exchanging fluid is water [218]. Positioning the foam structure at an inclination angle also slightly increases the heat exchange with the environment [217]; the exact angle however does not appear to play an important role. Finned foam structures [219] show a major enhancement in heat transfer rates compared to regular metal foam heat sinks. The heat transfer increases with the number of fins; nonetheless, the relative enhancement compared to normal foams decreased with each additional fin, suggesting the existence of an optimal number of fins, if other parameters (e.g. cost, weight, etc.) are factored into the design.

In summary, the heat exchange mechanism between metal foams and a single phase fluid has been studied under a variety of configurations but some key issues, such as the combined effect of configuration with the microstructure of the foam still need to be clarified in order to help these materials to unveil their full potential. Despite the substantial work conducted on the standard configuration, other configurations, such as the impingement jet, lack similar in-depth analysis. Factors such as the exact effect of microstructural (i.e. pore geometry, volume fraction) and macrostructural parameters (i.e. geometry) of the foam also need to be examined in more thorough studies. Since this particular configuration holds promise for industrial applications, it is deemed worth examining in a more rigorous manner; this is one of the main goals of the present thesis.

Chapter 3 Experimental Procedures

Experiments that were performed over the course of this investigation comprise the production of structures based on porous microcellular aluminium (also designated as aluminium foam hereafter) using the replication process, measurements of their performance in evacuating heat from a unidirectional heat source, and the production of integrated structures combining seamlessly a diamond reinforced aluminium composite, an AlN insulator plate, and microcellular aluminium, in that order. Aluminium foams of various pore sizes and porosity levels, and structures combining these with aluminium and aluminium/diamond composites, were fabricated in the laboratory by means of pressure infiltration. Two apparatuses were built and used to characterize heat dissipation capabilities of those metal foams and structures. By using the first experimental set-up, aluminium foams were tested under natural (free) convection, in an axisymmetric system, using a version of the hot guarded plate technique. The second set-up is a modification of the first, in which aluminium foams are tested under forced convection in a configuration that maintains the axisymmetry of the samples and apparatus.

3.1 Aluminium foam processing by replications

Aluminium foams that are studied in the present thesis were produced via replication. The process has been thoroughly described in the literature [100], [102], [220] and was presented in Chapter 2; in a nutshell, this is essentially a casting process, which consists in the production of a leachable preform (in this case, made of sodium chloride), pores of which are infiltrated with liquid metal. After infiltration and solidification of the metal, this preform is removed by leaching in water, resulting in an open-porosity metal foam, the structure of which is the complement in space of the porous preform used. Advantages of this technique are:

- Sodium chloride (salt) is easy to handle, non-toxic, inexpensive, environmentally benign and easy to remove in aqueous solutions. Its melting point, at 801°C exceeds that of aluminium, and NaCl is chemically inert in contact with molten aluminium.
- The pore size and the metal fraction of the foam can easily be controlled by controlling respectively, the particle size of the salt and the density of preform.

3.1.1 Controlling the metal foam pore size by sieving salt particles

NaCl particles were sieved in order to set the particle size in the preform within a predefined range and consequently, control the pore size of the metal foams; Ref. [100] describes the physics of sieving. A Fritsch Analysette 3 Pro sieving apparatus was used, mounted with ISO 565 sieves. The procedure used for the sieving method comprised low amplitude vibrations of 0.5 mm and medium amplitude vibrations of 1.4 mm, in consecutive steps of ≈ 30 minute durations. Sieves were

stacked in the following order, designated by the sieve pore size: 1300, 900, 450, 400, 180, and 125 μm. These values give, in turn, the range of pore diameters in replicated aluminium foams produced from each of these sieved batches. The NaCl used was mainly from Sigma-Aldrich Corp (St-Louis, USA); for the larger particles, commercial sea salt was used, namely the store brand of Coop Cooperative (Switzerland) retail stores. A more detailed analysis concerning the particle geometry resulting from the sieving process, can be found in [100].

3.1.2 Preform fabrication by densification of NaCl particles

The previously sieved NaCl powder is densified into a solid porous preform through cold-isostatic pressing, as illustrated in *Figure 3.1* [220]; the benefit of this procedure lies in the accessible range of the preform density values, and the fact that it does not create significant anisotropy in the resulting pressed compact [100]. Fabrication of the NaCl porous preform comprised the following steps:

- The salt particles are poured into a cylindrical silicon-rubber mould, 120 mm tall and with a diameter of 37 mm. Next, the mould is vibrated until no further variation in the powder level is observed, in order to ensure that random dense packing was achieved. Since the last action lowers the level of salt powder, a small amount of salt powder is added until the bed surface reaches the mould cap.

- The rubber mould is then hermetically sealed, using a latex condom.

- The rubber mould is placed inside a steel container filled with glycerine. A piston, tightly fitting the steel chamber and driven by a hydraulic press, pressurises the glycerine, applying hydrostatic pressure on the silicon mould.

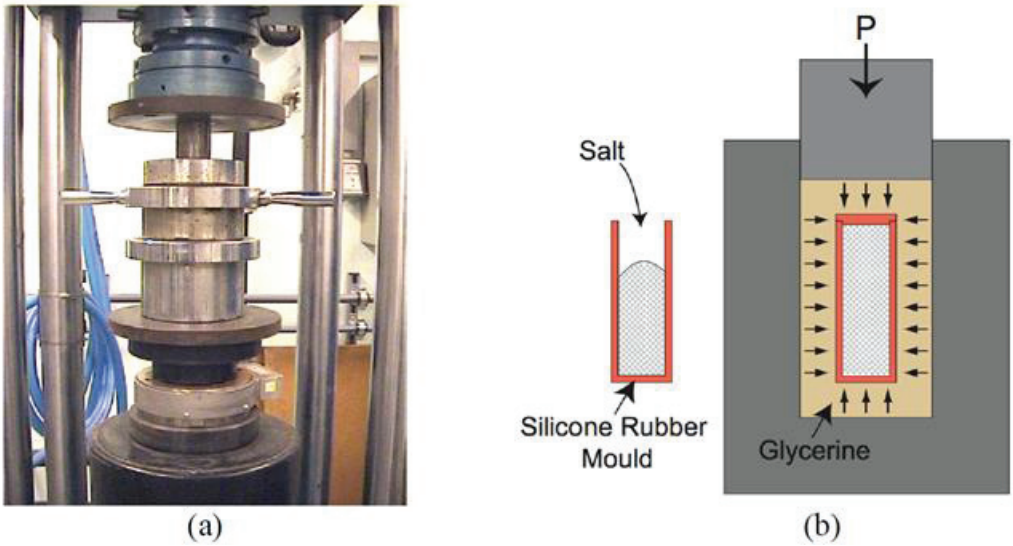

Figure 3.1: a) Cold Isostatic pressing apparatus and b) Sketch of the process. From Ref. [220].

3.1.3 Infiltration

The preform produced by the procedure described above is placed at the bottom of an alumina crucible, previously coated with graphite; then, a pure aluminium ingot is placed on top of this NaCl preform. The coating serves to impede sticking of NaCl or aluminium onto the crucible surface and thus, facilitates the extraction of the composite.

Infiltration is conducted in the apparatus shown in *Fig. 3.2* [220]. This comprises a 2 meter long vertical steel tube, which is encased within a furnace and insulated from the outside atmosphere via fittings at both ends. A vacuum pump connected to the interior of this tube can lower the pressure within the tube down to values on the order of 10^{-2} mbar and serves to evacuate the preform prior to infiltration. A copper chill, cooled via water circulation, is located at the lower end of the tube in order to induce directional solidification of the NaCl-aluminium composite bar once infiltration is completed.

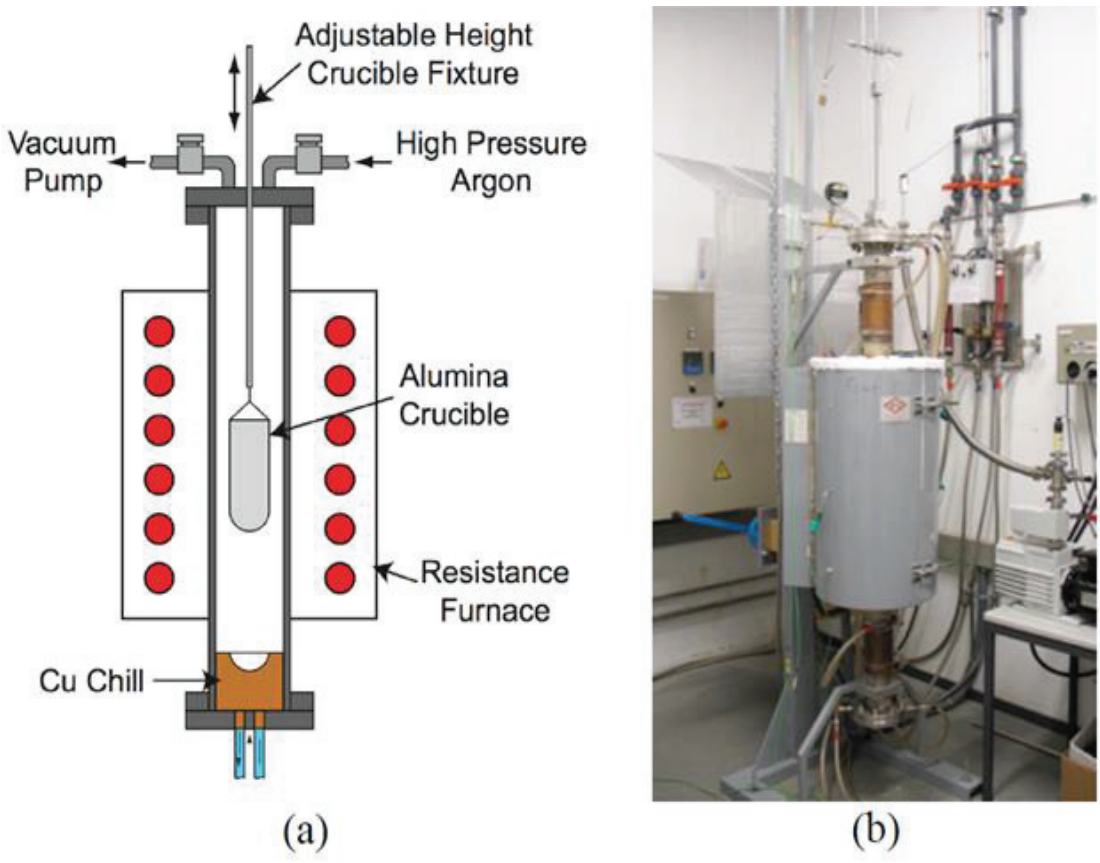

Figure 3.2: a) Schematic description and b) Photograph of the infiltration apparatus used. From [220]

The infiltration procedure, depicted in *Figure 3.3* [220], consists of the following steps:

- The alumina crucible, containing a NaCl preform and an aluminium ingot, is inserted from the opened flask top into the tube. The flask is closed and hermetically sealed by an O-ring, and the vertical position of the crucible is adjusted to the middle of the resistance furnace, ensuring subsequently temperature homogeneity within the crucible. The vacuum pump then operates for a time period of 12 hours; after this period, the furnace starts heating, with a set point temperature of 710 °C (this temperature causes complete melting of the aluminium while keeping NaCl particles solid). An electronic program controls the temperature ramp of the furnace at 10 °C / minute.

- Once the inside temperature of the tube is equal to the set point (± 10°C), and the inside pressure is lower than $2*10^{-2}$ mbar, while the vacuum pump is still connected, the temperature is held at 710°C for an extra hour in order to ensure complete melting and a homogeneous metal temperature inside the crucible. During this step, some sintering of NaCl powder may occur [220], [221].

- Then, pressurized argon gas is let into the infiltration chamber. The inert gas is selected so as to avoid any reactions with the liquid aluminium. The pressurized molten aluminium surrounding the NaCl preform then infiltrates the NaCl porous preform. The gas pressure determines the size of the smallest pores that can be infiltrated; its value hence influences the foam structure [100]. Typically a pressure around 3 bars was applied but in some infiltrations, higher pressures were exploited so as to test its effect on the convective properties of the aluminium foams.

- After 10 min of applied argon pressure, the alumina crucible is lowered onto the cold copper chill to induce directional solidification from the bottom to the top up, thus preventing the formation of solidification shrinkage within the NaCl-aluminium composite.

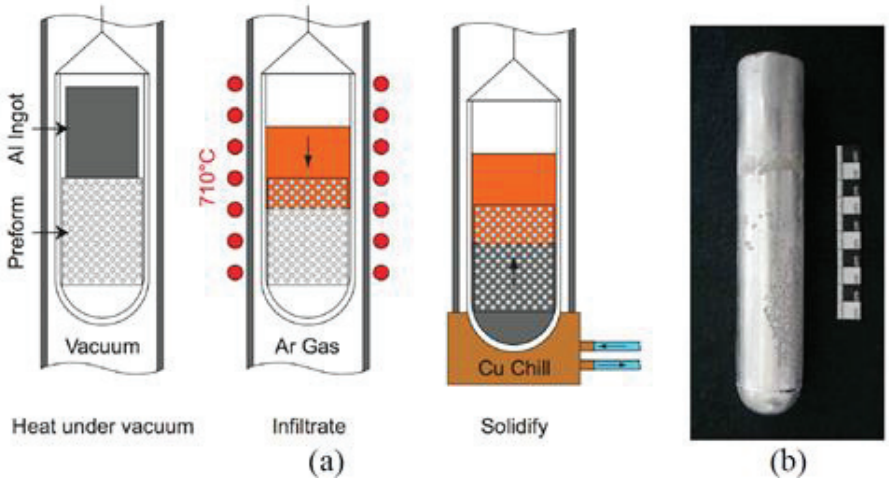

Figure 3.3: a) Schematic description of the infiltration process and b) an infiltrated composite bar outcome. From Ref. [220].

3.1.4 Sample shaping

Samples are brought to their final dimensions by conventional machining of the NaCl-Al composite. To assure a clean sample machined interface, to protect the cutting tool, and to avoid corrosion of the machining tools, all samples are machined without any lubricant.

Finally, NaCl particles are leached from the composite by immersion in water. To avoid the formation of a thick and irregular hydroxide layer on the surface of the foam [222], susceptible of deteriorating the permeability and thermal conductivity of the foam and the heat transfer to the fluid, a corrosion inhibitor solution is added to the solution, namely sodium chromate and sodium hydrogenocarbonate (0.01 mol/L each). The samples are immersed inside a beaker containing the chromate solution, in the upper third of the solution so as to create a halocline inside the solution, resulting from the heavier salt-containing liquid leaving the sample heading towards the bottom of the beaker; this technique eliminates the need for a renewal of the leaching solution. Occasionally, in order to speed up the process of leaching, the beaker was heated to 50°C, to increase the diffusivity of salt in water [223], [224] and consequently, the dissolution of the former to the latter inside the porous aluminium matrix. The leaching time typically ranged between 24 hours to one week, depending on the size of the samples, the size of the NaCl particles and on whether heating was applied.

3.2 Natural convection testing apparatus

3.2.1 Description of the apparatus

A set-up was designed and built to test the performance of replicated aluminium foam when is used to transfer heat from solid to gas under natural convection, aiming also to probe how properties of replicated aluminium foams influence their performance as cooling structures. The set-up heats foam samples from below, with the sides and top of the foam sample in ambient air. Foam characteristics under investigation were the pore size, the metal volume fraction and the overall geometrical shape of the samples.

The experimental apparatus, sketched in *Fig.3.4,* comprises:

- A vertical bronze cylindrical duct (of thermal conductivity k_d=26.4W/mK at room temperature, this value being deduced from a measurement of the electrical conductivity, conducted using the eddy current method). The duct is heated on its bottom by a resistive circuit. Three K-type thermocouples (T_1, T_2 and T_3) are used to deduce the top surface temperature ($T_{topduct}$) as well as the temperature gradient, allowing to calculate the heat flux there. All thermocouples are connected to a National Instruments ™ (Austin, USA) signal conditioning card SCXI 3260. The thermocouple that reads T_1 lies at the lower part of the duct, 1.5 cm above the heating circuit, and that reading T_3 at the upper part, at a distance of 0.5 cm from the top of the duct. The thermocouple reading T_2 is equidistant between these two, at 1.5 cm from either of the tips of thermocouples that read T_1 or T_3.

- A bronze outer ring which is also heated by the same resistive circuit. This ring serves to reduce lateral heat flow from the bronze duct to the environment. Its design is equivalent to that of the guarding plate concept in unidirectional heat flow experiments [225]–[227].

- Two rings, a base and a top cover made of porous ceramic insulation material ("PROMAFOUR™, Brussels, Belgium", k=0.17W/mK), which surrounds both the cylindrical duct and the outer ring

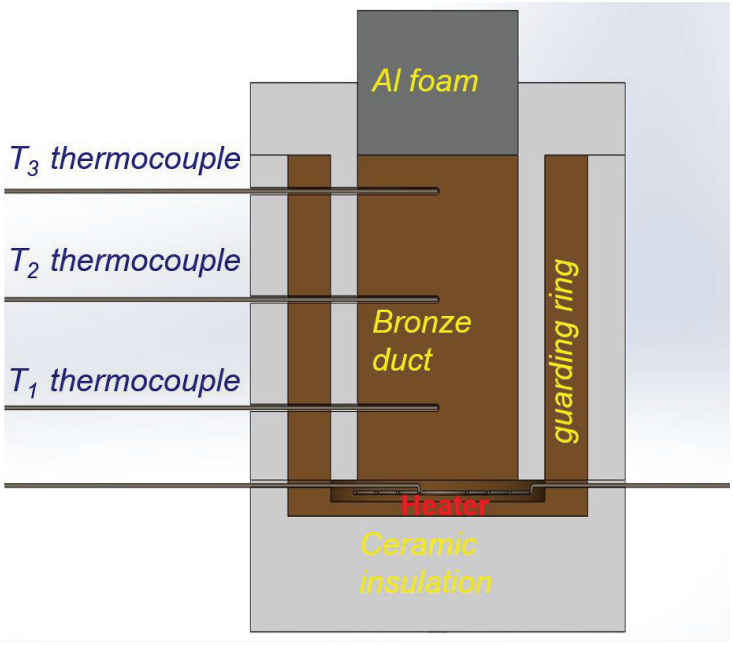

Figure 3.4: Schematic representation of the natural convection testing apparatus.

In essence, the device is a vertical heat duct, which conveys heat in near-unidirectional fashion from a source (the heater) to a flat upper surface; as mentioned before, the three thermocouples situated along the duct axis serve to estimate both the top surface temperature (T_{topduct}) and the flux of heat (q_{top}) that is vected across that surface. The estimation is made using an essentially 1-D heat flow model (see *Section 3.2.3*), in which temperature T within the bronze duct is taken to be a simple function of altitude z, with a gradual decrease in the temperature gradient caused by lateral heat losses governed by a single lateral heat transfer coefficient to constant temperature surroundings. Under those assumptions the duct temperature varies as a second order polynomial in z, the three parameters of the polynomial being deduced by measurement of the three temperatures, T_1, T_2 and T_3.

3.2.2 Correction of thermocouples

A two-step reference-type correction procedure was applied to ensure that temperatures, and hence thermal gradients are measured with high and known accuracy. For the first step, based on instructions in [228], a reference thermocouple situated alongside thermocouples to be calibrated were inserted in

a cylindrical hole drilled into a steel block placed in a furnace. Temperature gradients are minimised through the use of the steel thermal equalising block, such that the several thermocouple tips can safely be assumed to be at the same temperature [228]. The furnace temperature was set to 330°C and when it reached that temperature, the system was let to slowly cool until the ambient temperature was reached. The difference between the reference thermocouple and thermocouples to be correctedd was measured and interpolated for the given temperature range using the least squares method; a linear correction was deduced and implemented inside the Labview™ temperature measuring program to deduce, from data given by each thermocouple the temperature at its tip.

For the second step, an in-situ correction was applied. Here, the thermocouples were inserted in the measurement positions of the natural convection apparatus; therefore, the same correction took place in the same immersion depth as during operation, as suggested in [228]. Next, for the temperature range between 60 and 120°C, the difference in temperature read by the thermocouples was recorded under steady state conditions; from those data, a second order linear correction was deduced and implemented to eliminate this difference. Pooling data thus acquired, after the implementation of the two-step correction, a relative precision ± 0.05°C was estimated to have been reached for each of T_1, T_2 and T_3 measurements. Finally, the appropriateness of the correction function was periodically verified and confirmed that the electrical zero in the data acquisition card did not slide over time.

3.2.3 Data treatment

The temperature distribution within the duct is governed by the heat conduction equation:

$$k_{\mathrm{d}} \Delta T_{\mathrm{d}} + q = \rho_{\mathrm{d}} C_{p,\mathrm{d}} \frac{\partial T_{\mathrm{d}}}{\partial t} \tag{3.1}$$

where subscript d stands for the duct, Δ stands for the Laplace operator, q is the power source or sink term of the bronze duct per volume, C_{p}, ρ, and k are the thermal capacity, the density, and the thermal conductivity of the bronze, respectively. For simplicity, the temperature within the duct is taken to be a simple function of altitude z only. Lateral heat losses from the bronze duct to its surrounding are accounted for using the simple equation:

$$q = -\frac{h_{\mathrm{d}} P_{\mathrm{d}}}{A_{\mathrm{d}}} (T_{\mathrm{d}} - T_{\mathrm{w}}) \equiv -U(T_{\mathrm{d}} - T_{\mathrm{w}}) \tag{3.2}$$

where h_{d} is a constant and uniform heat transfer coefficient from the bronze duct to the guarding ring, P_{d} the perimeter of the duct and A_{d} its cross-sectional area along the vertical direction of heat flow, T is temperature (a function of height z) and T_{w} is the temperature of the guarding ring. Assuming steady-state, (*Eq.3.1)* and (*Eq.3.2)*, imply that:

$$k_{\mathrm{d}} \frac{\partial^2 T_{\mathrm{d}}}{\partial z^2} - U(T_{\mathrm{d}} - T_{\mathrm{w}}) = 0 \qquad (3.3)$$

This leads to a temperature distribution given by:

$$T(z) = c_1 e^{\sqrt{\frac{U}{k_{\mathrm{d}}}}z} + c_2 e^{-\sqrt{\frac{U}{k_{\mathrm{d}}}}z} + T_{\mathrm{w}} \qquad (3.4)$$

where c_1 and c_2 are constants defined by boundary conditions, namely the temperature measurements of the three thermocouples across the axis of the duct. By measuring simultaneously the temperature with K-type thermocouples at three different locations along the duct after stabilization of temperatures for a given setting of the heater, value of c_1, c_2 and U can be deduced.

Now, when h_{d} is such that the term $z^2 h_{\mathrm{d}}/k_d D_{\mathrm{d}} << 1$, *(Eq.3.4)* can be simplified to a simple second degree polynomial, through the Mac Laurin series:

$$T(z)=az^2+bz+c \qquad (3.5)$$

which, if $h_{\mathrm{d}}(T\text{-}T_{\mathrm{w}}) \approx 0$, reduces (as it should) to a linear distribution

$$T(z)=az+b \qquad (3.6)$$

Knowing these values, in turn, enables to deduce the temperature, T_{topduct}, and the heat-flux $q_{\mathrm{top}} = - k_{\mathrm{d}} \mathrm{d}T/\mathrm{d}z$, that is vected through the top of the duct, situated *at* $z = z_{top}$. The value of the thermal conductivity of the duct k_{d} used here, corresponds to the temperature at the top of the duct. The latter was evaluated at different temperatures using Matthiensen's rule.

Matthiesen's rule is an empirical rule which essentially states that the total electrical resistivity of a crystalline metallic specimen is the sum of the resistivity due to the presence of imperfections in the crystal and of the resistivity due to thermal agitation of the metal core ions on lattice points. The first term is largely determined by the purity of metal and is independent of temperature; the second term depens only on temperature. The electrical resistivity of the bronze duct at a given temperature is then the sum of the resistivity due to the thermal agitation of the ions of the copper matrix and the resistivity due to imperfections due to added metals (mainly tin) [229], as seen in *(Eq.3.7)*.

$$\rho_{\mathrm{br}}(T) = \rho_{\mathrm{imp}} + \rho_{\mathrm{cu}}(T) \qquad (3.7)$$

The electrical resistivity caused by imperfections in bronze can be estimated by extracting the known resistivity of copper at room temperature [230] from the measured resistivity of bronze at room temperature:

$$\rho_{\mathrm{imp}} = \rho_{\mathrm{br}}(21°\mathrm{C}) - \rho_{\mathrm{cu}}(21°\mathrm{C}) \qquad (3.8)$$

Using values for the resistivity of copper at various temperatures [230], the electrical resistivity of bronze can be estimated at various temperatures as:

$$\rho_{br}(T)= \rho_{imp}+\rho_{cu}(T) \tag{3.9}$$

and therefore, the electrical conductivity of the bronze, σ_{br}, can be calculated as

$$\sigma_{br}(T)=1/\rho_{br}(T) \tag{3.10}$$

By applying the Wiedemann-Franz law, the thermal conductivity of bronze was calculated for any temperature as follows:

$$k_{br}(T)= L*T*\sigma_{br}(T) \tag{3.11}$$

with L being the Lorentz number. That being so, the *global* heat transfer coefficient of the structure resting atop the duct surface, h, can now be deduced as:

$$h = \frac{q_{top}}{(T_{top} - T_a)} \tag{3.12}$$

where T_a is the ambient temperature.

In natural convection measurements, we take the temperature distribution inside the duct to be linear; in other words, the influence of lateral heat losses is neglected. The reason for doing so is the uncertainty present when we measure the exact temperature (T_1, T_2 and T_3) inside the duct, due to calibration uncertainty: we want to limit as much as possible the propagation of these errors in the calculation of the temperature at the top of the duct and in particular, the temperature gradient at the top, that influences directly the heat flux vected to the same point. Linear models have been well documented to be less sensitive in uncertainty propagation when compared to second degree (parabolic) models [231], [232]. For our case, this is illustrated in *Figs 3.5* and *3.6,* where the uncertainty determined during thermocouple correction, namely 0.05°C, was added successively to each of the three thermocouples. Best estimates were then taken for the temperature distribution assuming a linear profile, *Fig. 3.7,* or a parabolic temperature distribution, *Fig. 3.8*. As seen, if a parabolic temperature distribution is assumed, minor error in temperature values causes large swings in extrapolated values of temperature or temperature gradient at the top of duct, far larger than if a simpler linear temperature distribution is assumed. We therefore used the latter expression, accepting that the accuracy of flux measurements in natural convection is limited, while the underlying uncertainty is better contained and estimated.

.

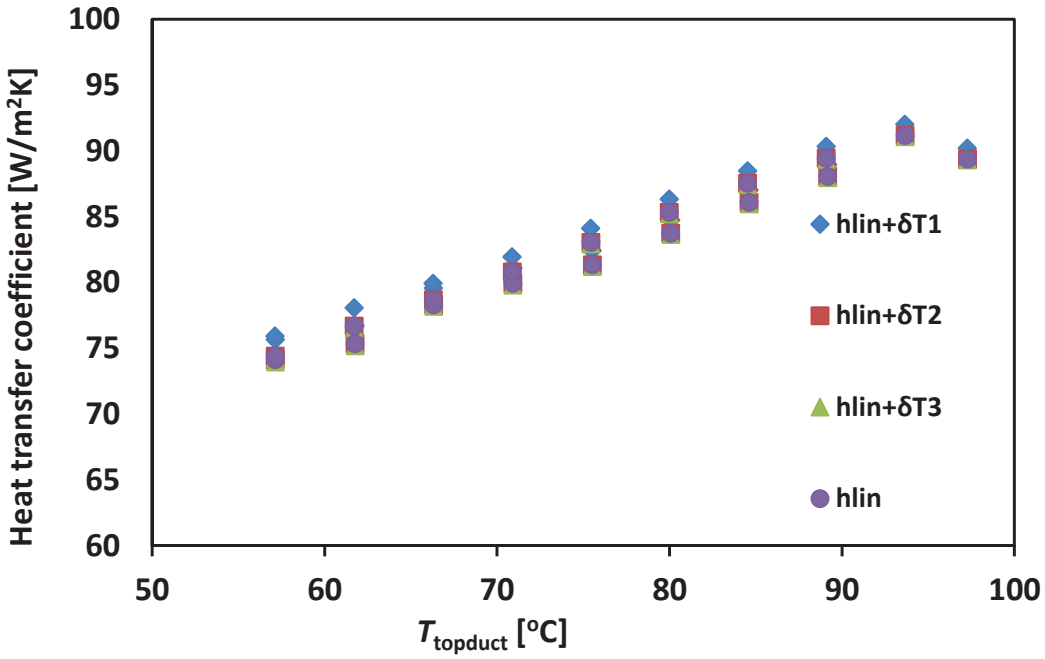

Figure 3.5: Sensitivity analysis for the global heat transfer coefficient under natural convection, using the linear model.

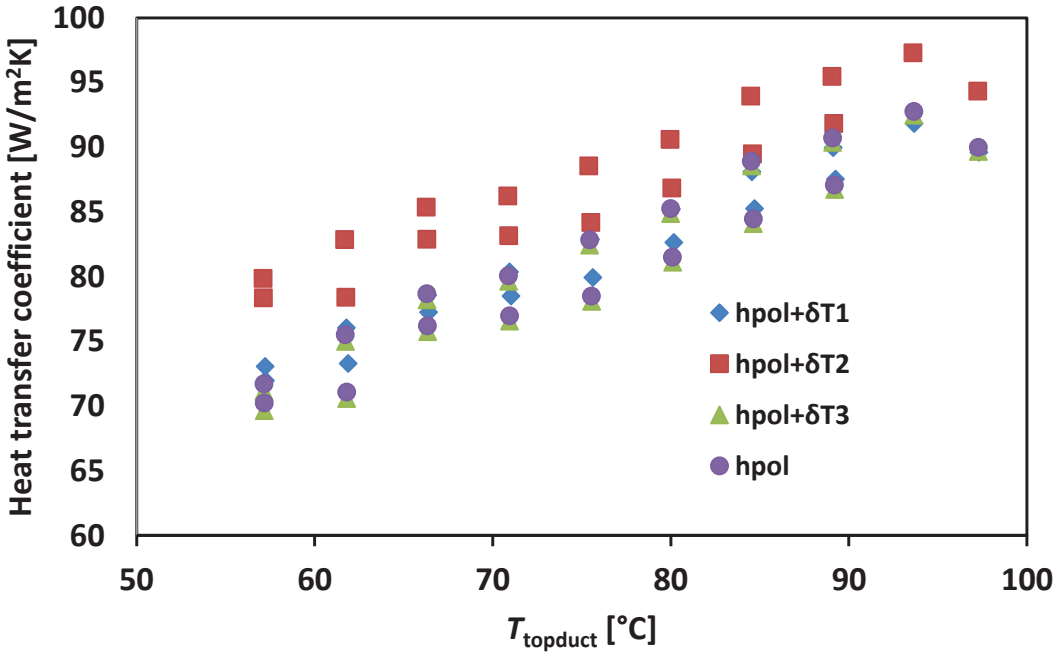

Figure 3.6: Sensitivity analysis for the global heat transfer coefficient under natural convection, using the parabolic model.

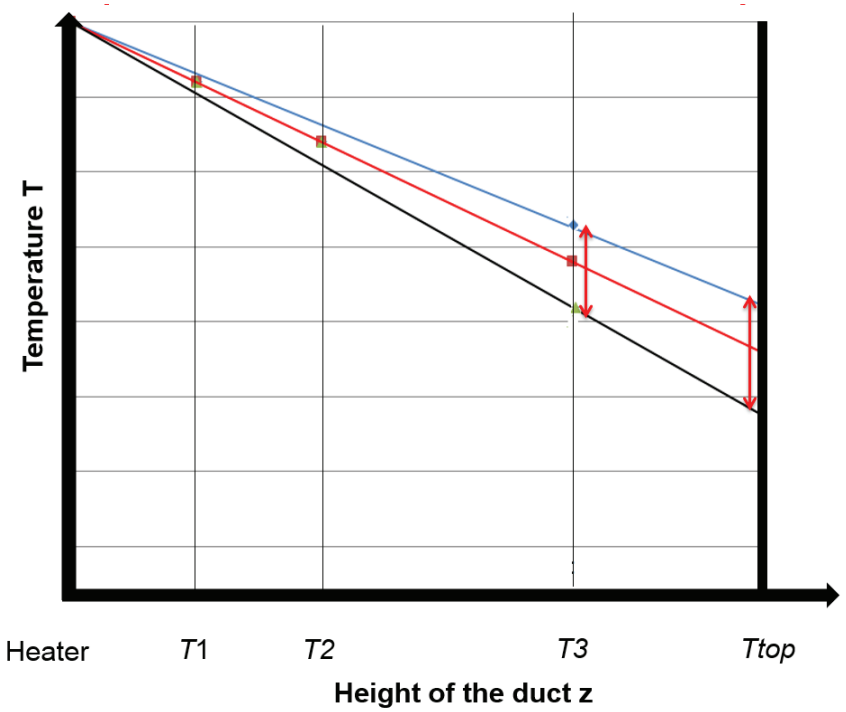

Figure 3.7: Schematic propagation of error in temperature measurement under a linear model. The distances between the thermocouples and the uncertainty assigned to T1, T2 and T3 are not in scale, to enhance the visibility of the phenomenon.

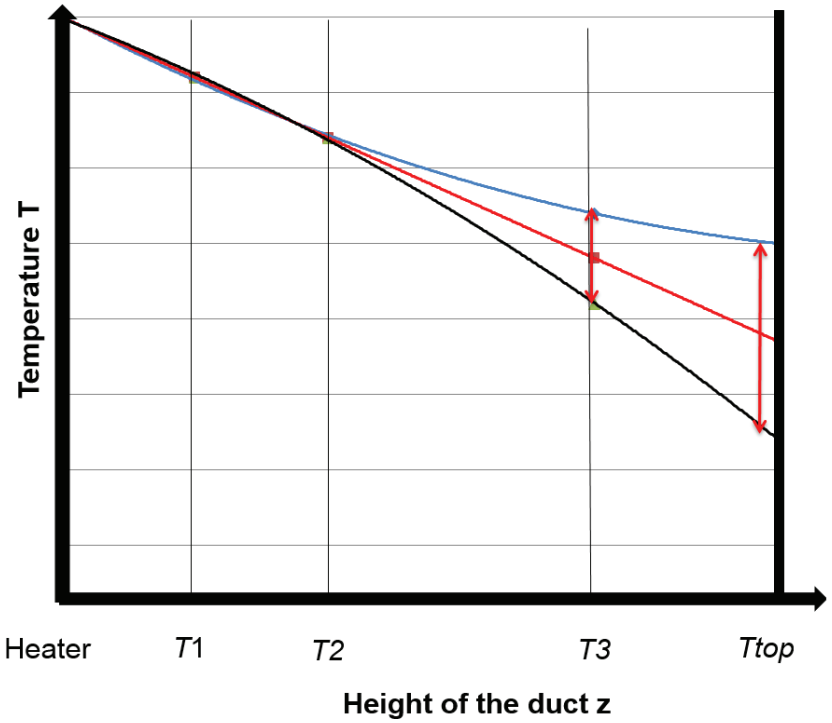

Figure 3.8: Schematic propagation of error in temperature measurement under a parabolic model. The distances between the thermocouples and the uncertainty assigned to T1, T2 and T3 are not in scale, to enhance the visibility of the phenomenon.

3.2.4 Error propagation

The *global* heat transfer coefficient of the structure resting atop the duct surface, h, is defined as

$$h = \frac{q_{\text{top}}}{(T_{\text{topduct}} - T_{\text{a}})} \tag{3.13}$$

The heat transfer from the duct to the sample sitting on its top is defined as:

$$q_{\text{top}} = -k_{\text{duct}}\left(\frac{\mathrm{d}T}{\mathrm{d}z}\right)_{\text{z=ztop}} \tag{3.14}$$

If we define now as $p=T_{\text{topduct}}-T_{\text{a}}$, *Eq.3.13* becomes

$$h = \frac{q_{top}}{p} \tag{3.15}$$

The uncertainty for the heat flux is calculated as

$$\frac{\delta q_{top}}{|q_{top}|} = \sqrt{\left(\frac{\delta k_{duct}}{k_{duct}}\right)^2 + \left(\frac{\delta(T_1 - T_{top})}{T_1 - T_{top}}\right)^2 + \left(\frac{\delta z}{z}\right)^2} \tag{3.16}$$

and the uncertainty in the global heat transfer coefficient is calculated as

$$\frac{\delta h}{|h|} = \sqrt{\left(\frac{\delta p}{p}\right)^2 + \left(\frac{\delta q_{top}}{q_{top}}\right)^2} \tag{3.17}$$

With

$$\delta p = \sqrt{(\delta T_{topduct})^2 + (\delta T_a)^2} \tag{3.18}$$

Uncertainties in the heat flux arise from:

- Uncertainty in $T_{\text{topduct}}-T_{\text{a}}$. Although the thermocouples were calibrated in situ, there is still an uncertainty in the measurement of the temperature difference (0.05°C) across the duct; this uncertainty is estimated to be around 1.6% or less (the smallest temperature difference inside the duct is 3°C).

- Uncertainty in the thermal conductivity of the duct. The thermal conductivity is determined by measuring the electrical conductivity of the duct at room temperature and then applying the Wiedeman-Franz law. The Lorentz number was found in literature, but it can change at higher

temperature [229]. We estimate that this causes an uncertainty of 5%, since we do not take into account the phononic contribution in the thermal conductivity.

- Uncertainty in the position of the thermocouples. The distance between them could vary by ±0.5mm. This means that an error of 1mm on a total distance of 15mm is possible, inducing an uncertainty of 6.6%.

Therefore, *Eq. 3.16*, yields

$$\frac{\delta q_{top}}{|q_{top}|} = \sqrt{(\frac{\delta k_{duct}}{k_{duct}})^2 + (\frac{\delta \Delta T}{\Delta T})^2 + (\frac{\delta z}{z})^2} = \sqrt{(0.05)^2 + (0.016)^2 + (0.06)^2} \sim 8\%$$

The uncertainty for the temperature difference from *Eq. 3.18* is estimated

$$\delta p = \sqrt{(\delta T_{top})^2 + (\delta T_a)^2} = \sqrt{(0.05)^2 + (0.05)^2} = 0.07K$$

Taking the worst case scenario, when the difference between T_{topduct} and T_{amb} is at 40°C, then, the error in the global heat transfer coefficient is calculated from (*Eq. 3.17)* as

$$\frac{\delta h}{|h|} = \sqrt{(\frac{\delta p}{p})^2 + (\frac{\delta q_{top}}{q_{top}})^2} = \sqrt{(\frac{0.07}{40})^2 + (0.08)^2} \sim 8\%.$$

It is worth mentioning that, since the temperature difference between the duct and the ambient is usually larger than 40°C, the 8% error is the maximum error induced in our data set.

3.2.5 Sample preparation and properties

Aluminium cylindrical samples of various height, porosity and pore size were fabricated by the procedure described in *Section 3.1*. Additionally, a commercially available foam, Corevo™ by Constellium, fabricated by a variant of the replication technique described in [101], was also tested; *Fig. 3.9* shows several samples. *Table 1* lists characteristics of all samples tested for the study of heat transfer under natural convection conditions. These include, in addition to porous metal samples, specimens with the same geometry that were machined out of solid bulk aluminium 6082 series alloy and tested similarly.

Samples tested	Height [mm]	Diameter [mm]	Pore volume fraction V_p ±1.5 [%]	Pore diameter [µm]	Material
Replicated Aluminium foams	10.0 20.0	30	84±1.5%	125-180	Aluminium
	10.0 20.0	30	78±1.5%	125-180	Aluminium
	10.0 20.0	30	86±1.5%	400-450	Aluminium
Constellium Corevo ™	84.5	30	80± 5%	~5000	Aluminium
Solid blocks	10.0 84.5	30	-	-	Aluminium alloy 6082 series

Table 1: Microstructural characteristics and geometry of the cylindrical specimens tested under natural convection.

Figure 3.9: From left to right:Corevo™ 5mm pore size commercial aluminium foam, replicated 125-180 µm pore size aluminium, replicated aluminium 400-450 µm pore size.

Plate fin samples were also produced out of aluminium foam and tested in the same apparatus, *Fig.3.10*. Their characteristics are outlined in *Table 2*. The distance between fins, z, was optimized through a derivation of the Elenbaas equation for the case of isothermal fins at $\Delta T=220^{o}C$, as given in Ref. [233]. These samples could not had been produced with a cylindrical symmetry due to difficulties in machining such a shape; rather, their base was rectangular (24x24 mm).

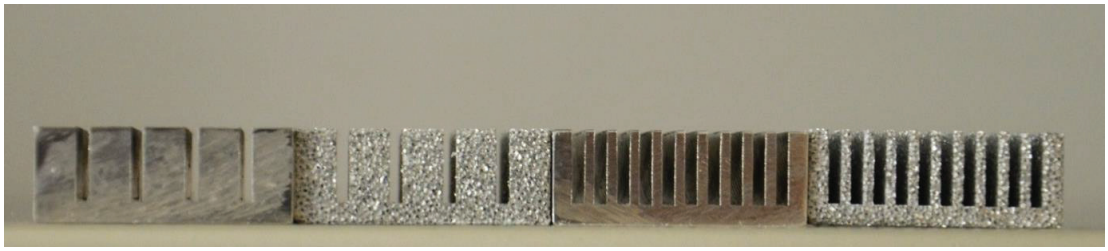

Figure 3.10: Aluminium foam fins and their equivalent bulk parts that were tested under natural convection.

	Height [mm]	Cross section [mm]	Porosity V_p	Pore diameter [μm]	Number of fins	Fin thickness [mm]	Distance between fins [mm]
Foamed fins	7	24	78±1.5%	400-450	11	1 (9 fins), 2 (2 fins)	1.2
	7	24	78±1.5%	400-450	5	4	1.2
Bulk alloyed aluminium fins (alloy 6082)	7	24	86±1.5%	-	11	1 (9 fins), 2 (2 fins)	1.2
	7	24			5	4	1.2

Table 2: Microstructural characteristics and geometry of the finned structures tested under natural convection.

Finally, a partially leached sample (a structure having a leached periphery of given thickness with the remainder being of dense Al-NaCl composite) was produced and tested. This sample was of 2.5 cm tall, with 400-450 μm pore size and 85% porosity and this test aimed to probe how deeply air convection might be operative within the microcellular metal in heat exchange by natural convection.

3.2.6 Testing procedure

Cylindrical metal or foam specimens are coated on their underside with a layer of Electrolube HTCPX™ (Leicestershire, UK) thermal paste and placed on top of the heating duct. In the case of the finned samples, due to their rectangular footprint,

a cylindrical aluminium block, almost flush with the ceramic insulation, was placed between the sample and the duct in order to raise the sample above the layer of insulating material surrounding the duct. The configuration is illustrated in *Fig.3.11.* With such samples, the measured temperature at the top of the aluminium block, T_{surf}, was used in the calculation of the global heat transfer coefficient instead of the temperature of the top of the duct, $T_{topduct}$.

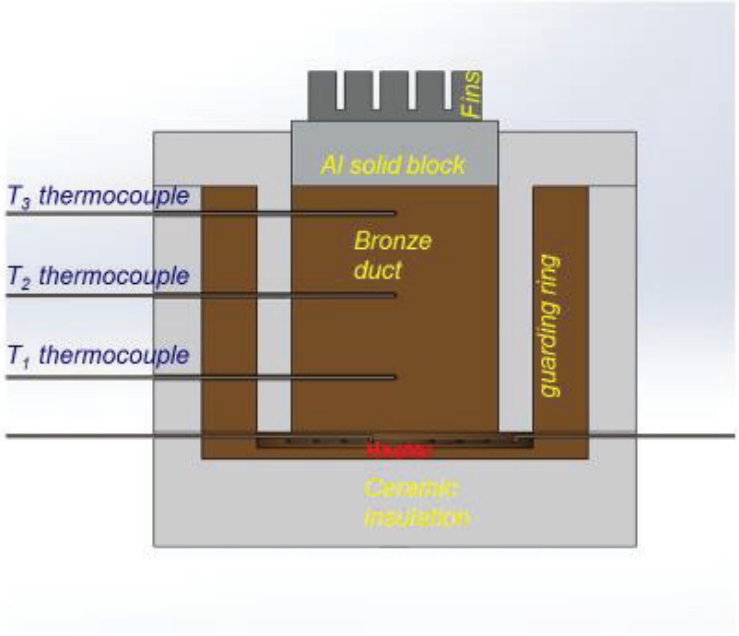

Figure 3.11: Schematic representation of the experimental apparatus illustrating how fins were mounted on the apparatus.

In all experiments, T_1 is used as a reference temperature, meaning that it is the value of T_1 that is used to control the heater using a PID controller, tuned and controlled by a Labview™ code. In each experiment, the control tempeature is initially set at 60°C; thereafter the system changes the set temperature every 30 minutes, so as to reach near-steady state conditions, defined as all temperatures varying by less than 0.1°C for 20 minutes, before changing the set temperature anew. The T_1 temperature is thus set to start at 60°C, rise in steps of 5°C up to 120°C, then return in similar steps to 60°C. T_1, T_2 and T_3 thermocouple readings are recorded every 5 seconds. From these recordings, the average temperature of each thermocouple for each steady state step is computed and used to determine the average thermal gradient within the duct as well as its top temperature $T_{topduct}$, from which the average heat transfer coefficient could be computed as a function of $T_{topduct}$, for rising or decreasing values of $T_{topduct}$.

We note that, contrary to the common practice of taking natural convection measurements inside a container, as a means to eliminate or reduce Rayleigh-Bernard convection cells, in present measurements the sample and set-up were let unconfined. The reason for this choice was a desire to probe the performance of the present samples under conditions close to those expected in actual service.

3.3 Forced convection testing apparatus

3.3.1 Description of the apparatus

The above set-up and procedure was adapted for measurements of the performance of replicated aluminium foams under conditions of forced convection. The experiment was designed for geometric and operational simplicity, in that it preserves the cylindrical symmetry of the set-up and of the samples. In brief, it resembles the previous set-up, with the difference that air if forced through a cylindrical hole drilled through the central axis of the sample; in a way, thus, the experiment can be viewed as placing a block of aluminum foam along the path of air in an impingement jet configuration.

Fig. 3.12 depicts the set-up, which comprises:

- A vertical bronze cylindrical duct (of thermal conductivity k_d=66 W/mK, this value being deduced from electrical conductivity measured using the eddy current method) heated on its bottom by a resistive circuit. Four K-type thermocouples (T_1, T_2, T_3 and T_4) are used to measure the top surface temperature as well as deduce the heat flux at that point. All thermocouples are connected to a National Instruments ™ (Austin, USA) signal conditioning card SCXI 3260. Temperatures T_1, T_2, T_3 are measured at locations and in the manner described above while the tip of the thermocouple reading T_4 lies at a distance 0.5 mm from the top of the duct. This results in the four thermocouples being successively placed at a distance of 1.5 cm from one another, with T_1 located at the lowest position along the duct.

- A bronze outer ring which is also heated by the same resistive circuit, designed to reduce lateral heat losses from the bronze duct to the environment and, by this, make the flow of heat within the duct closer to unidirectional.

- A layer of ceramic insulation made out of porous ceramic material ("PROMAFOUR™", Brussels, Belgium) which surrounds both the cylindrical duct and the outer ring.

- A hot plate flowmeter SFM3000 by Sensirion™ (Staefa ZH, Switzerland) that measures the incoming flow inside the aluminium foam. It has an accuracy of ±1.5% (relative error).

- A brass nozzle, with a constant internal diameter of 3.26 mm (and external diameter of 3.9mm), that injects air into the sample. The nozzle has a sufficient length (more than 10 times its diameter) to assure that the flow is fully developed before the air is injected into the sample.

- A differential piezoresistive pressure gauge Freescale MPX2010 by NXP Semiconductors (Eindhoven, Netherlands) that monitors the pressure difference between the ambient and the pressure inside the nozzle, with

one measurement probe placed as close as possible (within 10 mm) to the foam surface. The differential pressure gauge is connected to two hypodermic needles, inserted at two different heights alongside the nozzle surface, allowing simultaneously the benefits of a small tap diameter and a reasonably fast response time [234]. The error from the calibration of the pressure gauge is estimated at ± 30 Pa.

- A fifth thermocouple is placed along the air flow path, inside the pipe that channels the air to the nozzle, to measure the temperature of the air before it enters the foam.

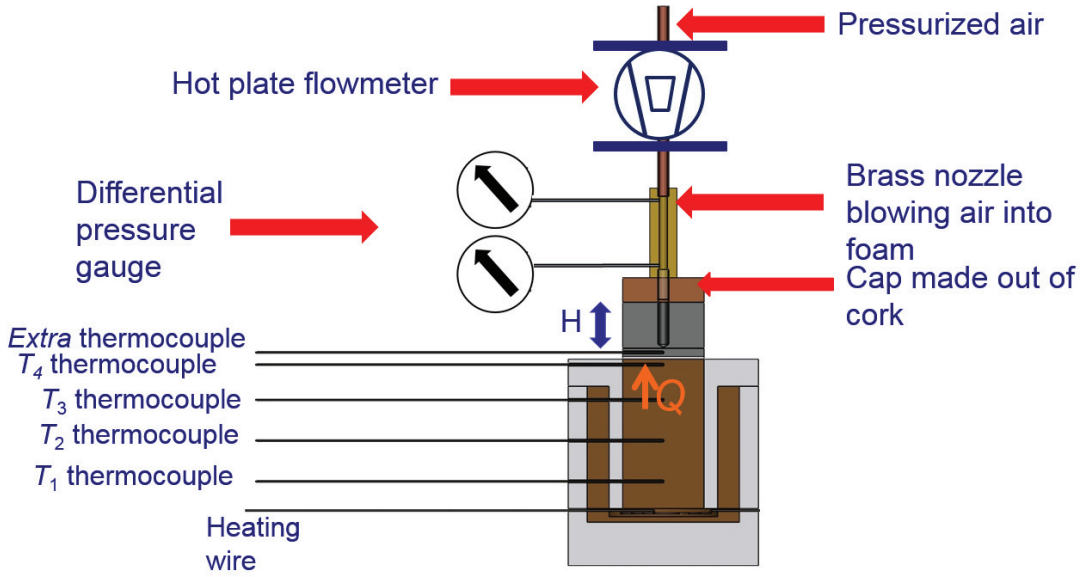

Figure 3.12: Schematic representation of the new set up, depicting relevant components.

3.3.2 Calibration of the apparatus

Thermocouples were corrected in two steps. The first step is identical with that which was used for the natural convection measurements. For the second step, all thermocouples were inserted together in a brass ring inside a steel solid block. To improve thermal contact, as suggested in [228], thermal paste was placed between the thermocouples and the brass ring and between the thermocouples themselves. Next, the block was heated up to 160°C and was then left to cool slowly under free convection. T_1 was again chosen as the reference thermocouple and the difference in temperature between the reference thermocouple and the rest was recorded under those transient state conditions. To decrease variations of temperature with time, as proposed in [228], a moving average was applied to the recorded values, after which a self-referenced second order polynomial correction was applied to the moving average recorded values. After the correction, agreement within ± 0.05°C between the readings of thermocouples was achieved. Lastly, the appropriateness of the correction function was periodically verified and as in natural convection apparatus, it was confirmed that the electrical zero in the data acquisition card did not slide over time.

To test the above correction, the following calibrating procedure was applied: a highly conductive copper block (electrolytic tough pitch copper), with 5 thermocouples placed centrally across its length and isolated from the ambient air, was placed on top of the duct. Thermal paste was used to bring the bronze duct and the copper block in good thermal contact. On top of the copper block, a water-flooded block was placed, regulated at 70°C, while the T_1 thermocouple was set to cover the range of 100 to 150°C, thus creating a temperature gradient through both the copper block and the bronze duct. Thermocouples were attached across the height of the copper piece, so as to measure the temperature gradient along its length, *cf Fig. 3.13*. In principle, heat transferred through the copper block, calculated via an extrapolated second order polynomial, should equal the heat transferred along the duct. The discrepancy between the two measured fluxes was found to be less than 11% at low flux values (<2.5 W/cm^2) and less than 5% for fluxes greater than 4 W/cm^2).

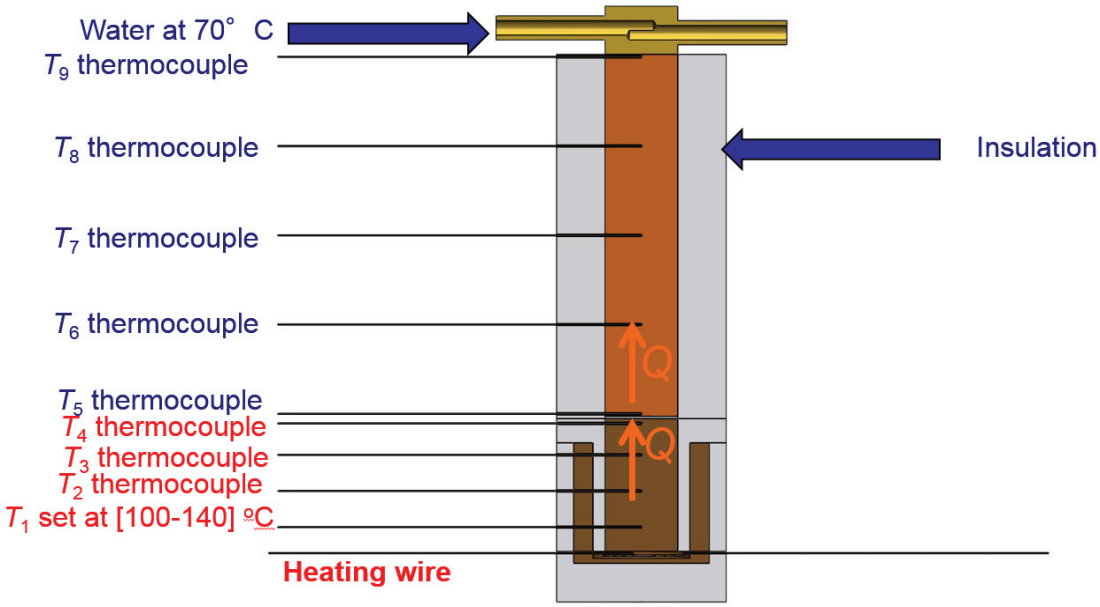

Figure 3.13: Schematic representation of the apparatus calibration procedure.

Finally, a calibration of the differential pressure gauge (dpg) was performed via a U-tube manometer, containing distilled water, using the difference in the water level of two connected straight quartz tubes connected respectively to the pressure line and the ambient; the pressure range of the calibration was between 150 and 7000 Pa. A second order parabolic correction was used, limiting the error to ±30 Pa.

3.3.3 Data treatment

The temperature distribution within the duct is governed by:

$$k_{\mathrm{d}} \Delta T_{\mathrm{d}} + q = \rho_{\mathrm{d}} C_{\mathrm{p,d}} \frac{\partial T_{\mathrm{d}}}{\partial t} \qquad (3.1)$$

where subscript d stands for the duct, Δ stands for the Laplace operator, q is the power source or sink term of the bronze duct per volume, C_p, ρ, and k are the thermal capacity, the density, and the thermal conductivity of the bronze, respectively.

The rate of heat dissipation through the bronze duct being much higher than under natural convection, the temperature gradient along the duct, and hence the difference between the bronze duct and the guarding ring temperatures is no longer negligible, *cf. Fig.3.14.* It peaks in the upper (and hence, coldest) part of the duct.

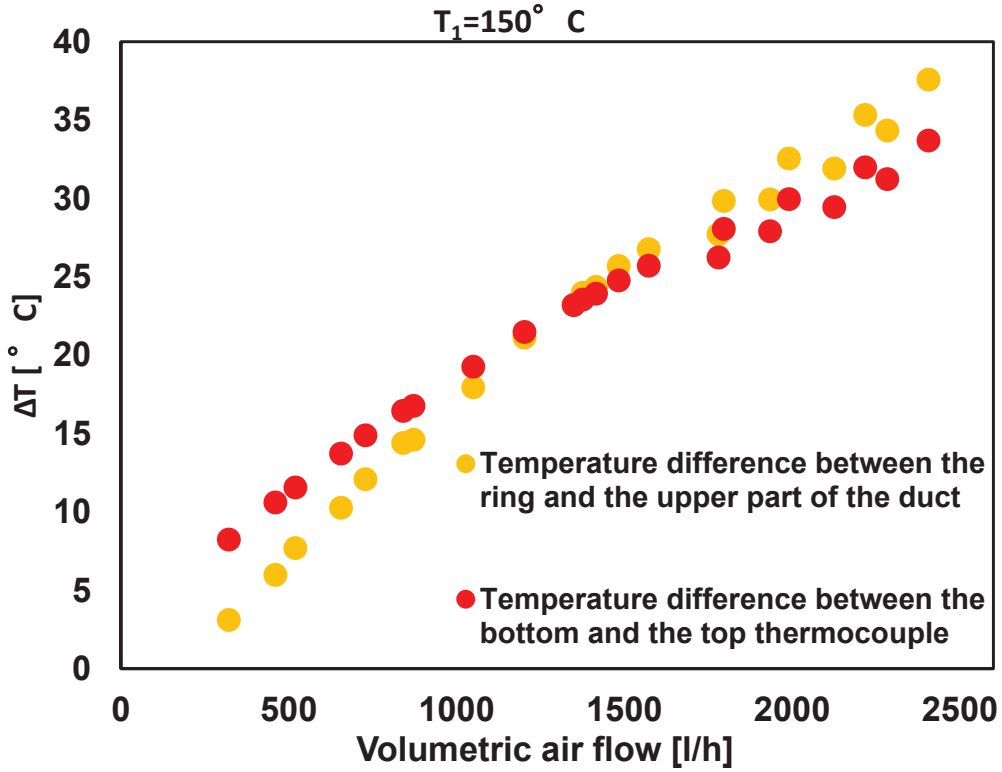

Figure 3.14: Measured evolution of the temperature difference between the guarding ring and the upper part of the duct with the volumetric air flow. A temperature difference between 5 and 35°C, similar to the temperature gradient across the duct, explains the noticeably nonlinear temperature profile.

Therefore, in this case, there is appreciable heat transfer to the bronze duct from the guarding ring. We model again these heat gains using the simplified equation

$$q = \frac{h_d P_d}{A_d}(T_d - T_w) \equiv U(T_d - T_w) \qquad (3.19)$$

where h_D is a constant and uniform heat transfer coefficient governing heat transfer from the bronze duct to the guarding ring, P_{duct} its perimeter and A_{duct} its cross-sectional area along the vertical direction of heat flow, T is temperature (a function of height z) and T_w is the temperature of the guarding ring. Assuming

horizontal isotherms in the duct and at steady-state, *Eqs.(3.1)* and *(3.19)* yield as before:

$$k_{\mathrm{d}} \frac{\partial^2 T_{\mathrm{d}}}{\partial z^2} + U(T_{\mathrm{d}} - T_{\mathrm{w}}) = 0 \qquad (3.20)$$

which again leads to :

$$T(z) = c_1 e^{\sqrt{\frac{U}{k_{\mathrm{d}}}}z} + c_2 e^{-\sqrt{\frac{U}{k_{\mathrm{d}}}}z} + T_{\mathrm{w}} \qquad (3.21)$$

where c_1 and c_2 are constants defined by boundary conditions. By measuring simultaneously the temperature with K-type thermocouples at four different locations along the duct after stabilization of temperatures for a given setting of the heater, values of c_1, c_2 and U can be deduced using the least-square method.

When h_{d} is such that $z^2 h_D / k_d D_{\mathrm{d}} << 1$, *Eq.3.21* can again be simplified to a simple second degree polynomial:

$$T(z)=az^2+bz+c \qquad (3.22)$$

Given that in forced convection experiments lateral heat transfer can no longer be neglected, this parabolic temperature profile is used to deduce constants a, b and c, by extrapolation from the measurements of T_1, T_2, T_3 and T_4 using the least squares method. The deduced vertical temperature profile is then used to compute an average heat-flux $q_{\mathrm{top}} = - k_{\mathrm{d}} \mathrm{d}T/\mathrm{d}z$, transferred across the top of the duct, situated *at* $z = z_{top}$; using for k_{d} the value corresponding to T_{topduct}, calculated using the same procedure as that one described in *Section 3.2.3*. From this, the *global* heat transfer coefficient of the structure resting atop the duct surface, h, can be deduced as:

$$h = \frac{q_{\mathrm{top}}}{(T_{\mathrm{top}} - T_{\mathrm{a}})} \qquad (3.23)$$

where T_{a} is the measured temperature of the incoming air flow. T_{topduct} is thereafter assimilated to T_4, which is measured in a position only 0.5 mm from the top of the duct.

Taking as the maximum theoretical heat transfer coefficient h_{max}, the heat transfer scenario under which all incoming air reaches the temperature of the surface of the metallic duct T_{topduct}, then the efficiency ε of the foam can be calculated as

$$\varepsilon = \frac{A_{\mathrm{footprint}} h}{\rho C_{\mathrm{p}} V} = \frac{h}{h_{max}} \qquad (3.24)$$

Where C_p and ρ are the thermal capacity and density of air, V the volumetric air flow rate and $A_{footprint}$ the footprint of the sample. In a few experiments, the temperature at the bottom of the sample, T_{surf}, was separately measured. As depicted in *Figures 3.15 and 3.16*, when T_{surf} was measured separately, the difference between T_{surf} and $T_{topduct}$ was less than 5%, for temperatures up to 120°C, leading to a relative error that is also smaller than 5% when using the extrapolated temperature at the top of the duct, $T_{topduct}$, instead of T_{surf} to compute the global heat transfer coefficient.

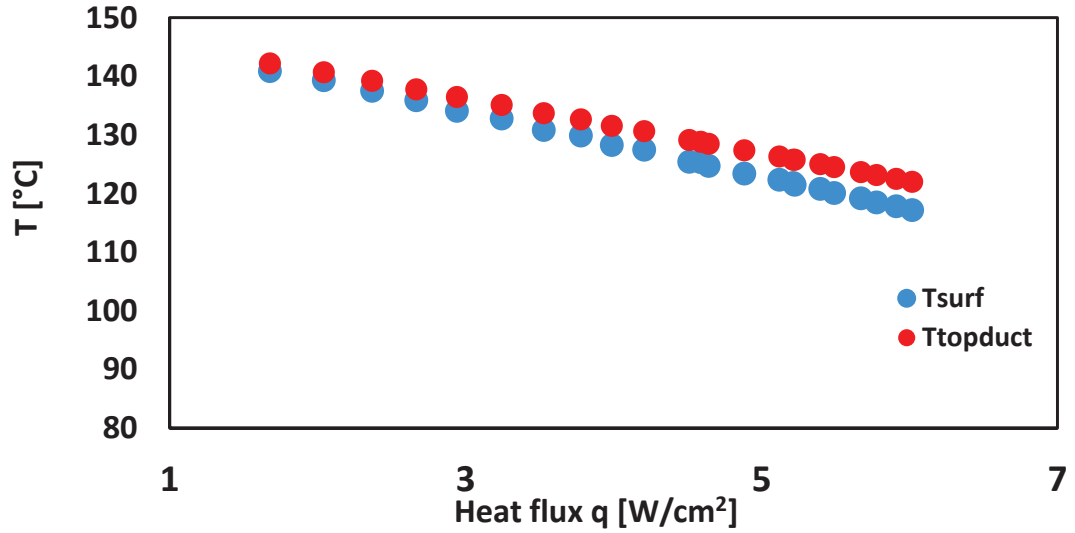

Figure 3.15: Evolution of the temperatures at the top of the duct $T_{topduct}$ and at the bottom of the sample T_{surf}, with heat flux for a 28 mm tall aluminium foam, with 125-180 µm pore size, 85% porous fraction and infiltrated at 70 bars.

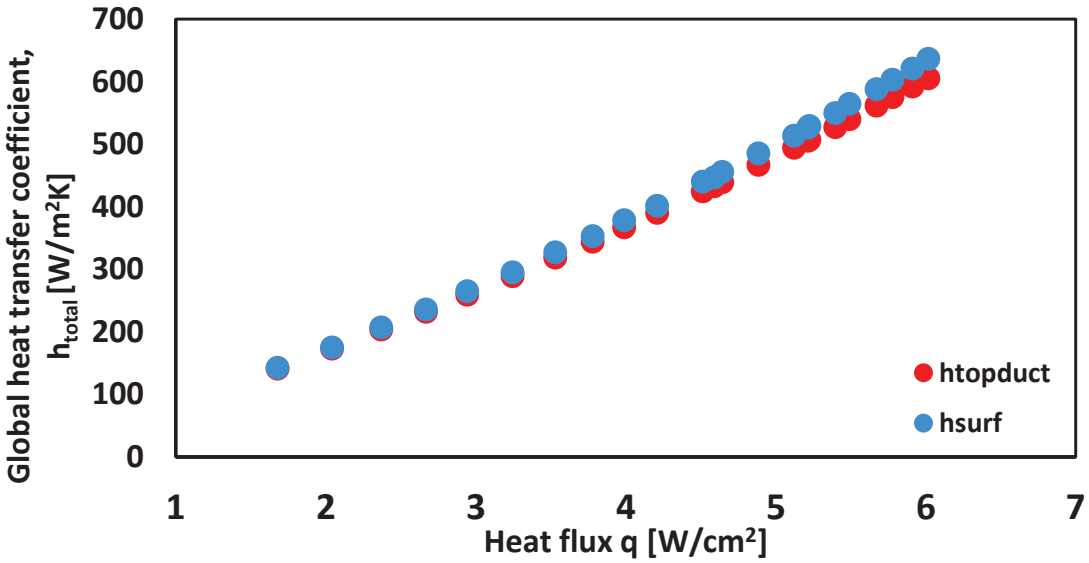

Figure 3.16: Evolution of the global heat transfer coefficient with heat flux using different input temperatures (T_{surf} and $T_{topduct}$) for a 28 mm tall aluminium foam, with 125-180 µm pore size, 85% porous fraction and infiltrated at 70 bars.

As mentioned in *Section 3.3.1*, the static pressure is measured inside the nozzle at two different points ($P_{s,a}$ and $P_{s,b}$), separated by distance z_o = 2.4 cm. From these readings, a linear extrapolation is applied to estimate the static pressure at the exit of the nozzle, z_{edge}:

$$P_s(z = z_{\text{edge}}) = \frac{P_{s,a} - P_{s,b}}{z_o} * z_{\text{edge}} + P_{s,b} \tag{3.25}$$

with z=0 being set at the upper of the two pressure measurement points.

Moreover, since the volumetric air flow V is constantly recorded, the dynamic pressure at the edge of the nozzle $P_{d,edge}$ can also be estimated and therefore, the total pressure $P_{t,edge}$ and the pumping work W needed at the same point can also be estimated from *Eqs. 3.26 to 3.28:*

$$P_d = \tfrac{1}{2}\rho(V / A_{\text{nozzle}})^2 \tag{3.26}$$

$$P_t(z = z_{\text{edge}}) = P_{d,z_{edge}} + P_{s,z_{edge}} \tag{3.27}$$

$$W = P_t * V \tag{3.28}$$

where A_{nozzle} is the cross section of the nozzle (~83 cm^2) and ρ the density of air at ambient temperature, namely ~1.21 kg/m^3. The spumping work W defined above, which will be henceforth used to express the needed energy required to operate the system, does not take into consideration the power consumption of the system that was used to compress the air; consequently, it is an ideal (minimal required) pumping power.

3.3.4 Error propagation and experimental discrepancy.

In order to find the temperature distribution inside the duct, we extrapolate a 2nd order curve through 4 points, by solving $\boldsymbol{Z*a=T,}$ with $\boldsymbol{Z}$ being the Vandermonde matrix [235], $\boldsymbol{T}$ and $\boldsymbol{a}$ the vectors of temperature and of polynomial coefficients, as seen in *Eq (3.29)* below

$$\begin{bmatrix} z_1 & z_1^2 & z_1^3 \\ z_2 & z_2^2 & z_2^3 \\ z_3 & z_3^2 & z_3^3 \\ z_4 & z_4^2 & z_4^3 \end{bmatrix} * \begin{bmatrix} a \\ b \\ c \end{bmatrix} = \begin{bmatrix} T_1 \\ T_2 \\ T_3 \\ T_4 \end{bmatrix} \tag{3.29}$$

Then, in order to calculate the polynomial coefficients, the vector $\boldsymbol{\alpha}$ is

$$\alpha = (\boldsymbol{Z}^T * \boldsymbol{Z})^{-1} * \boldsymbol{Z}^T * \boldsymbol{T} \tag{3.30}$$

Since the analytical extraction of error propagation from the equations above is cumbersome, a numerical sensitivity analysis was performed instead. Randomised values of the thermocouple positions and temperature readings were generated between the error limits for 250 different cases and applied to real data with the goal to measure induced variations in the computed global heat transfer coefficient h^*, caused by such experimental uncertainty. *Figures 3.17, 3.18 and 3.19* depict the relative difference between the initial heat transfer coefficient h and the altered h^*, under various volumetric air flows.

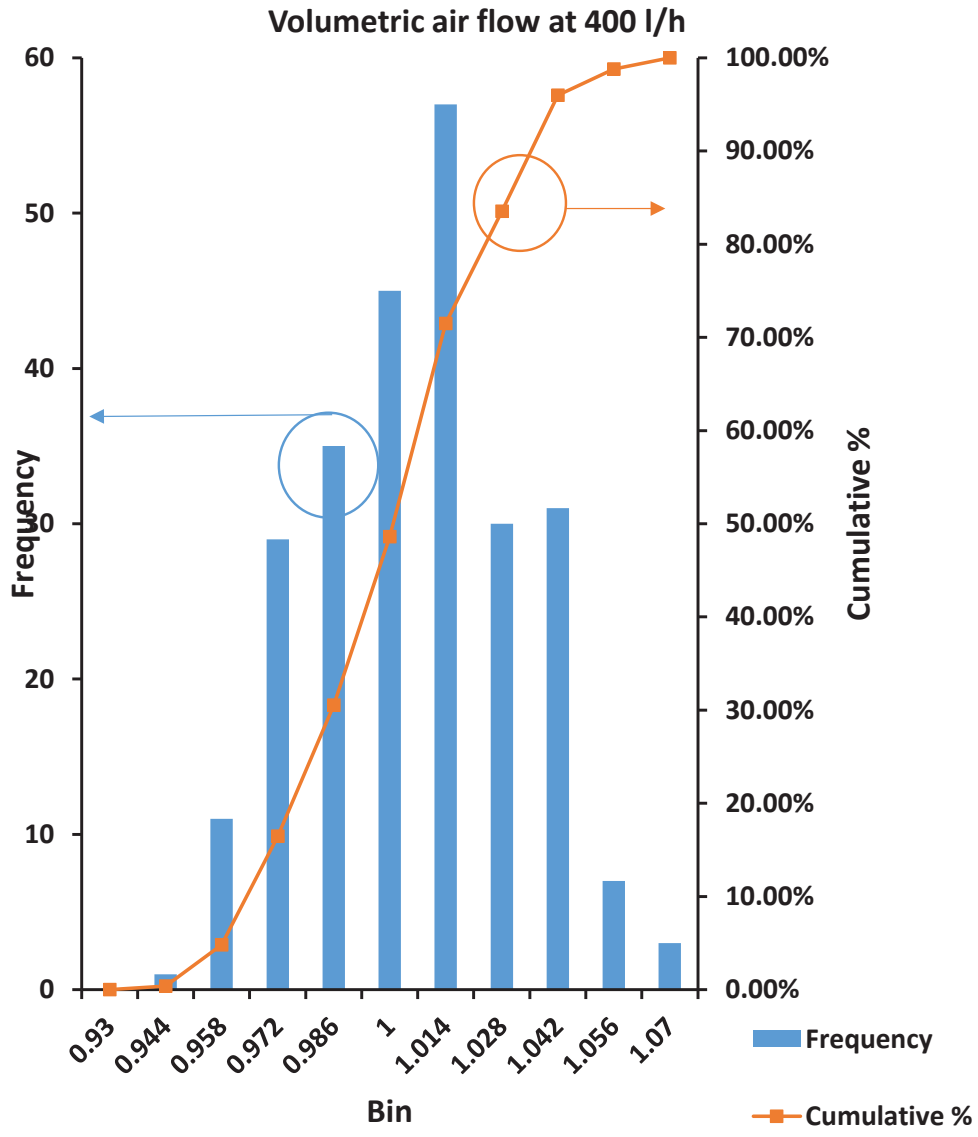

Figure 3.17: Cumulative and binned frequency plot for the relative change of the global heat transfer coefficient under 400l/h, after a randomized change of parameters. The number of bins follows Rice's rule.

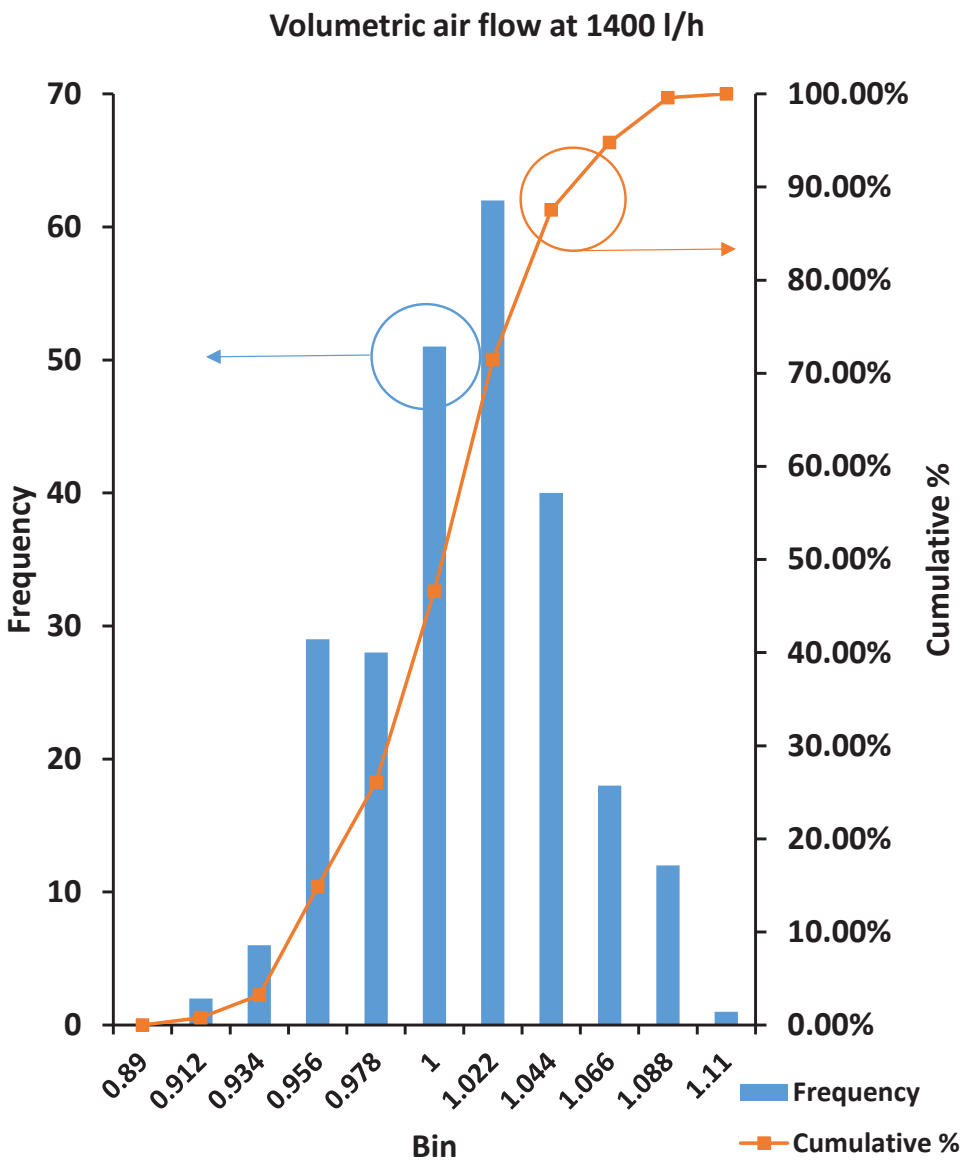

Figure 3.18: Cumulative and binned frequency plot for the relative change of the global heat transfer coefficient under 1400l/h, after a randomized change of parameters. The number of bins follows Rice's rule.

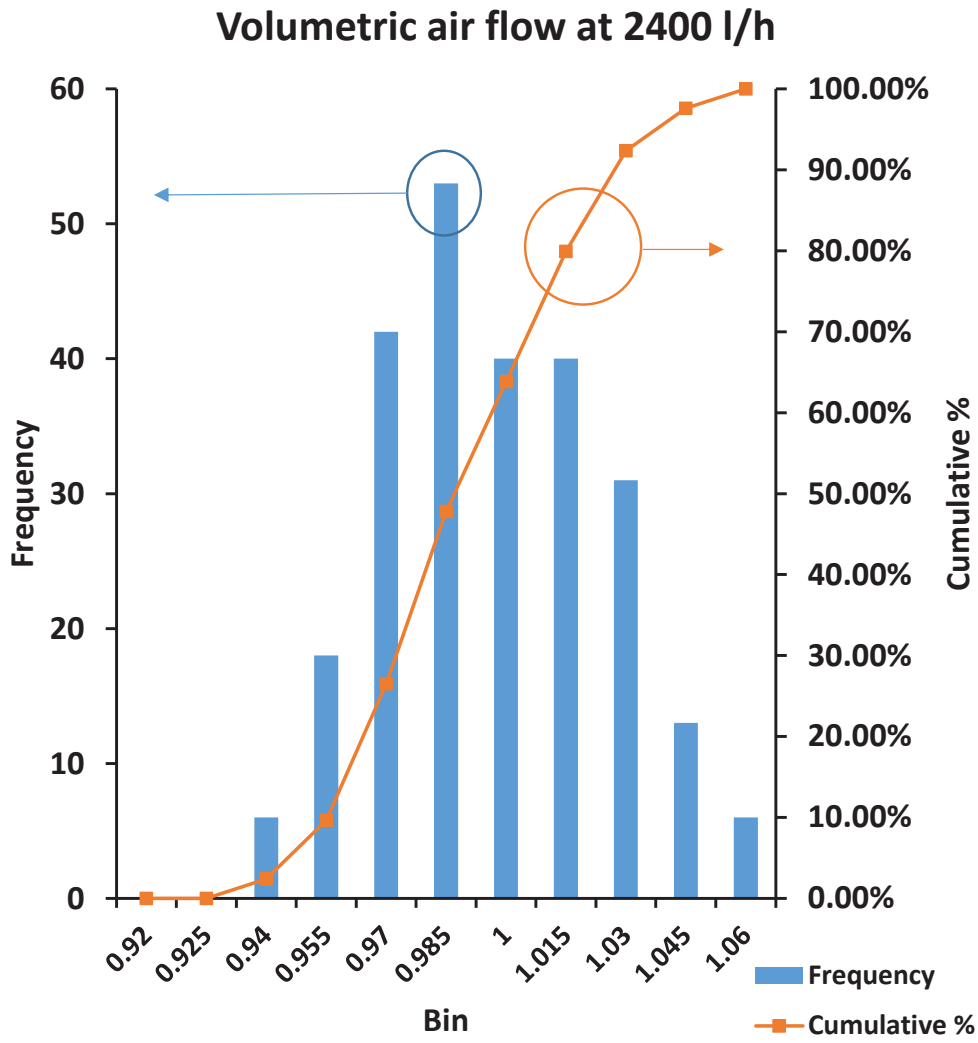

Figure 3.19: Cumulative and binned frequency plot for the relative change of the global heat transfer coefficient under 2400l/h, after a randomized change of parameters. The number of bins follows Rice's rule.

As seen above, the maximum error in the calculation of the global heat transfer coefficient of our samples is found to be as ~10%, with typical uncertainty rather around 5%.

3.3.5 Sample preparation and properties

Microcellular cylindrical samples of 4N purity aluminium were fabricated by the procedure described in *Section 3.1* and tested under forced convection. These samples had an integrated metal skin on their bottom (to decrease contact thermal resistance) and a central hollow cylindrical channel 4 mm in diameter drilled along their height. *Figure 3.20* illustrates two of these samples after the leaching process. It should be noted here that the said metal skin on the bottom of the samples can increase the uncertainty on the pore volume fraction of these samples up to 1%. Finally, an annular piece of cork having the same outer and inner

diameters as the sample and a height of 1 cm was glued on top of each microcellular aluminium sample in order to force the air to exit the foam along the outer diameter and minimize heat flow through the sample top surface. A silicone adhesive sealant, (Type 744 from Dow Corning™, Midland, USA), that can withstand high temperatures up to 200°C was used to fix the cork cap onto the samples. The main reasons for using cork as a cap are that

- cork can, for the present purpose, be considered to be airtight [236], [237],
- cork can withstand temperatures up to 200°C with low thermal degradation [237], [238] and
- cork has a low thermal conductivity, so heat dissipation through natural convection is limited [236], [237].

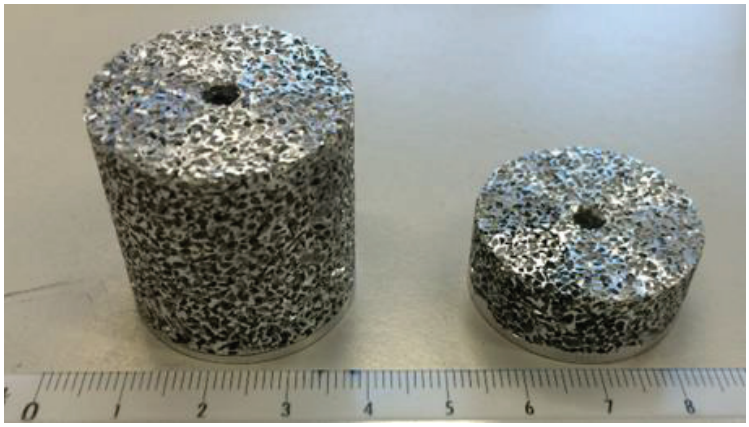

Figure 3.20: Samples after leaching. There is a ≈ 2 mm thick full metal skin at their bottom to improve thermal contact with the duct.

Tested samples had varying values of height, porosity, and pore size, and were infiltrated under different pressures. As illustrated in *Fig. 3.21* [100], infiltration pressure affects directly the microstructure of the foam by producing bigger metal struts and vertical lamellas around the ligaments. Microstructural and geometrical properties of the samples tested under forced convection are summarised in *Table 3*. Impingement jet, pin fins and a cylindrical solid bulk piece, the latter two out of aluminium alloy 6082, were additionally tested under the same conditions as the foamed samples. The finned structure consisted of 110 pins, 7 mm tall, 1 mm thick and with 1 mm gap between them, machined on a 1 mm thick cylindrical plate; the cylindrical bulk sample had a height of 10 mm. Both samples had a 30 mm diameter circular base, the same as aluminium foam samples.

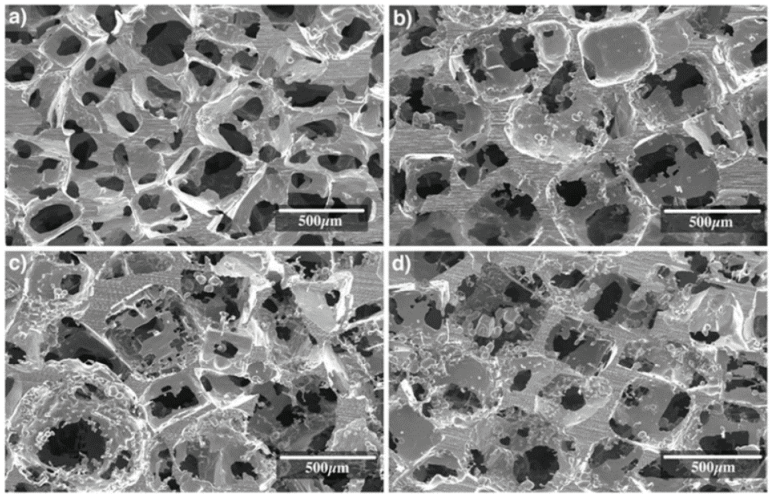

Figure 3.21: SEM pictures of pure Al replicated foams made out of similar salt preforms (porosity≈ 25%) infiltrated at various pressures P_{inf}: a) P_{inf} = 2 bars, b) P_{inf} = 5 bars, c) P_{inf} = 10 bars, c) P_{inf} = 155 bars. Figure reproduced from [100].

No.	Total Height [mm]	Pore volume fraction± 2.5 [%]	Pore Size [μm]	Infiltration pressure [bar]	Skin height [mm]	Material
1	10	85	400-450	9.7	2	Al foam
2	30	85	400-450	9.7	2	Al foam
3	30	85	400-450	2.7	2	Al foam
4	10	75	400-450	3.3	2	Al foam
5	30	75	400-450	3.3	2	Al foam
6	10	75	400-450	10.3	2	Al foam
7	10	70	400-450	3.4	2	Al foam
8	30	70	400-450	3.4	2	Al foam
9	10	85	125-180	70	2	Al foam
10	30	85	125-180	70	5	Al foam
11	10	75	125-180	70	2	Al foam
12	10	85	900-1300	3.3	2	Al foam
13	30	85	900-1300	3.3	2	Al foam
14	10	-	-	-	-	Bulk Al alloy 6082
15	7	75	1000 as distance between the fins	-	1	Al alloy 6082 fins

Table 3: List of tested samples and their properties

3.3.6 Testing Procedure

To measure its heat transfer characteristics, the foam specimen is placed on top of the heating duct. Between the duct and the specimen, Electrolube HTCPX™ thermal paste (Leicestershire, UK) is spread to decrease the contact thermal resistance. The nozzle outlet is placed inside the central hole in the cork cap, aligned with the internal channel of the foam. Temperature T_1, which is used as the control temperature, is set to 150°C; the system is managed using a PID controller, controlled by a Labview™ code. When the system has reached steady state conditions (defined by temperature variations of less than 0.1°C), then air is blown into the samples, initially at a value close to 200 l/h. The system is let to reach again steady state conditions as defined above; this takes roughly 20 minutes. The averaged values of the recorded temperatures of the 4 thermocouples placed along the duct are used to calculate the heat dissipated and the global heat transfer coefficient, for the specific volumetric flow value. The same procedure is repeated after increasing the volumetric air flow rate V by 200 l/h, until it reaches 2400 l/h, taking measurements at each step. Following this, the flow rate is reduced to 2300 l/h and then measurements are taken, reducing before each measurement the flow rate by 200 l/h until it reaches 300 l/h. The resulting plot of volumetric flow rate with time takes the form of a step pyramid, as depicted in *Fig. 3.22*. As the volumetric flow waxes and wanes, the $T_{topduct}$ temperature of the duct ebbs and flows, allowing for measurement of the global heat transfer coefficient at different sample temperatures (and consequently, at different volumetric air flows).

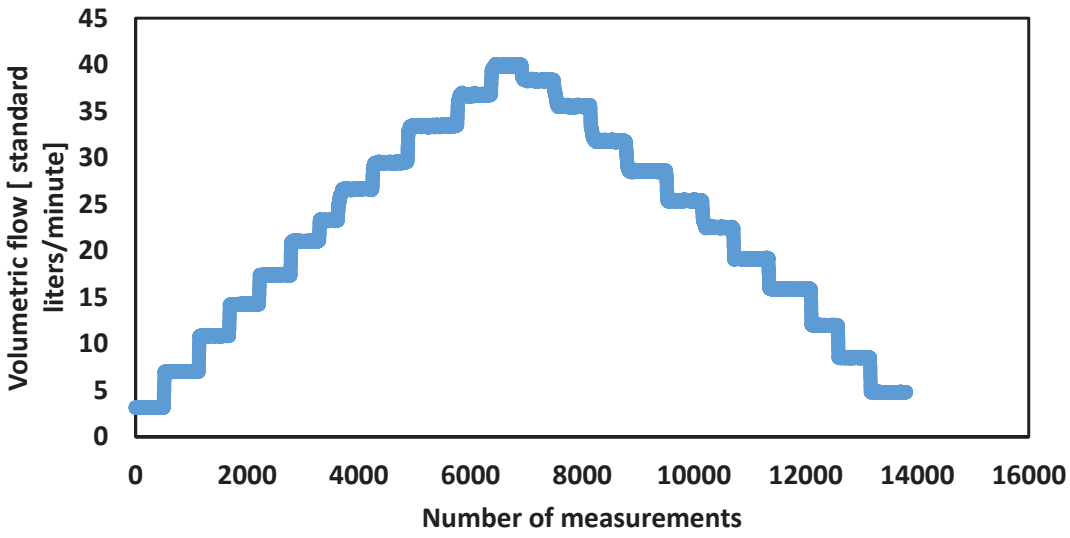

Figure 3.22: Typical evolution of volumetric air flow with time in forced convection experiments

During these measurements, the volumetric air flow is recorded every second. The static pressure across the nozzle is recorded manually for each volumetric flow rate value, such that the static and dynamic pressure before the foam can be calculated at each step.

3.3.7 Surface Temperature measurements

Measurements of the surface temperature of samples were additionally conducted using an infrared (IR) camera COX CX320™ (Seoul, South Corea). A flat bevel was machined along the cylindrical sample outer surface in order to avoid deviations from Lambert's cosine effect caused by the cylindrical shape of foam samples. Two samples were used for these measurements, namely Samples 2 and 13 of *Table 3*. Moreover, the temperature of the outflowing air was measured, at two different distances (18 and 27 mm) from the heated surface using two K-type thermocouples, placed as close as possible to the foam, without touching it, at a distance smaller than 50 μm. This distance was measured using Johansson gauges.

3.3.8 Measuring the static pressure inside the central channel

In order to characterize the air flow field through the foam under forced convection, a new set-up was built to measure the total and static pressure along the central cavity in the foam samples as a function of altitude z. This task was performed using an air flow test bench, designed to measure the static and dynamic pressure profiles inside the internal cylinder of the samples, as shown in *Figs.3.24* and *3.25*.

The measurements are taken by inserting one hypodermic needle vertically up along the sample central channel, from its bottom; a hole (0. 2 mm) on the side of the needle, gives the static pressure. Two separate sets of samples were produced without the bottom metal skin (in contrast to the samples tested under the forced convection apparatus) and tested for the static pressure distribution along the central cavity:

- samples of height 5, 15, 20 and 28 mm, [400-450] μm pore size, 82% V_p, infiltrated at a pressure of 3.4 bars.
- samples of 28 mm height, [900-1300] μm pore size, 83% V_p, infiltrated at a pressure of 4.4 bar.

To conduct these measurements, each specimen is placed between two aluminium circular plates, as illustrated in *Fig. 3.23 and 3.24*. Three screws, evenly distributed held the plates together. Vacuum grease is spread between the foam and the two plates, to prevent air from escaping between the sample and the plates. The top plate has a hole into which the brass nozzle is positioned. An annular rubber with vacuum grease, seals the area between the nozzle and the plate. The lower plate has a larger hole into which a circular Teflon piece is held, using an aluminium tightening ring. The measurement needles pass through the predescribed Teflon piece to the inner central channel of the foam. An extra rubber seal and vacuum grease are additionally used to prevent air passing along the gap between the needle and Teflon piece.

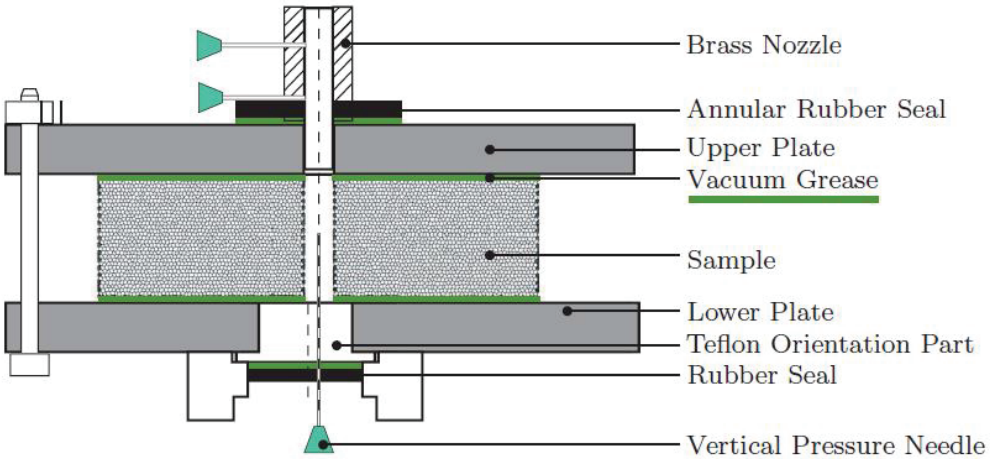

Figure 3.23: Mechanical drawing of the of the air flow bench, indicating its parts (image courtesy D. Ingram)

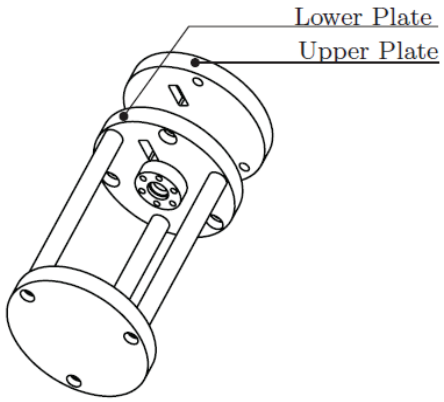

Figure 3.24: Trimetric projection of the air flow bench (image courtesy D. Ingram)

It should be noted that the inserted needle inside the central channel of the foam, distorts both the flow and the pressure field, inducing an error in our measurements (the measurement of pressure in a flowing stream can be achieved only by intrusive means [234]). Sources of this uncertainty are:

- The shear effect. When a long pressure tube is inserted inside a flow, having its axis aligned with the flow direction, the measured static pressure inside is somewhat lower than the free-stream pressure; this is due to the flow acceleration around the nose. Using Refs. [234], [239], this error was calculated to account for up to 1% of the dynamic pressure inside the channel. Elementary analysis shows that for our case this might be up to 6%, however for reasons of simplicity we have followed the textbooks' approach.

- The wall proximity effect. Since our needle is close to the porous metal wall, it partially blocks air flow in its vicinity, displacing streamlines away from the wall. This should distort the pressure measurement by about 1.5% of the dynamic pressure inside the channel [234].

- Flow turbulence. A disturbance of the measurements due to turbulence should not be neglected for turbulence intensities above 15%. Correction methods are not of general validity since the error should depend not only on the turbulent intensity but also on the length scale of the turbulence, the turbulence structure, the tube geometry etc. [234], [239]. Moreover, the literature on this field is considered "incomplete and contradictory" [234]. Using *Eq.8.19* of Ref.[234], the resulting error was calculated to reach up to 13% of the dynamic pressure inside the channel. In all cases, the error is likely to be significant and not easy to correct for.

In comparison, errors due to viscous or compressibility effects are considered negligible and therefore, have not been accounted for in the present thesis. Summing up, the above reasons can lead to an error in static pressure of 50 Pa for air flow rates of 720 l/h, 200 Pa for air flow rates of 1260 l/h, 350 Pa for 1800 l/h air flow rates and 700 Pa for air flow rates of 2520 l/h.

3.4 Integrated heat-sink fabrication and forced convection testing thereof

3.4.1 Geometry and structure of the integrated heat sink

A cylindrical integrated heat sink with a structure such as that proposed in *Section 1.2* was produced and tested under forced convection, thus providing a proof-of-concept experiment validated in a laboratory environment. The integrated heat sink has a diameter of 30 mm and an overall height of ~15 mm and consists of:

- a first layer of 350 μm diameter diamond particle reinforced aluminium matrix composite, 1 mm thick, designed to act as the heat spreader

- a second dense layer of AlN, 400 μm thick, creating an electrical insulation barrier and

- a third layer of replicated aluminium foam, with pores [900-1300] μm in diameter, 80% porosity and of 9 mm height, allowing air to extract the heat out of the stack. The upper part of the foam has a cast-in aluminium skin of 4 mm, replacing the cork caps used in experiments of *Section 3.3.* As for aluminium foam samples tested under forced convection, an inner channel 4 mm in diameter traverses the middle of the aluminium foam layer, allowing air to travel to the bottom part of the aluminium foam and to traverse the foam along a flow path having cylindrical symmetry. The integrated structure is shown in *Fig.3.25.*

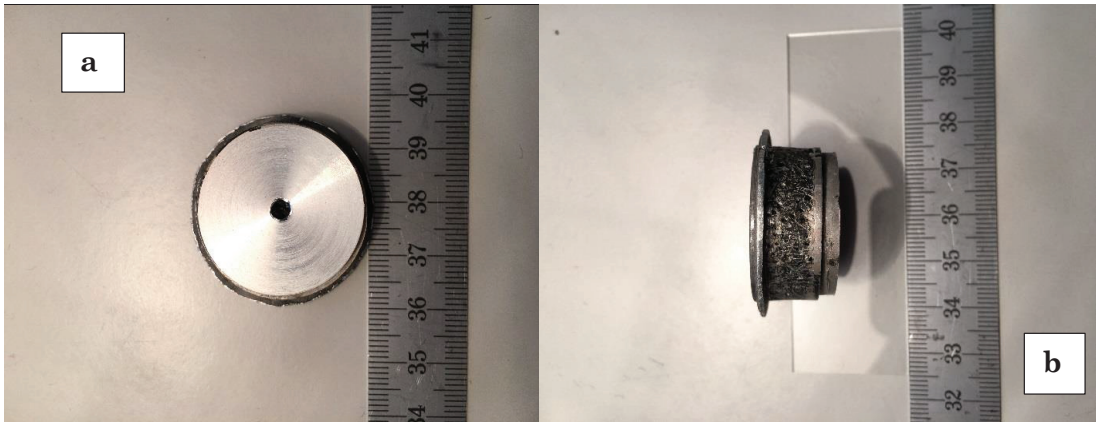

Figure 3.25: (a)Top and (b) side view of the integrated structure.

3.4.2 Manufacturing of the integrated heat sink

To produce this integrated structure, a uniaxially pressed body of sodium chloride particles with a monomodal size distribution (between 900 and 1300 μm) and weighing 10.2 g, was pressed under an axial force of 36.8 MPa inside a cylindrical steel mould 30 mm in diameter. This produced a salt preform of the same diameter, with a height of ~9mm and a porosity of ~20%. The two last structural characteristics were chosen because (i) high porosity foams were found to perform best in terms of pressure drop and (ii) samples of shorter height, under forced convection, were found to provide the best thermal performance at given gas flow rate.

The predescribed bed of salt particles was packed inside the left part of a graphite mould, the latter being separated in two parts by the AlN plate. The other side of the graphite mould was filled with 1.7 g of synthetic mono-crystalline diamond particles having a narrow size distribution (mean particle size 350 μm) *Fig.3.26* depicts the graphite moulds used.

Prior to infiltration, the filled mould was deposited at the bottom of an alumina crucible and a pure aluminium ingot is placed on top of this mould. Both the graphite mould and the inner surface of the alumina crucible were previously sprayed with graphite to facilitate their recovery from the infiltrated structure.

The infiltration process took place in the custom-made apparatus illustrated in *Fig. 3.27*; a detailed description is given in Ref.[240]. The infiltration chamber is composed of three stainless steel parts: top and bottom caps and a middle cylinder. The three parts are held together using greased threads. Carbon foil rings are placed between the top and middle parts as well as along the bottom and middle parts to ensure airtightness. The top part, through which a thermocouple passes to measure the instantaneous temperature in the chamber, can be connected either to a vacuum pump or an argon gas bottle with the aid of a three-way valve.

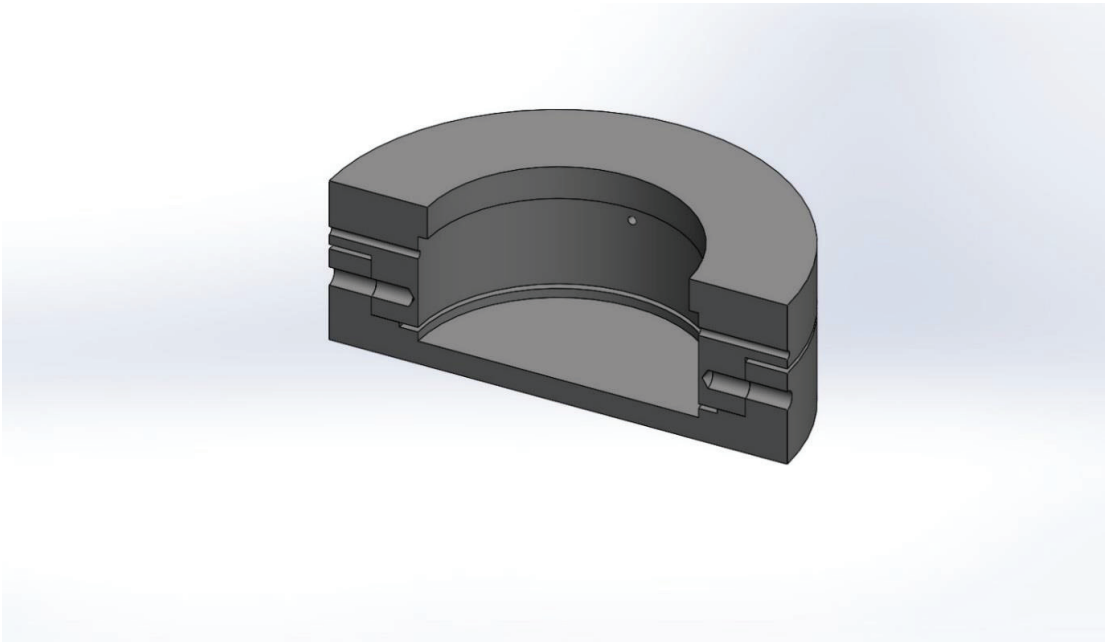

Figure 3.26: Cross sectional view of the graphite mould used for the fabrication of the integrated structure.

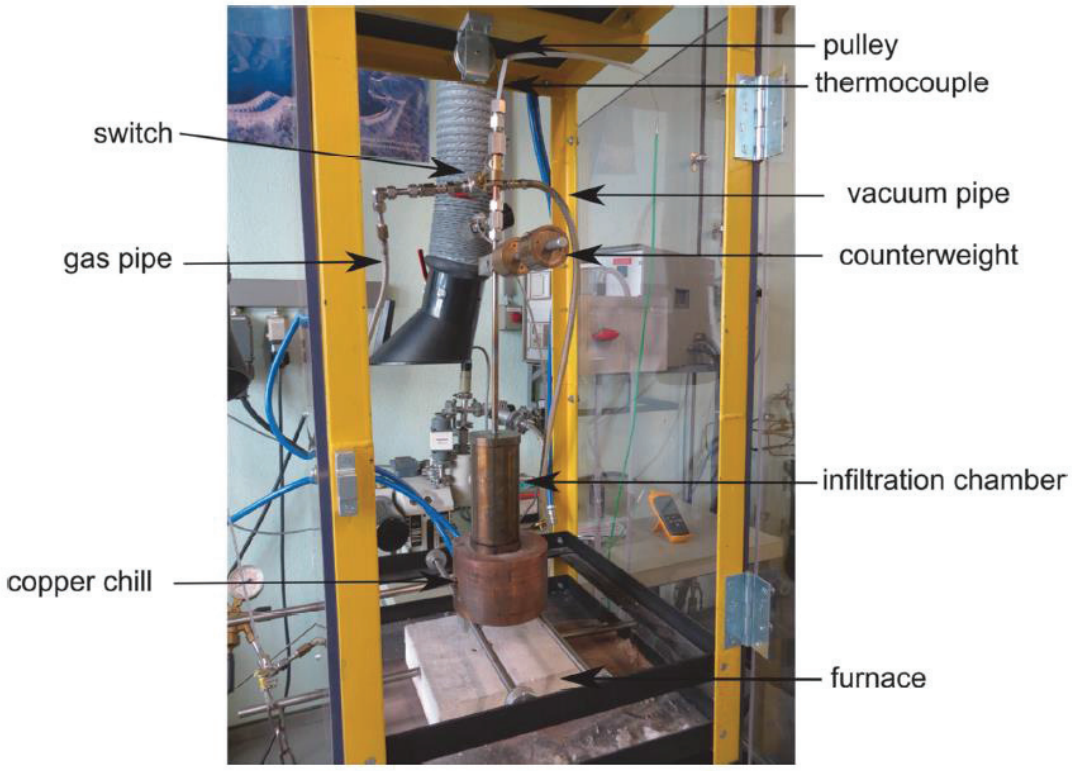

Figure 3.27: The infiltration set-up, with its infiltration box (yellow frame), having Plexiglas® walls. The infiltration chamber is attached at the pulley above the furnace and the gas and vacuum pipe are connected with a three-way valve. This apparatus was used and described in Ref.[240]

The infiltration procedure was as follows: Once the chamber containing the crucibles is sealed and placed under vacuum (0.2 mbar), it is suspended into the infiltration set-up comprising of a box with Plexiglas® walls as a security protection, as illustrated in *Figure 3.27* [240]. A counterweight is attached to the chamber in order to keep it at all times vertical. The chamber is then slowly lowered inside the furnace, using a pulley (*Figure 3.28 (a-c)*) [240]. After roughly 120 min (60 min to heat up the crucibles to the temperature of 700°C and 60 min as a security time to ensure that the ingots are entirely molten), the switch connector releases argon pressurized to 15 bar (1.5 MPa). This pushes the molten aluminium to enter the mould and to infiltrate the diamond and salt preforms. In order to make sure that the infiltration process was completed, the pressure was applied for 15 minutes while the chamber was still at 700°C. Next, the chamber is taken out of the furnace (*Figure 3.28 (d&e)*)[240] and placed onto a copper block cooled by air flow pipes (*Figure 3.28 (f)*)[240], to promote directional solidification.

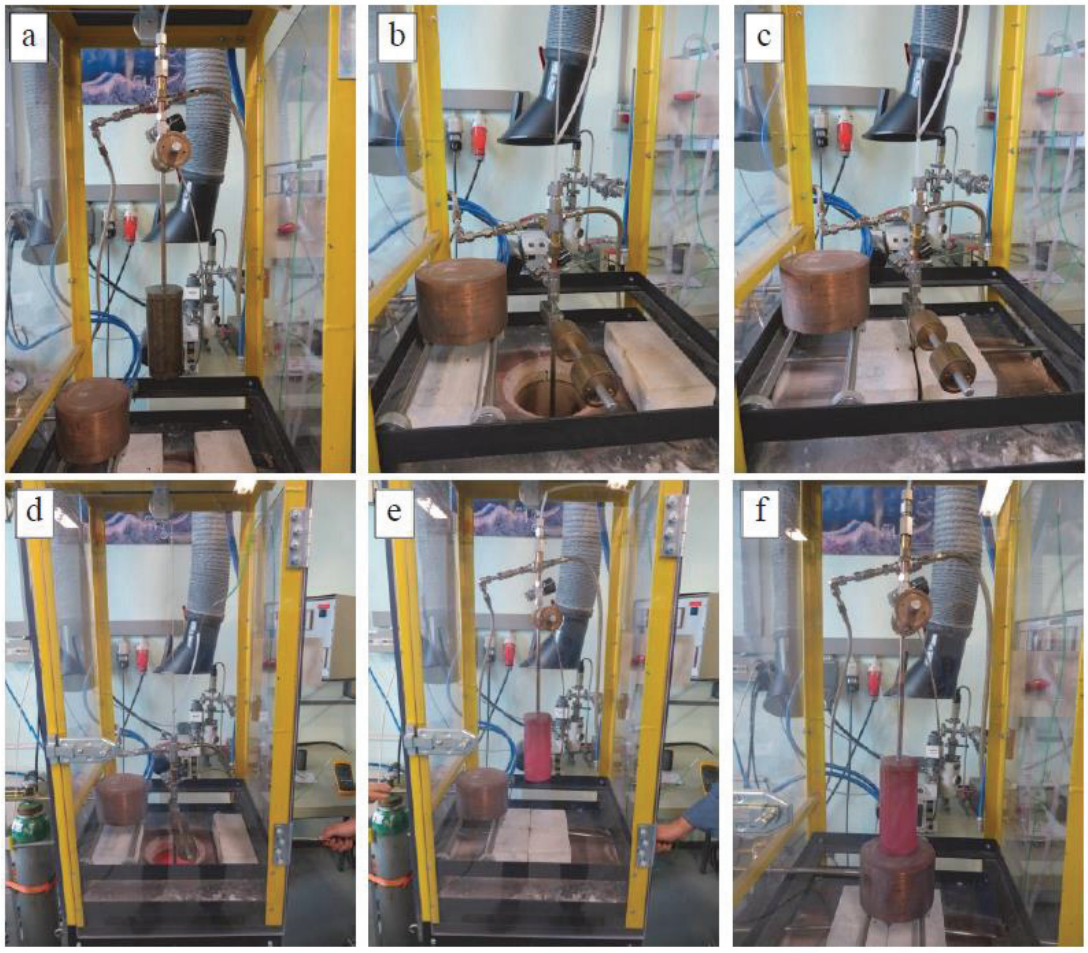

Figure 3.28: Photographs from a) to f), depict the different consecutive steps of the infiltration procedure described in the text. From Ref. [240].

Once cooled and solidified, aluminium metal surrounding the infiltrated carbon mould is removed from the crucible and the graphite mould is extracted manually using a hand saw, a hammer and chisels. The infiltrated composite is then separated from the mould and a 4 mm diameter central hollow channel is machined at the centre of its aluminium foam layer, similarly to the method presented in *Section 3.1.4.* Finally, the salt is leached out of the structure, as described in *Section 3.1.4.*

3.4.3 Forced convection testing

The heat dissipation capabilities of the integrated structure were tested under forced convection, using the same set-up and method as for aluminium foam samples. The heat sink was placed on top of the apparatus described in *Section 3.3.1*, with thermal paste Electrolube HTCPX™ spread between the bronze duct and the aluminium/diamond layer. The outlet of the nozzle was placed inside the hole of the aluminium cap (which lies on its centre), aligned with the internal channel of the foamed area. The experimental characterisation followed the modus operandi of *Section 3.3.6,* with the data extracted and treated as described in *Section 3.3.3.*

Chapter 4 Experimental Results

In this chapter, the convective behaviour of the previously described samples (foams and an integrated structure) is presented. Specifically, the global heat transfer coefficient, h_{total}, meaning the heat transfer coefficient referenced to the footprint area of the samples, is determined, first under natural convection, then under forced convection. Moreover, the static pressure gradient (as a function of the volumetric flow rate) under forced convection inside the central channel of samples is also presented.

4.1 Foams under natural convection

The reproducibility of our experiments is good; *Fig.4.1* depicts two different measurements conducted on the same sample, on two different days. The difference in the global heat transfer coefficient between these consecutive measurements is less than our estimated experimental error.

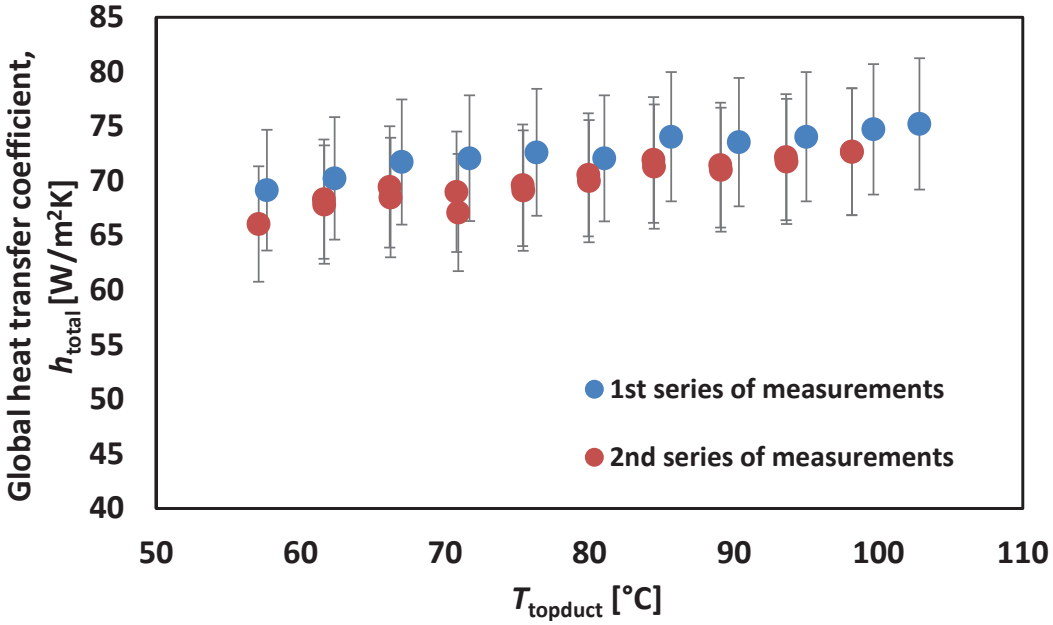

Figure 4.1: Global heat transfer coefficient of one of our samples, tested twice in two different days. The discrepancy is less than the maximum experimental error possible (8%).

The global heat transfer coefficient of near-flat samples, under natural convection, for various surface temperatures, is depicted in *Fig.4.2*. As a means of comparison, we have included in the figure the heat transfer coefficient of a dense aluminium solid of the same height and at the same temperatures.

Theoretical predictions for the global heat transfer coefficient of a bulk sample having a 2 mm height are also depicted in *Fig.4.1*. These values, $h_{vertical}$ and $h_{horizontal}$,were calculated using *Eqs [9.27]* and *[9.30]* from [241], which in the thesis at hand are *Eqs 4.1* and *4.2* respectively:

$$Nu_{\text{vertical}} = 0.68 + \frac{0.67Ra^{1/4}}{[1 + (0.492/Pr)^{9/16}]^{4/9}} \quad (4.1)$$

$$Nu_{\text{horizontal}} = 0.54Ra^{1/4} \quad (4.2)$$

where Nu, Ra and Pr are the Nusselt, Rayleigh and Prandtl non-dimensional numbers respectively.

Using the Nusselt number from *Eqs. 4.1* and *4.2*, the respective heat transfer coefficient is calculated with the characteristic length being chosen as i) the ratio of surface to perimeter for the horizontal surface and ii) the height for the vertical surface [241]. Thus, the total extracted heat flux yields:

$$Q_{\text{total}} = Q_{\text{vertical}} + Q_{\text{horizontal}} \quad (4.3)$$

or

$$q_{\text{total}} A_{\text{footprint}} = q_{\text{vertical}} A_{\text{vertical}} + q_{\text{horizontal}} A_{\text{horizontal}} \quad (4.4)$$

Since the heat flux dissipated via natural convection is small compared to the thermal conductivity divided by the characteristic dimension of our samples (in other words, that its Biot number falls below 0.1), we can assume that our samples are isothermal. Therefore *Eq.4.4* gives:

$$h_{total}(\pi r^2)(T_{\text{top}} - T_{\text{ambient}}) = 2\pi r H(T_{\text{top}} - T_{\text{ambient}}) * h_{\text{vertical}} + h_{\text{horizontal}}\pi r^2(T_{\text{top}} - T_{\text{ambient}}) \quad (4.5)$$

or

$$h_{\text{total}} = 2H\frac{h_{\text{vertical}}}{r} + h_{\text{horizontal}} \quad (4.6)$$

With H being the height of the sample and r its radius.

Figs.4.2 and *4.3* plot the global convection coefficient of microcellular aluminium samples 2 and 12 mm high, respectively. The theoretically predicted global heat transfer coefficient (blue line) is calculated again using *Eq. 4.6* with h_{vertical} and $h_{\text{horizontal}}$ given by *Eqs. 4.1* and *4.2*. As seen with the near flat (2 mm high) samples, the measured convection coefficient is significantly higher than is predicted by theory, also for the dense aluminium cylinder. On the other hand, within experimental uncertainty, replicated aluminium foams transport heat in natural convection at a rate equal to that of solid blocks of alloyed aluminium having the same dimensions, too; we do not find any strong difference in foam performance as the pore density or pore size varied.

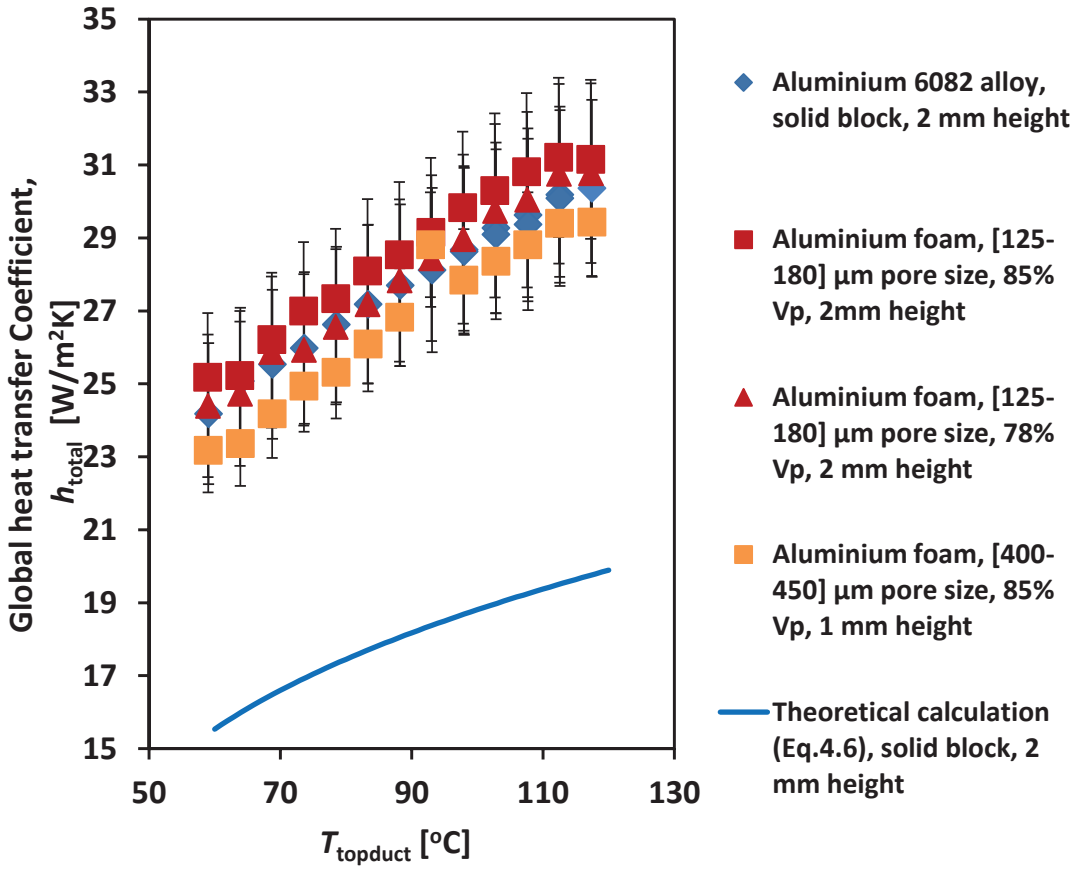

Figure 4.2: Evolution of the global heat transfer coefficient of nearly flat samples versus the temperature at the top of the duct, $T_{topduct}$. The samples have a varying pore size 125-180 and 400-450 µm) and porosity (78 and 85%).

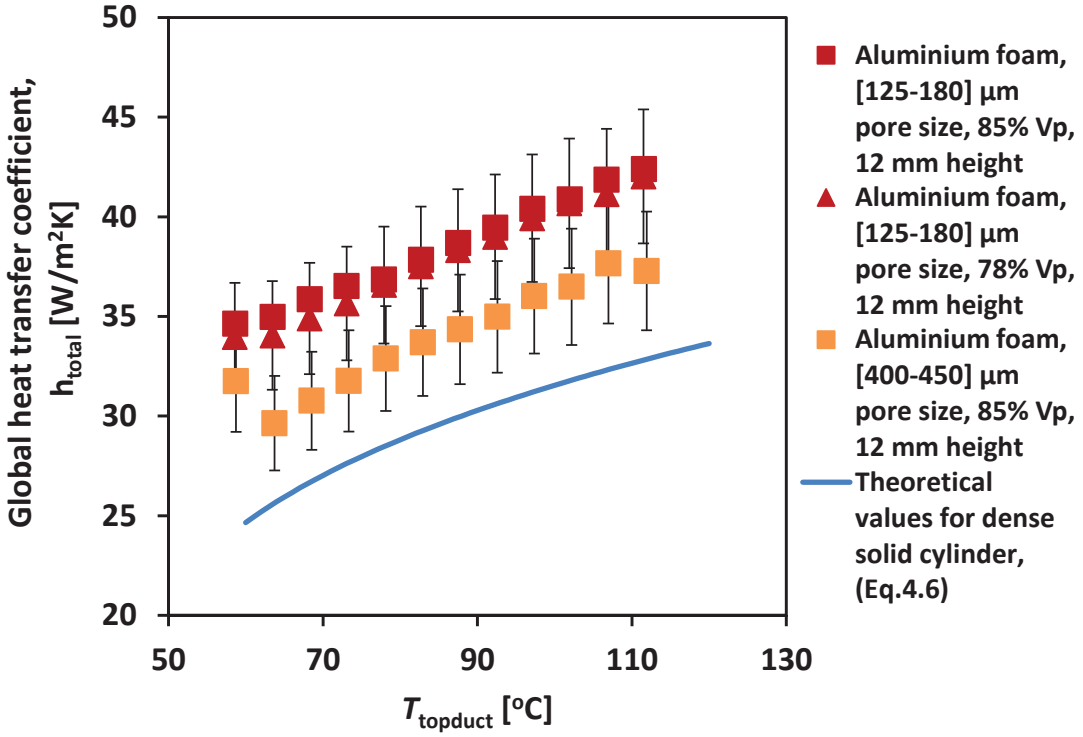

Figure 4.3: Evolution of the global heat transfer coefficient of 12 mm tall samples versus the temperature at the top of the duct, $T_{topduct.}$ The samples have a varying pore size (between 125-180 µm) and porosity (78 and 85%).

Figure 4.4 compares the thermal behaviour of the Corevo™ aluminium foam sample with its analogue out of dense aluminium alloy, under natural convection. Despite of the relatively large pore size, no significant increase of heat dissipation is observed when compared with a solid block of aluminium.

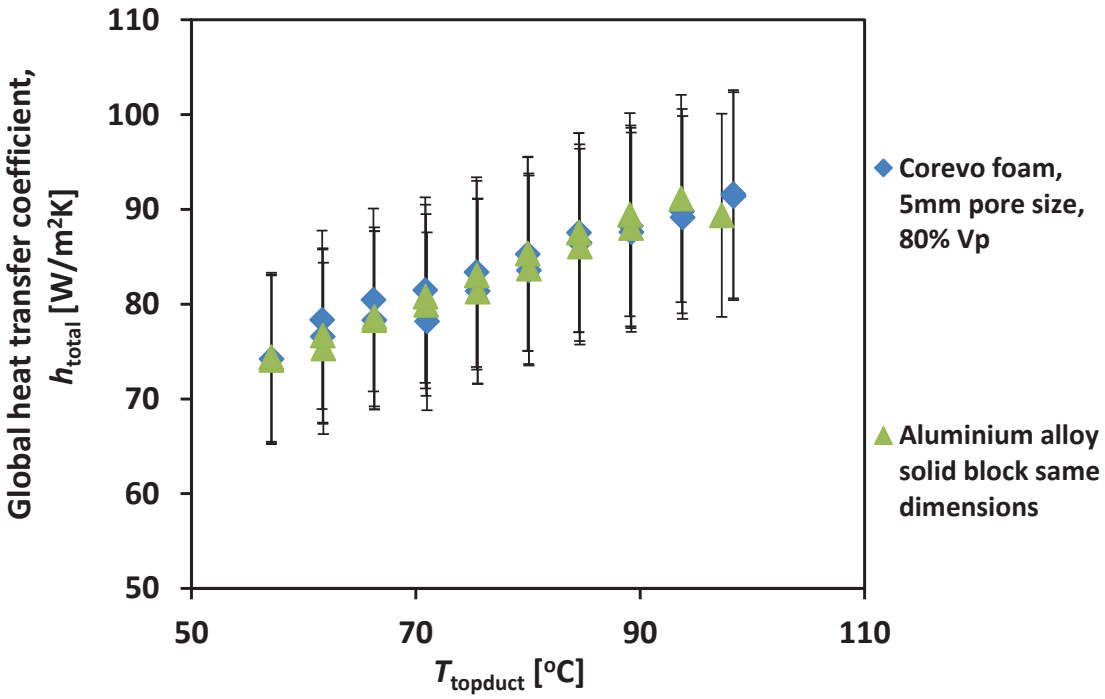

Figure 4.4: Evolution of the global heat transfer coefficient of a Corevo aluminium foam of 5 mm pore size, 80% V_p and 75 mm height versus the temperature at the top of the duct, $T_{topduct}$.

Figure 4.5 depicts the evolution of the global heat transfer coefficient of finned dense aluminium alloy or aluminium foam structures with the surface temperature. As elaborated in *Section 3.2.6*, the temperature at the top of the aluminium block onto which the fins were placed, was used in the calculation of the global heat transfer coefficient, instead of the temperature at the top of the bronze duct. Again, within the limits of experimental uncertainty, finned structures appear to behave in like manner whether they consist out of bulk aluminium or foamed aluminium.

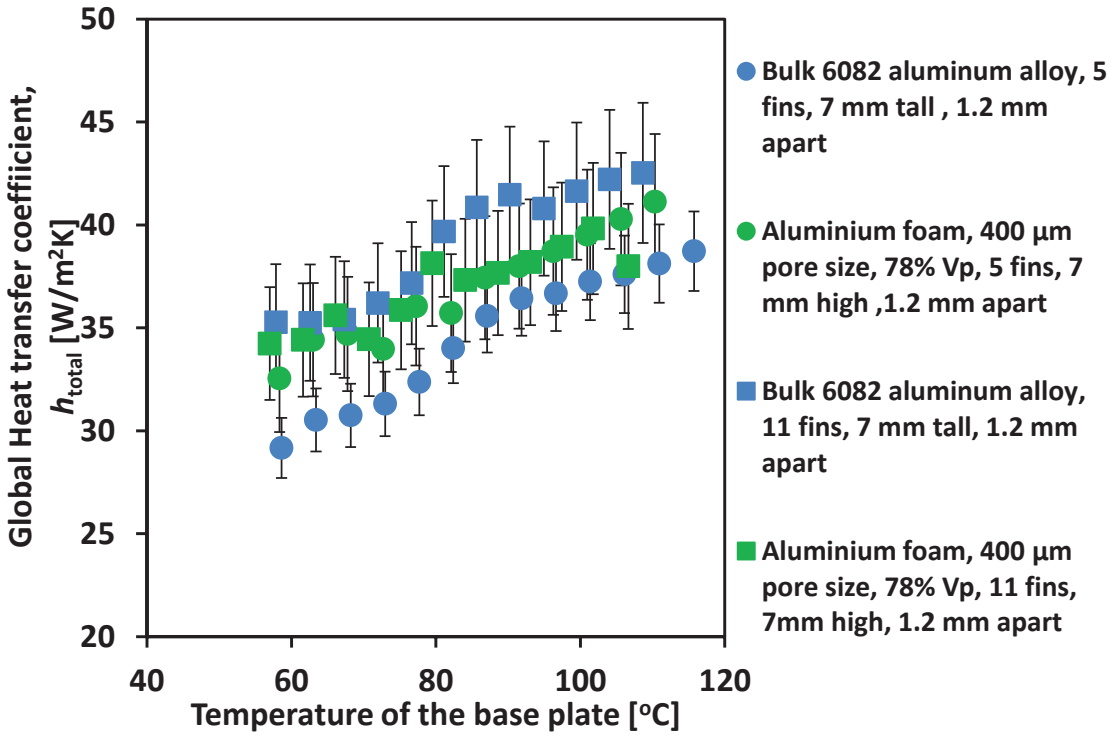

Figure 4.5: Overall heat transfer coefficient for two different finned geometries made out of both aluminium foam and solid aluminium alloy. One geometry consists of 5 fins and one of 11 fins. In both geometries, fins have 7 mm height and are 1.2 mm apart.

Finally, *Figure 4.6* plots the global heat transfer coefficient of an a) unleached, b) partially leached and c) fully leached aluminium foam sample. As seen, after the first series of pores are leached, the global heat transfer coefficient rised and then, does not appear to change significantly after further leaching of the NaCl.

.

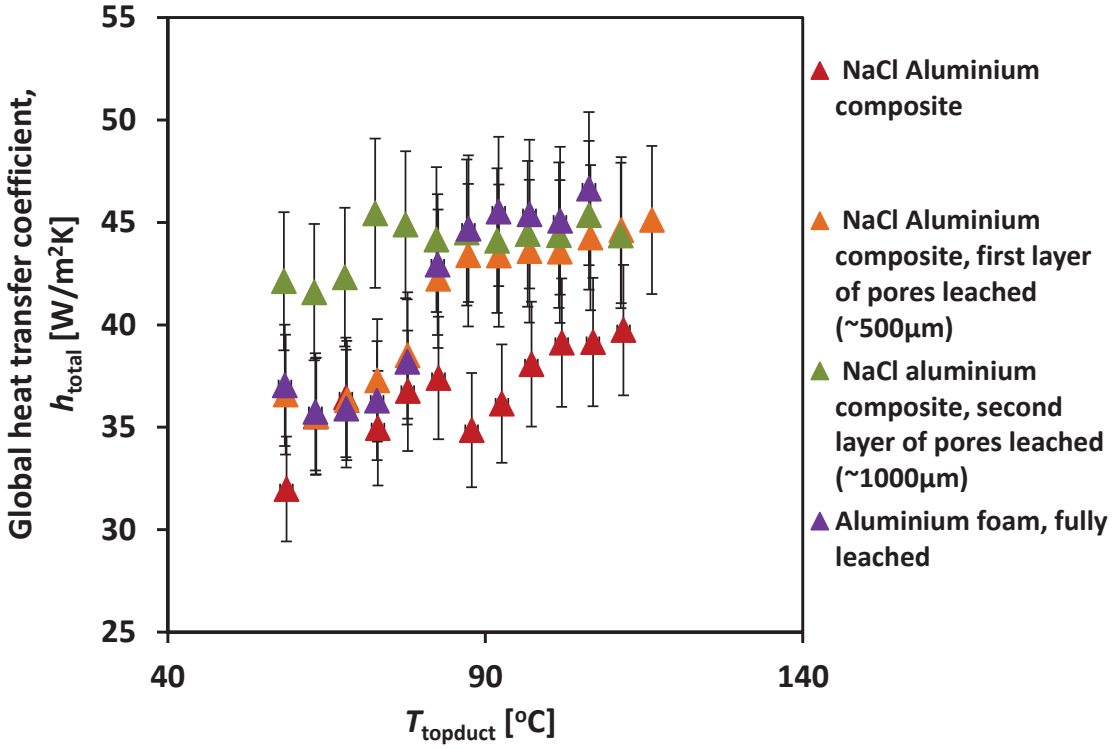

Figure 4.6: Overall heat transfer coefficient for unleached, partially leached and fully leached aluminium foam sample.

4.2 Foams under forced convection

4.2.1 Evolution of the global heat transfer coefficient with the volumetric flow

4.2.1.1 Foams with pore size of 400-450 µm

Figs. 4.7 and *4.8* plot the heat transfer coefficient of samples with 400-450 µm pore size and 28 mm height. As seen, foams with higher porosities and infiltrated at lower pressures dissipate more heat for the same air flow rate. The same trend also appears (however not far out of experimental uncertainty) for shorter (1 cm height) foams of the same pore size, as shown in *Figs. 4.9* and *4.10*.

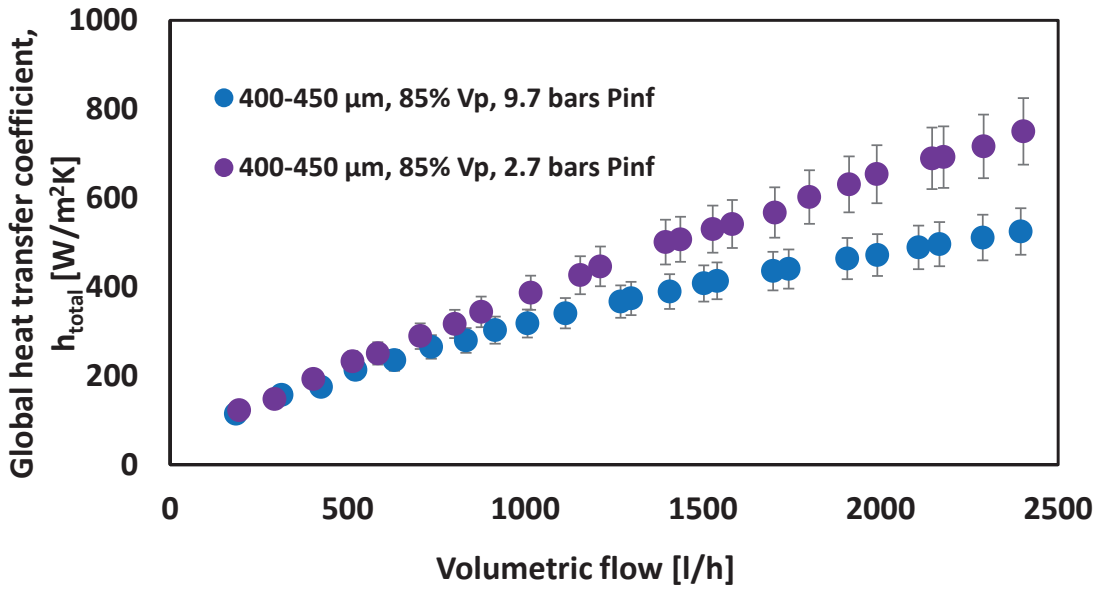

Figure 4.7: Evolution of the global heat transfer coefficient h_{total} with volumetric flow for 28 mm tall samples of same pore size and porosity but infiltrated at different pressures. In the present geometry a flow rate of 2500l/h corresponds to roughly 1 m/s average inflow superficial velocity over the heat transfer footprint area, equal in the present experiments to $7.07*10^{-4}$ m².

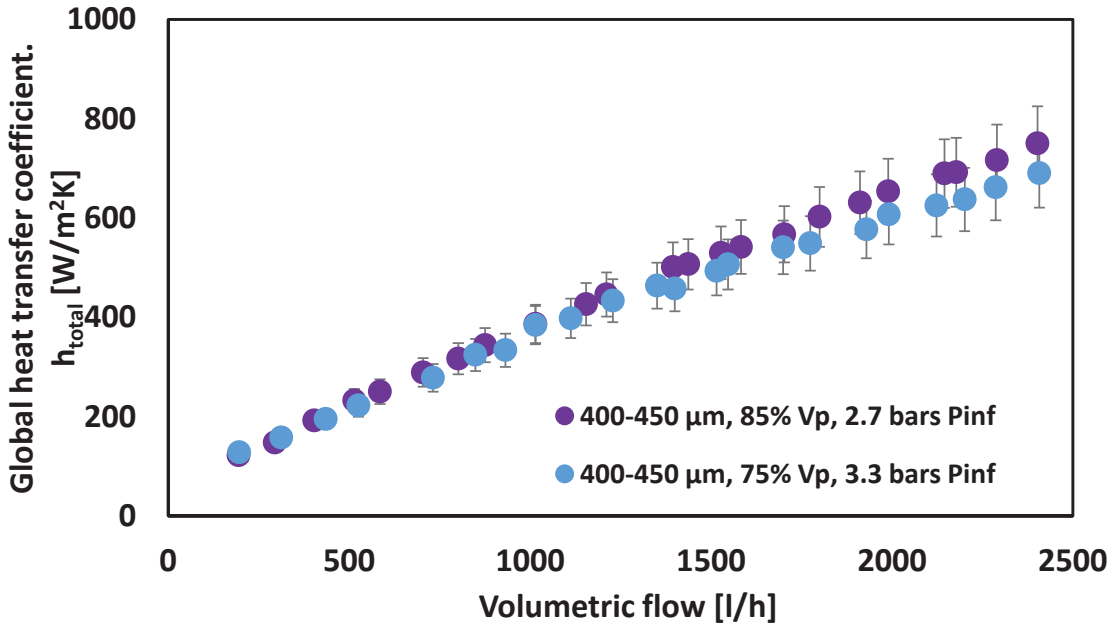

Figure 4.8: Evolution of the global heat transfer coefficient h_{total} with volumetric flow for 28 mm tall samples of same pore size and infiltrated at nearly the same pressure but of different porosity In the present geometry a flow rate of 2500l/h corresponds to roughly 1 m/s average inflow superficial velocity over the heat transfer footprint area, equal in the present experiments to $7.07*10^{-4}$ m².

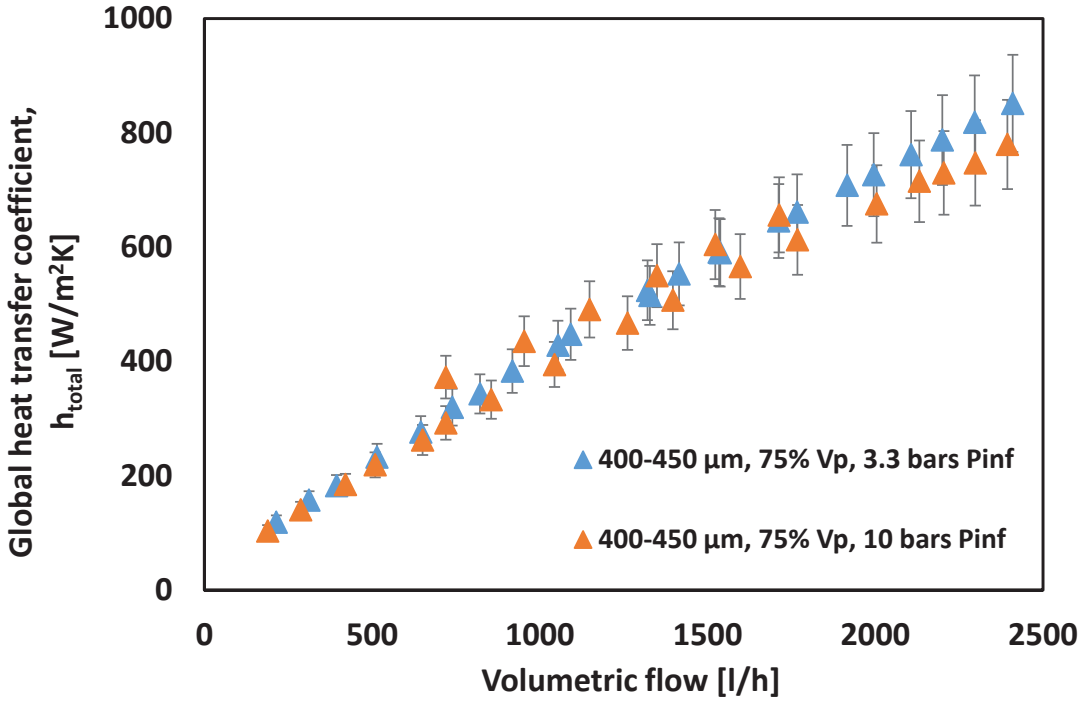

Figure 4.9: Evolution of the global heat transfer coefficient h_{total} with volumetric flow for 10 mm tall samples of same pore size and porosity but infiltrated at different pressures. In the present geometry a flow rate of 2500l/h corresponds to roughly 1 m/s average inflow superficial velocity over the heat transfer footprint area, equal in the present experiments to $7.07*10^{-4}$ m².

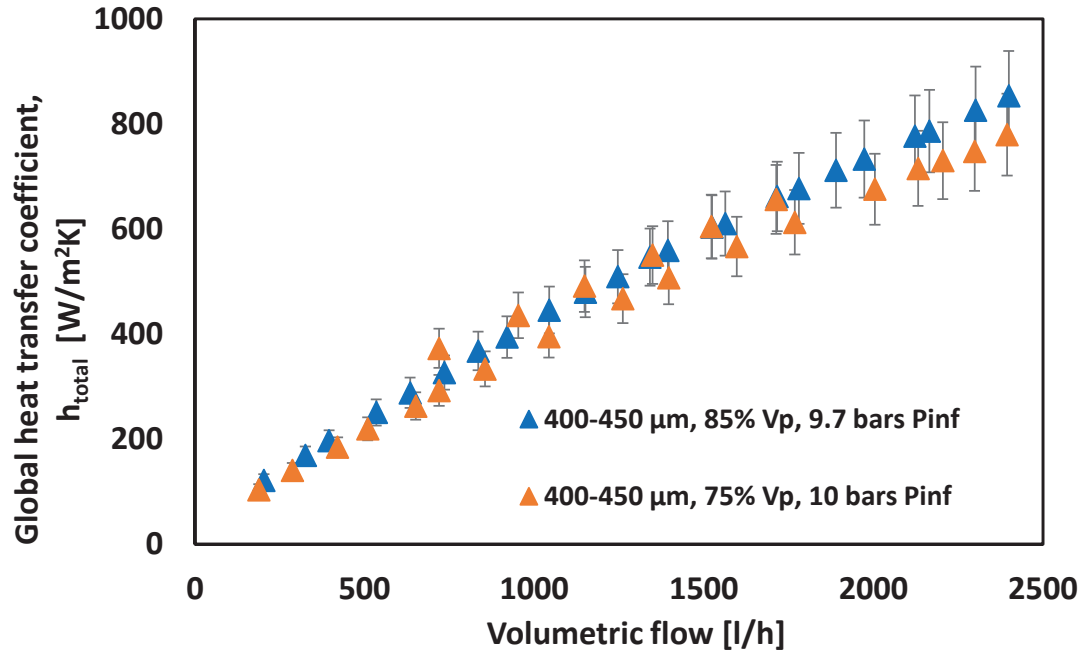

Figure 4.10: Evolution of the global heat transfer coefficient h_{total} with volumetric flow for 10 mm tall samples of same pore size and infiltrated at the same pressure range but of different porosity. In the present geometry a flow rate of 2500l/h corresponds to roughly 1 m/s average inflow superficial velocity over the heat transfer footprint area, equal in the present experiments to $7.07*10^{-4}$ m².

Figure 4.11 compares two foams with the same pore size, porosity and infiltrated at the same pressure but of different heights. As observed, the height strongly influences h_{total}, with the shorter height giving a higher heat transfer coefficient at given overall volumetric flow rate.

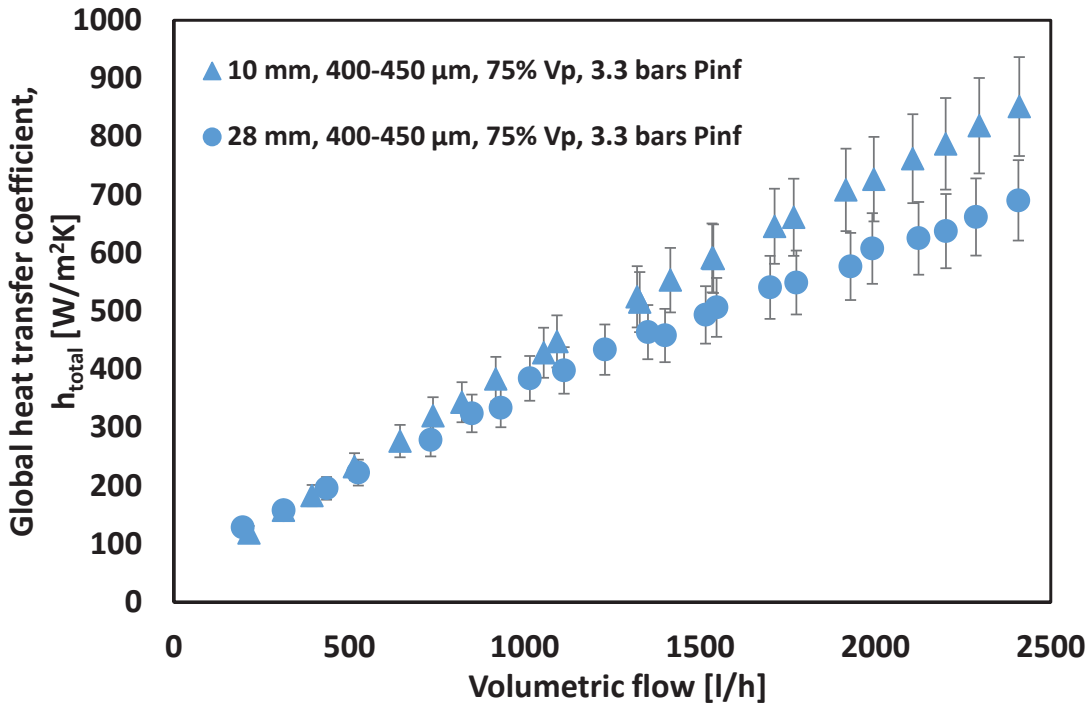

Figure 4.11: Evolution of the global heat transfer coefficient h_{total} with volumetric flow for samples of same pore size, porosity and infiltrated at the same pressure range but of different height. In the present geometry a flow rate of 2500l/h corresponds to roughly 1 m/s average inflow superficial velocity over the heat transfer footprint area, equal in the present experiments to $7.07*10^{-4}$ m².

4.2.1.2. Foams with pore size of 125-180 µm

Figure *4.12* plots the heat transfer coefficient of 125-180 µm pore size foams and 10 mm tall samples. As was found with 400-450 µm foams (*Fig. 4.*8 and *4.10*), samples with higher porosity dissipate more heat under the same volumetric air flow. Moreover, here again shorter samples dissipate more heat at fixed overall volumetric flow rate, *Fig. 4.13*.

Figures *4.14 and 4.15* compare the heat transfer coefficient of 125-180 µm pore size foams with the heat transfer coefficient of foamed samples of 400-450 µm pore size, of the same porosity and height for a duct control temperature of 150°C: the influence of pore size is relatively weak in this range at equal overall volumetric flow rate, with a slight edge for the coarser pores at higher volumetric flow rates (obviously the finer pores necessitate a higher pumping power).

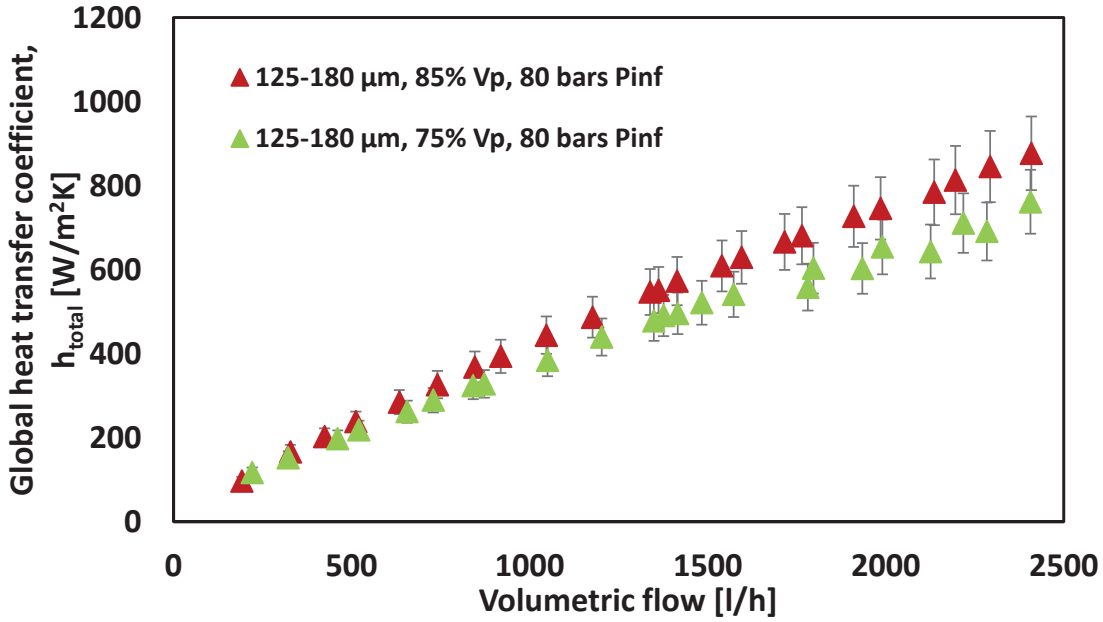

Figure 4.12: Evolution of the global heat transfer coefficient h_{total} with volumetric flow for 10 mm tall samples of same pore size and infiltrated at the same pressure range but of different porosity. In the present geometry a flow rate of 2500l/h corresponds to roughly 1 m/s average inflow superficial velocity over the heat transfer footprint area, equal in the present experiments to $7.07*10^{-4}$ m².

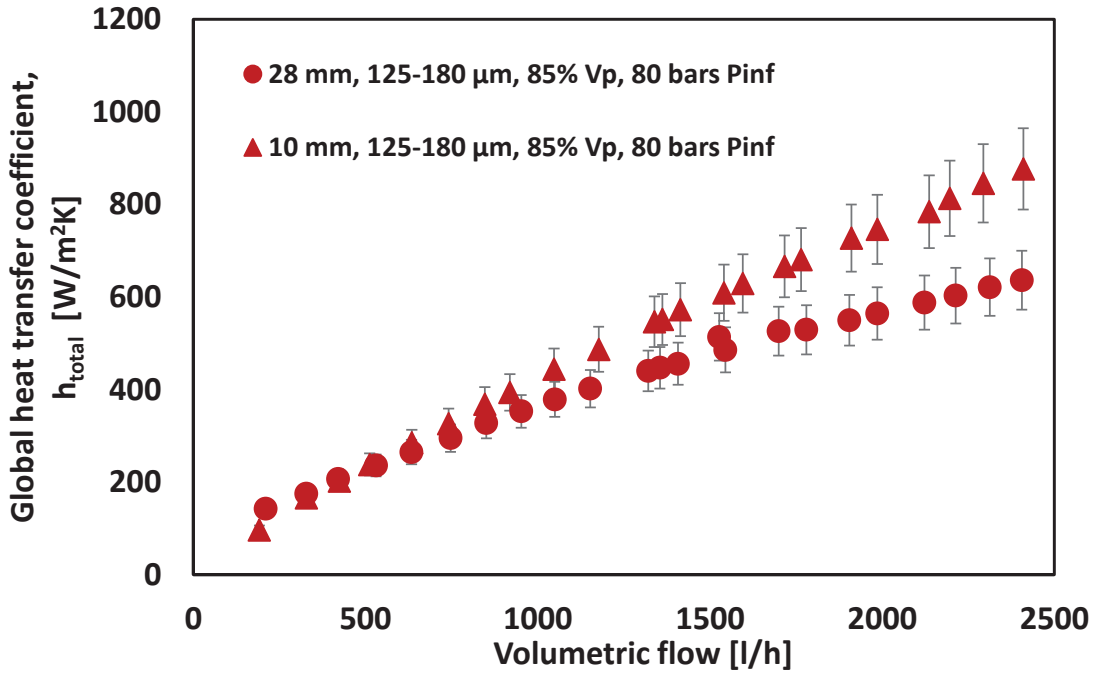

Figure 4.13: Evolution of the global heat transfer coefficient h_{total} with volumetric flow for samples of same pore size, porosity and infiltrated at the same pressure range but of different height. In the present geometry a flow rate of 2500l/h corresponds to roughly 1 m/s average inflow superficial velocity over the heat transfer footprint area, equal in the present experiments to $7.07*10^{-4}$ m².

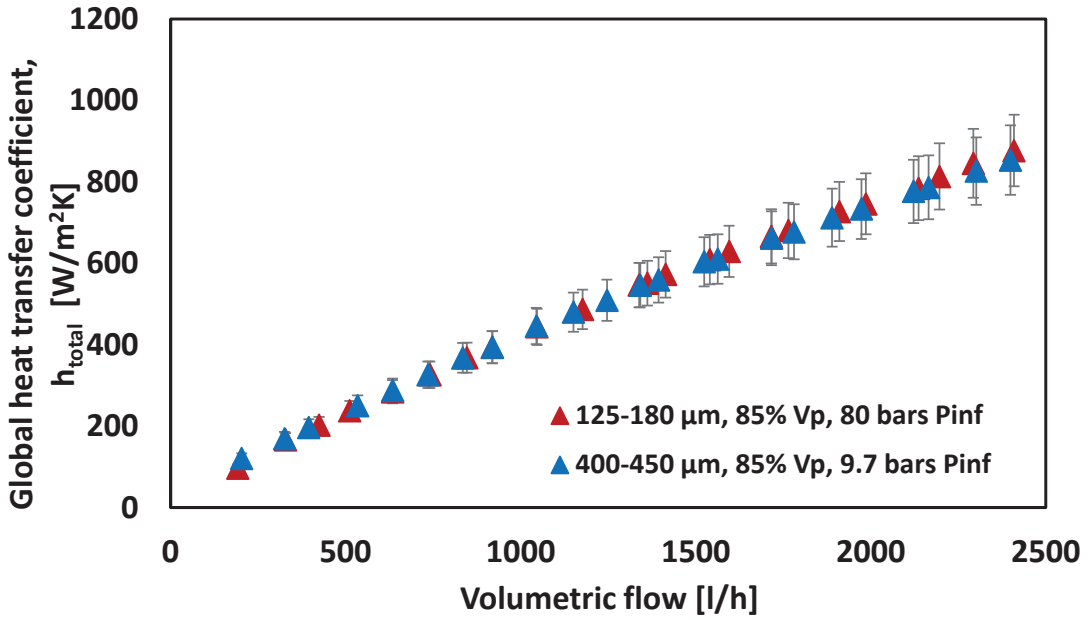

Figure 4.14: Evolution of the global heat transfer coefficient h_{total} with volumetric flow for 10 mm tall samples of same porosity but of different pore size. In the present geometry a flow rate of 2500l/h corresponds to roughly 1 m/s average inflow superficial velocity over the heat transfer footprint area, equal in the present experiments to $7.07*10^{-4}$ m².

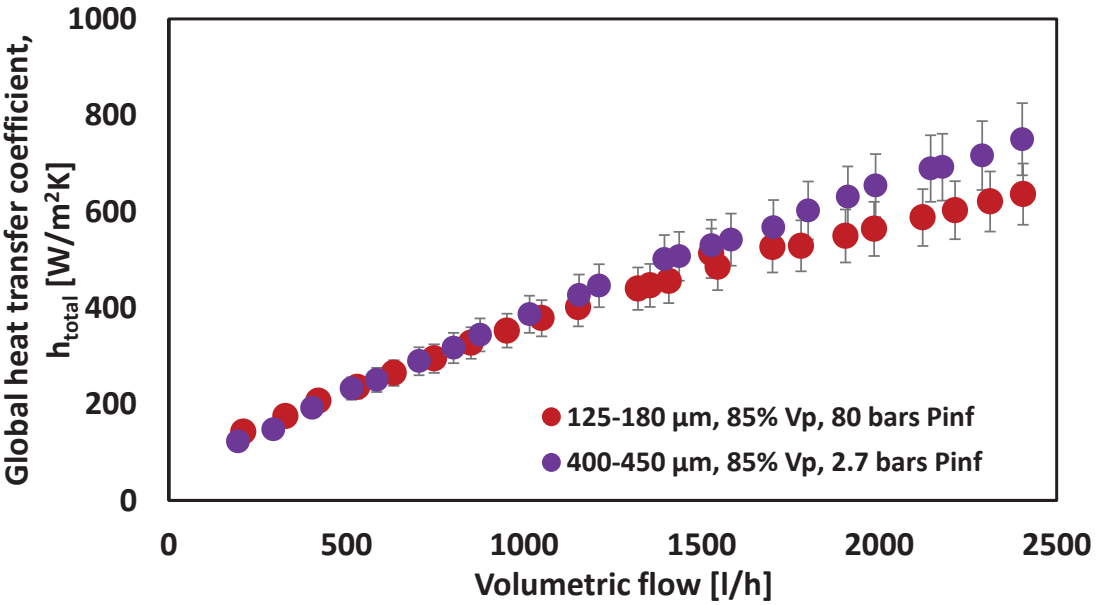

Figure 4.15: Evolution of the global heat transfer coefficient h_{total} with volumetric flow for 28 mm tall samples of same porosity but of different pore size. In the present geometry a flow rate of 2500l/h corresponds to roughly 1 m/s average inflow superficial velocity over the heat transfer footprint area, equal in the present experiments to $7.07*10^{-4}$ m².

4.2.1.3. Foams with pore size of 900-1300 µm

Figure 4.16 depicts the evolution of the global heat transfer coefficient with the volumetric flow rate for two different heights; as was observed with samples of other pore sizes, the smaller samples yet again dissipate noticeably more heat at given global volumetric flow rate.

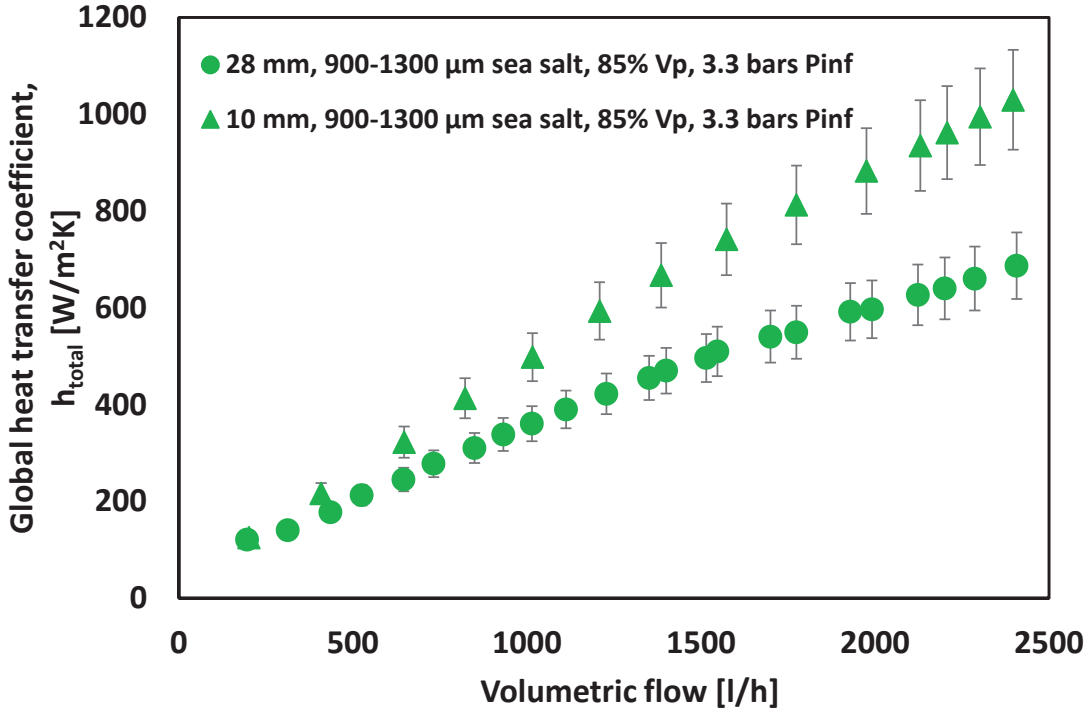

Figure 4.16: Evolution of the global heat transfer coefficient h_{total} with volumetric flow for samples of same pore size, porosity and infiltrated at the same pressure range but of different heights. In the present geometry a flow rate of 2500l/h corresponds to roughly 1 m/s average inflow superficial velocity over the heat transfer footprint area, equal in the present experiments to $7.07*10^{-4}$ m².

Figure 4.17 compares samples of the same height and porosity, infiltrated at nearly the same pressure but with different pore sizes. Foams with the ≈ 1 mm pores give, at equal global flow rate, a higher global heat transfer coefficient than do foams with smaller pores.

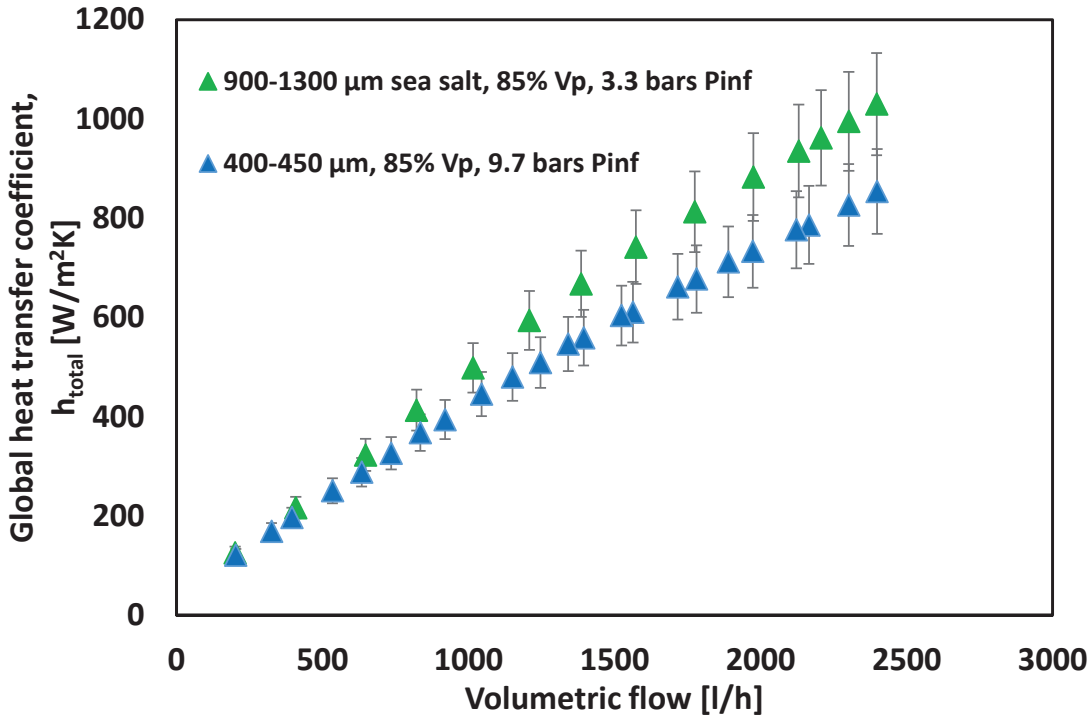

Figure 4.17: Evolution of the global heat transfer coefficient h_{total} with volumetric flow for 10 mm tall samples of same porosity but of different pore size. In the present geometry a flow rate of 2500l/h corresponds to roughly 1 m/s average inflow superficial velocity over the heat transfer footprint area, equal in the present experiments to $7.07*10^{-4}$ m².

Finally, a comparison of the global heat transfer coefficient of two different samples (those with the higher values for each pore size) with the impingement jet on i) a flat surface and ii) on pin fins, is illustrated in *Fig.4.18*. Both foams dissipate more heat than the impingement jet on a flat surface; likewise, foams with higher pore sizes noticeably outerperform pin fins in terms of heat dissipation under the impingement jet configuration.

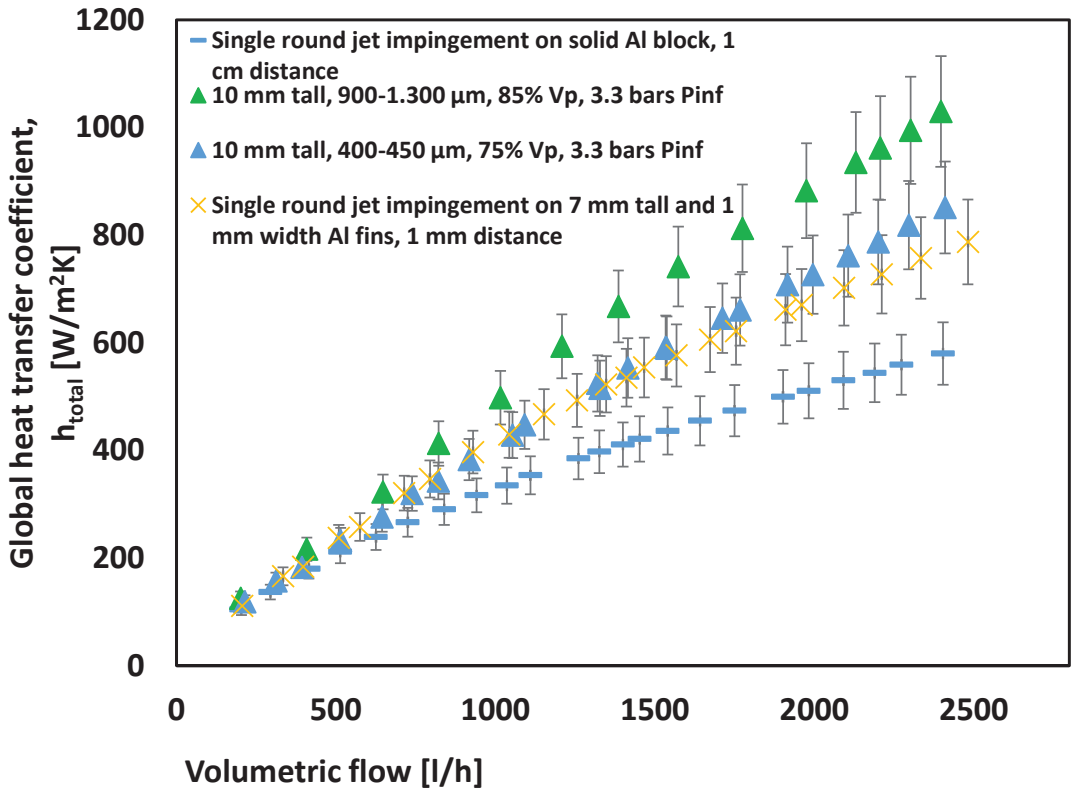

Figure 4.18: Evolution of the global heat transfer coefficient h_{total} with volumetric flow for different samples. In the present geometry a flow rate of 2500l/h corresponds to roughly 1 m/s average inflow superficial velocity over the heat transfer footprint area, equal in the present experiments to $7.07*10^{-4}$ m^2.

4.2.2 Global heat transfer evolution with the ideal pumping power

4.2.2.1 Foams with pore size of 400-450 µm

Figure 4.19 shows the evolution of the global heat transfer coefficient with the specific pumping power for two different samples of the same height and pore size (2.8 cm and 400-450 µm respectively) and infiltrated at the same pressure. The pumping power that is reported in all graphs is the ideal pumping power, calculated without inclusion of the power required to compress the air. As already observed, foams with higher porosities dissipate a little (≈ 10%) more heat for the same pumping power. The evolution of the global heat transfer coefficient with the specific pumping power for two samples infiltrated at different pressures is illustrated in *Fig. 4.20*. Lower infiltration pressure appears to be beneficial in terms of heat dissipation at given pumping power, the difference nearing 50% at high pumping power.

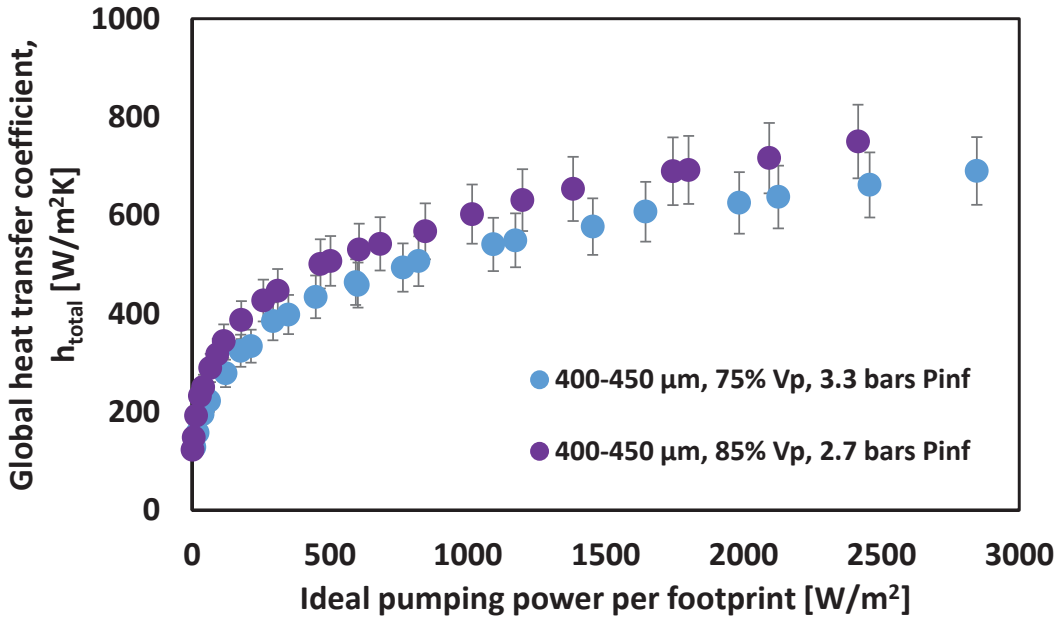

Figure 4.19: Evolution of the global heat transfer coefficient h_{total} with ideal pumping power per footprint for 28 mm tall samples of same pore size and infiltrated at the same pressure range but of different porosity.

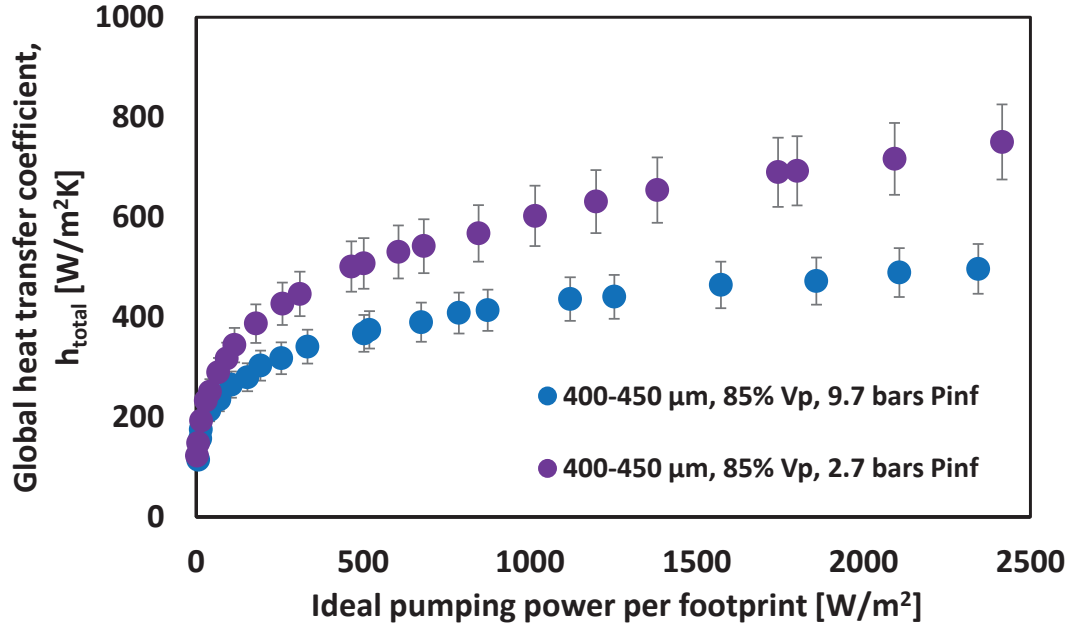

Figure 4.20: Evolution of the global heat transfer coefficient h_{total} with ideal pumping power per footprint for 28 mm tall samples of same pore size and porosity but infiltrated at different pressures.

Figures 4.21 and 4.22 show the effect of porosity and infiltration pressure for foams of the same pore size but of smaller height (10 mm). As with taller equivalent samples, high porosities and low infiltration pressures influence positively the heat dissipation for the same pumping power. The infiltration pressure has less influence this time than does the relative density.

Figure 4.23 depicts the effect of height in the heat dissipation for the same foam versus pumping power: now the shorter sample appears less performant, since at given pumping power it evacuates less heat.

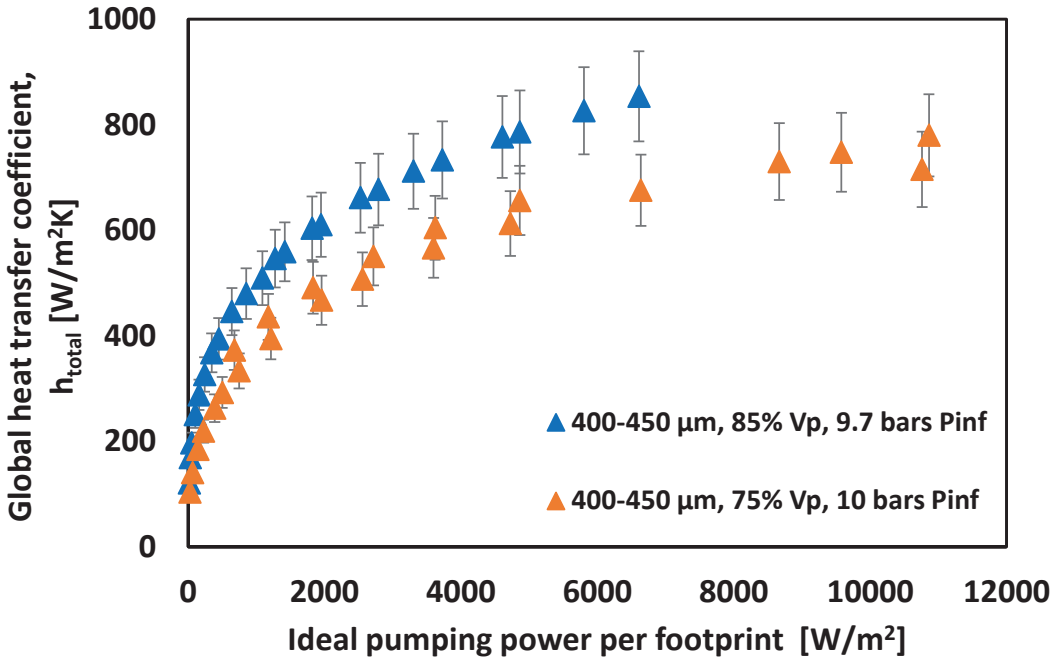

Figure 4.21: Evolution of the global heat transfer coefficient h_{total} with ideal pumping power per footprint for 10 mm tall samples of same pore size and infiltrated at similar pressures but of different porosities.

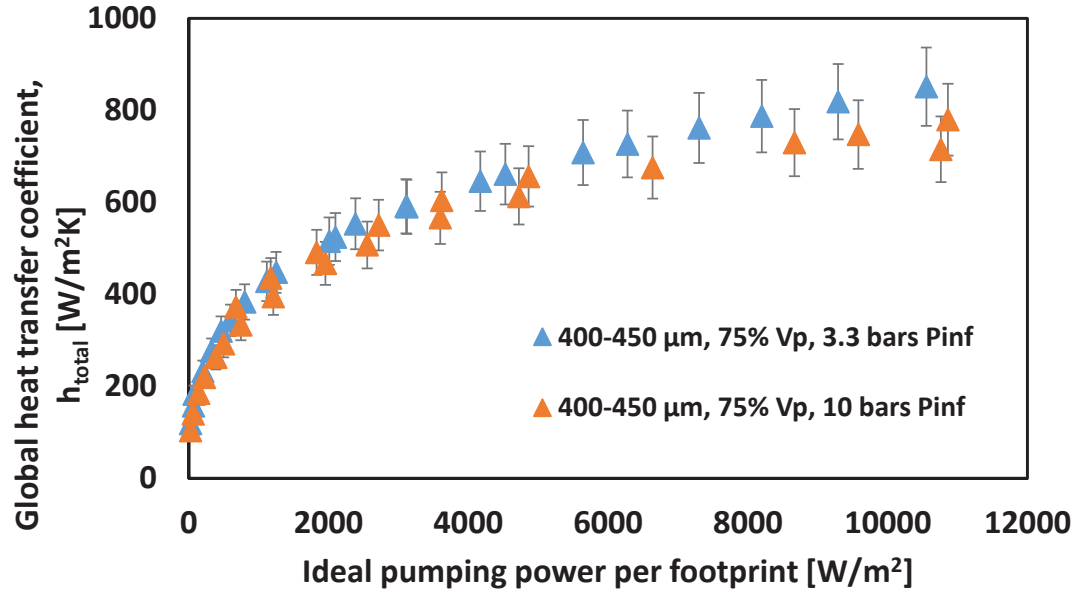

Figure 4.22: Evolution of the global heat transfer coefficient h_{total} with ideal pumping power per footprint for 10 mm tall samples of same pore size and porosity but infiltrated at different pressures.

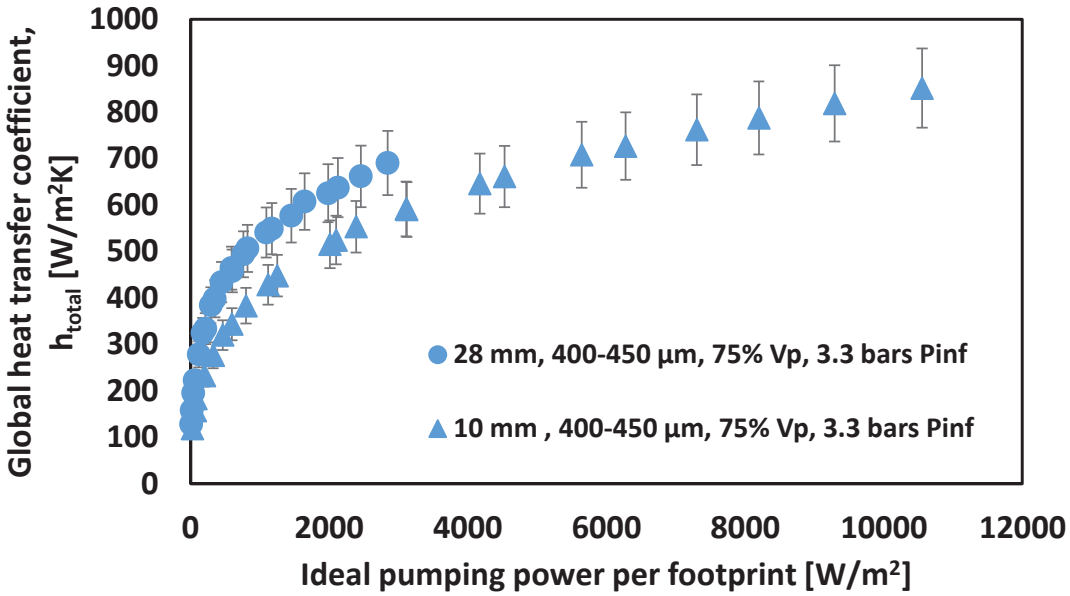

Figure 4.23: Evolution of global heat transfer coefficient h_{total} with ideal pumping power per footprint for samples of same pore size, porosity and infiltrated at the same pressures but of different height.

4.2.2.2 Foams with pore size of 125-180 µm

Figure 4.24 plots the heat transfer coefficient of samples having the same height, pore size and infiltrated at the same pressure, but having a different porosity. As seen, the higher the porosity, the higher the heat transfer rate for the same specific pumping power. Samples of smaller height are this time more performant, *Fig. 4.25*, contrarily to what was found with samples of pore size 400-450 µm (*Fig. 4.23*).

Finally, in *Figure 4.26*, a comparison between samples of the same height and porosity, but with different pore size (400-450 µm and 125-180 µm) is depicted: samples with 400-450 µm pore size can dissipate as much heat as samples with 125-180 µm but with much smaller pumping power cost.

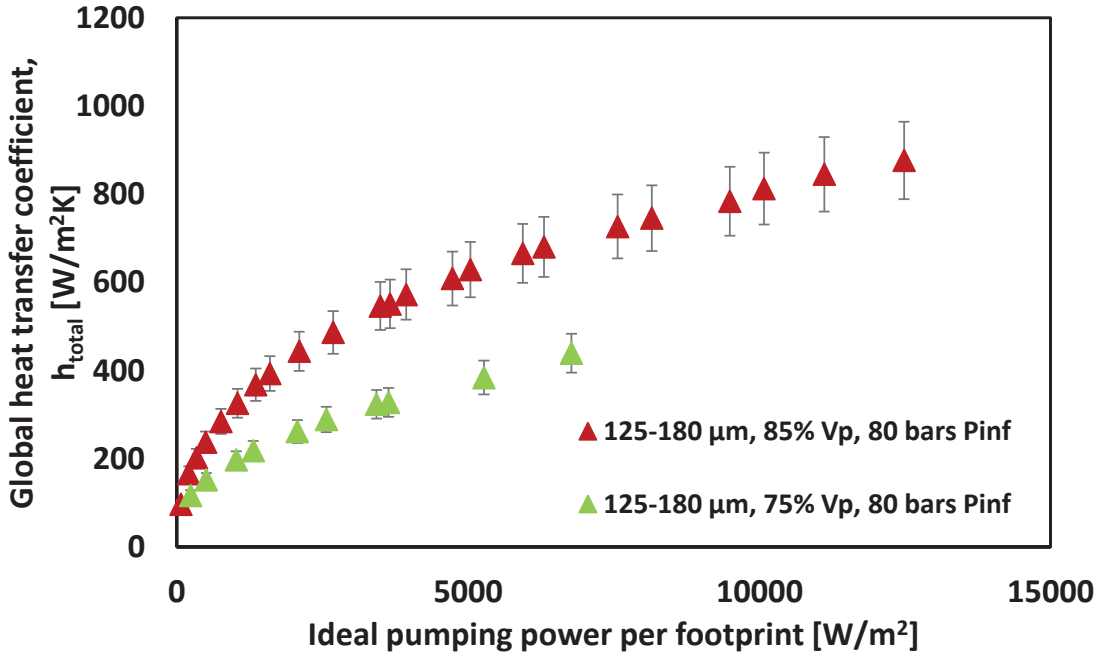

Figure 4.24: Evolution of the global heat transfer coefficient h_{total} with ideal pumping power per footprint for 10 mm tall samples of same pore size and infiltrated at the same pressures but of different porosities.

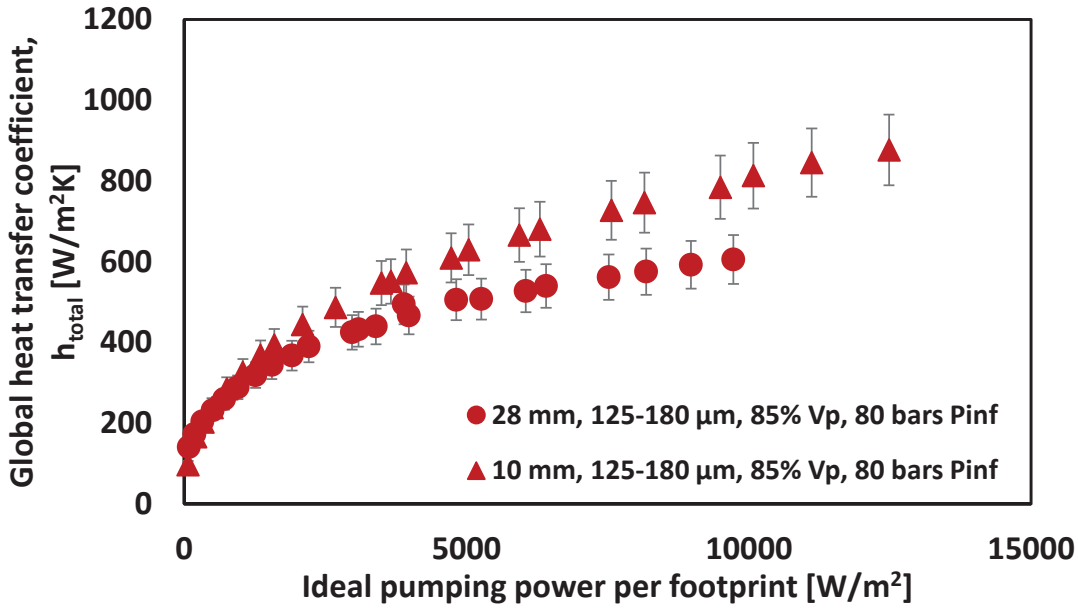

i

4.2.2.3 Foams with pore size of 900-1300 µm

Figure 4.27 gives data for samples of 85% porosity V_p, with pores 900-1300 µm in size, infiltrated at the same pressure and of different height. As seen with 400-450 µm pore size foams (but not the finer, 125-180 µm pore size foam), smaller heights dissipate more heat at fixed specific pumping power.

Figure 4.28 compares samples of the same height and porosity, but with different pore size (400-450 µm and 900-1300 µm): samples with larger pores dissipate more heat, no matter the porosity or the infiltration pressure, at given pumping power cost. Note also that the value h = 1000 W/(m²K) was reached at the highest pumping power with the of 900-1300 µm pore size foam.

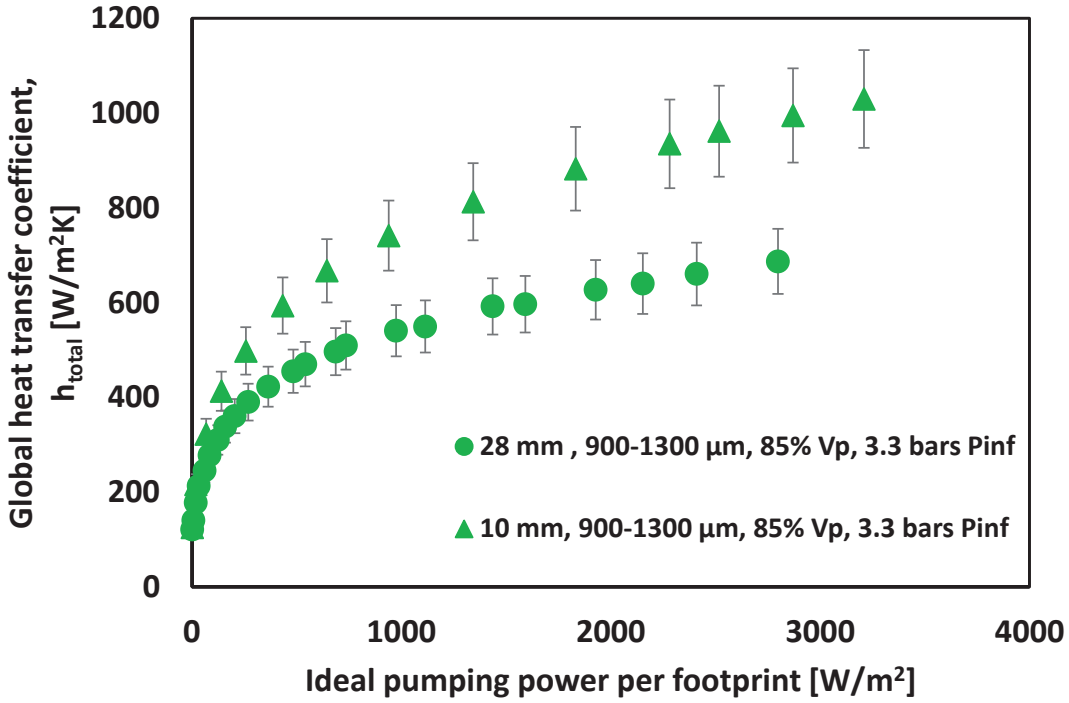

Figure 4.25: Evolution of the global heat transfer coefficient h_{total} with ideal pumping power per footprint for samples of the same pore size, porosity and infiltrated at the same pressures but of different heights.

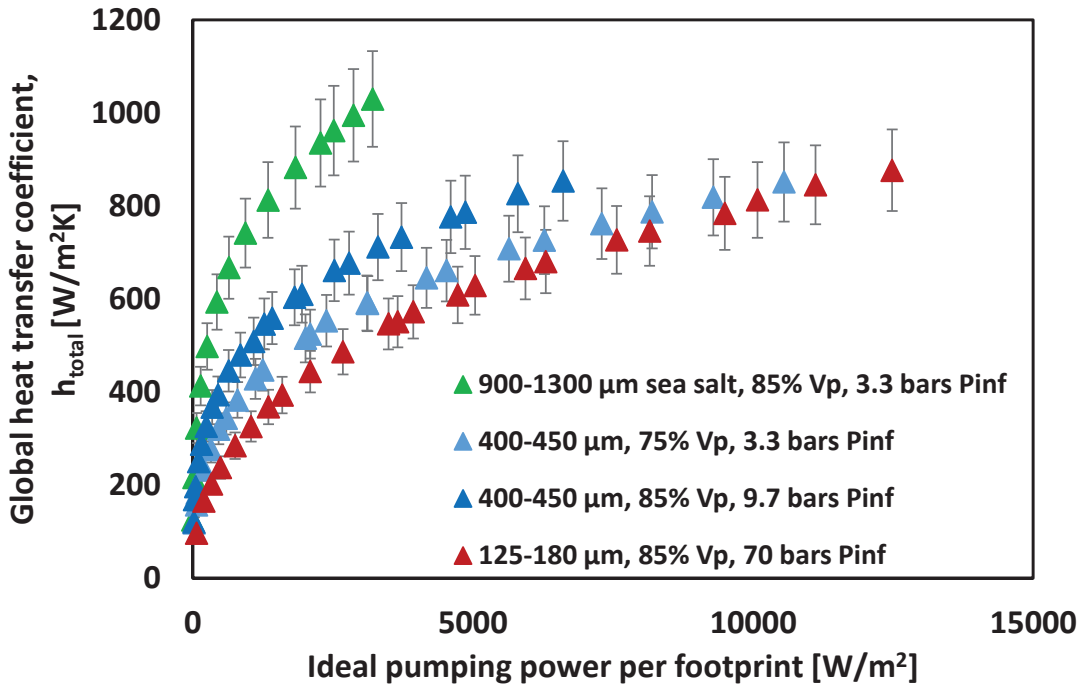

Figure 4.26: Evolution of the global heat transfer coefficient h_{total} with ideal pumping power per footprint for samples of the same height (10 mm) but with different pore size, porosity and infiltrated at different pressures.

A comparison of the global heat transfer coefficient of two different samples (the ones with the highest values for each pore size) with the impingement jet on i) a flat surface and ii) on pin fins, is illustrated in *Fig.4.29*. Foams of 400-450 µm pore size dissipate more heat than a conventional fin structures, but at the cost of a much higher pumping power, while foams with of 900-1300 µm pore size strongly outperform conventional fins.

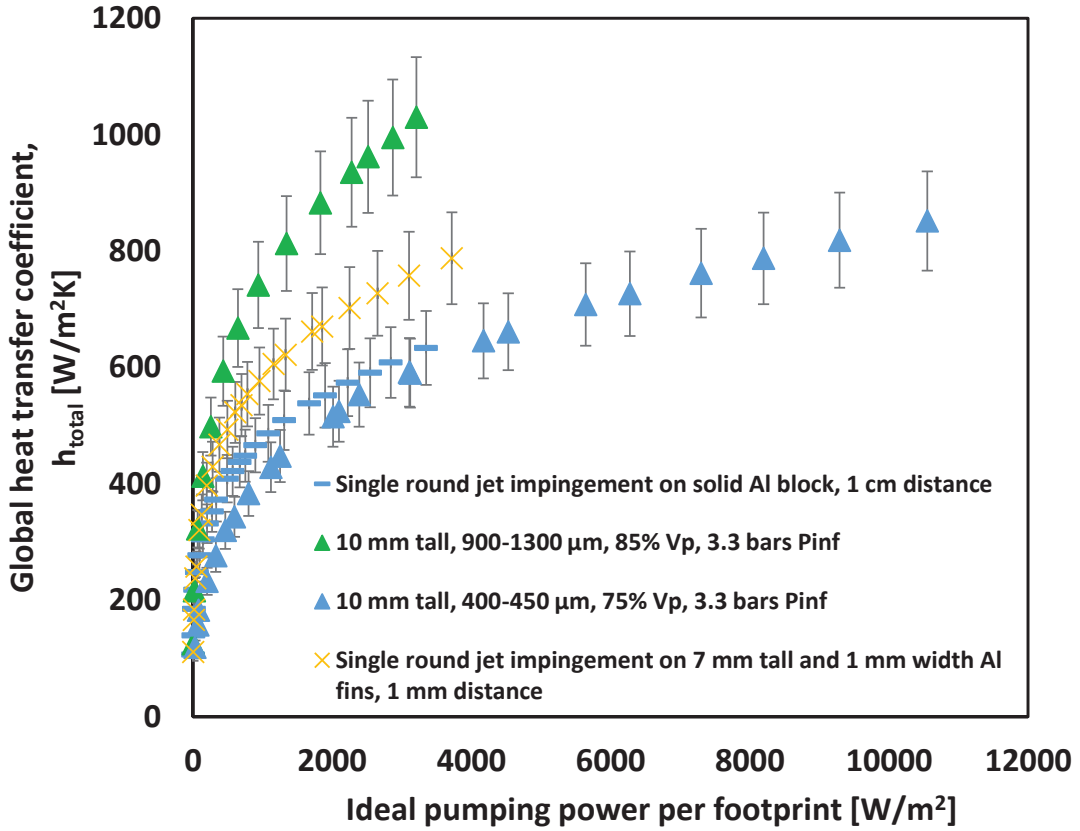

Figure 4.27: Evolution of the global heat transfer coefficient h_{total} with ideal specific pumping power for different samples.

Finally we show the reproducibility of the forced convection experiments is good; as illustrated in *Figs.4.30 and Fig.4.31* the discrepancy between two different series of measurements for the same sample on two different days, is smaller than 10% for both the measurements of the total pressure P_t and the global heat transfer coefficient h.

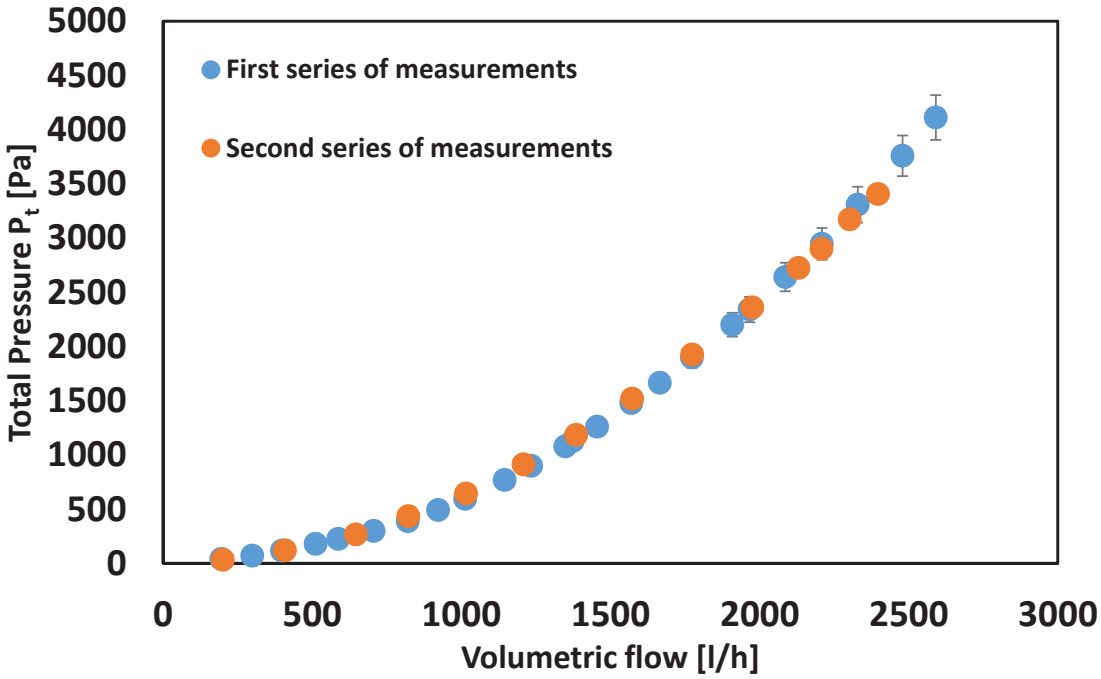

Figure 4.28 : Total pressure for one of our samples, tested twice in two different days. The discrepancy is around 9%. In the present geometry a flow rate of 2500l/h corresponds to roughly 1 m/s average inflow superficial velocity over the heat transfer footprint area, equal in the present experiments to $7.07*10^{-4}$ m².

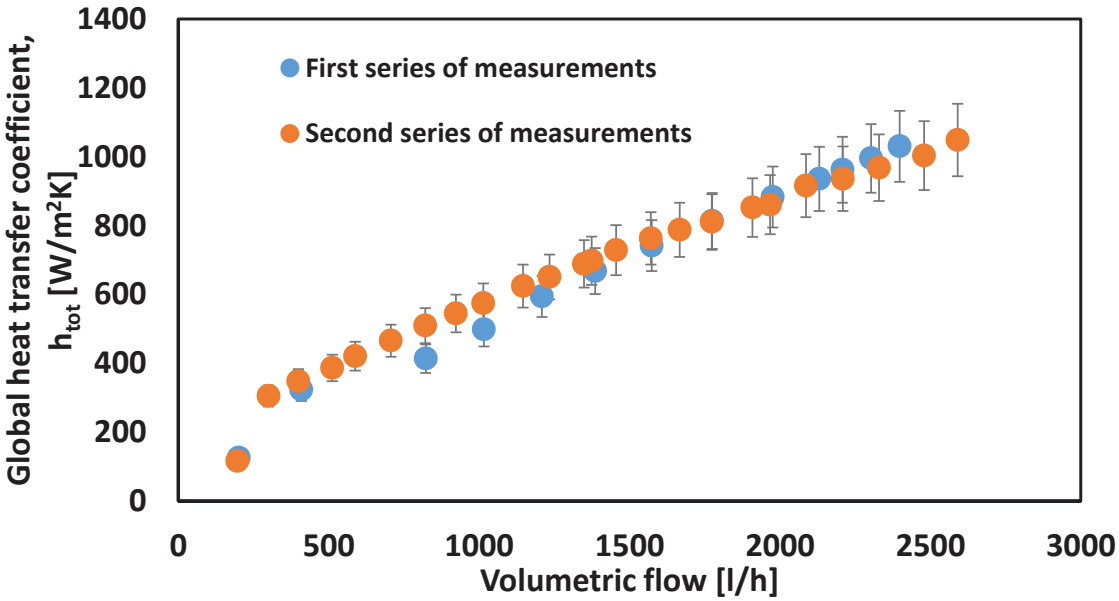

Figure 4.29: Global heat transfer coefficient of one of our samples, tested twice in two different days. The discrepancy is less than the maximum estimated experimental error (10%). In the present geometry a flow rate of 2500l/h corresponds to roughly 1 m/s average inflow superficial velocity over the heat transfer footprint area, equal in the present experiments to $7.07*10^{-4}$ m².

4.3 Fluid flow through the foam

Figures 4.32 to 4.35, depict the measured gradient in static pressure along the height of the central channel in the foamed samples, under various volumetric air flow rates for a foam of 400-450 µm pore size, 85% V_p and infiltrated at 4.4 bar. *Figure 4.36* depicts the same gradient for a sample of 900-1300 µm pore size, 28 mm tall and infiltrated at 4 bars. As seen, independently of the volumetric flow, the static pressure follows a quasi-linear profile, reaching its maximum at the bottom of the channel and its minimum at the top of the sample. There is a negative static pressure at the top of the tallest samples; the effect becomes stronger as the air volumetric flow increases while the height at which negative static pressures appear (where relevant) seems not to be much influenced by the overall sample height.

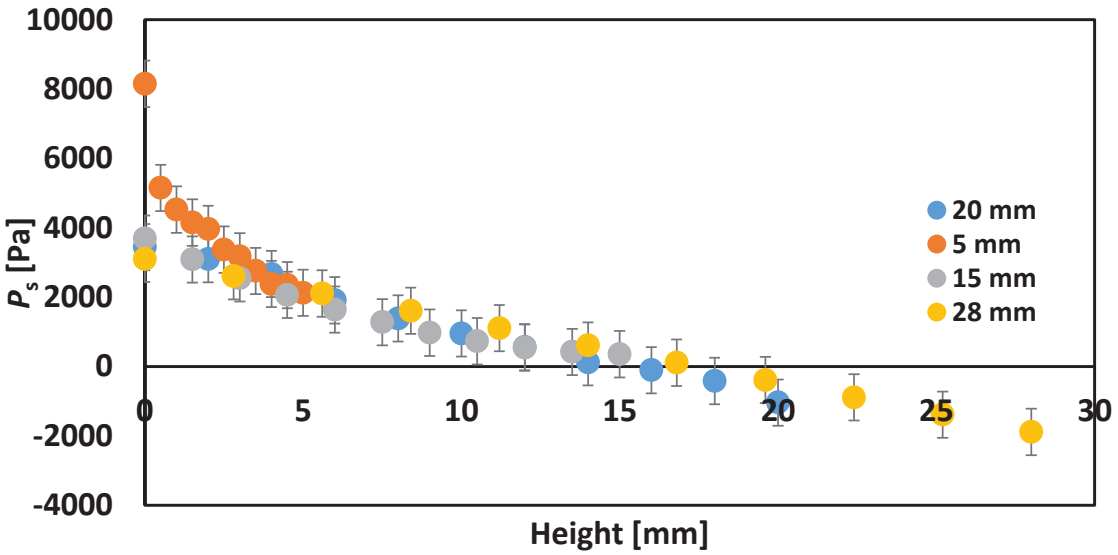

Figure 4.30: Distribution of the static Pressure P_s for samples of 400-450 µm pore size, 85% V_p, infiltrated at 4.4 bar and of different heights, under a volumetric flow of 2520 l/h.

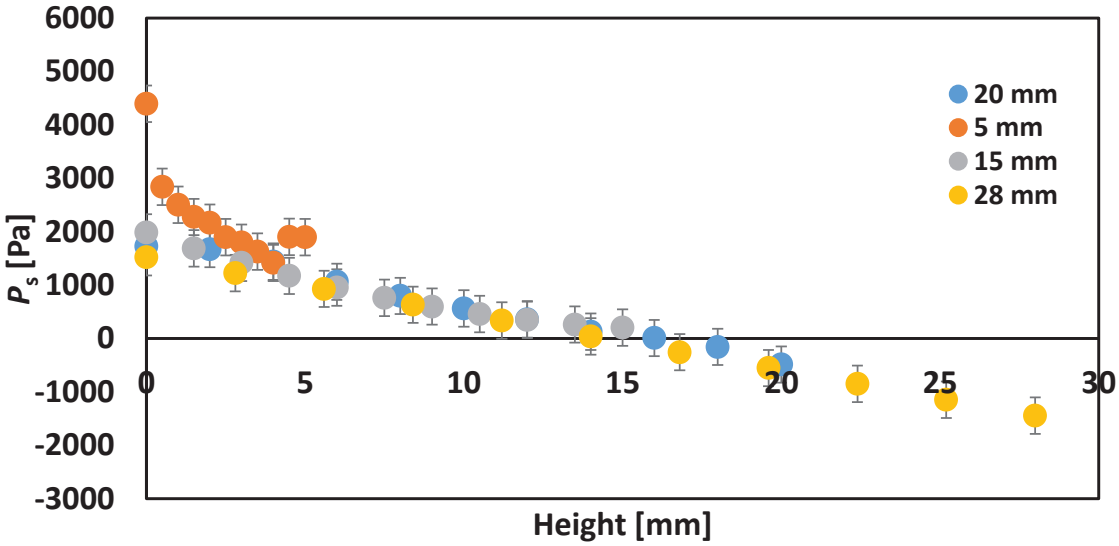

Figure 4.31: Distribution of the static Pressure P_s for samples of 400-450 µm pore size, 85% V_p, infiltrated at 4.4 bar and of different heights, under a volumetric flow of 1800 l/h.

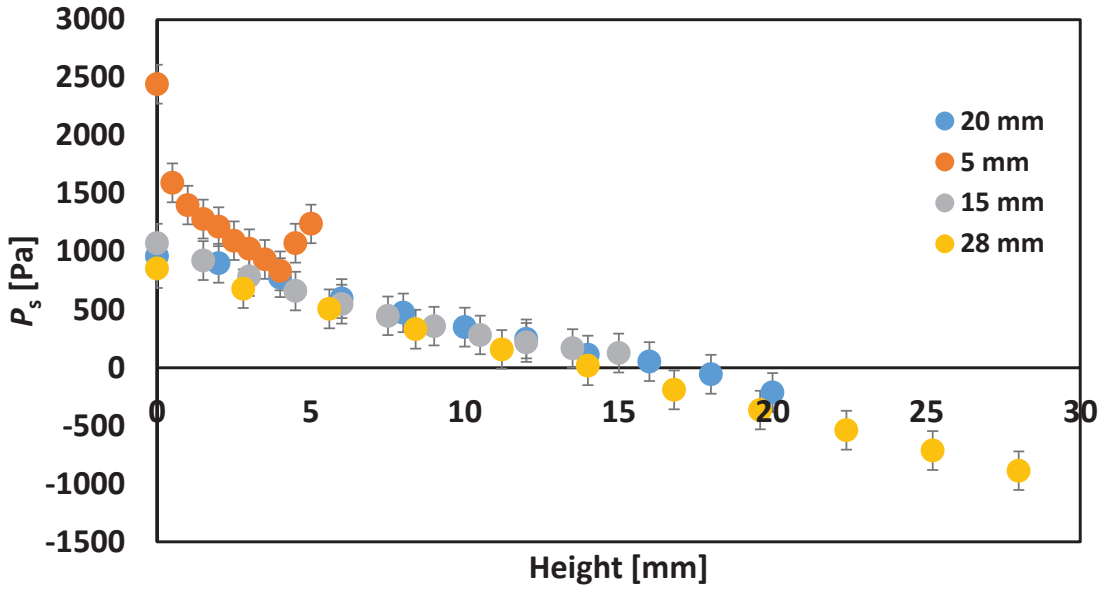

Figure 4.32: Distribution of the static Pressure P_s for samples of 400-450 µm pore size, 85% V_p, infiltrated at 4.4 bar and of different heights, under a volumetric flow of 1260 l/h.

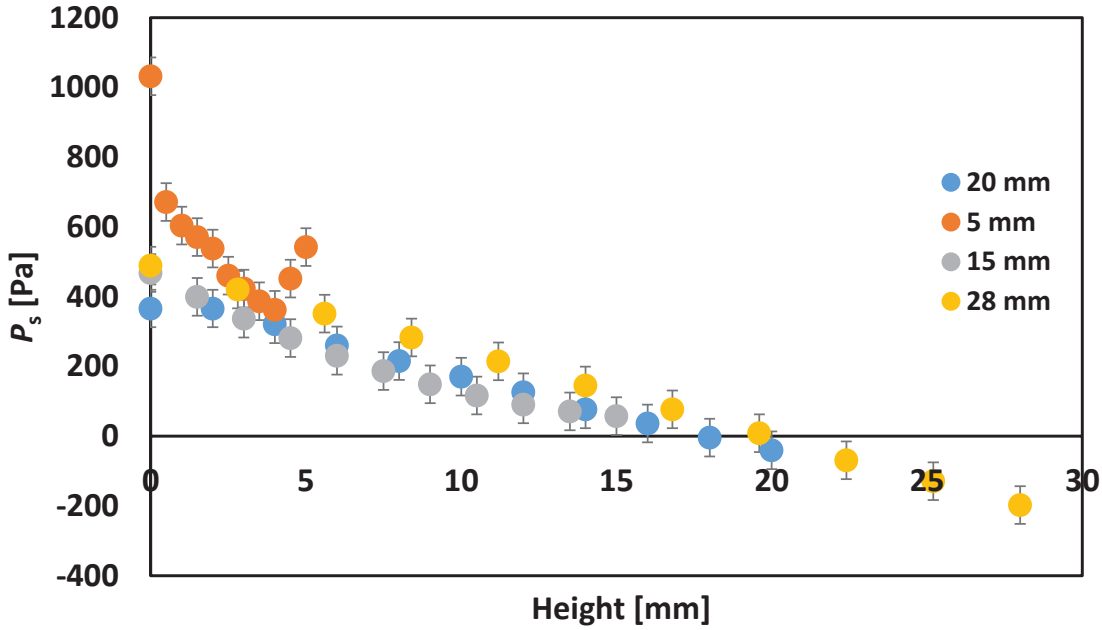

Figure 4.33: Distribution of the static Pressure P_s for samples of 400-450 µm pore size, 85% V_p, infiltrated at 4.4 bar and of different heights, under a volumetric flow of 720 l/h.

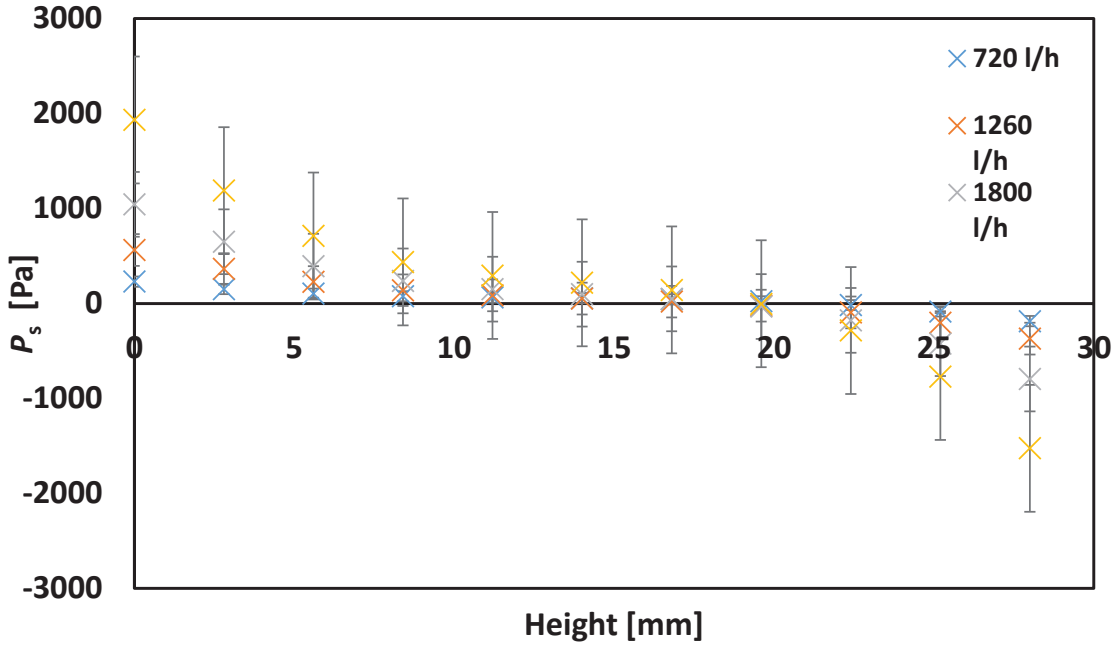

Figure 4.34: Distribution of the static pressure P_s for a sample of 900-1300 µm pore size, 85% V_p, infiltrated under 4 bars and of 28 mm height, under different volumetric flows.

4.4 Temperature profiles

Measurements of temperature profiles along the foam sample outer surface (as elaborated in *Section 3.3.7*), which were conducted at four flow rates for two 28 mm high 85% porous samples (of pore size 400-450 µm and 900-1300 µm) are depicted in *Figs. 4.37 and 4.38,* respectively. It is found that:

(i) There is a noticeable temperature gradient in the solid aluminium, on the order of 10 to 20 °C/cm, corresponding to a total bottom to top temperature decrease between 25 and 35 °C;

(ii) Near the bottom of the structures, the exiting gas temperature is lower than that of the metal by only 5°C or less;

(iii) Near the top of the structures, the gas is significantly colder than the metal, the difference reaching even up to 20°C .

In other words, the porous metal heats significantly the through-flowing air, and transfers more heat to air flowing near the hot metal surface than it does to air flowing through the top portion of the microcellular metal heat exchanger.

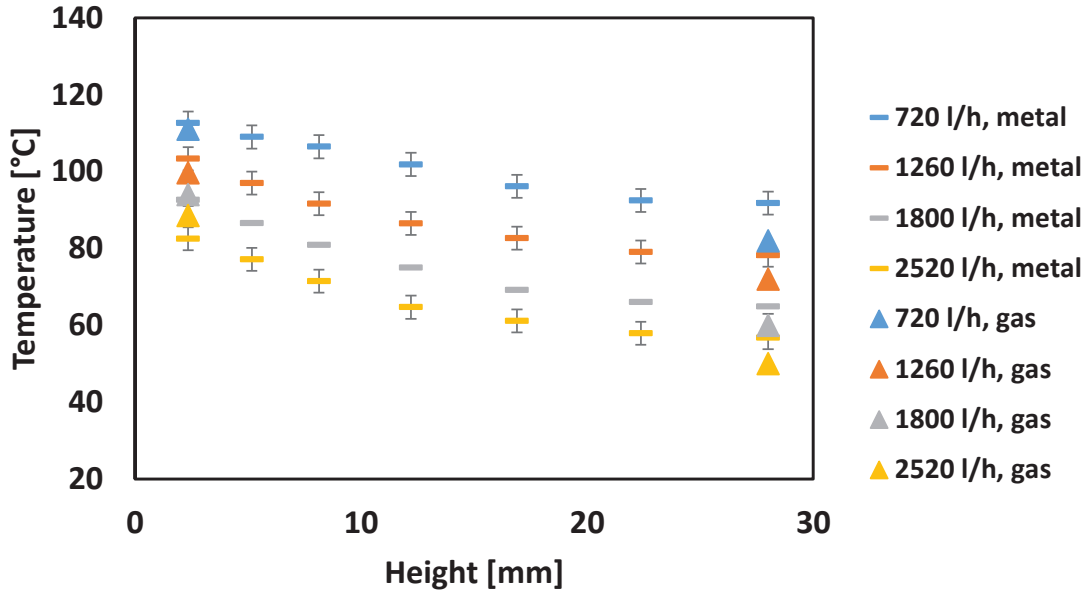

Figure 4.35: Evolution of the temperature of outflowing air and metal surface as a function of distance from the heated surface under different volumetric air flows. The sample has 400-450 µm pore size, 85% V_p and was infiltrated at 9.7 bars.

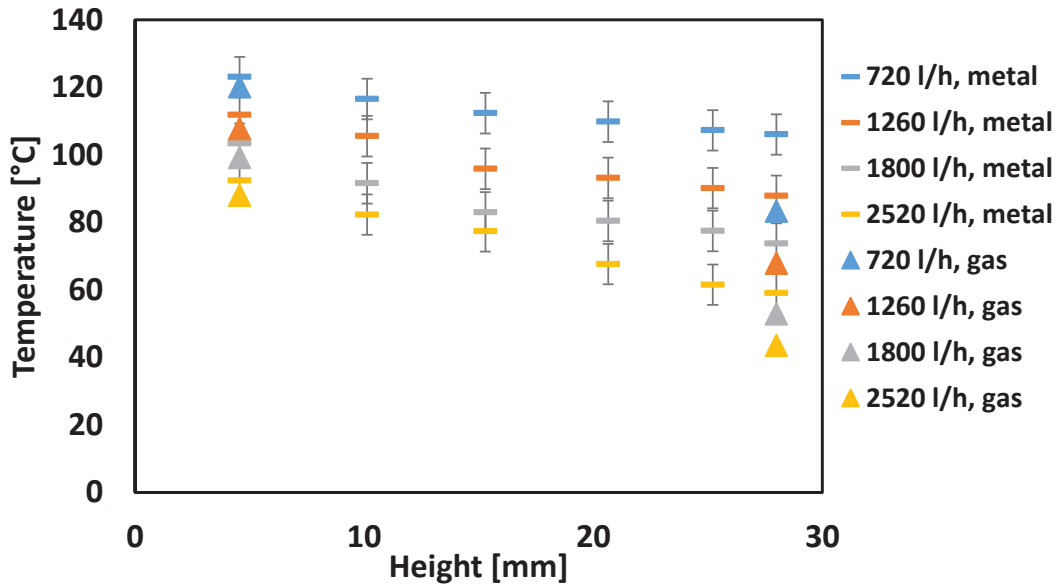

Figure 4.36: Evolution of the surface temperature of the microcellular aluminium as a function of distance from the heated surface for different volumetric air flows. The sample has 900-1300 µm pore size, 85% V_p and was infiltrated at 3.4 bars.

4.5 Integrated Structure

The global heat transfer coefficient of the Integrated Structure (IS), both with regard to the volumetric air flow and the specific pumping power, is plotted in *Figs. 4.39 and 4.40*. When results are compared with the thermal efficiency of a foamed sample of similar microstructure (Sample 12 of *Table 3*), it appears that the integrated structure has a somewhat lower thermal efficiency, reaching a peak

value h = 600 W/(m²K), versus h = 1000 W/(m²K) for the ≈ 1 mm pore size foam. Note, however, that the integrated structure has a slightly different height and porosity than the foam and was infiltrated at much higher infiltration pressures (*Sections 3.4.1 and 3.4.2*).

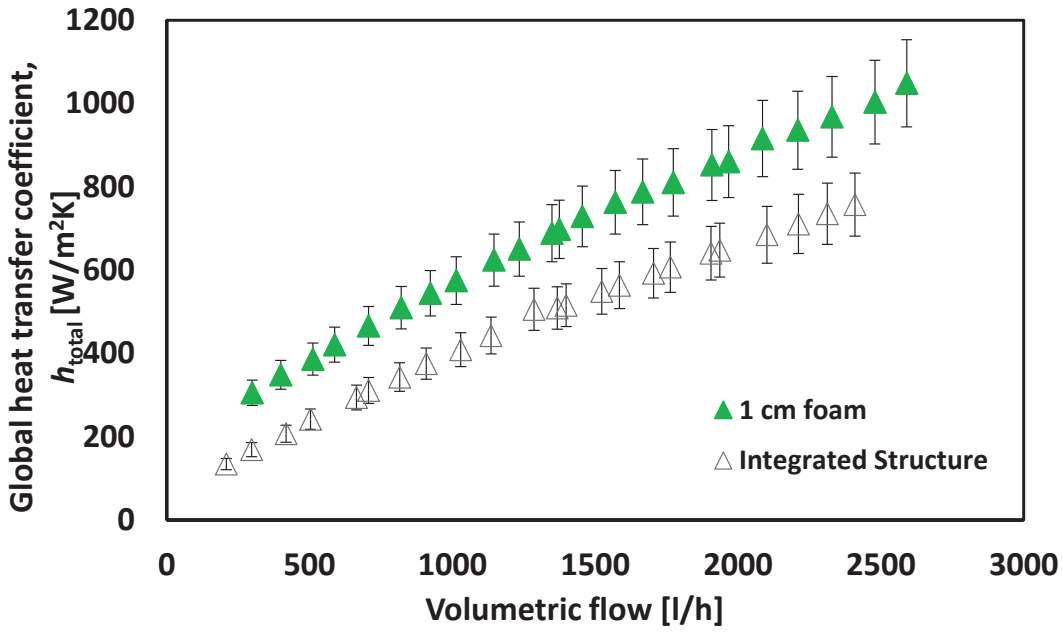

Figure 4.37: Evolution of the global heat transfer coefficient h_{total} with volumetric flow for the integrated structure. In the present geometry a flow rate of 2500l/h corresponds to roughly 1 m/s average inflow superficial velocity over the heat transfer footprint area, equal in the present experiments to 7.07*10^{-4} m².

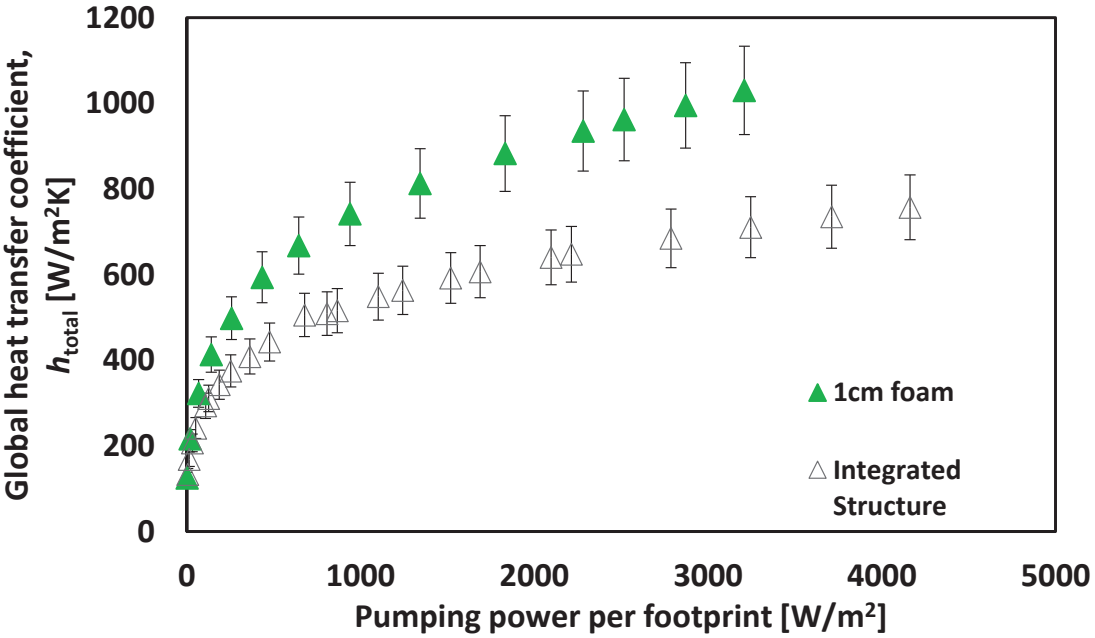

Figure 4.38: Evolution of the global heat transfer coefficient h_{total} with ideal pumping power per footprint for the integrated structure. In the present geometry a flow rate of 2500l/h corresponds to roughly 1 m/s average inflow superficial velocity over the heat transfer footprint area, equal in the present experiments to 7.065*10^{-4} m²

Chapter 5 Theoretical model and Results

In this chapter, a numerical thermal transport code is used to elucidate how the various parameters influence the rate of heat transfer of the present cylindrical foam structures. The code was *developed and written by Dr. David Ingram*, except for the following parameters which were altered: The local Nusselt number, the height of the samples, and consequently, the pressure gradient inside their central channel, the number of nodes, the thermal resistance between the foam and the visual representation of the contour plots. The model is based on the Darcy-Forchheimer formulation of fluid flow in porous media, the results of which are then coupled to a convective/conductive heat transfer model of the same structure. Outputs of the model are the pressure field inside the sample, the velocity fields, and the temperature field inside the sample for both the fluid and solid phases, namely air and aluminium. Parametric studies depicting the effect of height and pore size on the thermal behaviour of replicated foams were performed, using this model.

5.1 Description of the air flow model

Air flow inside the foam is modelled through an axisymmetric finite-volumes scheme with radial and axial coordinates (r,z); the elementary volume elements are regular cylindrical rings of thickness Δr and height Δz. The air is assumed to be incompressible, meaning there is no divergence of the superficial velocity field. The microcellular metal structure is assumed to be isotropic.

Being difficult to predict, the static pressure along the foam's central channel (cf. *Fig. 3.23* and *3.24*), was measured experimentally (cf. *Figs 4.32-4.35*), as discussed in *Section 3.3.8* and was imposed as a boundary condition along the central entrance to the foam sample. For the heights (represented in axial coordinates) where measurements were not taken, a second order extrapolation of static pressures was used. Along the outer sample surface, a pressure of one atmosphere is adopted as the boundary condition. Top and bottom surface are assumed impervious to fluid flow. The air flow model determines the static pressure distribution $P_s(r,z)$ together with the superficial velocity field $\mathbf{v}(v_r(r,z), v_z(r,z))$ everywhere inside the foam.

Air flow inside the sample is modelled using two independent (meaning that the permeability matrix is diagonal) Darcy-Forchheimer equations, one for each direction (radial and axial):

$$\frac{\partial P_s}{\partial r} = -\frac{\mu}{K_p} v_r - \frac{\rho}{K_f} v_r^2 \tag{5.1}$$

$$\frac{\partial P_s}{\partial z} = -\frac{\mu}{K_p} v_z - \frac{\rho}{K_f} v_z^2 \tag{5.2}$$

The above equations are solved iteratively, assuming at each iteration a Darcy-type model, which assimilates inertial pressure losses to a velocity-dependent decrease in the porous medium's apparent permeability, as follows:

$$\frac{\partial P_s}{\partial r} = -\hat{K}_r v_r = -\left(\frac{\mu}{K_p} + \frac{\rho}{K_f}|v_r|\right) v_r \tag{5.3}$$

$$\frac{\partial P_s}{\partial z} = -\hat{K}_z v_z = -\left(\frac{\mu}{K_p} + \frac{\rho}{K_f}|v_z|\right) v_z \tag{5.4}$$

During each iterative step, the Darcy model calculates the pressure inside the foam, using the velocity field obtained from the previous iteration in order to calculate the generalized permeability matrix $\boldsymbol{K_p}$. The permeability and the Forchheimer coefficient are estimated according to a model that was constructed while developing this algorithm (described in Appendix A). The numerical model then yields the static pressure distribution which is then used to obtain the superficial velocity field according to the Darcy-Forchheimer equation written for both velocity components:

$$V_z = \frac{-\mu/K_p \pm \sqrt{(\mu/K_p)^2 - (4\rho/K_f)\dfrac{\partial P_s}{\partial z}}}{2\rho/K_f} \tag{5.5}$$

$$V_r = \frac{-\mu/K_p \pm \sqrt{(\mu/K_p)^2 - (4\rho/K_f)\dfrac{\partial P_s}{\partial r}}}{2\rho/K_f} \tag{5.6}$$

with the sign in front of the square root depending on the local sign of velocity; positive radial velocities are chosen to mean that the air flows outwards and positive vertical velocities are upwards. These correspond to the globally expected flow fields (since flow is globally outwards and since the static pressure at the bottom is higher than the static pressure at the top along the central channel.

The full set of boundary conditions, depicted in *Fig.5.1* reads:

$$\frac{\partial P_s}{\partial z} = 0, r_i < r < r_o, z = 0 \quad (5.7)$$

$$\frac{\partial P_s}{\partial z} = 0, r_i < r < r_o, z = Z_{top} \quad (5.8)$$

$$P_s = P_{s,measured}, r = r_i, 0 < z < Z_{top} \quad (5.9)$$

$$P_s = P_{ambient}, r = r_o, 0 < z < Z_{top} \quad (5.10)$$

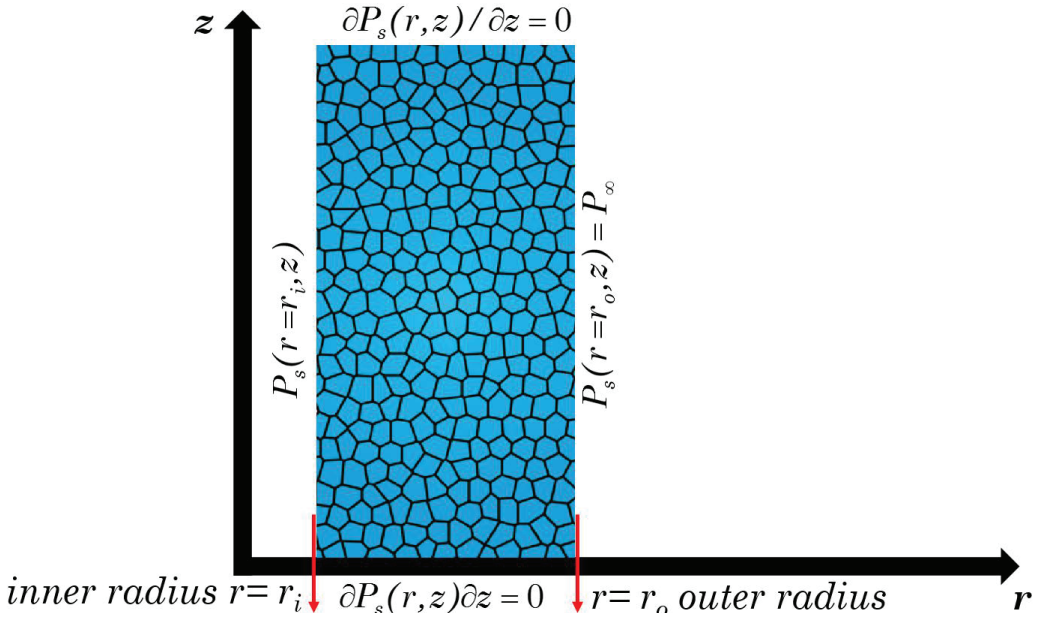

Figure 5.1: Schematic representation of the fluid flow boundary conditions.

The implementation of the numerical method is as follows: the Gauss theorem is applied over an elementary volume element Ω_e, according to *Eq.5.11:*

$$\int_{\Omega_e} \nabla \bullet \vec{V} d\Omega_e = \int_{\partial\Omega_e} \vec{V} \bullet \vec{n} \partial\Omega_e = 0 \quad (5.11)$$

The integral is calculated over the four surfaces of each element, two in each direction. The pressure gradient is assumed to remain constant over each surface of the volume element, of area *S*:

$$-\frac{1}{K_r}\frac{\partial P_s}{\partial r} S_{j+1,k} - \frac{1}{K_r}\frac{\partial P_s}{\partial r} S_{j-1,k} - \frac{1}{K_z}\frac{\partial P_s}{\partial z} S_{j,k+1} - \frac{1}{K_z}\frac{\partial P_s}{\partial z} S_{j,k-1} \quad (5.12)$$

Therefore, the numerical discretization is now given by the expression (5.13):

$$-\frac{1}{K_r}\frac{P_{s,j+1,k}-P_{s,j,k}}{\Delta r}S_{j+1,k}-\frac{1}{K_r}\frac{P_{s,j-1,k}-P_{s,j,k}}{\Delta r}S_{j-1,k}\cdots$$
$$-\frac{1}{K_z}\frac{P_{s,j,k+1}-P_{s,j,k}}{\Delta z}S_{j,k+1}-\frac{1}{K_z}\frac{P_{s,j,k-1}-P_{s,j,k}}{\Delta z}S_{j,k-1} \quad (5.13)$$

The surfaces of an elementary volume are :

$$S_{j+1,k}=2\pi(r_{j,k}+\frac{\Delta r}{2})\Delta z \quad (5.14)$$

$$S_{j-1,k}=2\pi(r_{j,k}-\frac{\Delta r}{2})\Delta z \quad (5.15)$$

$$S_{j,k+1}=\pi(r_{j,k}+\frac{\Delta r}{2})^2-\pi(r_{j,k}-\frac{\Delta r}{2})^2 \quad (5.16)$$

$$S_{j,k-1}=S_{j,k+1} \quad (5.17)$$

The system's discretization is performed by defining N_r and N_z elements along the radial and vertical direction, respectively. The number of spatial elements is an adjustable parameter, which produces more or less refined meshes. For all present calculations, the grid was chosen to have 60 nodes in each direction ($N_r = N_z = 60$).

The general discretization of the mesh is expressed as a set of linear equations:

$$(\frac{S_{j+1,k}}{K_r\Delta r}+\frac{S_{j-1,k}}{K_r\Delta r}+\frac{S_{j,k+1}}{K_z\Delta z}+\frac{S_{j,k-1}}{K_z\Delta z})P_{s,j,k}\cdots$$
$$-\frac{S_{j+1,k}}{K_r\Delta r}P_{s,j+1,k}-\frac{S_{j-1,k}}{K_r\Delta r}P_{s,j-1,k}-\frac{S_{j,k+1}}{K_z\Delta z}P_{s,j,k+1}-\frac{S_{j,k-1}}{K_z\Delta z}P_{s,j,k-1}=0 \quad (5.18)$$

The above equation describes the grid elements in the middle of the mesh; boundary elements are written according to boundary conditions above. After being formalised into a matrix form, the equations are solved using a standard matrix inversion method. The equations are solved for each iterative step, since the coefficients K_r and K_z change after each iteration; the surface elements need to be calculated only once, since the mesh does not change from one iteration to another.

5.2 Description of the heat transfer model

Using the predicted pattern of fluid flow through the foam, a second finite volumes model based on the same mesh as for air flow computes both the pattern and rate of heat transfer including both conductive and convective heat transfer across the aluminium foam flooded by flowing air. Heat transfer in the foam is modelled

under the assumptions of a fully developed flow pattern of the air inside an isotropic foam with separate metal and air temperatures inside each element, using average temperatures within each phase at the microscale and assuming that heat exchange between the solid and the fluid can be described by a single heat transfer coefficient h_{sf}, assumed to be given by the same law across the foam structure. Foam and air are assumed to both be initially at room temperature (T_{amb} = 293 K), the heat conduction through air is assumed negligible, and steady-state conditions are sought iteratively for the given boundary conditions, using the finite volumes scheme.

As with the air flow model, the governing equations were discretized using Gauss's divergence theorem for the integral over an elementary element and solved again using the finite volumes method.

The governing equations are [98] :

$$V_p Cp_f \rho_f \frac{\partial T_f}{\partial t} + \rho_f Cp_f \vec{V} \nabla T_f = h_{sf}(T_s - T_f) \tag{5.19}$$

$$(1 - V_p)\rho_s Cp_s \frac{\partial T_s}{\partial t} = (1 - V_p)^{1.5} k_s \Delta T_s + h_{sf}(T_f - T_s) \tag{5.20}$$

where ρ_f, is the density of the fluid, Cp_f is the thermal capacity in Joules per mass of the fluid, V_p is the volumetric porosity, T_s is the (locally uniform) temperature of the solid, T_f is the average temperature of the fluid, k_s is the bulk thermal conductivity of the solid, 1.5 is the exponent of the DEM model for the thermal conductivity of open-pore microcellular aluminium foam and h_{sf} is the local heat transfer coefficient between the solid and the fluid.

This last parameter is calculated using the following equation [242]:

$$\frac{A_{ss}}{h_{sf}} = \frac{2r_p}{Nu_{sf} k_f} + \frac{2r_p}{10 k_s} \tag{5.21}$$

where r_p is the radius of the pore, and Nu_{sf} is the local Nusselt number, calculated from a correlation of the form of the Wakao and Kaguei predictive scheme for heat transfer through a pack of spherical beads [242]:

$$Nu_{sf} = C + \frac{1.1}{V_p} Pr^a \, Re^b \tag{5.22}$$

Nu_{sf} is treate as an adjustable parameter and constants a,b and c here were chosen as 1/3, 2/3 and 0.3 respectively in order to match as close as possible the experimental results (as will be discussed in Chapter 6). The Reynolds number is defined as

$$Re = \frac{\rho V_p d_p}{\mu \xi} \left| \vec{u} \right| \tag{5.23}$$

where ξ is the tortuosity of the porous metal, d_p the pore diameter and μ the dynamic viscosity of the fluid.

The global h of the structure can be calculated as follows:

$$h = 2\pi R \int_0^H Cp_f u \rho_f (T_{g,out} - T_{g,in}) dz \tag{5.24}$$

Where u is the velocity of air entering the foam, $T_{g,in}$ is the temperature of air entering the foam and $T_{g,out}$ is the temperature of the air leaving the foam.

Thermal boundary conditions for the foam and air are defined as follows:

- Lower Boundary (Foam):
  $q_{measured}=q_{solid}$, $r_i<r<r_o$, $z=0$ (5.25)

- Lower Boundary (Air):
  $q_{fluid}=0$, $r_i<r<r_o$, $z=0$ (5.26)

- Outer Boundary (Foam):
  $q_{solid}=0$, $r=r_o$, $0<z<Z_{top}$ (5.27)

- Outer Boundary (Air):
  $q_{fluid}=0$, $r=r_o$, $0<z<Z_{top}$ (5.28)

- Upper Boundary (Foam):
  $q_{solid}=0$, $r_i<r<r_o$, $Z=Z_{top}$ (5.29)

- Upper Boundary (Air):
  $q_{solid}=0$, $r_i<r<r_o$, $Z=Z_{top}$ (5.30)

- Inner Boundary (Foam):
  $q_{\text{fluid}}=0,\ r_i=r,\ 0<z<Z_{\text{top}}$ (5.31)

- Inner Boundary (Air):
  $T_{\text{fluid}}=T_{\text{amb}}.\ r_i=r,\ 0<z<Z_{\text{top}}$ (5.32)

Figure 5.2 sketches the above boundary conditions for each of the solid and fluid phases. Physical constants used in calculations are presented in Table *4*.

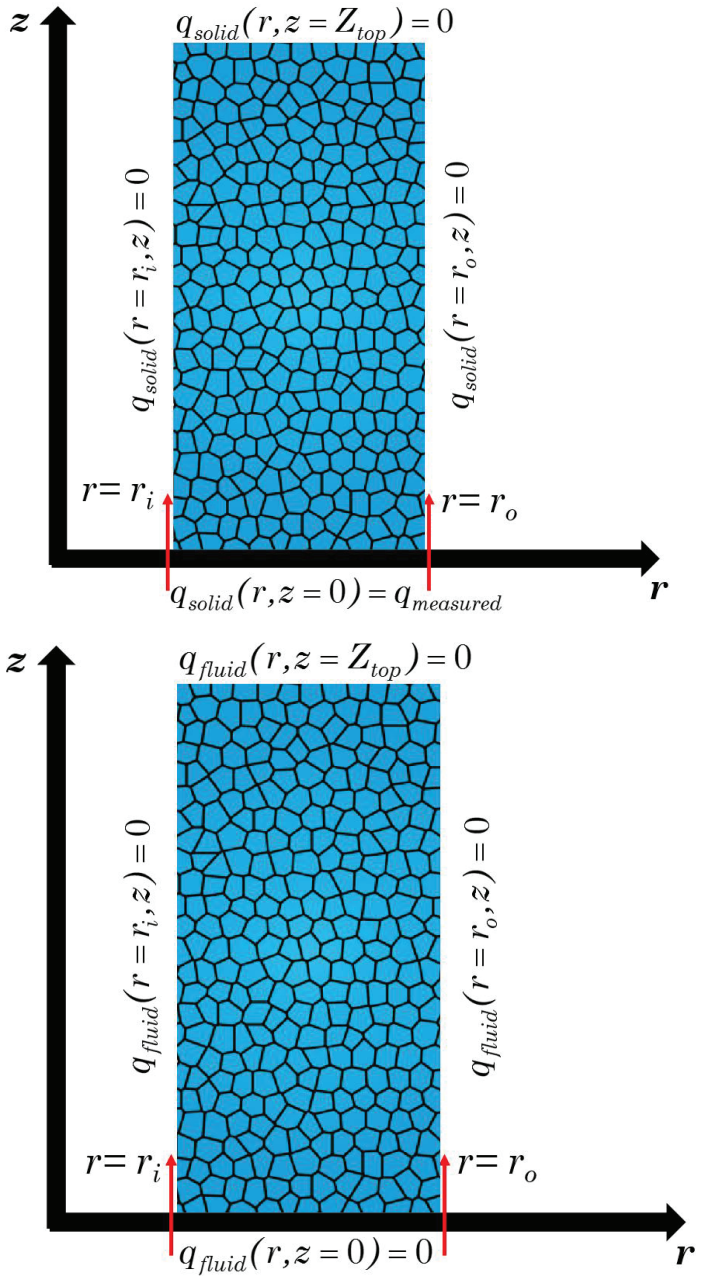

Figure 5.2: (a) Schematic representation of the boundary conditions for the solid phase (b) Schematic representation of the boundary conditions for the fluid phase

Aluminium thermal conductivity	237 W/mK
Aluminium thermal capacity	905 J/kgK
Aluminium density	2700 kg/m^3
Ambient Air thermal conductivity	0.026 W/mK
Ambient Air thermal capacity	1009 J/kgK
Ambient Air density	1.2 kg/m^3
Ambient Air kinematic viscosity	1.4 10^{-5} m^2/s
Ambient Air dynamic viscosity	1.8 10^{-5} kg/ms
Ambient Temperature	293 K
Tortuosity	0.2

Table 4: Physical constants used by the model and their values.

5.4 Results

The numerical model was employed to investigate the influence of height and pore size on pressure, temperature and velocity fields, under different volumetric air flow rates. Results for a sample of 28 mm height, 400 μm pore size and 85% porosity, under various volumetric flows, are illustrated in *Figs.5.3 to 5.6. Figures 5.7 to 5.10* show results for a foam of the same microstructural characteristics but with a height of 10 mm. *Figures 5.11 to 5.13* are for a sample of 28 mm height and 85% porosity but with a pore size of 1.1 mm, also under various volumetric flows.

Based on the results illustrated in these figures, the following general conclusions can be deduced:

(i) as the air flow rate increases, the temperature gradient in the metal phase decreases and therefore, the rate of heat dissipation through the foam also rises.

(ii) Metal and fluid phase temperatures seem to be in thermal equilibrium after the first 10 mm in the axial direction.

(iii) Recirculation of the pumped air, from midway along the foam to the top of the central channel, appears in tall samples, no matter the pore size; this recirculation becomes stronger as the volumetric air flow increases. On the contrary, the fluid flow field in smaller samples is fairly homogeneous, independently of the air flow rate.

(v) Finally, the greatest decrease in (static) pressure occurs around the central channel of the samples, where the air stream abruptly changes direction and enters the foam.

The apparent temperature oscillations in the gas medium on the upper inner part of the system (*cf. 5.3-5.6, 5.11-5.14*) are due to the numerical method chosen to solve the system of equations, and were ignored when it comes to the interpretation of the results.

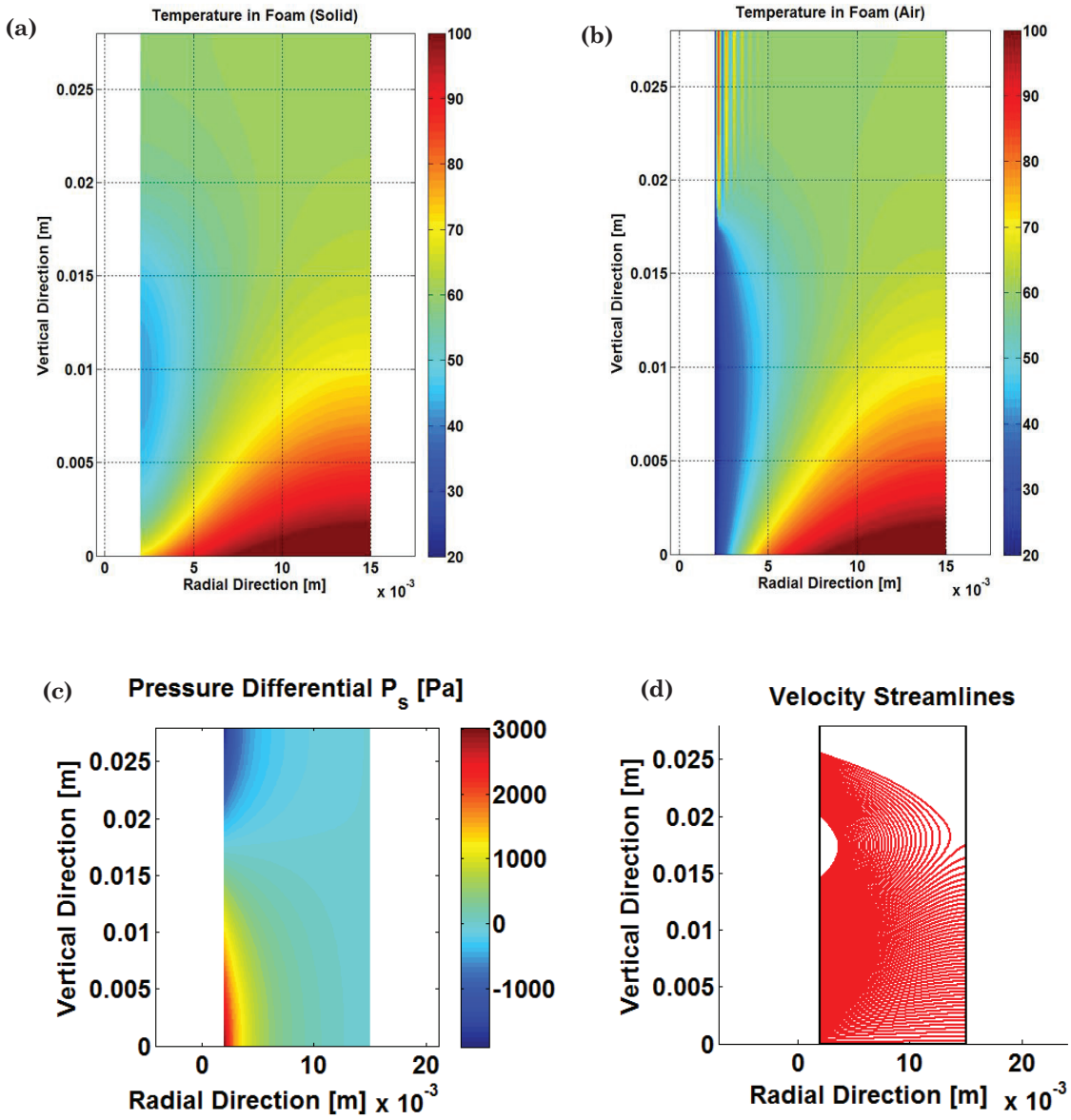

Figure 5.3 (a)-(d): Results of the model for a foamed sample of 28 mm height, 400 µm pore size and 85% V_p, under 2520 l/h. (a) Solid temperature field, (b) Fluid temperature field, (c) Pressure differential, (d)Velocity Vector Field.

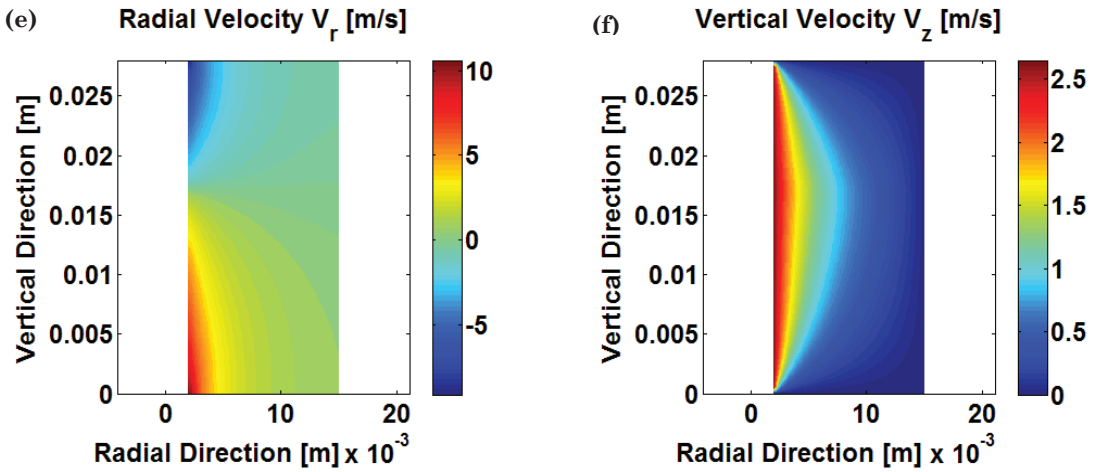

Figure 5.3 (e)-(f) : Results of the model for a foamed sample of 28 mm height, 400 µm pore size and 85% V_p, under 2520 l/h. (e) Radial velocity field and (f) Vertical velocity field.

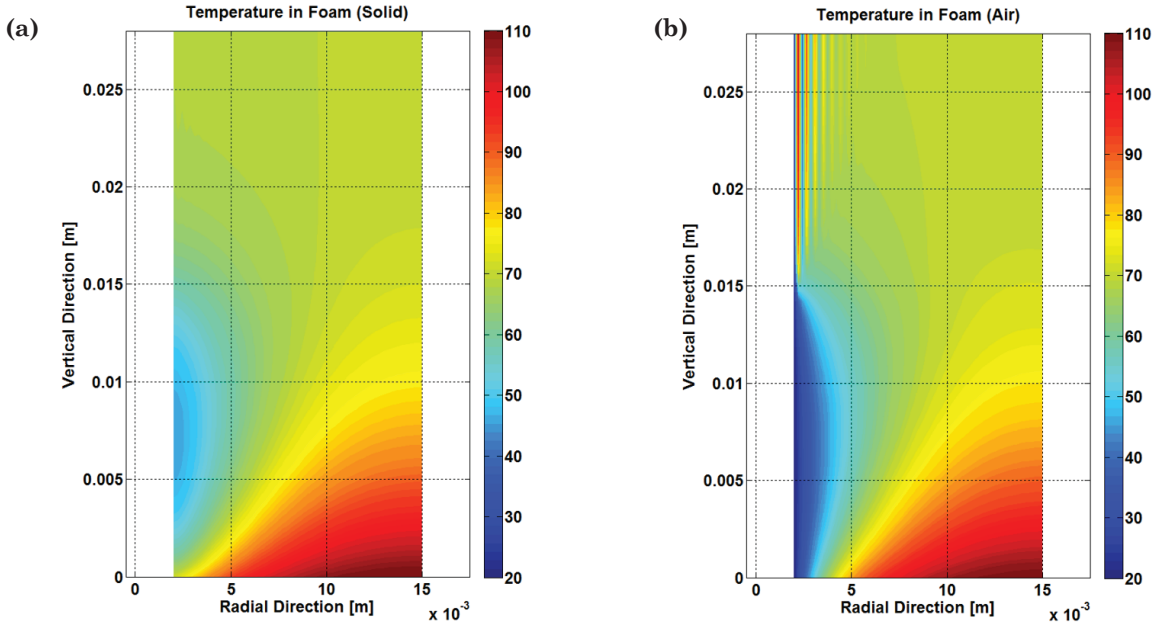

Figure 5.4 (a)-(b) : Results of the model for a foamed sample of 28 mm height, 400 µm pore size and 85% V_p, under 1800 l/h. (a) Solid temperature field, (b) Fluid temperature field.

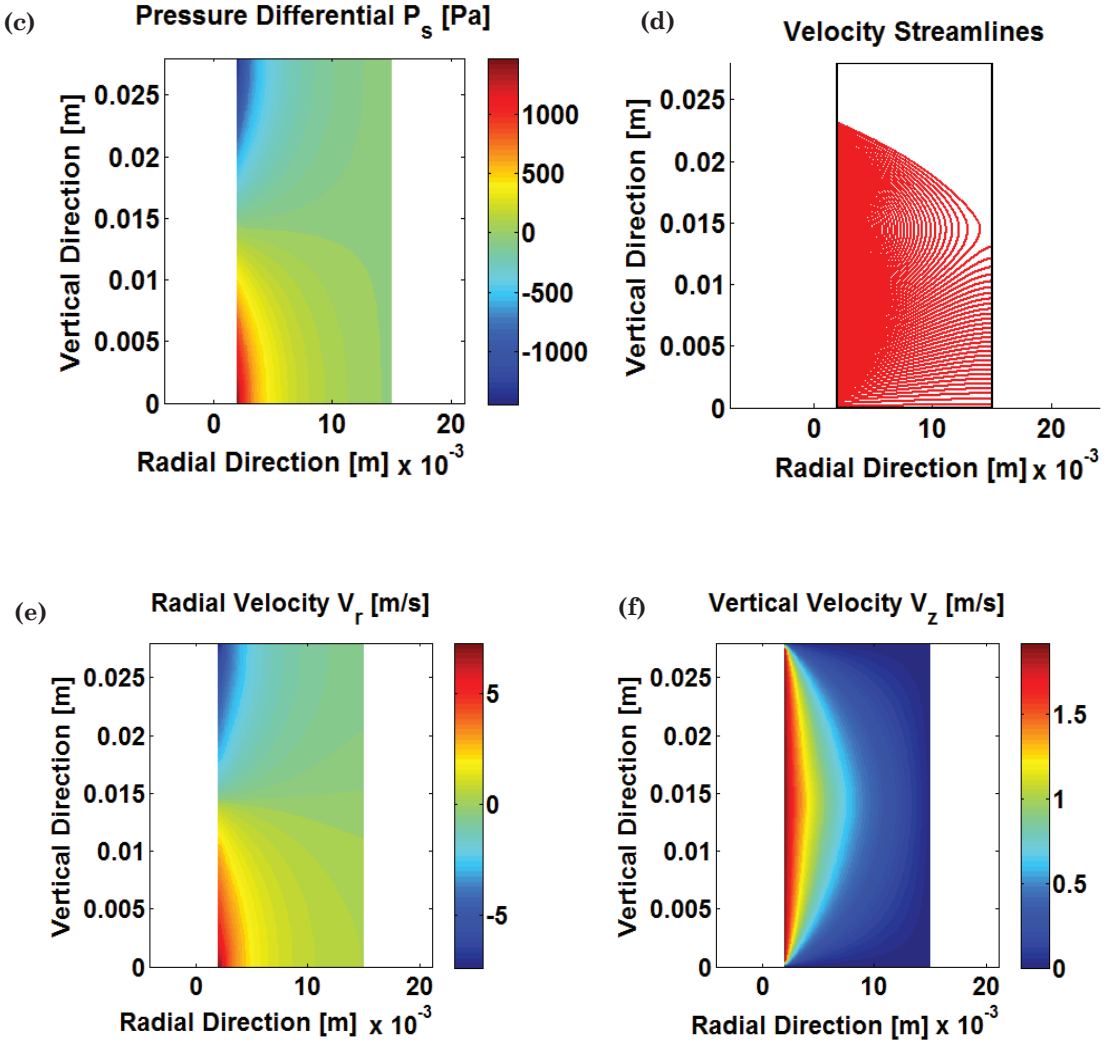

Figure 5 .4 (c)-(f) : Results of the model for a foamed sample of 28 mm height, 400 µm pore size and 85% V_p, under 1800 l/h. (c) Pressure differential, (d) Velocity Vector Field (e) Radial velocity field and (f) Vertical velocity field.

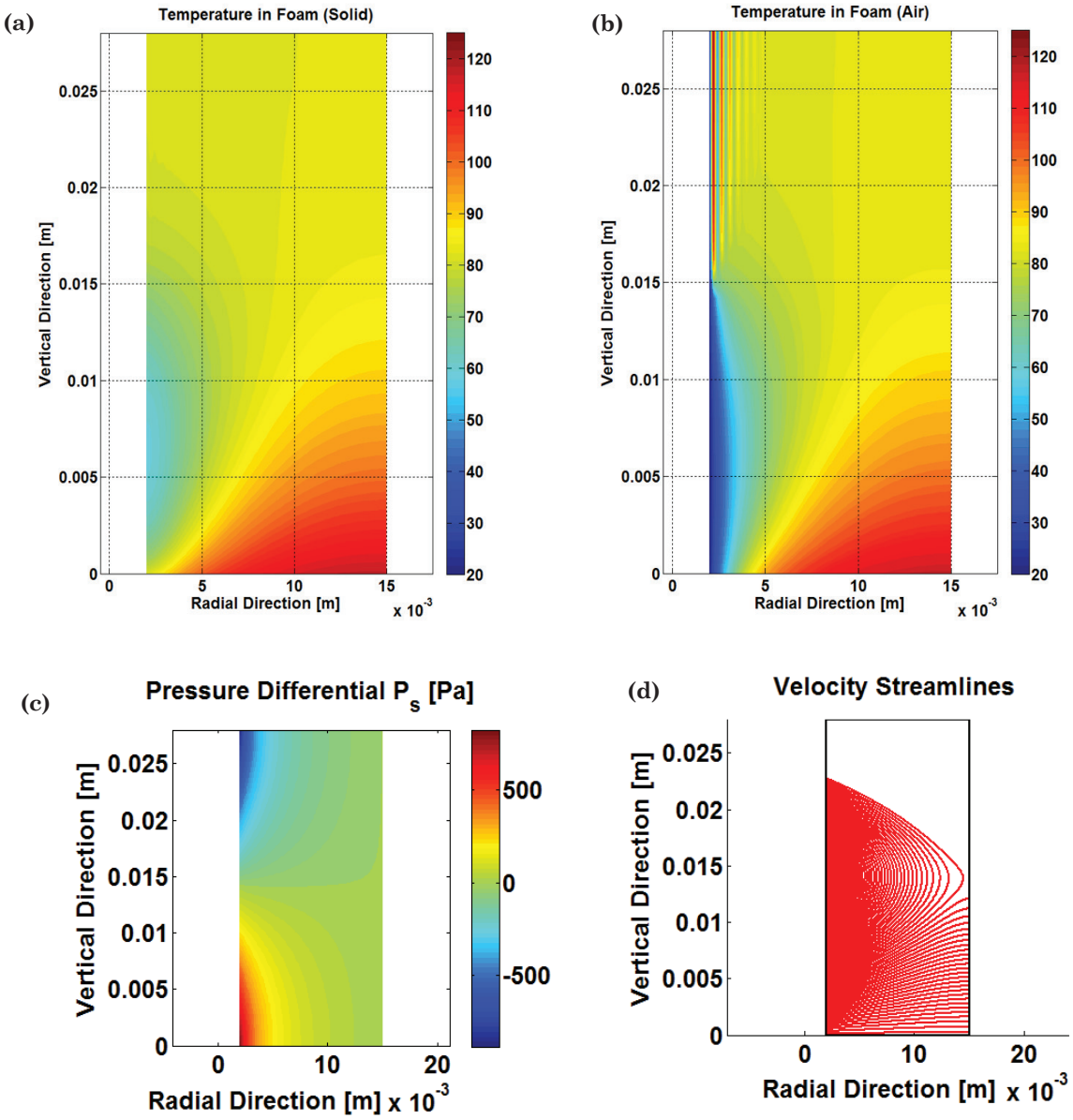

Figure 5.5 (a)-(d) : Results of the model for a foamed sample of 28 mm height, 400 µm pore size and 85% V_p, under 1260 l/h. (a) Solid temperature field, (b) Fluid temperature field, (c) Pressure differential, (d)Velocity Vector Field.

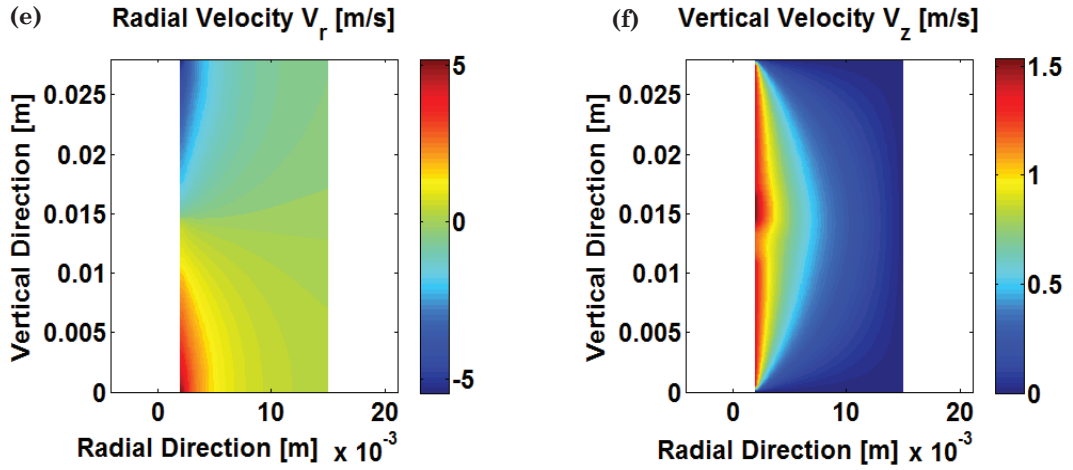

Figure 5.5 (e)-(f) : Results of the model for a foamed sample of 28 mm height, 400 µm pore size and 85% V_p, under 1260 l/h. (e) Radial velocity field and (f) Vertical velocity field.

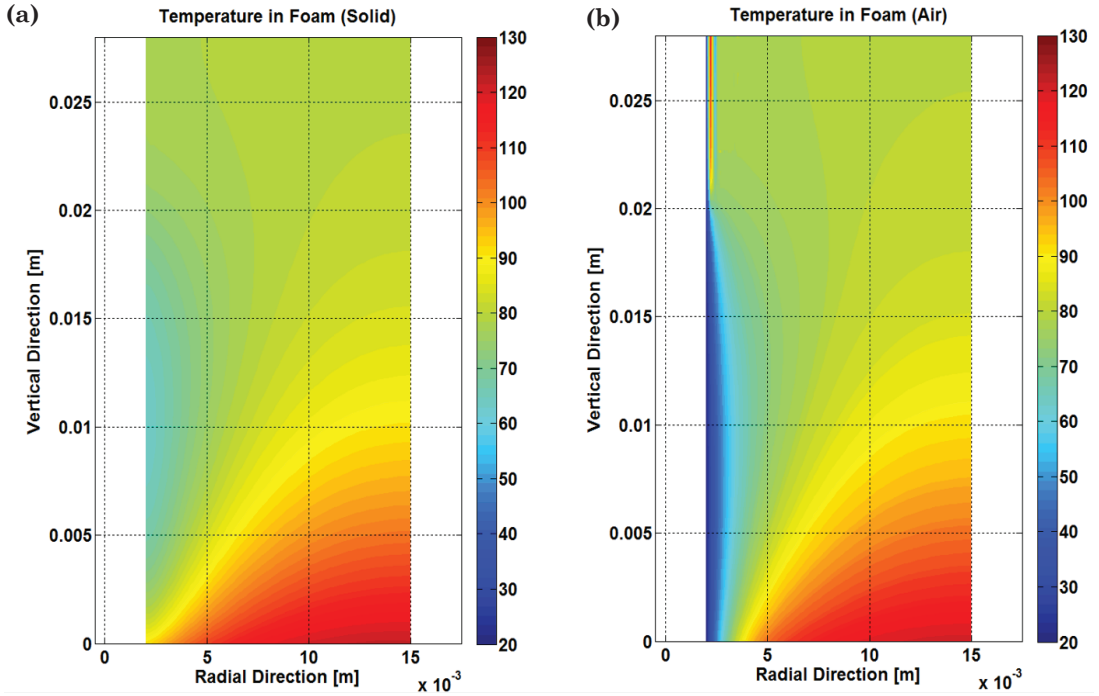

Figure 5.6 (a)-(b) : Results of the model for a foamed sample of 28 mm height, 400 µm pore size and 85% V_p, under 720 l/h. (a) Solid temperature field, (b) Fluid temperature field.

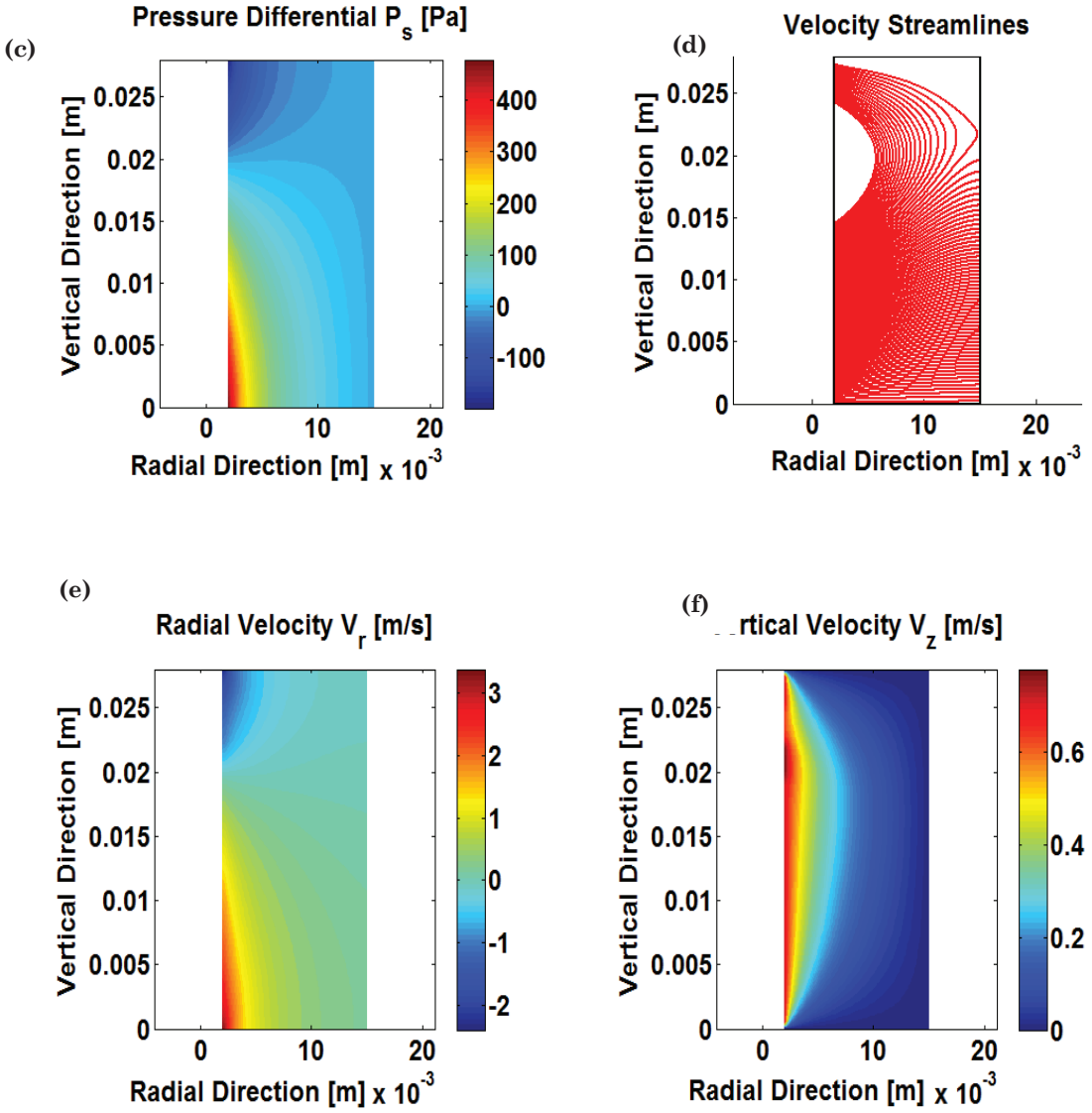

Figure 5.6 (c)-(f) : Results of the model for a foamed sample of 28 mm height, 400 µm pore size and 85% V_p, under 720 l/h. (c) Pressure differential, (d) Velocity Vector Field (e) Radial velocity field and (f) Vertical velocity field.

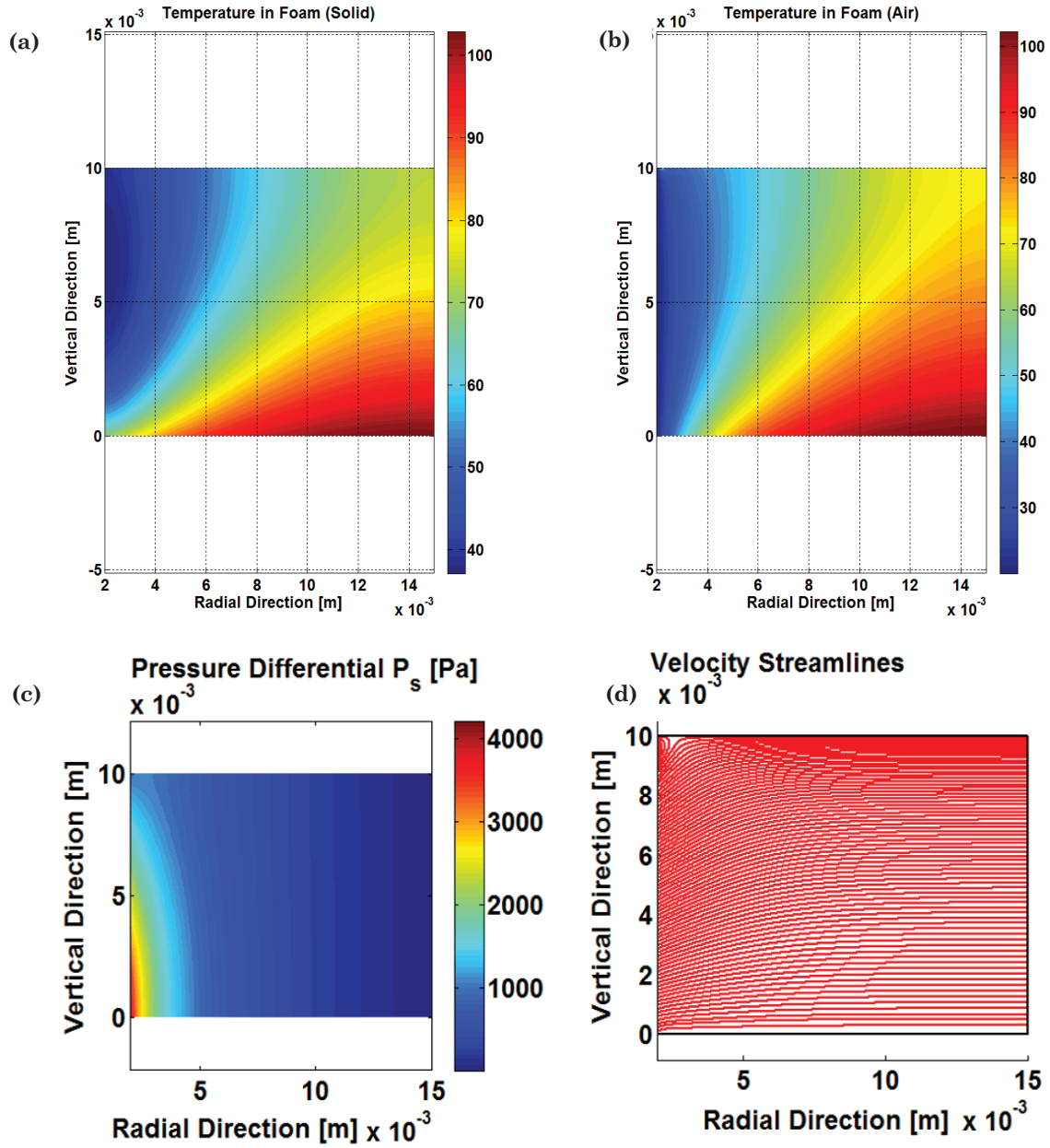

Figure 5.7 (a)-(d) : Results of the model for a foamed sample of 10 mm height, 400 µm pore size and 85% V_p, under 2520 l/h. (a) Solid temperature field, (b) Fluid temperature field, (c) Pressure differential, (d)Velocity Vector Field.

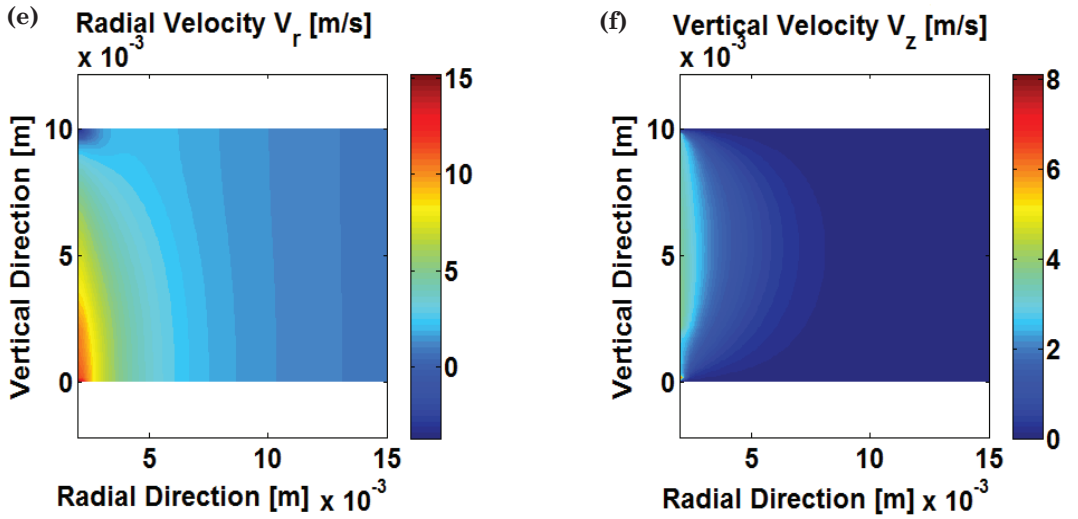

Figure 5 .7 (e)-(f): Results of the model for a foamed sample of 10 mm height, 400 µm pore size and 85% V_p, under 2520 l/h.(e) Radial velocity field and (f) Vertical velocity field.

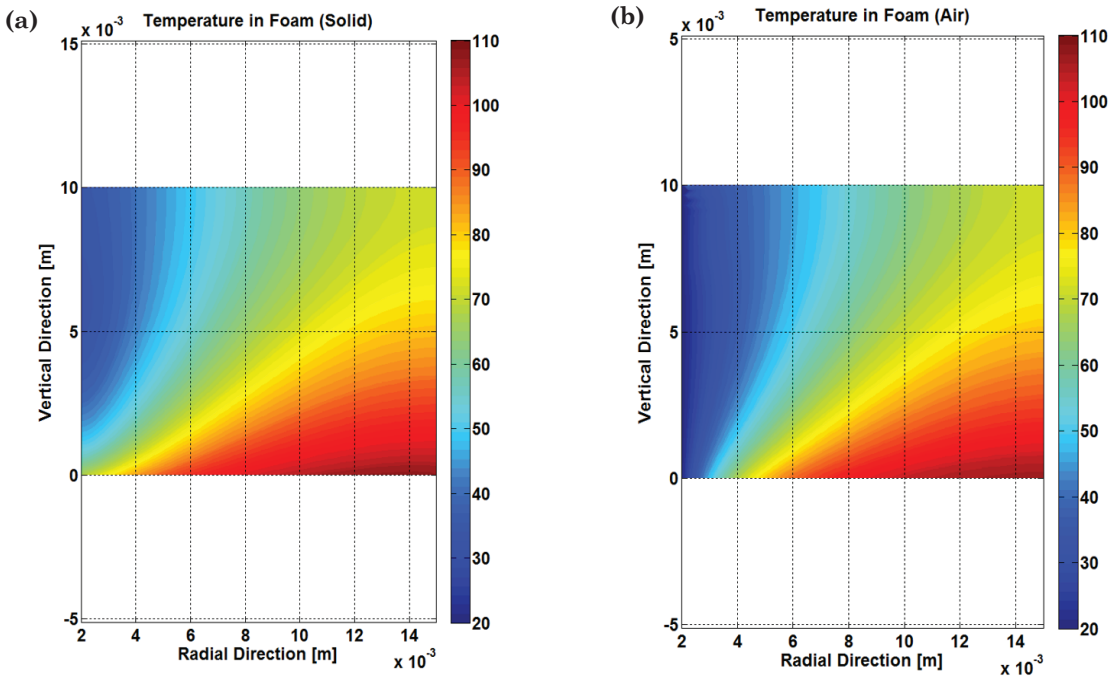

Figure 5.8 (a)-(b): Results of the model for a foamed sample of 10 mm height, 400 µm pore size and 85% V_p, under 1800 l/h.(a) Solid temperature field, (b) Fluid temperature field.

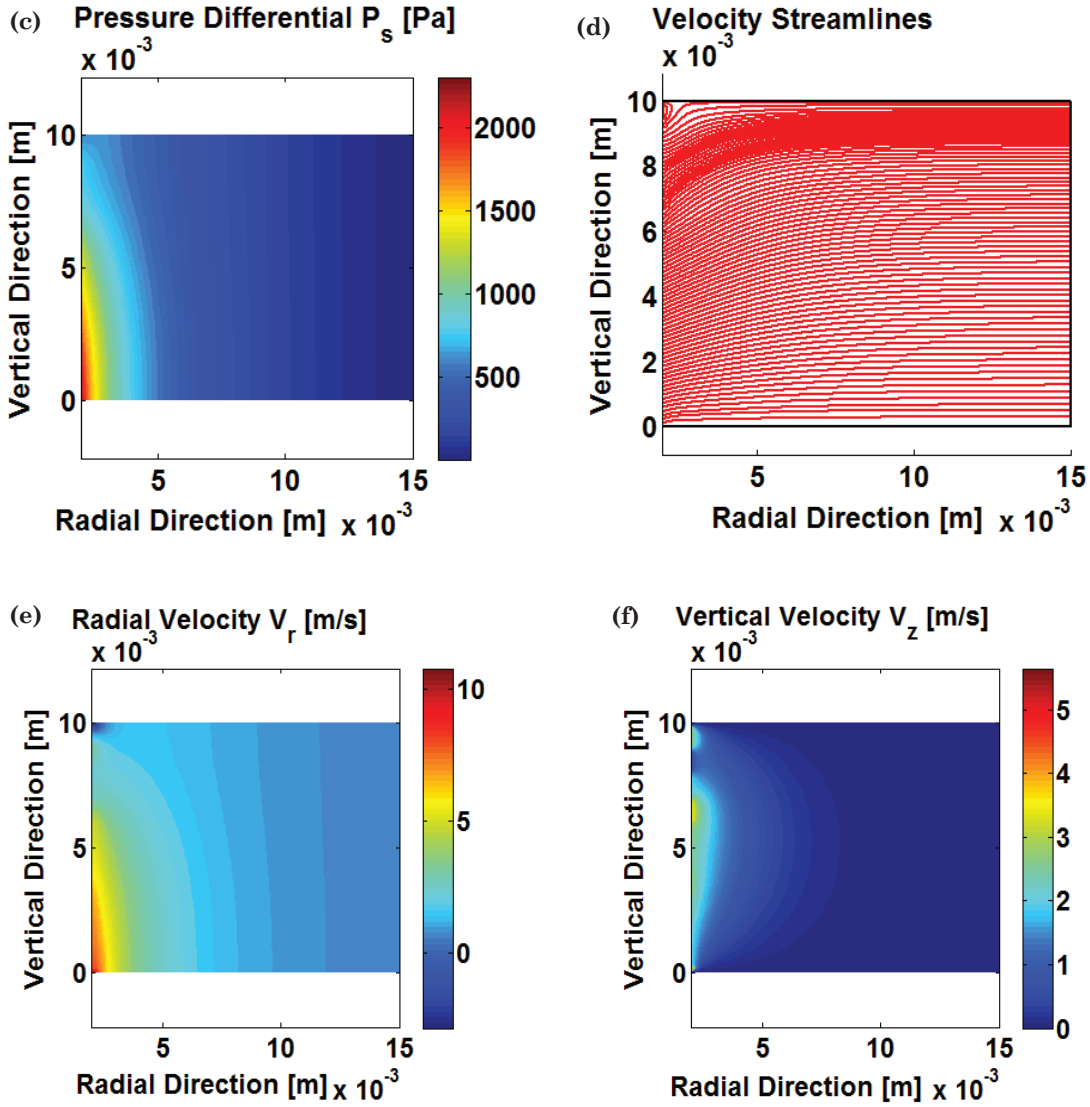

Figure 5.8 (c)-(f) : Results of the model for a foamed sample of 10 mm height, 400 µm pore size and 85% V_p, under 1800 l/h: (c) Pressure differential, (d)Velocity Vector Field (e) Radial velocity field and (f) Vertical velocity field.

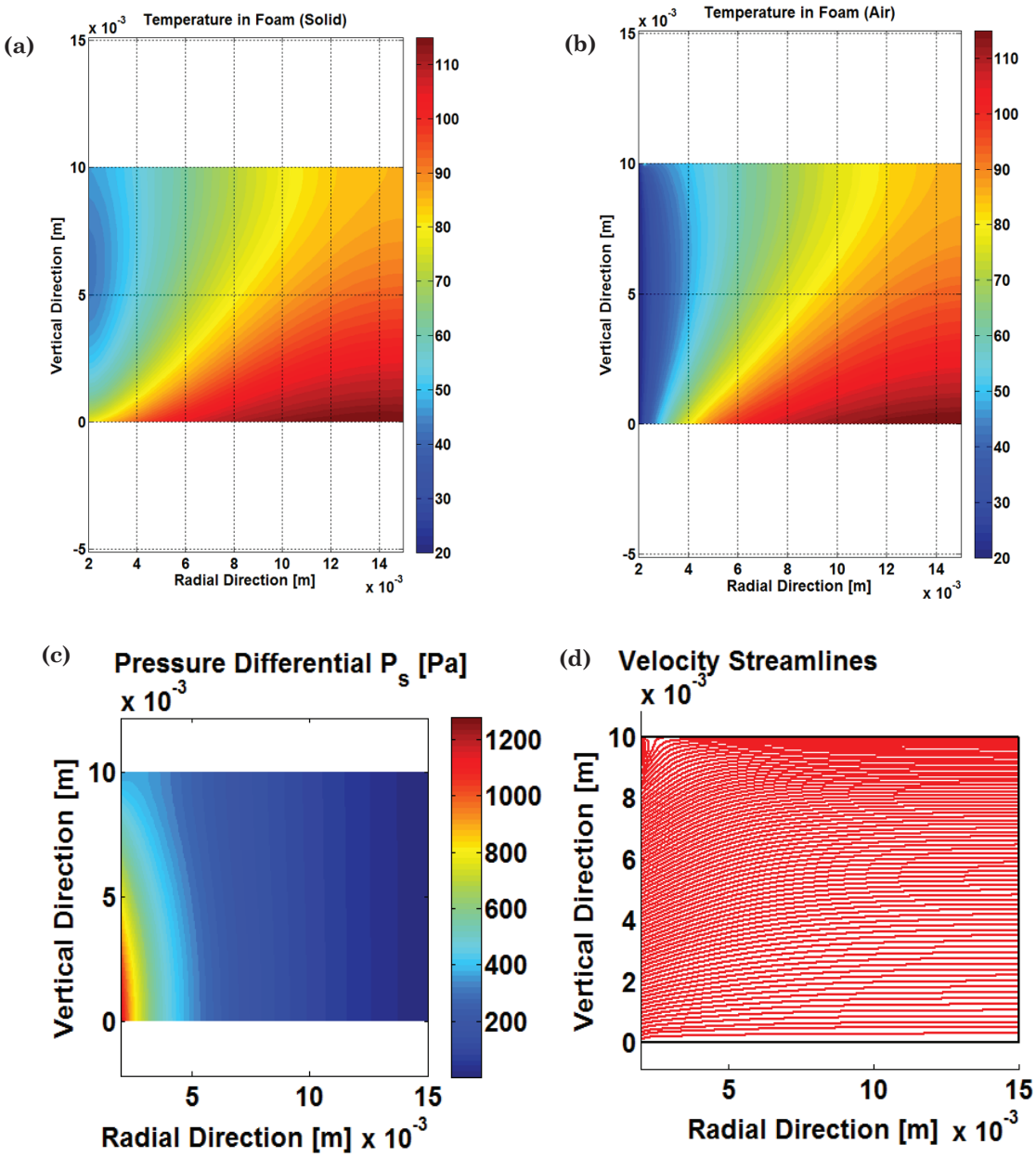

Figure 5.9 (a)-(d): Results of the model for a foamed sample of 10 mm height, 400 µms pore size and 85% V_p, under 1260 l/h (a) Solid temperature field, (b) Fluid temperature field, (c) Pressure differential, (d) Velocity Vector Field.

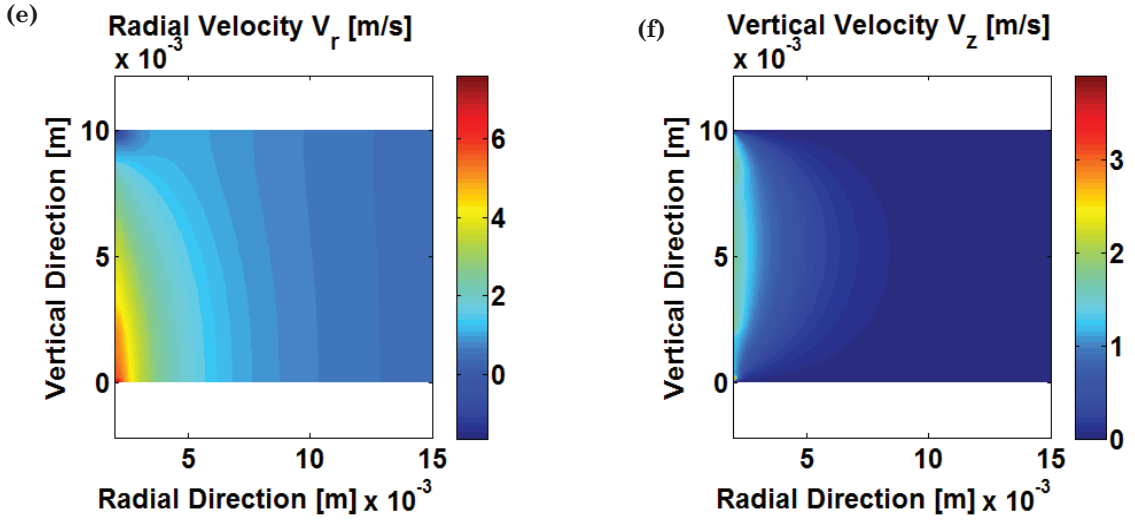

Figure 5.9 (e)-(f): Results of the model for a foamed sample of 10 mm height, 400 µm pore size and 85% V_p, under 1260 l/h (e) Radial velocity field and (f) Vertical velocity field.

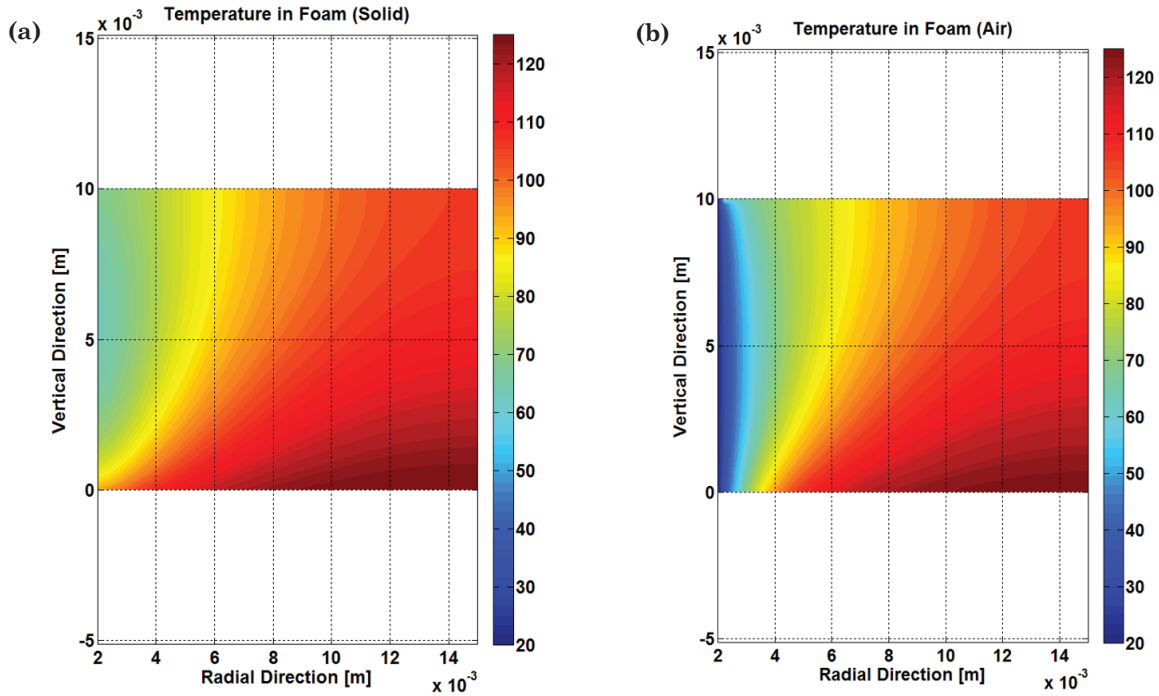

Figure 5.10 (a)-(b) : Results of the model for a foamed sample of 10 mm height, 400 µm pore size and 85% V_p, under 720 l/h (a) Solid temperature field, (b) Fluid temperature field.

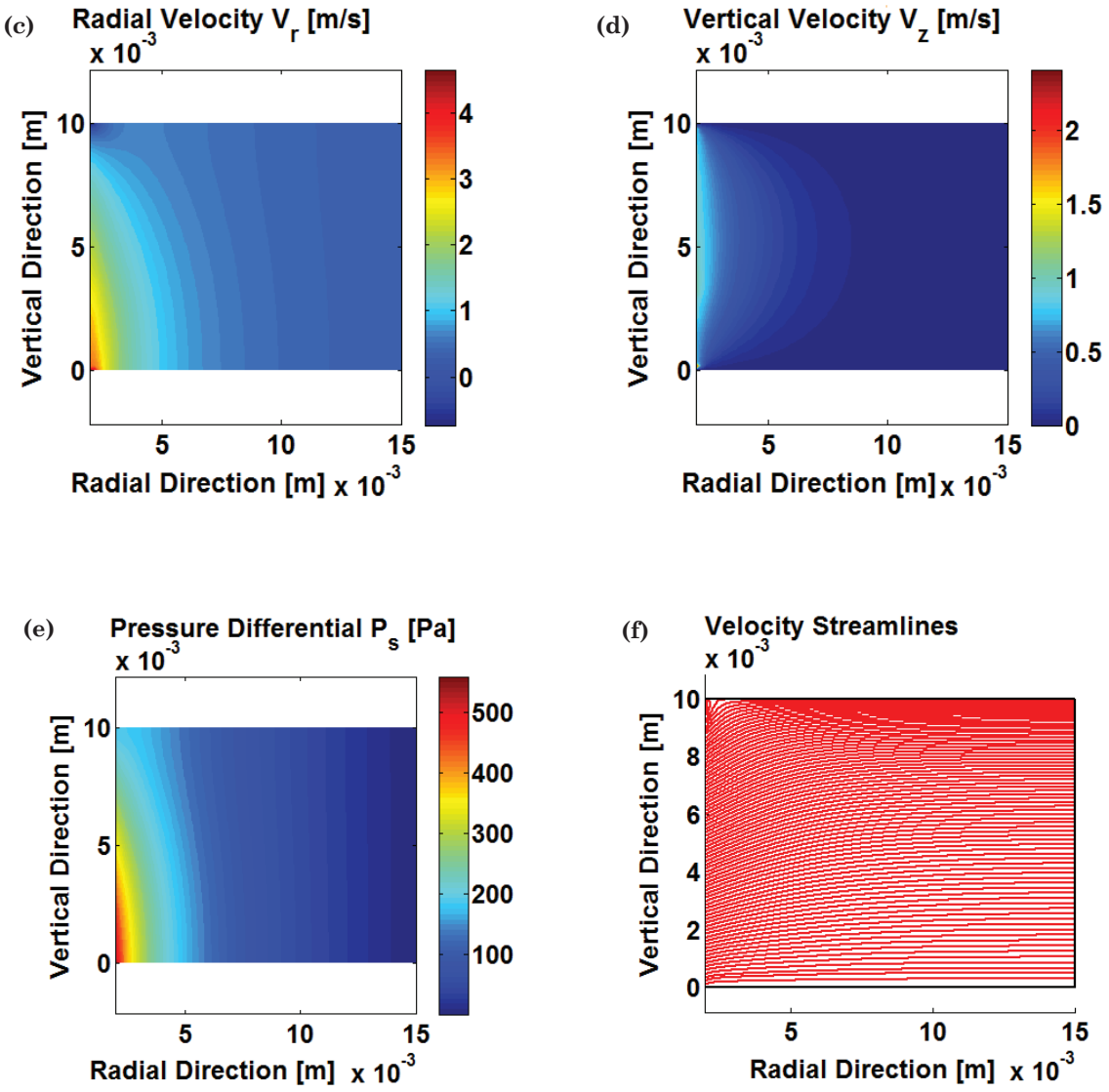

Figure 5.10 (c)-(f): Results of the model for a foamed sample of 10 mm height, 400 µm pore size and 85% V_p, under 720 l/h. (c) Pressure differential, (d) Velocity Vector Field (e) Radial velocity field and (f) Vertical velocity field.

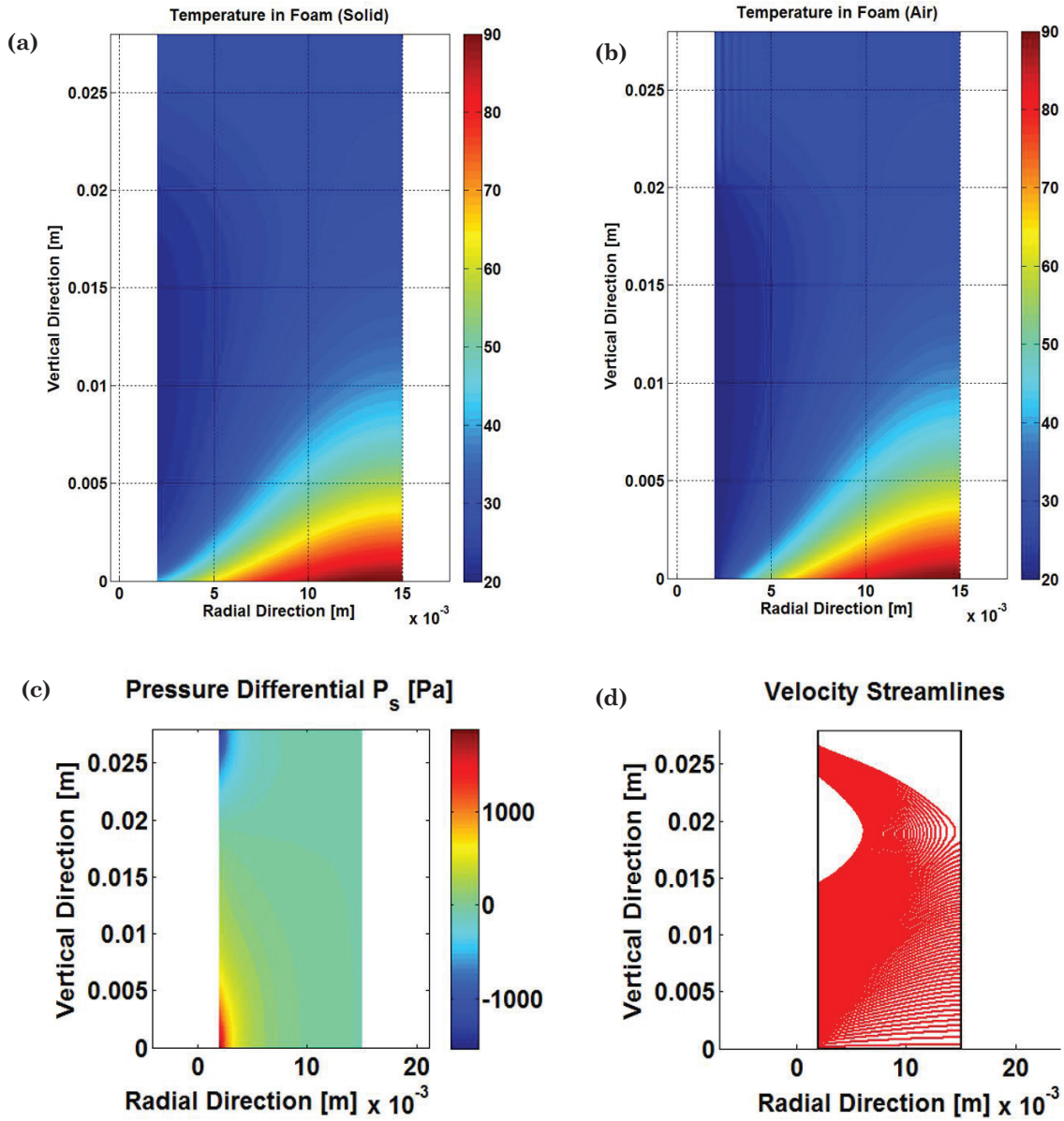

Figure 5.11 (a)-(d) : Results of the model for a foamed sample of 28 mm height, 1100 µm pore size and 85% V_p, under 2520 l/h. (a) Solid temperature field, (b) Fluid temperature field, (c) Pressure differential, (d)Velocity Vector Field.

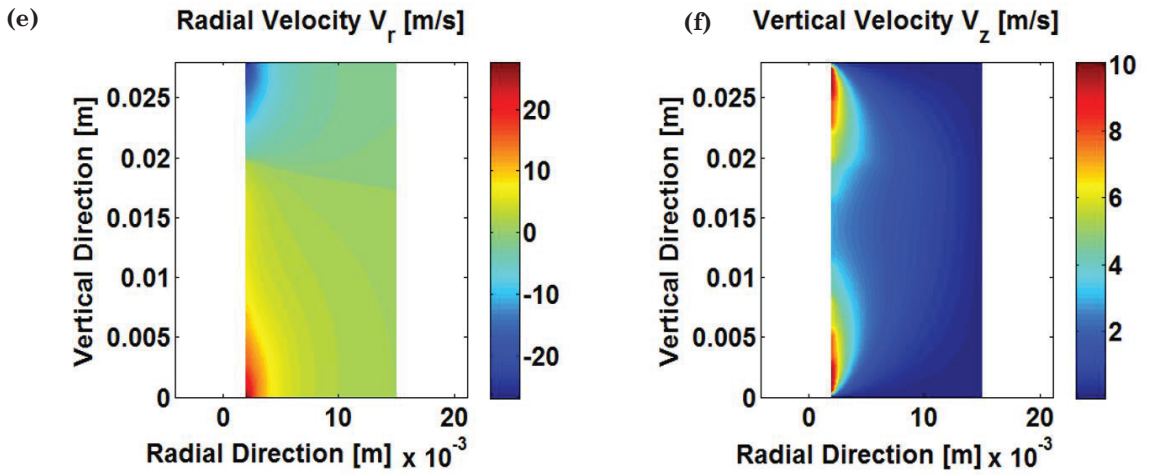

Figure 5.11 (e)-(f) : Results of the model for a foamed sample of 28 mm height, 1100 µm pore size and 85% V_p, under 2520 l/h (e) Radial velocity field and (f) Vertical velocity field.

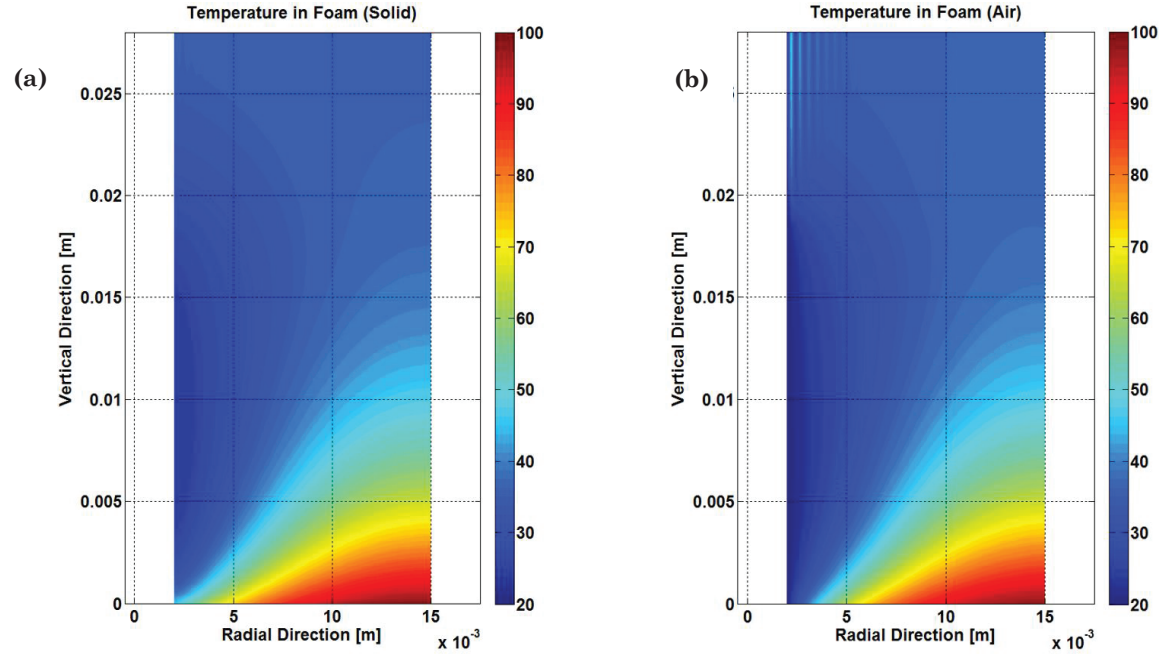

Figure 5.12 (a)-(b) : Results of the model for a foamed sample of 28 mm height, 1100 µm pore size and 85% V_p, under 1800 l/h. (a) Solid temperature field, (b) Fluid temperature field.

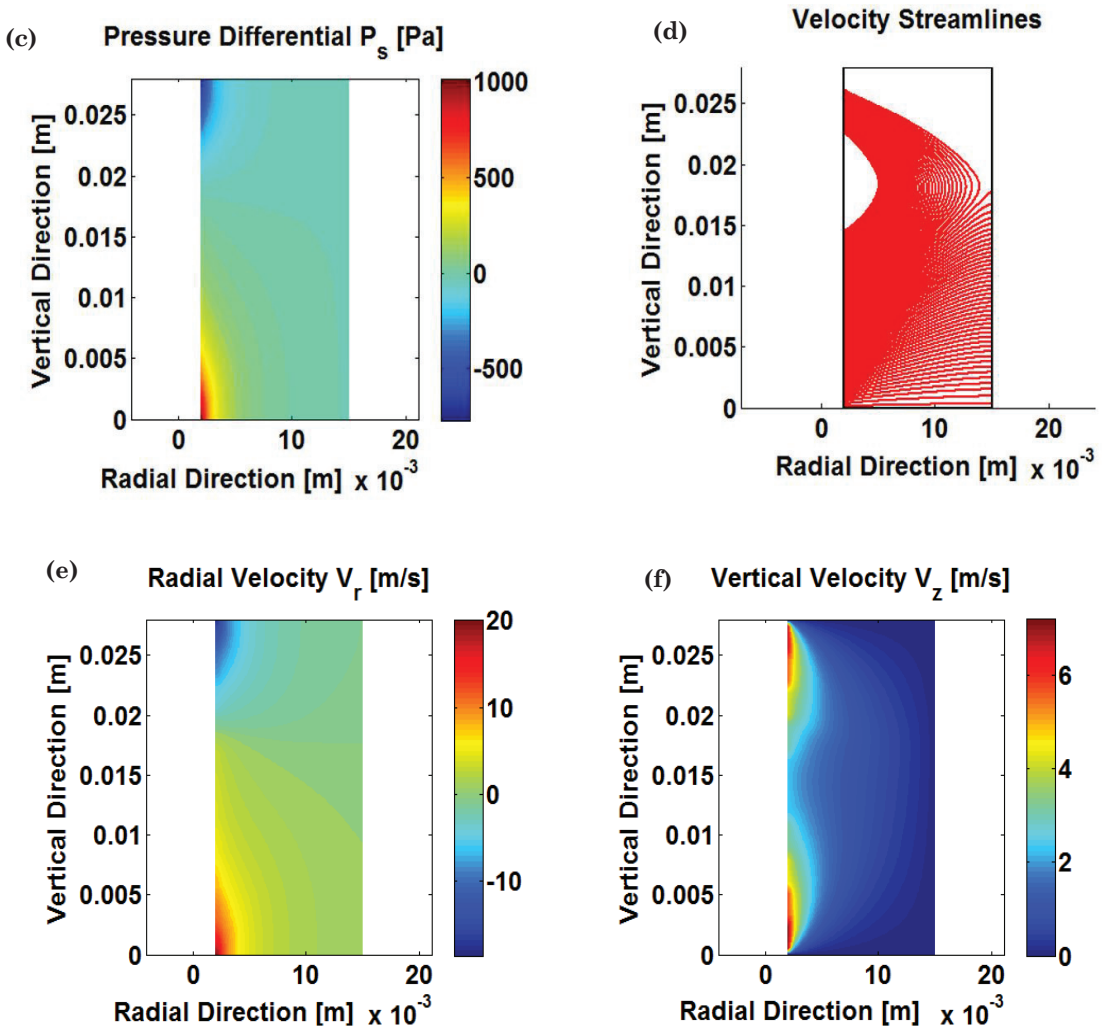

Figure 5.12 (c)-(f) : Results of the model for a foamed sample of 28 mm height, 1100 µm pore size and 85% V_p, under 1800 l/h. (c) Pressure differential, (d)Velocity Vector Field (e) Radial velocity field and (f) Vertical velocity field.

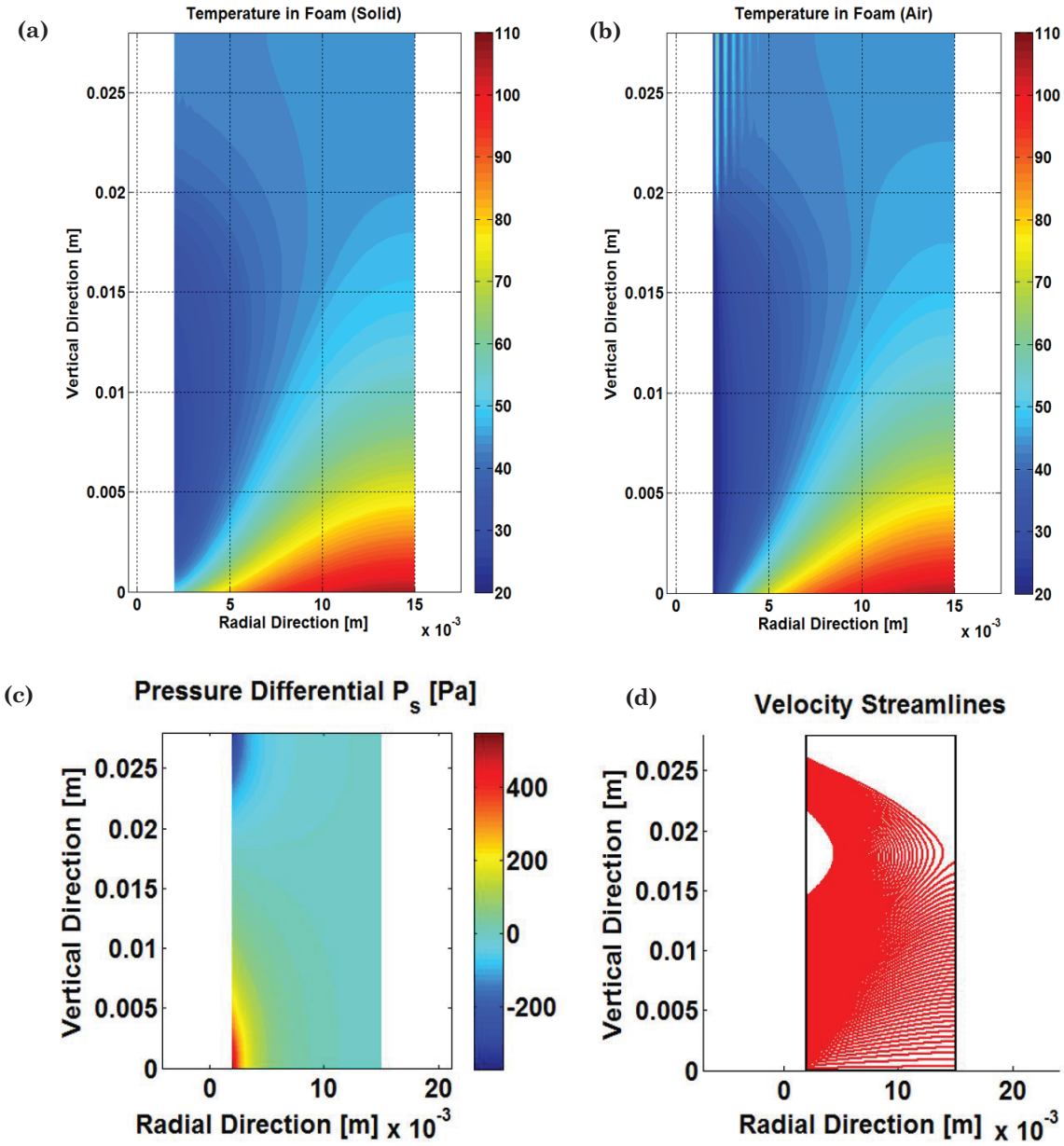

Figure 5.13 (a)-(d) : Results of the model for a foamed sample of 28 mm height, 1100 µm pore size and 85% V_p, under 1260 l/h. (a) Solid temperature field, (b) Fluid temperature field, (c) Pressure differential, (d)Velocity Vector Field.

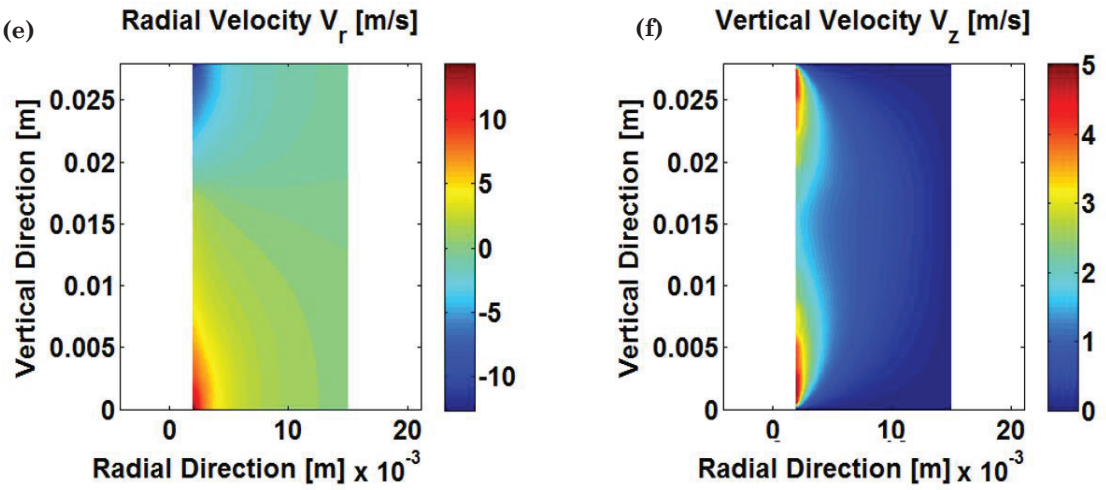

Figure 5 .13 (e)-(f) : Results of the model for a foamed sample of 28 mm height, 1100 µm pore size and 85% V_p, under 1260 l/h. (e) Radial velocity field and (f) Vertical velocity field.

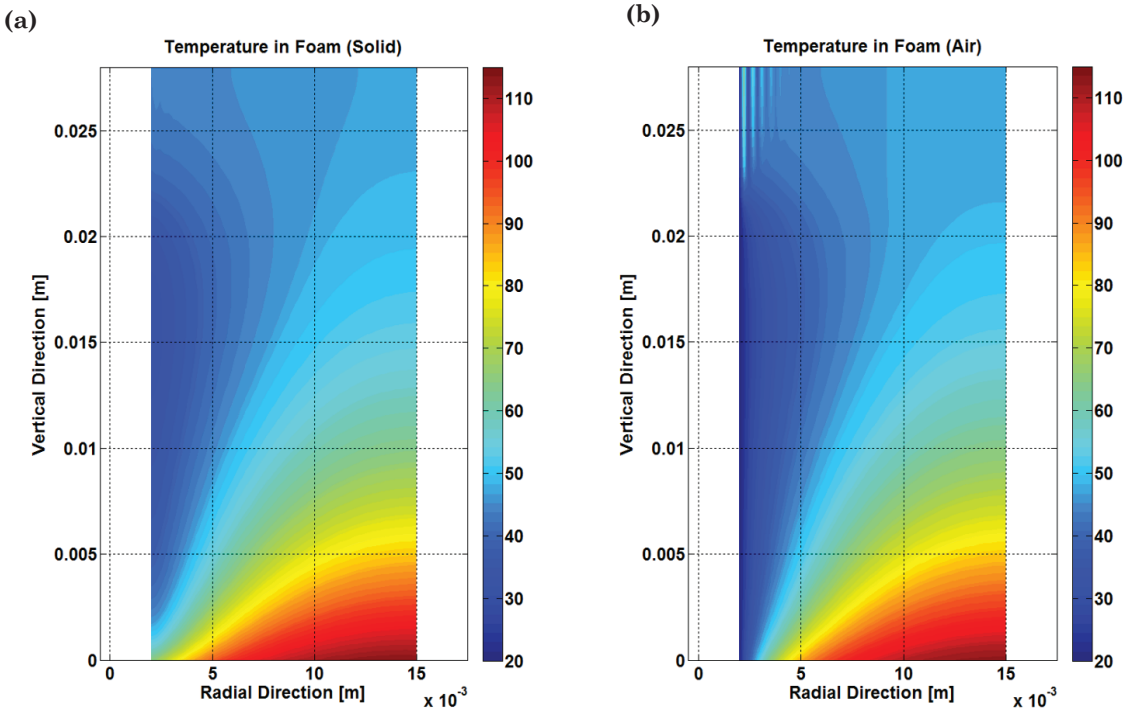

Figure 5.14 (a)-(b) : Results of the model for a foamed sample of 28 mm height, 1100 µm pore size and 85% V_p, under 720 l/h. (a) Solid temperature field, (b) Fluid temperature field.

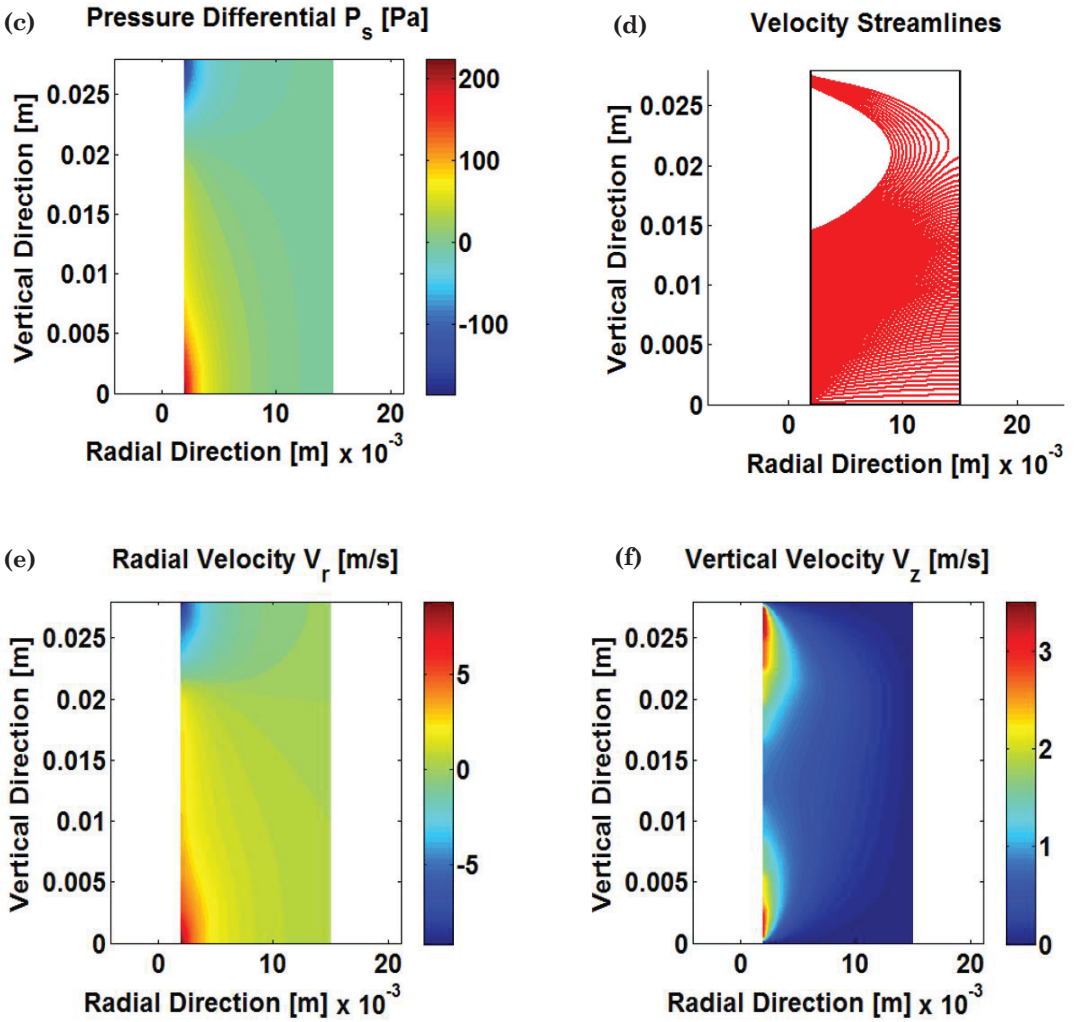

Figure 5 .14 (c)-(f) : Results of the model for a foamed sample of 28 mm height, 1100 µm pore size and 85% V_p, under 720 l/h. (c) Pressure differential, (d)Velocity Vector Field (e) Radial velocity field and (f) Vertical velocity field.

Chapter 6 Discussion

The present chapter analyses and critically examines the results produced during the thesis. More precisely, results for the performance of replicated aluminium foams under both natural and forced convection, presented in Chapter 4, are juxtaposed with the data in the literature and general remarks are made concerning how the foam microstructure and geometry influence its performance. In addition, the static pressure data and the technique used to harvest them, taken out of the experimental procedure described in Chapter 3, are also discussed, considering the literature from a similar, albeit not identical, field. Then, results from calculations performed using the model analysed in the previous chapter are compared with the experimental data, to draw conclusions, where possible, with regard to the design of high-performance foam structures for heat extraction under the impingement jet configuration.

6.1 Thermal performance under natural convection

Replicated aluminium foams have been investigated under natural convection exploring different pore sizes, porosities, heights and geometries (cylindrical samples and finned structures), and varying also the degree of NaCl dissolution.

By comparison with their bulk equivalents, cylindrical aluminium foams do not exhibit any significant difference in the evolution of the heat transfer coefficient with surface temperature, *cf. Figs. 4.2 to 4.5*. In this light, the observation that taller samples dissipate more heat is simply due to an overall increased heat exchange area along the vertical hot surfaces, which typically have slightly higher heat transfer coefficients in free convection than their horizontal counterparts. The same was true for samples with fins: for similar fin geometry the bulk samples and the foam samples did not show any significant difference (on the order of 10%).

Variations of pore size and of porosity exert no measurable effect on the curve of global heat transfer coefficient versus surface temperature; under natural convection, other researchers also report similar results [22], [214].

Regarding other studies reporting an increased heat transfer through natural convection with porous metal heat exchangers compared to their dense metal analogues, an analysis comparing the characteristic length scale of the surface structure to the thermal boundary layer can rationalize the contradictory results: the tested foams in other studies reporting an increased heat transfer through natural convection [22], [214]–[219], had pore sizes and porosities significantly larger than in the present replicated foams. For instance, Duocel foams ™ (Oakland,USA) have larger pores (5, 10, 20 Pores Per Inch which stands respectively for nominal pore sizes of 5.080 mm, 2.540 mm and 1.270mm) and V_p above 86% (88-97%) [243]. In this work, we have been using aluminium foam with pores 125-180 μm, 400-450 μm or 5mm in diameter and porosities between 78% and 86%: seemingly this causes pores to play a limited role in heat transfer.

Results for the partially leached samples are, however, interesting in that regard: even if one takes into account the non-negligible experimental uncertainty in our data, the unleached NaCl/Al composite sample has a significantly lower effective heat transfer coefficient in natural convection than do the partially or completely leached structures (the relative difference is within the range of 12 to 20%). If one removes just a portion of the NaCl along the microcellular metal surface, then the heat transfer coefficient h increases to match what is found for bulk aluminium. This shows that the surface structure of the microcellular metal matters: removing NaCl along the heat exchanger surface and exposing the rough surface presented by the first row of pores to the outside air causes an enhancement in the rate of heat transfer. This is in line with the literature, where it is well known that surface roughness promotes heat exchange in natural convection [244], [245]; however, it does not explain the fact that the porous metal then matches what is found with a bulk metal having a smoother outer surface than the leached microcellular metal.

Theoretical correlations for bulk samples predicted systematically a somewhat smaller heat transfer coefficient than the one found experimentally, for both foamed and bulk samples. This systematic overestimation of our global heat transfer coefficient may perhaps be due to the linear data treatment model that we apply, that improves our experimental precision but limits the accuracy of our experiments (as analysed in *Section 3.2.3*). In addition, a possible overestimation of the thermal conductivity of the duct (in the said section), above the uncertainty level that it has been considered in the error estimation, should not be excluded. In all cases, the systematic error, if present, does not influence the conclusions to be drawn from the data.

Pooling the results, in natural convection it is found that the present replicated foams do not perform better than similarly sized and shaped smooth dense aluminium alloy heat-exchange structures. This said, compared to dense metal, the present microcellular material may be of interest where the selection of simple and low-weight solutions is of key importance, for example in the transportation sector (i.e., railway, aerospace etc.), since with all else equal, producing the heat exchanger out of replicated aluminium will save roughly 80% of the weight of the heat-exchanging structure. For high heat extraction rates, on the other hand, it is clear that replicated aluminium foams unlock their full potential under forced convection only.

6.2 Thermal performance under forced convection

The global heat transfer coefficient and the ideal pumping power cost of foams under forced convection have both been studied, since for overall performance evaluation, the combination of both factors should be considered.

Both the microstructure (porosity, pore shape and size) and the overall geometry of the impinging central jet cylindrical heat exchangers studied here were found to influence the thermal behaviour of foams. The exact level of influence depends on the volumetric flow (with the effects becoming more prominent at higher air flows) and on the other characteristics of the foams (e.g. the infiltration pressure

had a much higher effect on the global heat transfer coefficient for taller samples). In what follows, the reported percentage values will refer to the highest volumetric airflows.

Foams with higher porosities (ceteris paribus), were found to dissipate more heat (on the order of ~10%) for a given pressure driving flow of the working fluid. This pressure drop was on the order ~16% to ~40%, depending on the sample height, *cf. Fig.4.19* & *4.21;* the trend was stronger for taller samples. Increasing the porosity increases the Darcian permeability and the Forchheimer coefficient; analytical correlations describing the relation between porosity and permeability and the Forchheimer coefficient are given in *Appendix A*; at a given applied pressure, more air will flow through the foam if it is more porous. This effect seemingly dominates negative consequences of an increased porosity (reduced thermal conductivity through the solid foam and reduced local metal surface area in the foam). It may also be that the increased porosity favours air flow to the lower end of the foam and therefore, promotes heat exchange between the flowing air and the metal surface; this last argument is motivated by the observation in the literature that porosity can affect positively unconfined impingement jet flows[201]–[203] and negatively confined ones [204]; however, more research would be required to correctly assess the exact underlying mechanism(s).

Lowering the infiltration pressure appears to be slightly beneficial in terms of heat transfer, even if one judges data at fixed volumetric flow rate (between ~9% and ~25%, depending on the height), with the benefit increasing further if one takes into account the pressure drop (improvement on the order of ~5% regardless of the height), *cf. curves* in *Fig. 4.7, 4.9, 4.20 and 4.22*. As before, this phenomenon was stronger for taller samples. That a lower infiltration pressure would be beneficial at equal volumetric rate is counterintuitive because lower infiltration pressures produce a generally smoother surface of the metal ligaments that form the foam cells, see *Figure 6.1*. An explanation for this effect can be air stagnation; vertical lamellae around the ligaments might trap air between them, reducing the amount of air exchanging heat with the metal surface (or in other words lowering the local metal/air heat transfer coefficient h_{sf}). Another explanation is based on the local thermal conductivity of the cells: since increasing the infiltration pressure at fixed volume metal fraction of the solid redistributes the metal from foam ligaments to small "dead end" structures, foam cells infiltrated under lower infiltration pressures have thicker peripheral ligaments than foams infiltrated at higher infiltration pressures for the same relative density. The reason for the above is that higher infiltration pressures force the liquid metal to infiltrate even the local cravices of the salt grains, leaving less metal for the space between the grains and hence, producing thinner ligaments along the part of heat flow. Nevertheless, this means that there is less metal for the rods that form the cell, a fact that might lower the local thermal conductivity of the foam.

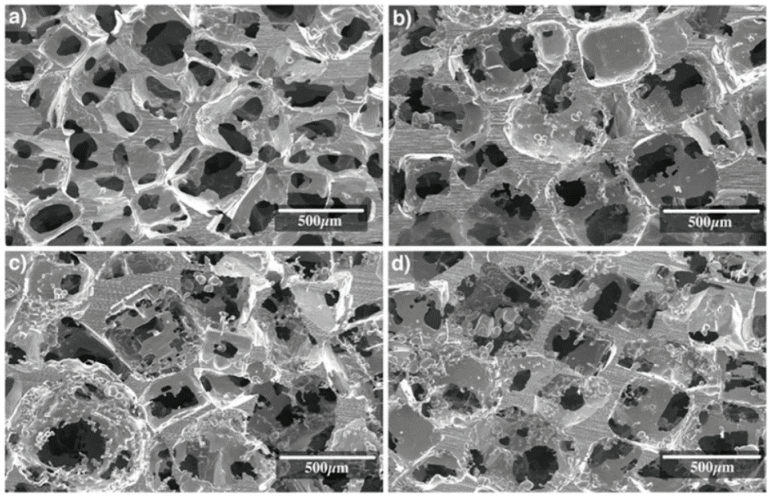

Figure 6.1: SEM pictures of pure Al replicated foams made out of similar salt preforms (porosity≈ 25%) infiltrated at various pressures P_{inf}: a) P_{inf} = 2 bars, b) P_{inf} = 5 bars, c) P_{inf} = 10 bars, c) P_{inf} = 155 bars. Figure reproduced from [100]. It is the same image as *Fig.3.21*.

Larger pores increase the rate of heat transfer and reduce the pressure drop in the fluid (within the examined range in this thesis); this beneficial influence is in agreement with part of the literature. The largest pore sizes explored here (900-1300 μm) had a higher global heat transfer coefficient, by ~15%, than was found with 400-450 or 125-180 μm pores. At the same time, the pumping power per footprint was ~2 to ~3 times lower. While the reduced pressure drop with larger pore sizes is expected (both the permeability and the Forchheimer coefficient decrease with increasing pore size), the reasons for a rising heat dissipation rate at fixed overall volumetric flow rate (compare *Figs. 4.14* and *4.17*) remain unclear. In the examined literature, two potential explanations for an improved heat transfer coefficient with increasing cell size have been advanced, namely (i) that the increased cell size leads to thicker ligaments [121], [128], [185], which in turn increases the heat transfer from the metal to the air flowing around the ligament. Note however that as the ligament's diameter grows bigger, the number of ligaments over a finite space decrease, suggesting that ther might exist an optimum pore size that combines a sufficient number of ligaments with a sufficient thickness for each.

The second hypothesis proposed in the literature is that there are changes in tortuosity accompanied with smaller cells, leading to increased dispersion and consequently, saturation [246]. Hence, this would not be a size effect as such but an effect due to concomitant changes in the microstructure as size increases. Given that larger pore size means lower specific surface, the observed trend suggests that, at the flow rates investigated here, heat transfer between the metal and the flowing air is complete, i.e. the air has reached the metal temperature when it leaves the foam. This is supported by the performed simulations (see *Figs. 5.3* to *5.14*), which suggest that after a radius of 8 mm for 400 μm and 10 for 1.1 mm sea salt foams, the solid and fluid phases of the system are near perfect thermal equilibrium. The shorter saturation length of air for foams of smaller pore sizes

might reduce their thermal efficiency: heat extraction is most efficient when ΔT is large.

Finally, another possible explanation, which focuses on our particular geometry, lies on the pressure distribution in the inner channel of our samples. The pressure distribution in the inner channel of our samples is such that, at low Darcy-Forchheimer pressure drops, it generates a flow field in which more air flows close to the hot surface; then more air is on average in contact with the hotter part of the foam, resulting in higher heat extraction rates. Note also that all these mechanisms are not mutually exclusive.

Both the pressure drop and heat transfer increase at constant volumetric flow rate as the height of the sample decreases, *cf. Fig. 4.11, 4.13, 4.16, 4.23, 4.25 and 4.27;* however, shorter foams demand a higher pumping power (between ~13% and 35% depending on the pore size) and simultaneously, had a higher global heat transfer coefficient by between ~19 and 30% (again depending on the pore size). This concurrent increase has conflicting effects on the operating cost and the heat dissipation. The better thermal performance can be explained by the temperature of the samples (as shown by simulations, smaller samples are generally hotter for a given heat flux from the solid surface) and by the recirculation of air that appears in higher samples, a factor that reduces the efficiency of the foam. On the other hand, this increased thermal efficiency comes with a non-negligible operating cost; the pressure drop is almost the double in comparison with taller samples at given overall volumetric flow rate. Likely, an optimal height may exist, since a large decrease in the sample height would decrease the surface of the foam and therefore, it would limit its capacity to exchange heat.

Putting all results together, the apparent heat transfer coefficient, h, is seen to be a property that is related both to microstructure (pore size and shape, porosity) and macroscopic geometry of the foam (not only the height but likely also the radius, or in more general terms the distance over which the air travels through the foam). At fixed volumetric flows, foams of high porosities (~ 85%) and pore sizes (~1 mm), infiltrated at lower pressure appear to be the most appropriate choices. With regard to the height, its choice depends on whether the global heat transfer coefficient or the ideal pumping power are what is aimed for. If the goal is to dissipate a predefined amount of heat at minimal operating cost, then a greater height (~3 cm) appears to be the appropriate choice. If the aim is to achieve the maximum global heat transfer coefficient possible, a smaller height (~1 cm) should be selected. Over the course of the present thesis, the maximum global heat transfer coefficient we have reached is 1029 W/m^{2}K under a 2400/h air flow for a ΔT=91°C; this demanded a 3200 W/m^2 specific pumping power and was reached using a 10 mm tall foam of 85% Vp and having 900-1300 μm pore size, infiltrated under a pressure of 3.3 bars. This imeans the invested pumping power was 3.5% of the cooling power, much better than active cooling by other technologies, e.g. thermoelectric elements.

Figs. 6.2 and *6.3* depict the evolution of the thermal efficiency of foams, as elaborated in Section 3.3 (*Eq.3.24*), with the global heat transfer coefficient. Efficiencies higher than one ($\varepsilon \geq 1$) signify that our foams dissipate more heat than

the maximum theoretical value possible under forced convection. We therefore operate under the so called "mixed convection" regime, where our foams dissipate heat both under forced and natural convection. This conclusion is corroborated by the experimental results; under forced convection, a volumetric flow rate of 200 l/h resulted in a global heat transfer coefficient on the order of 100 W/m^{2}K (*cf. Fig.4.9, 4.10 and 4.12)*. Under natural convection, samples of the same characteristics (pore size, height, porosity), *cf Fig.4.3*, had a global heat transfer coefficient on the order of 40 W/m^{2}K for similar ΔTs. Hence, natural convection is not negligible at these volumetric flow rates. It should be noted here that as the volumetric flow increases, ΔT decreases significantly and therefore, heat exchange under natural convection becomes negligible. Precise calculations of how much heat our samples actually dissipate through natural convection are complicated due to two reasons: (i) the hot air flows unhomogenously out of the foam, creating a non-linear gradient at its outer surface and (ii) the mathematical expression describing the mixed convection is not a simple superposition of the two phenomena, since in transversed flows the forced convection is assisted by buoyancy [241]. They are hence left aside in this thesis.

With regard to the efficiency of the samples (depicted in *Figs. 6.2* and *6.3*), as the volumetric flow increaes the efficiency of the foams decreases. This can be attributed to two factors: firstly, at higher volumetric flows the air spends less time inside the foam and therefore, it has less time available to achieve local thermal equilibrium with the metal phase; this has been described in terms of longer saturation lengths. In addition, as the volumetric flow rises, the flow pattern changes and more air passes through the higher and consequently, colder parts of the foam. The latter is also the main reason why taller samples are less efficient than their shorter equivalents. In the matter of microstructure and how it affects the thermal efficiency of the samples, given that the apparent differences between samples are smaller than the experimental error of these measurements, no solid conclusion can be drawn. Note in closing the fact that the top performing foam (900-1300 μm, 85% V_p, 10 mm height and 3.3 bars ilinfitration pressure) has an efficiency near unity also at high volumetric flow rates.

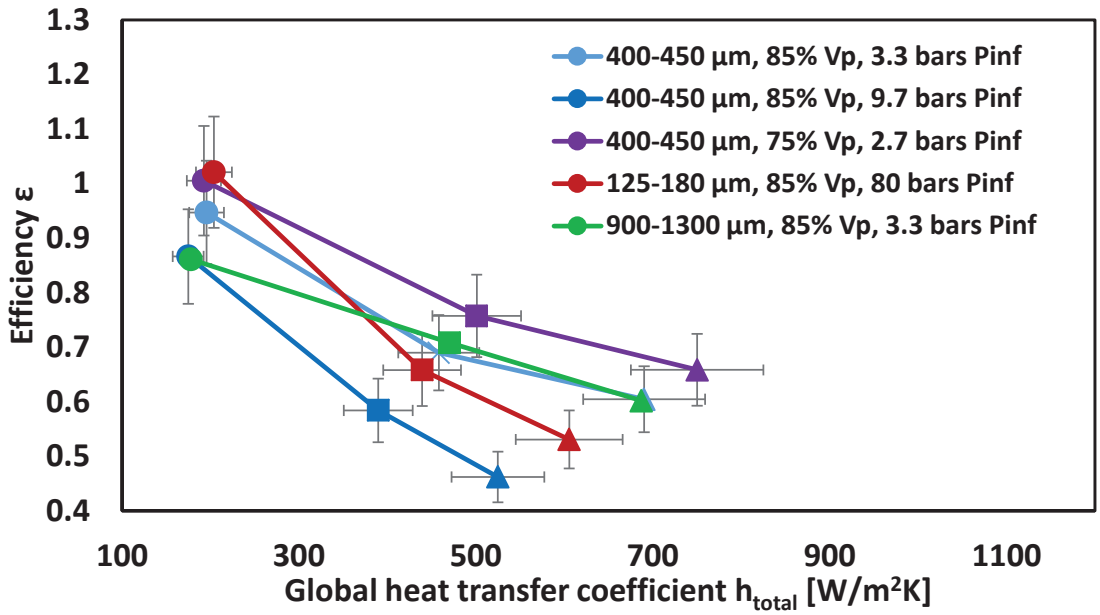

Figure 6.2: Thermal efficiency of 28 mm tall samples under three different volumetric flows: 400, 1400 and 2400 l/h

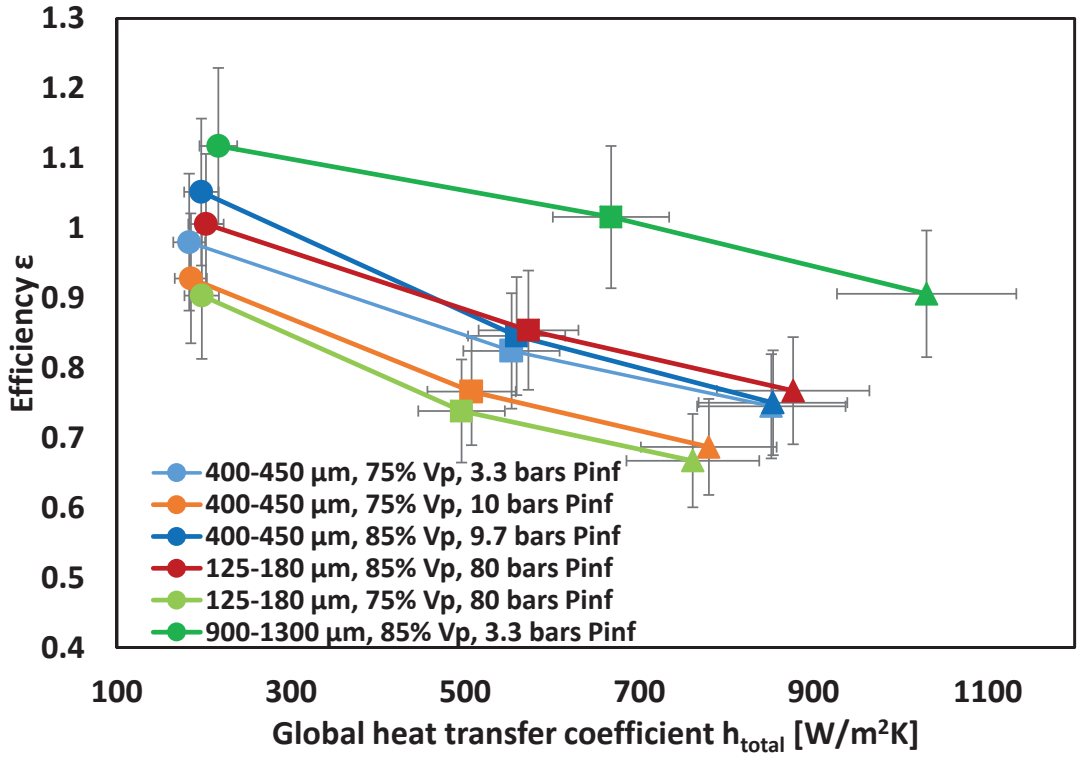

Figure 6.3: Thermal efficiency of 12 mm tall samples under three different volumetric air flows: 400. 1400 and 2400 l/h.

6.3 Fluid flow through the foam

Static pressure measurements inside the central channel of the foam show a rise of the static pressure inside the channel, with lower static pressures at its top and

higher pressures at the bottom of the sample. This is as expected, as the air velocity is expected to have the exactly opposite behaviour, decreasing across the channel and becoming zero at the bottom of the sample. This implies that air does not enter the sample homogeneously; rather the larger part of the flowing air enters inside the foam through its lower part.

The detailed flow pattern of air through the foam depends on the ratio of dynamic to static pressure; the smaller this gets, the closer the flow pattern gets to simply radial. Such a tendency is seen when the microcellular sample has a reduced height (*cf. Fig. 5.7-5.10*) and is expected for smaller pores sizes and lower porosities (the latter influencing both the permeability and the Forchheimer coefficient, *cf. Appendix A*). Such flow patterns resemble to some extent the one known from the confined impingement jet configuration [247], see *Figs. 6.4 and 6.5* from Ref. [247].

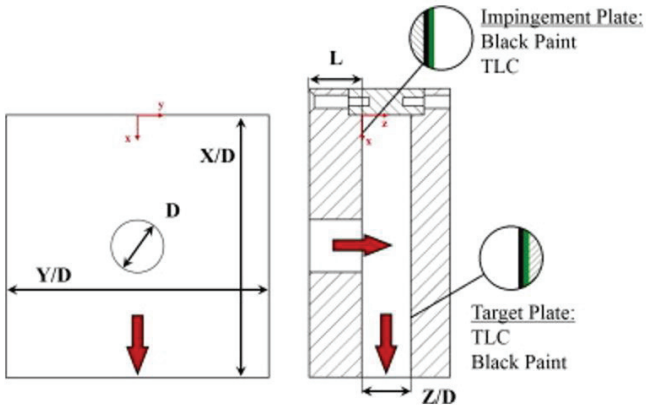

Figure 6.4: Schematic representation of the confined impingement box used in the experimental work of Ref. [247]

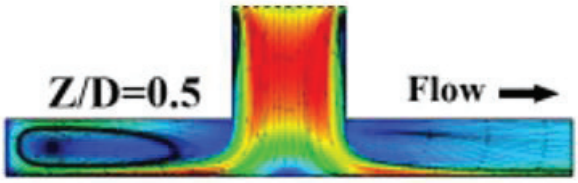

Figure 6.5: Velocity magnitude contours and Stokes streamlines obtained from the CFD results in the symmetry from Ref. [247]

This said, we must note that our experiment has its limitations since the intrusive method that we used to measure the static pressure inside the channel might induce error, as discussed in *Section 3.3.8*, this being a shortcoming often recognized in the literature [234], [239]. Note that the error in these measurements is carried on to our simulations, since the latter use the experimental values of static pressure inside the channel as a boundary condition.

6.4 Thermal performance of the foam

The overall foam performance compared against pin fins, under the jet impingement configuration, *cf. Fig. 4.18 and 4.29*, indicates that both structures have a comparable heat extraction capacity. The maximum global heat transfer coefficient we have reached using foams is 1030 W/m^{2}K under a volumetric air flow of 2400 l/h and a ΔT of 91°C which demands 3210 W/m^2 as a pumping cost—this was achieved using a 10 mm tall foam with 85% V_p and 900-1300 µm pore size, infiltrated under a pressure of 3.3 bars. Pinned fins under a volumetric air flow of 2480 l/h produced a global heat transfer coefficient of 788 W/m^{2}K at a ΔT of 100°C, demanding a pumping power of 3720 W/m^2. Thus, foams need to be optimised in order to outperform pin fins, but can achieve this (note that pin fins are the fins with the best performance in the impingement jet configuration [248]). Taking into account that the overall cost of machined fins is significantly smaller than the current manufacturing cost of metal foam products, metal foam geometries might, however, need to be further investigated and improved, in order for them to replace fins in engineering practice.

Comparing our own results to those published in the literature is a difficult task, since different groups use different configurations with different fluids, at different mass flows, temperature ranges and foam materials and often report different physical quantities, e.g. the global heat transfer coefficient, the local heat transfer coefficient, the global Colburn factor, the local Colburn factor, the overall thermal resistance, the ratio of dissipated heat per pumping power, the Number of Transfer Units (NTU), the local temperature of the sample, the global temperature of the sample, the efficiency of the foam, the global Nusselt coefficient, the local Nusselt coefficient etc. Additionally, where non-dimensional numbers are used, two issues are often met: the first, already pointed out in the literature review, is that different authors use different characteristic lengths, therefore making the comparison of even the same dimensional numbers, such as the Reynolds or the Nusselt number, burdensome. The second is that not all contributions in the literature provide all dimensions needed to extract different physical quantities from the relevant non-dimensional numbers, preventing thus a comparison with other works. Nonetheless, a short comparison could be produced, using data from research groups who reported all relevant dimensions; *Figs. 6.6 and 6.7* juxtapose our results with results from other working groups, where the highest reported value of the global heat transfer coefficient from each reference is plotted, and reproduce illustrations of heat exchanger designs used in those references.

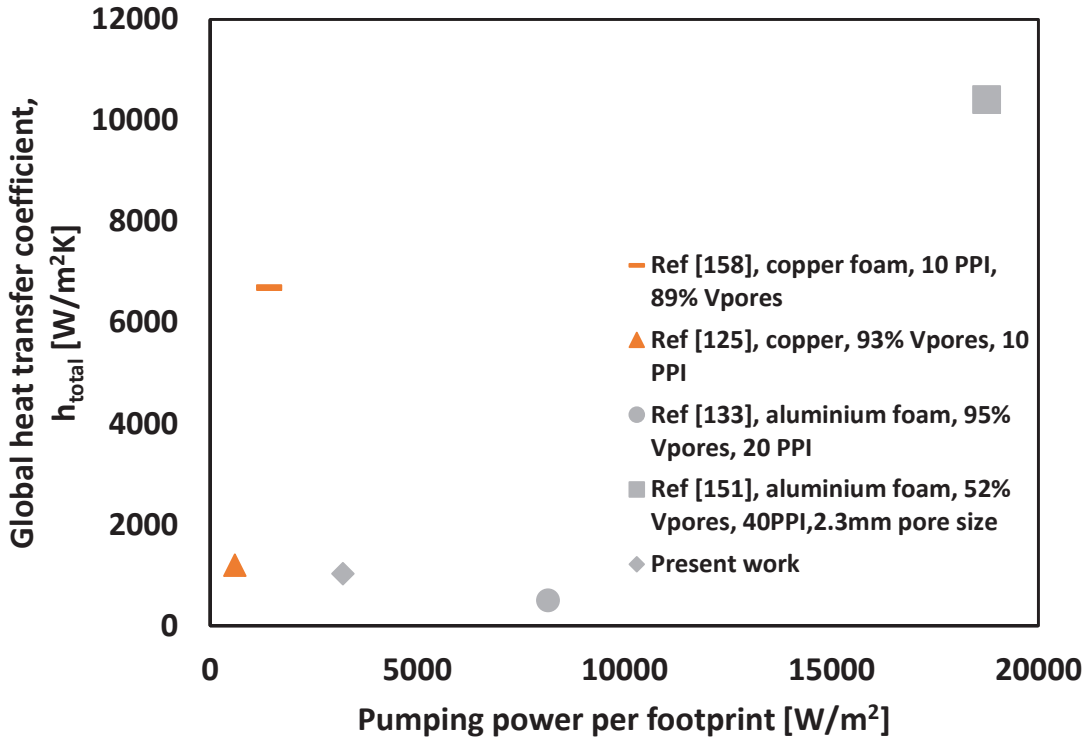

Figure 6.6: Comparative presentation of other studies with regard to the global heat transfer coefficient of foams: silver colour stands for aluminium foams and orange for copper. [125],[133],[151], [158].

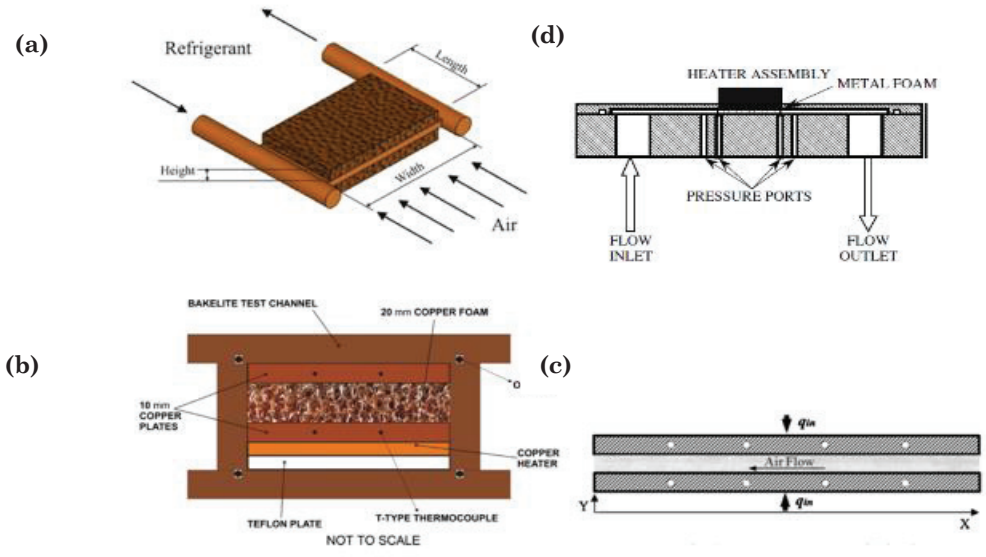

Figure 6.7: Schematic representation of the testing configurations used in the work whose results are summarised in *Fig.5.4. a) description in* [158], *b) description in* [125] , *c) description in* [133], *d) description in* [151]

As shown in *Fig. 6.6*, our configuration appears to be capable of achieving heat transfer coefficients of the order of 1000W/m^{2}K using air at a relatively low pumping cost per footprint. This can be attributed to the central channel of our samples, allowing air ejected from the nozzle to arrive at the lower and hotter part of the foam, increasing the heat dissipation without the need of a lengthy heat exchanger. This behaviour is supported by the simulations results and will further be analysed in the discussion of the theoretical model results. It should be noted here that our configuration can stand improvement; since the majority of the pressure drop comes from the release of kinetic energy in the air, a larger channel in the middle of the foam or the use of multiple inlets should result in an improved performance.

The exact orientation of each configuration seems to significantly influence its thermal performance: a rectangular foam footprint has a different cooling performance and pressure drop depending on whether air is pressed through in the direction of the long or the short side. In all cases, the above comparison uses the orientation used by the researchers in the original paper.

The fluid medium appears to play an important role; configurations using air have similar results in both terms of heat transfer and pumping power. Reference [125] has smaller pressure drops since foams with larger pore sizes (Duocel™) were used. In addition, the higher thermal conductivity of copper might have been of benefit, producing a higher rate of heat dissipation despite the use of the standard configuration technique (placing the heat source below the foam and having a horizontal homogeneous flow across the length of the foam, does not maximise the heat extraction through the foam). Reference [151] used compacted aluminium foam, and its high pressure drop-high heat transfer results are due to the liquid mixture that was used as a fluid medium. Liquids have a much higher density and thermal capacity than air, enabling them concurrently to dissipate more heat at a higher pumping power cost, the latter as an outcome of the increased dynamic viscosity of liquids when compared to gases. Reference [158] reached high heat transfer rates at low pressure drop because the foam was used to condense the fluid R600 via air cooling; the phase change of the fluid medium increases the heat exchange between the foam and the environment. Note that the last two studies cases, the existence of a closed circuit to collect the liquid and the vapour is required, which calls for a more complex set-up.

6.5 The theoretical model: confontration with experiment

6.5.1 Flow field

Simulation results imply, as shown in *Fig. 5.3-5.14*, that most of the air flows through the lower part of the foam, similar to other confined jet configurations [247]. The effect is stronger for taller samples and less intense for smaller heights, where the flow is more homogeneous. The physical reason for this is that the central channel is blocked at the bottom of the sample, forcing the air to escape sideways. This backpressure deploys its effect also further up in the central channel but is strongest in the lowest part. Presented differently, one can alternatively link this to the static pressure distribution in the central channel as

reported in *Fig. 4.32-4.36:* the highest static pressure is at the bottom of the central channel and hence the largest radial flow rate is also found at the bottom, i.e. z=0.

The recirculation predicted by simulations has been reported in other studies using foams under impingement configuration [206] or in works studying porous media under the impingement jet configuration [207]; The recirculation is larger for foams of higher permeability and increases with the Reynolds number, in agreement with other studies [206]. The latter grows from 5% of the overall volumetric flow for 400-450 μm and 28% for 900-1300 μm pores size at low volumetric flows to 35% and 40% of the overall volumetric flow respectively, at 2520 l/h. Despite the decrease in the required pumping power, since practically foam sucks the air from the nozzle into the central channel, this behaviour is expected to have a detrimental effect on heat transfer, as it preheats the incoming air before it reaches the bottom of the sample, and therefore decreases its capacity to absorb heat from the hottest part of the structure in the bottom part of the heat exchanger. On the other hand, recirculation seems to help the fluid to reach the metal temperature for larger pore sizes, indicating that its effect on the overall thermal behaviour of the foam is a complicated matter.

6.5.2 Temperature field and heat extraction

In order to benchmark our model, experimental measurements of the metal and gas temperature taken at the outer periphery of our sample, as described in *Section 3.3.7* were collected. One of the goals was to verify that the interpolation constants used in the local Nusselt correlation (*Eqn. 5.23*) are consistent with the present data.

Figures 6.8 to 6.12 compare experimental and simulated results for foams of 28 mm height, 85% V_p and 400-450 μm pore size, under various volumetric flows. As seen, our model is in fairly good agreement (the relative error is typically <25%). With regard to the global heat transfer coefficient (*Eqn.5.24*), the model correctly predicts the values, the trend and the slope for three of the volumetric flow rates; for the highest volumetric flow rate, however, the model gives too low a value. A possible explanation for this could be error in the static pressure measurements at this high flow rate.

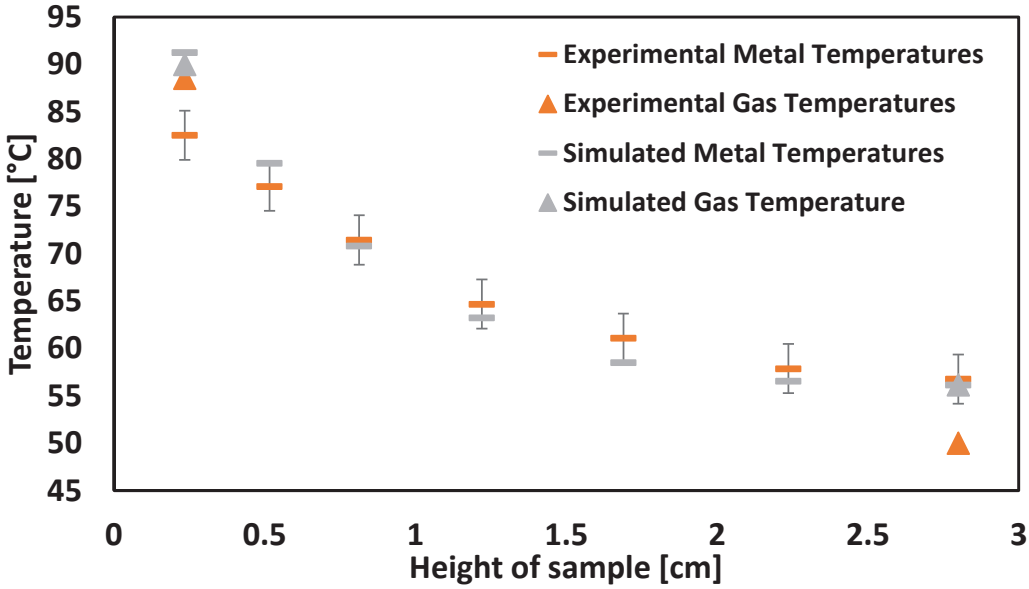

Figure 6.8: Evolution of the surface temperature of the aluminium foam (400-450 µm, 85% V_p) and the outflowing air under a 2520 l/h air flow rate as a function of the distance from the heated surface.

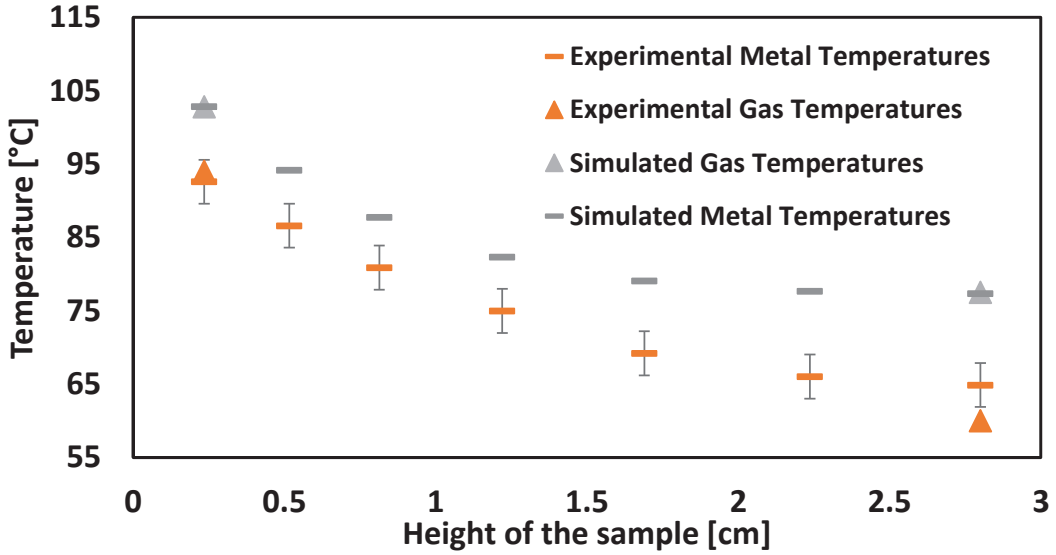

Figure 6.9: Evolution of the surface temperature of the aluminium foam (pore size 400-450 µm, 85% V_p) and the outflowing air under a 1800 l/h air flow rate as a function of the distance from the heated surface.

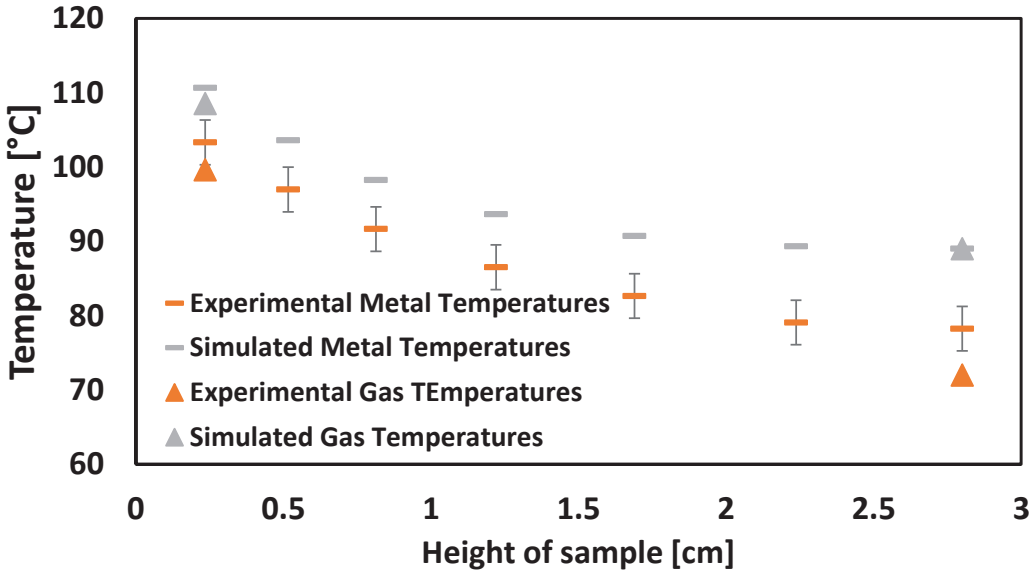

Figure 6.10: Evolution of the surface temperature of the replicated aluminium foam (400-450 µm, 85% V_p) and the outflowing air under 1260 l/h air flow rate as a function of the distance from the heated surface.

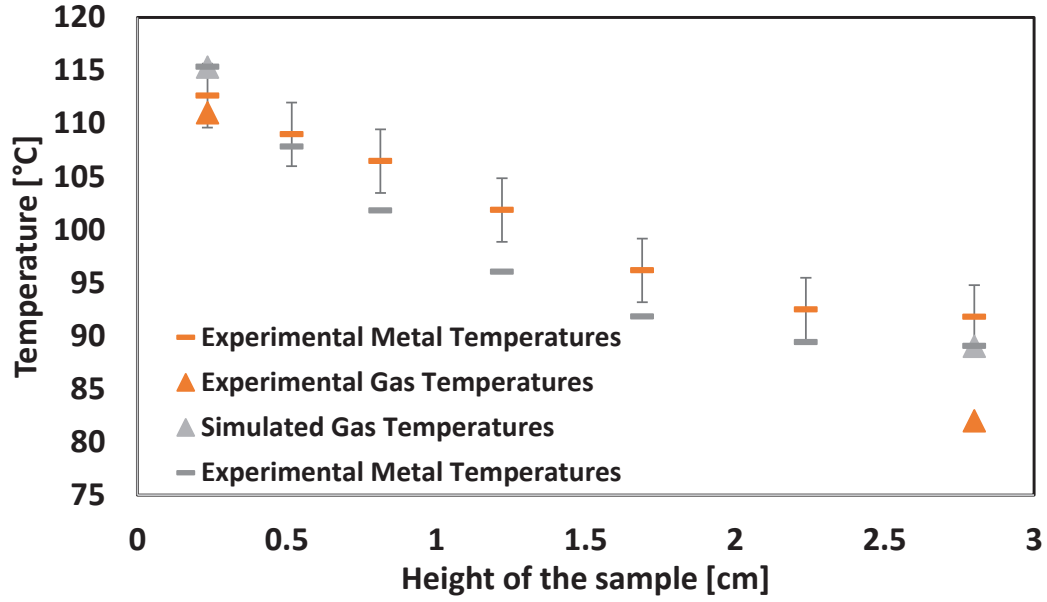

Figure 6.11: Evolution of the surface temperature of the aluminium foam (400-450 µm, 85% V_p) and the outflowing air under a 720 l/h air flow rate as a function of the distance from the heated surface.

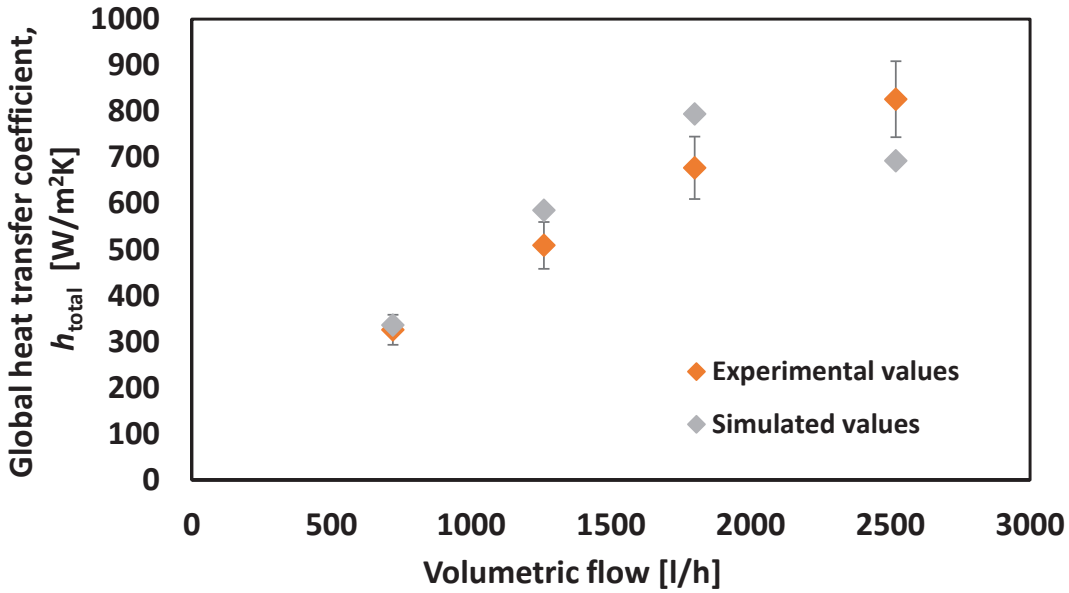

Figure 6.12: Evolution of the global heat transfer coefficient of the replicated aluminium foam (400-450 µm, 85% V_p) under various air flow rates for both experimental and simulated results.

Figures 6.13 to 6.17 juxtapose again simulated and experimental results for a foam of 28 mm in height, 85% V_p and 1100 µm pore size, under various volumetric flows. As in the previous case, despite our model correctly predicting the decrease in the temperature of both phases, we overestimate the metal and gas temperatures; this overestimation occurs for all flow rates and equals roughly 30% (typically d_{solid}, $d_{fluid} \leq 1/3$). Moreover, the global heat transfer coefficient, *cf. Fig.6.17* is also overestimated by 23% to 100%, the latter value obtaining for very small flaw rates. Attempts to solve this discrepancy by altering the interpolation constants in the local Nusselt correlation (*Eq.5.24* in *Chapter 5*) did not lead to a better result; therefore, we do have a significant discrepancy between experimental results and predictions of the numerical model.

A possible explanation for this discrepancy is with the boundary conditions inside the central channel, which could be better defined if a more sophisticated fluid flow model was used (the present model calculates the fluid flow pattern based on the pressure drop measurements across the static channel, which have some degree of error, induced by notably the measurement probe). The latter is coherent with the increased overestimation of the global heat transfer coefficient in *Fig. 6.17*, indicating that also our radial velocities might be overestimated due to an understimation of the static pressures. Additionally, recirculation as predicted by the model influences the set boundary conditions inside the channel in a dual way: (i) the air in the central channel is likely not to be at ambient temperature, since part of the air flow has recirculated and thus been preheated by the foam (up to 40% of the air for the highest volumetric rates) and (ii) the mass flow rate inside the central channel is higher than what is assumed in the model, since to the original flow the recirculated air is added. Both issues do exist also for the 400-450 µm simulated case; nevertheless, as with the pressure drop measurements, the discrepancy this creates scales with the pore size: a smaller pore size means a

higher pressure drop through the foam. In *Figs.6.18 and 6.19* we performed a sensitivity analysis for both foamed samples, for the 2520 l/h air flow rate. The latter is the most extreme case, with the highest dynamic pressure and consequently, the highest level of error. The sensitivity analysis was done by adding and subtracting the estimated level of experimental error of static pressure measurements: as seen, its effect is noticeable.

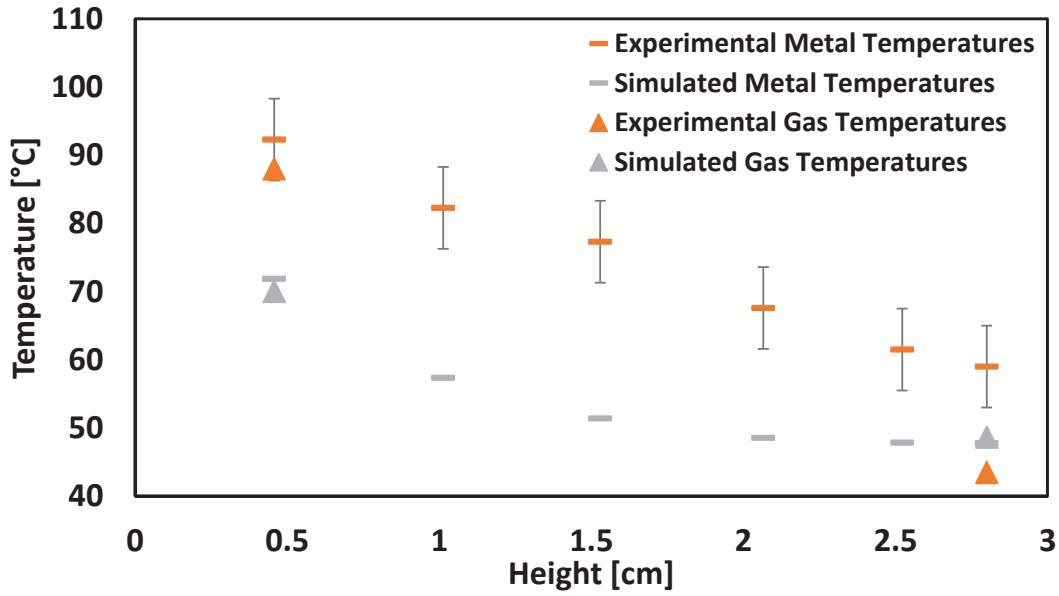

Figure 6.13: Evolution of the surface temperature of the aluminium foam (900-1300 µm sea salt, 85% V_p) and the outflowing air under a 2520 l/h air flow rate as a function of distance from the heated surface.

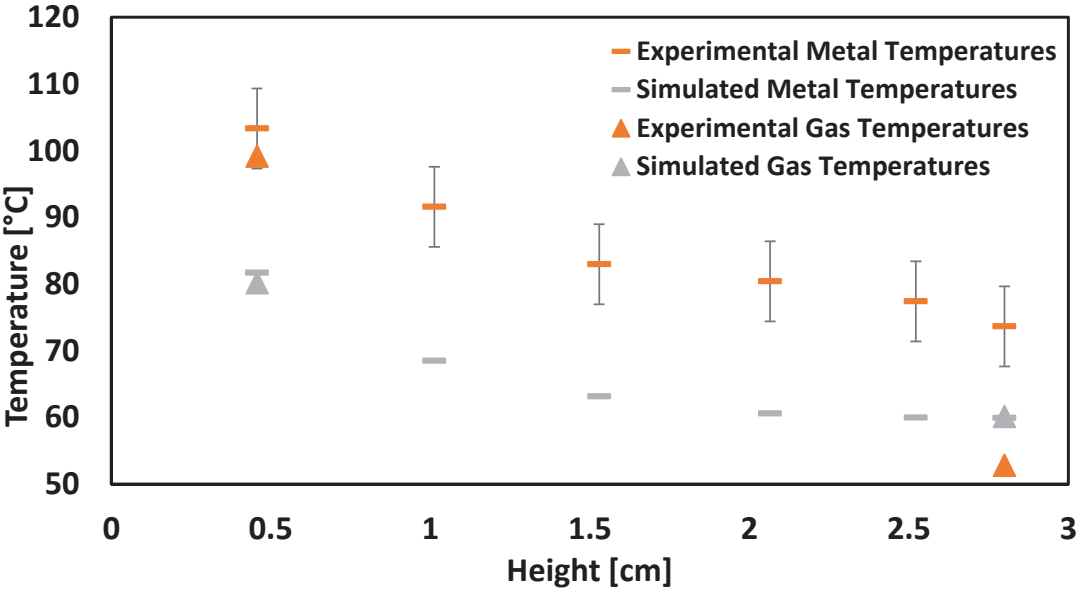

Figure 6.14: Evolution of the surface temperature of the aluminium foam (900-1300 µm sea salt, 85% V_p) and the outflowing air under a 1800 l/h air flow rate as a function of distance from the heated surface.

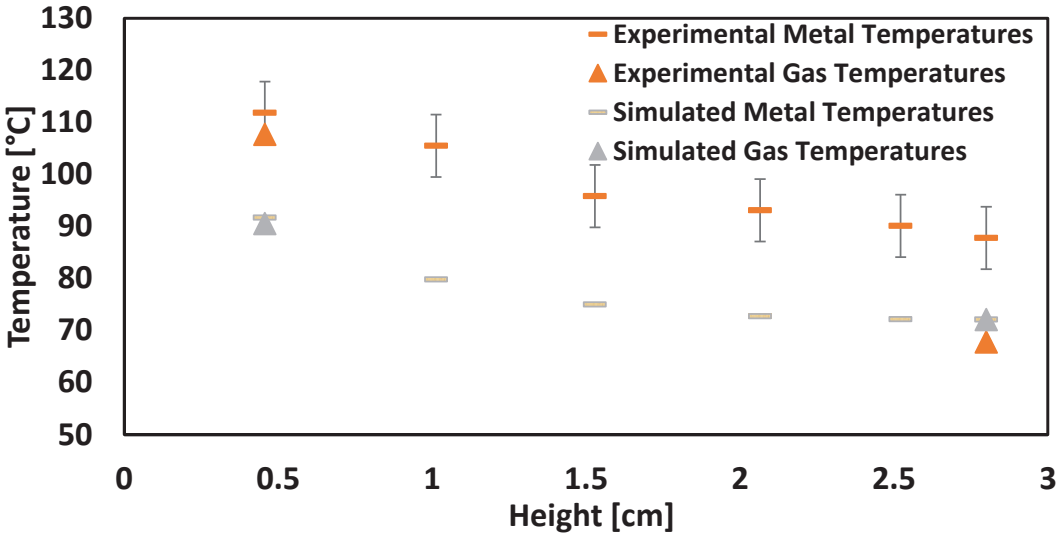

Figure 6.15: Evolution of the surface temperature of the aluminium foam (900-1300 µm sea salt, 85% V_p) and the outflowing air under a 1260 l/h air flow rate as a function of distance from the heated surface.

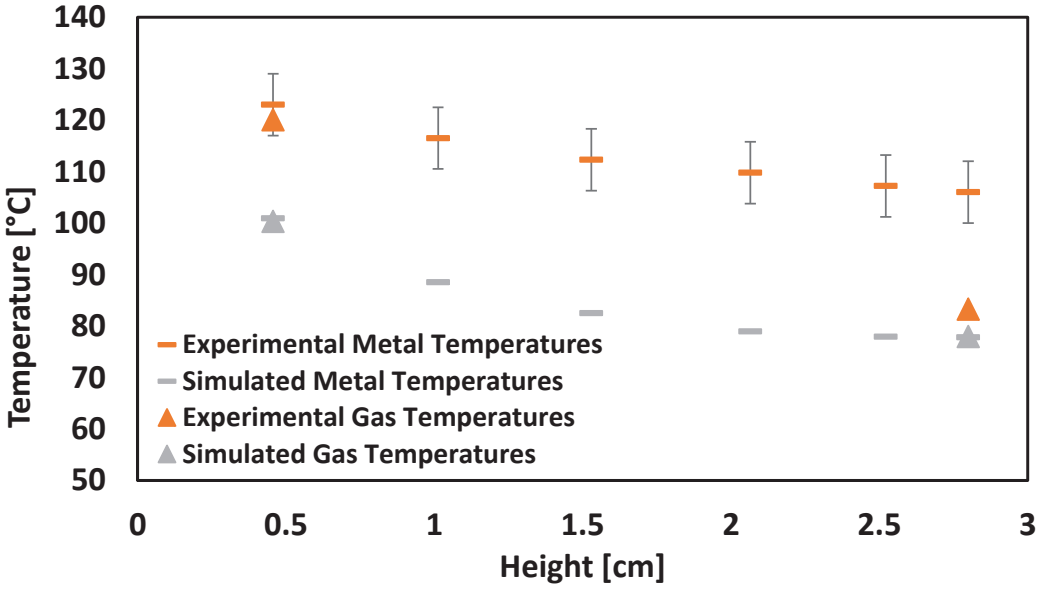

Figure 6.16: Evolution of the surface temperature of the aluminium foam (900-1300 µm sea salt, 85% V_p) and the outflowing air under a 720 l/h air flow rate as a function of distance from the heated surface.

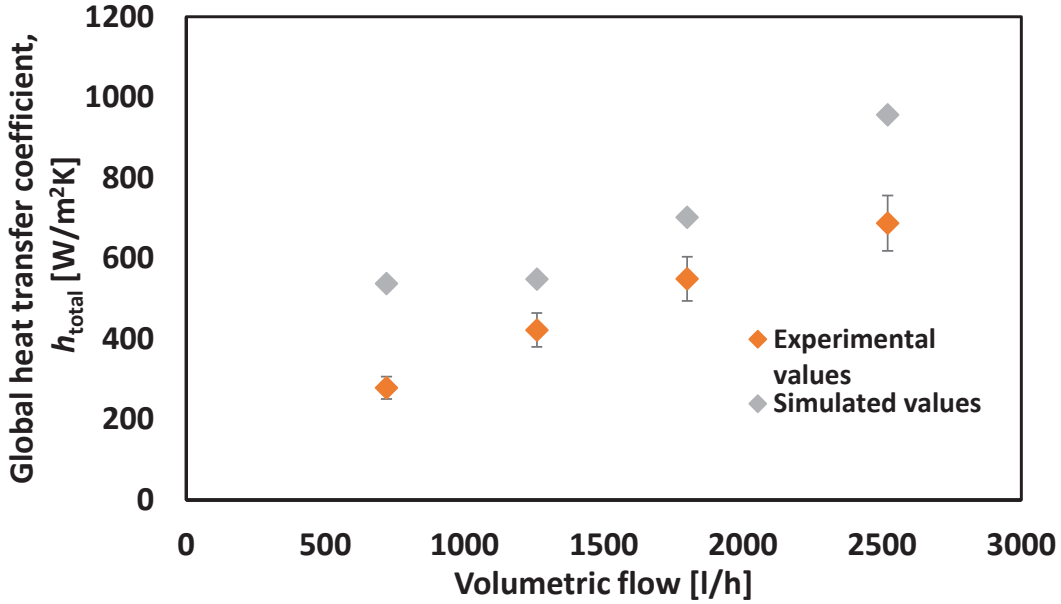

Figure 6.17: Evolution of the global heat transfer coefficient of the replicated aluminium foam (900-1300 µm sea salt, 85% V_p) under various air flow rates for both experimental and simulated results.

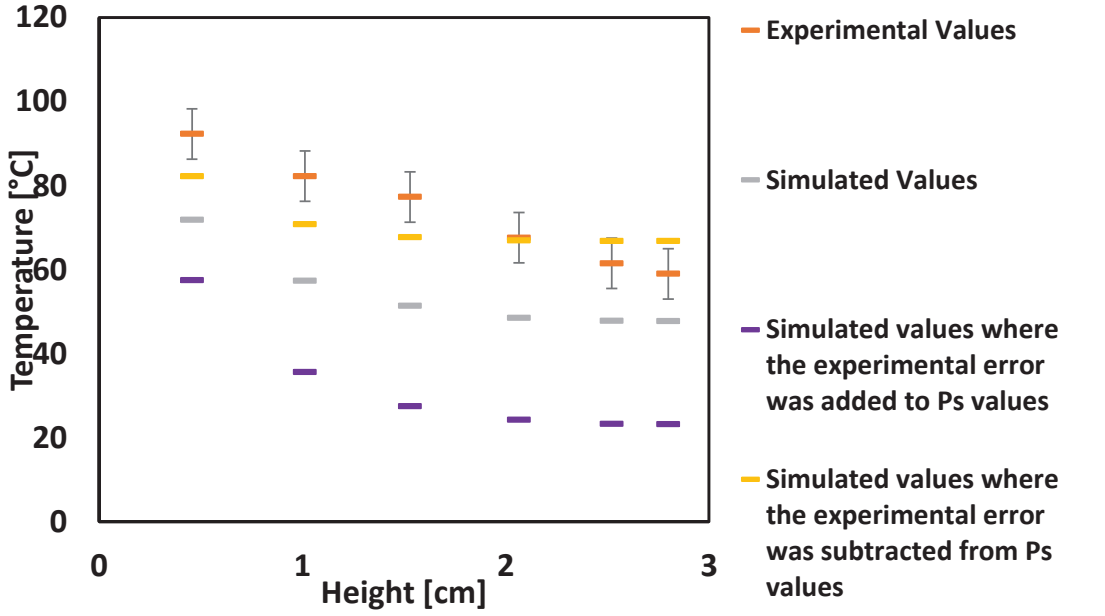

Figure 6.18: Sensitivity analysis for the replicated aluminium foam (900-1300 µm sea salt, 85% V_p) under 2520 l/h air flow rate. The experimental error was added and subtracted to the measured static pressure values inside the central channel.

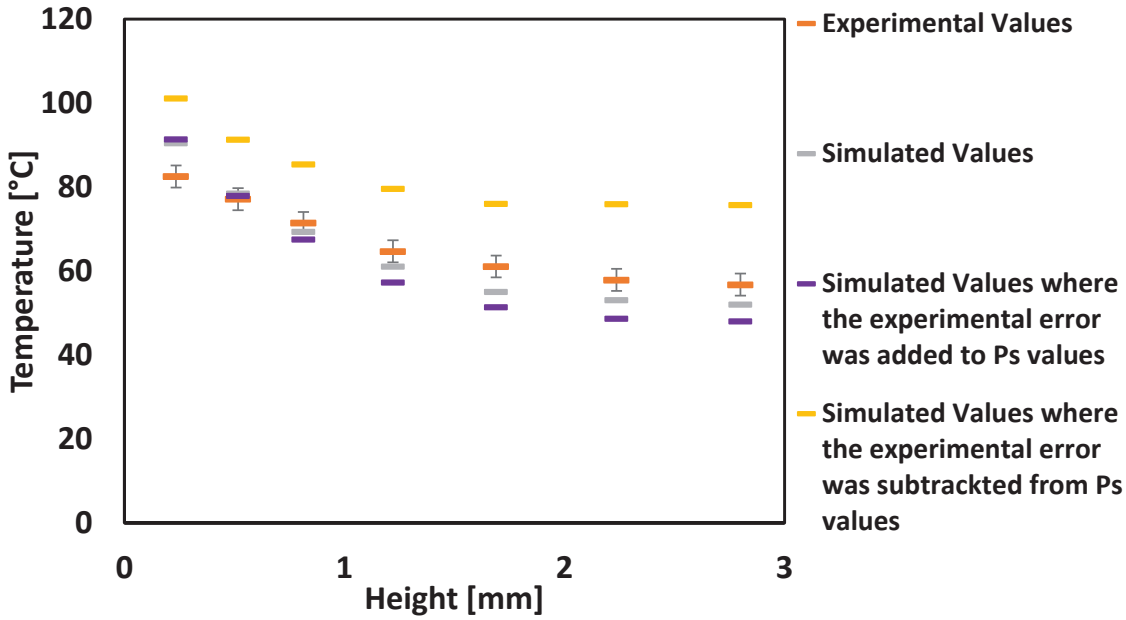

Figure 6.19: Sensitivity analysis for the replicated aluminium foam (400-450 μm, 85% V_p) under 2520 l/h air flow rate. The experimental error was added and subtracted to the measured static pressure values inside the central channel.

Finally, the solid and fluid temperature fields as calculated by the model, *cf. Figs 5.4 -5.14*, indicate that in the region closest to the central channel (the first 5 mm), the temperature difference between the air and the metal foam is non-negligible. This comes in contrast with the often-used hypothesis of Local Thermal Equilibrium (LTE) when studying heat transfer in porous media [249]–[251]. The use of the LTE assumption can lead to significant error [183], [252], its validity depending on the size of the boundary layer, the mean pore size, the interstitial heat transfer coefficient, the exact geometry and thermophysical properties of the foam (i.e. conductivity, permeability, etc.)[249].

In order to further demonstrate the existence of Local Non Thermal Equilibrium for our system, *Figs. 6.20 to 6.22* plot the temperature difference between the metal and the fluid phase for two different volumetric flow rates, namely 720 and 2520 l/h, for three selected volumetric flows. As seen, the difference between the two phases near the central inner channel can exceed 50°C for the 400-450 μm foams and is higher than 10°C for the 0.9-1.3 mm foams. The greater temperature difference between the two phases for foams of smaller pore size can be explained by the flow field: as the permeability decreases with the pore size, the bigger portion of the cooling air flows through the lower part of the foam. Since air flow is concentrated at this specific region, more heat is needed to bring the gas and the metal in thermal equilibrium. Foams of greater pore size (and consequently, of higher permeability) allow for a more homogeneous distribution of the air mass inside the foam and therefore, a more homogeneous temperature difference between both phases is achieved. This argument can be supported by *Figs. 5.3(e) to 5.14(e)*; the greater the pore size, the more homogeneous the radial component of the velocity (for a given volumetric flow rate). The weaker radial temperature difference between the two phases across the height of all foams at higher flower

rates can be attributed to the colder metal phase near the central channel region which, hence, is closer to the temperature of the fluid.

To recapitulate, the existence of the central inner channel has both advantages and disadvantages. It increases the thermal efficiency of our foams by allowing air to reach the lower and therefore hotter end of the foam, and keeps the overall pumping operating cost reasonably low; the latter occurs since the air arrives at the lower part of the foam without having to pass first through a porous area. Yet again, this design tends to augment recirculation and makes numerical modeling a challenging task given the complex static pressure distribution over the region where air enters the foam.

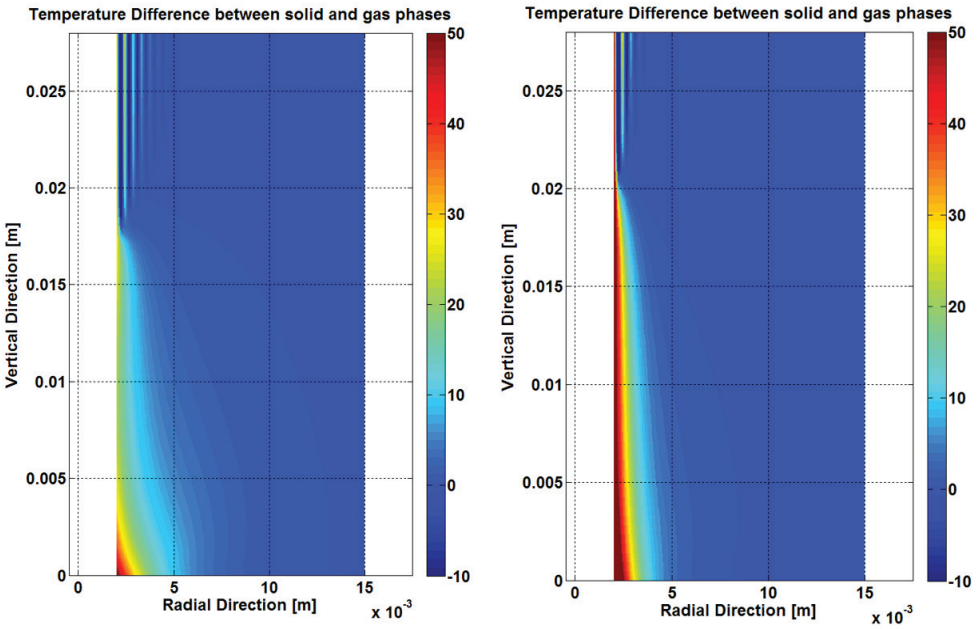

Figure 6.20: Temperature difference between the metal and air for a 28 mm tall replicated aluminium foam (400-450 µm, 85% V_p) under 2520 (left) and 720 l/h (right) air flow rate.

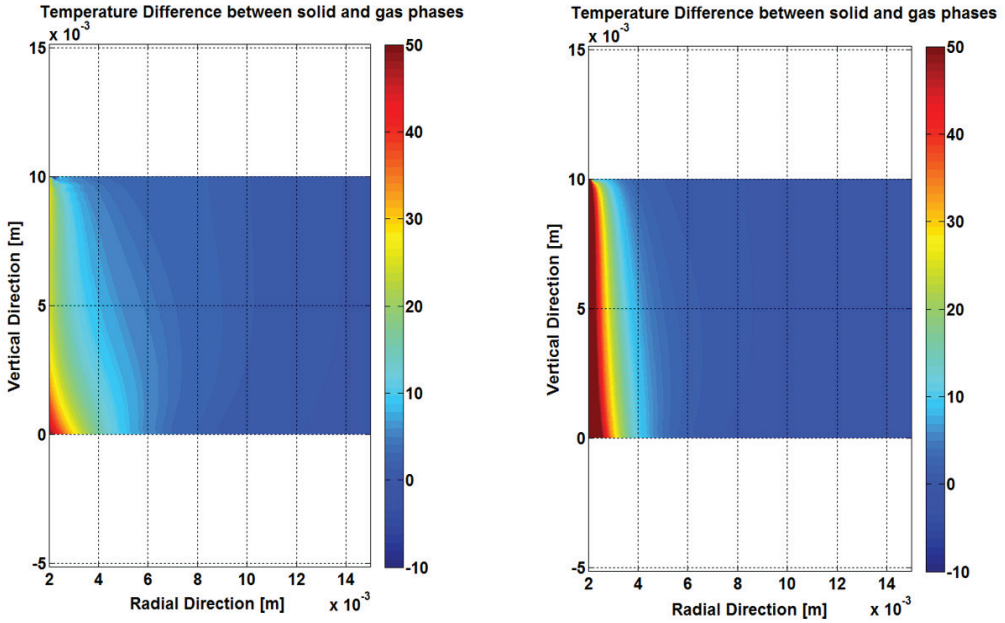

Figure 6.21: Temperature difference between the metal and air for a 10 mm tall replicated aluminium foam (400-450 µm, 85% V_p) under 2520 (left) and 720 l/h (right) air flow rate.

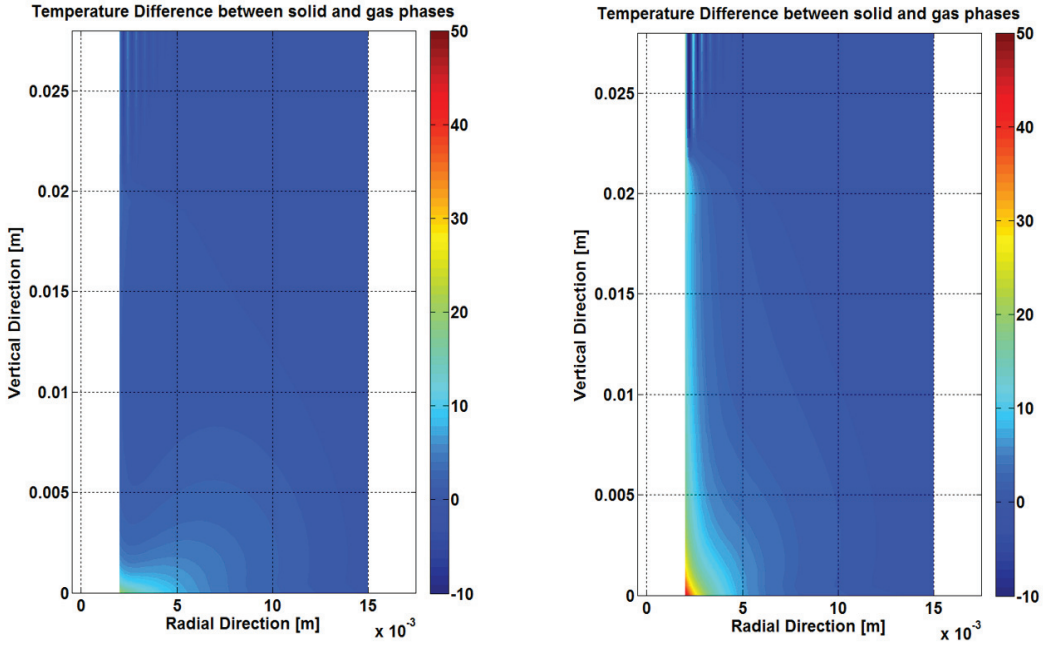

Figure 6.22: Temperature difference between the metal and air for a 28 mm tall replicated aluminium foam (900-1300 µm, 85% V_p) under 2520 (left) and 720 l/h (right) air flow rate.

6.6 The Integrated Structure

An integrated structure, consisting of one layer of aluminium diamond composite, one layer of AlN and one layer of replicated aluminium foam, described in *Section 3.4*, was fabricated successfully in one step. This structure is free of thermal interfaces produced by brazing or by contacting surfaces bridged by thermal

grease. The manufacturing process of the structure is clearly made more complicated by this integration, and bringing fabrication costs to an acceptable level for commercial applications will require significantly more work [22]: the manufacturing process used here is cumbersome and challenging. The composite has to be infiltrated inside costly graphite moulds, whose removal in order to recover the piece is not always easy. Moreover, since the uniaxial pressing of the salt particles takes place using a steel mould, whose surface is hard, the outer surface of the salt preform is less porous compared to preforms produced using a Cold Isostatic Pressing procedure. This not only obliges us to infiltrate the packed bed at higher pressure, but also affects the outer surface of the replicated foam, giving it a less porous external surface. Additionally, directional solidification of the composite is necessary, in order to prevent formation of porosity due to solidification shrinkage in the infiltrated body of compressed salt inside the graphite moulds.

The manufactured integrated heat sink was tested under an impingement jet configuration, using the same apparatus as that in which replicated foam samples were also tested. Results (*c.f. Figs. 4.37* and *4.38*) demonstrate a comparable behaviour for the integrated structure and a foamed sample of similar characteristics. Both specimens need roughly the same pumping power for a given volumetric flow rate but the simpler foam sample dissipates more heat by ~25%, with 10% being our experimental uncertainty.

The reasons for this discrepancy are not perfectly clear to us as a number of factors might have influenced the final outcome of the experiment. Firstly, the foamed part of the integrated structure is less porous (80% V_p) than the foamed part (85% V_p), a factor that was shown to affect the thermal behaviour: less porous replicated aluminium structures dissipate slightly less heat. Secondly, the simple metal foam sample was fabricated using a different route— the NaCl preform for the simple foam specimen was produced using cold isostatic pressure, whereas the integrated structure had its metal foam part manufactured using uniaxial compression of the salt grain preform. This different production route might affect the microstructure and consequently, affect the local fluid flow and/or heat transfer rate. Thirdly, the infiltration pressure was different for both specimens; 15 bars for the integrated structure and 3.3 bars for the foam sample: as previously discussed, higher infiltration pressures have a negative effect on the thermal behaviour of replicated metal foams. Together, all these factors can influence the final outcome to a significant degree.

Since the pumping power comes essentially from the acceleration of the air and the pressure drop in the foam is small compared to the Bernouilli term, this means that the influence of the above factors is less important as concerns the pumping power.

Notwithstanding the above mentioned findings, this experiment is successful in its main goal: to prove the feasibility of fabricating an integrated structure: i) near net-shape and in one step, ii) amenable to being brazed on top of an IGBT and iii) having significant capabilities in dissipating heat at low pumping cost.

Chapter 7 Concluding Remarks

7.1 Summary of present work

The present work has sought to explore replicated aluminium foams as a part of an integrated heat sink manufactured in one step that seamlessly combines metal and ceramic phases. In particular, we sought to understand the influence of foam characteristics (pore size, porosity) on fluid transport across and heat transfer out of the foam sample. The results of this study could help to develop better heat sinks for power electronics. The following list is a brief summary of the achievements that have been accomplished:

- A testing apparatus was built in house to test these foams; this apparatus heats the samples from the bottom and uses the "guarding wall" technique, is capable of testing the thermal behaviour of foams both under natural and forced convection, the latter under the impingement jet configuration.

- Under natural convection, we tested replicated Al foams of different pore sizes (125-180 µm, 400-450 µm and 5mm), porosities (between 75 and 85%) and geometries (near flat, cylindrical and finned structures). Furthermore, we additionally tested a sample before, during and after the leaching process to investigate how each step influences its thermal behaviour.

- Using the jet impingement configuration, we tested replicated Al foams of different pore sizes (125 µm to 1.3 mm), porosities (75-85%), height (28 and 10 mm) and infiltrated at different pressures. All of the foams had a central channel in the middle of the sample in order to guide the cooling air until the lower and therefore, hotter part of the structure. Global (footprint) heat transfer coefficients were calculated and plotted against volumetric flow and pumping power per footprint.

- Using aluminium foams, the maximum global heat transfer coefficient we have reached is 1029 W/m^2K under a 2400/h air flow, under a $\Delta T=91°C$; this demanded a 3200 W/m^2 pumping power per footprint and was reached using a 10mm tall foam of 85% V_p and having 900-1300 µm pore size, infiltrated under a pressure of 3.3 bars. The pumping power was hence roughly 30 times smaller than the extracted power.

- In a separate test rig, the static pressure inside the central channel of the foamed foams was measured at room temperature for different heights and pore sizes. Two different microcellular aluminium types were tested: The first category of height 5, 15, 20 or 28 mm, a 400-450 µm pore size, an ~82% volumetric porosity V_p and the samples were infiltrated at a pressure of 3.4 bars. The second sample, had a 900-1300 µm pore size, a ~83% porosity, a 28 mm height and the samples were infiltrated at a pressure of 4.4 bars.

- A theoretical model, using the finite-volumes technique was used to elucidate how the various parameters influence the heat transfer. The model was based on the Darcy-Forchheimer formulation of fluid flow in porous media, which is

then coupled to a convective/conductive heat transfer model of the same structure. These simulations were used to perform parametric studies on the influence of height and pore size with regard to the thermal behaviour of replicated foams.

- We successfully manufactured an integrated multimaterial structure and we tested it under forced convection, using the same conditions as the replicated aluminium foams

The major conclusions of this thesis can be summarised as follows:

Under natural convection:

- The thermal behaviour of microcellular samples did not differ significantly from the thermal behaviour of their equivalent bulk solids; any difference was within the range 10%-15%, i.e. slightly above our experimental error. Variations in microstructure (different porosity or pore size) or geometry within the examined range in this thesis did not seem to influence the final result.

- Testing the thermal behaviour of a sample before, during and after the leaching process showed that our samples breathe air up to depth one cell depth size, which explains the above conclusions.

Under forced convection:

- The microstructure and the exact geometry of the foam were both found to influence the final performance of microcellular air-cooled metal heat exchangers. The exact extent depends on the given volumetric flow and the other characteristics, e.g. the infiltration effect was stronger for taller samples. More analytically:

- Higher porosity influences positively both heat dissipation (up to ~10%) and pressure drop (up to ~40%); the effect was found to be more profound for the taller samples. While the explanation for the lower pressure drop lies with the higher Darcian and Forhheimer permeabilities of foams, the exact reason behind a better thermal behaviour due to a higher porosity, has to be further clarified.

- Lower infiltration pressures are beneficial in terms of both heat dissipation (up to ~25%) and pressure drop (up to ~5%). The exact reason behind this phenomenon is not identified; however many causes exist (lower local thermal conductivity, lower permeability, air stagnantion).

- Larger pore size affects positively the heat transfer (up to 15% within the tested range in the present thesis) and the pressure drop (up to 3 times lower), the former in a rather not sufficiently clear way. Literature attributes this effect to the thickness of the ligament and the thermal saturation of the cooling fluid. We advance a further explanation, based on the form of the flow

field. In all cases, this corroborates the claim that an optimum pore size must exist which will depend on the overall size of the sample.

- Height dominates the thermal behaviour of replicated aluminium foams, with lower foams dissipating more heat (up to 35%) at the cost of a much increased pressure drop (up to 30%). Reasons for the higher thermal efficiency could be the higher average temperatures of shorter samples and the induced recirculation that takes place in taller samples. This concurrent increase also indicates that the height of foams used in this configuration can be optimised.

- Foams under the impingement jet configuration have a thermal behaviour similar to pin fins. In order to achieve far better thermal results than the standard pin configurations, optimization of the foam properties should take place.

- The static pressure inside the central channel of the foamed foams was measured at room temperature for different heights and pore sizes. It was found to decrease with the height, indicating that air does not enter the sample homogeneously; rather the larger part of air enters inside the foam through its lower part.

- Agreement between the 2-D CFD simulations and the experimentally measured external temperatures of both foam phases was reasonably accurate (within the range of 1/3) whereas agreement with the heat transfer measurements was not as good as the external temperatures. The phenomena observed in these CFD studies, such as recirculation of air in taller samples may explain our experimental findings.

- The fabrication in one step of an integrated multimaterial composite substrate of metal and ceramic comprising three stacked layers, is feasible but yet cumbersome and challenging.

- The thermal behaviour of the said integrated structure is close to that of foam sample of similar characteristics, demonstrating that it can be used to effectively cool power electronics in the automotive industry.

7.2 Suggested Future Work

Several possible avenues for future research could lead to further understanding of forced convection phenomena in replicated aluminium foams and the consequent improvement of integrated structures acting as heat sinks:

- The geometry of foams could be further optimized. In the present work, it was found that the most important feature is their central hollow channel, which significantly influences the level of the pressure drop and heat dissipation. Performance improvements could likely be achieved by enlarging this diameter and therefore inducing smaller pressure drops. Additionally, the overall thickness of the foams could also be examined to understand how it affects the foam thermal efficiency.

- The nozzle's characteristics could also be optimised. The exact shape of the cross section of the nozzle and its distance from the bottom influence the fluid flow and consequently, might be used to achieve an increased thermal dissipation for the same pressure drop.

- Another direction for future work is to further characterize the flow field inside foams using smoke. The field of smoke as the air exits the foam could indicate the flow path, helping us improve our understanding of the fluid phenomena inside the foam and to further validate the numerical model.

- Additional CFD studies are warranted based on the agreement of some of the benchmark tests in the present work. More sophisticated studies such as LES simulations could lead to insight into the microscale phenomena (e.g. vortices into the central channel) inside the sample and the recirculatory zone.

- A model that accurately predicts the pressure inside the central channel without the need of experimental values would be useful because it would allow a more precise description of the flow field inside the channel without the use of an intrusive pressure measurement method.

- In the design of multilayer integrated structure, the fabrication method could be facilated by using salt moulds which could be leached and hence easily allow the extraction of the manufactured structure.

Chapter 8 Appendix

Appendix A: Estimation of the permeability and Forhheimer coefficients of Open-pore replicated foams

The performance of thermal management structures produced in the course of this project depends on the energetic cost of circulating air through their porous metal section. To quantify this, we have developed in our laboratory a simple model to calculate the Darcy and Forchheimer coefficients of replicated aluminium foam.

The Darcian permeability of those materials was derived in earlier work [253] ; under this project we have extended the approach to tackle the Forchheimer term, which is dominant in the regime of air flow through the porous aluminium structures when these are used for heat transfer. The starting point of the derivation is to view open pore aluminium foam samples as comprised of cells connected by a finite number of windows, which represent the most important bottlenecks for a fluid flowing through the foam. The derivation begins by considering a single window, which is modelled as a circular orifice. The pressure drop across the window is given in terms of the volumetric flow rate Q_f through the window, as follows:

$$\Delta P_s = \frac{\rho K_1}{2\pi^2 r_w^4} Q_f^2 + \frac{\mu K_2}{4\pi r_w^3} Q_f \qquad (8.1)$$

with Q_f given by:

$$Q_f = V r_w^2 \pi \qquad (8.2)$$

where r_w is the average window radius, K_1 is a constant for high Reynolds numbers often referred to as the Hagenbach coefficient and K_2 is a constant for creeping flow referred to as the Couette coefficient. The value of K_2 has been well established at 37.7[254]–[256] and the value of K_1 has been experimentally verified for our case as 0.5. A more systematic approach with regard to the value of K_1 can be found to a paper submitted for publication.

The next step in the derivation is to make the link between the pressure drop and the average velocity v through the orifice on the one hand, and the pressure gradient as well as the superficial velocity of the fluid flowing through the microcellular aluminium structure on the other hand. To this end, one has to calculate the number of windows and their area as a function of the average pore size and the pore volume fraction. This can be accomplished on the basis of an analysis of the physics of powder densification [100], [257], which gives the average window area a_w as:

$$a_w = r_p^2 \frac{\pi}{3}\left(\frac{V_p - V_o}{1 - V_o}\right) \tag{8.3}$$

where r_p is the radius of the sphere having the same volume as the cell, V_p is the volumetric porosity and V_o , in principle fixed at 0.64, the volumetric density of a random dense packing of mono-sized spheres, is left as a fitting variable, to account for the fact that, in making the microcellular aluminium, initial salt particle packing fractions before compaction vary with the average particle size (tending to decrease as the salt particle size decreases).

From the window area, the average radius of a window r_w is:

$$r_w = \left(\frac{a}{\pi}\right)^{1/2} = \frac{1}{\sqrt{3}}\left(\frac{V_p - V_o}{1 - V_o}\right)^{1/2} r_p \tag{8.4}$$

In order to find the number of pores per unit volume, we consider a square slab of foam of depth 2 r_p oriented along the direction of fluid flow, and of cross-sectional area 1 m^2. The number of pores in the slab is:

$$N_p = \frac{V_{SAMPLE}}{V_{PORE}} \quad V_p = 2r_p \frac{3}{4r_p^3 \pi} V_p = \frac{3V_p}{2r_p^2 \pi} \tag{8.5}$$

which is also roughly the number of windows crossed by the flowing fluid per unit volume (assuming no significant lateral flow of the fluid). Now, since the fluid flowing through the slab will cross each pore only once, the superficial velocity of the fluid through the porous medium, v, is then deduced from the volumetric flow rate Q_f across a single window:

$$v = N_p Q_f = \frac{3V_p}{2r_p^2 \pi} Q_f \tag{8.6}$$

The total pressure drop across the slab is that across one window; allowing in turn to write:

$$-\Delta P_s = \frac{\rho K_1}{2\pi^2 r_w^4 N_p^2} v^2 + \frac{\mu K_2}{4\pi N_p r_w^3} v \tag{8.7}$$

Then, the pressure drop across the slab is $2r_p$ times the macroscopic pressure gradient dp/dx

$$-\nabla P_s = \frac{\rho K_1}{4 r_p \pi^2 r_w^4 N_p^2} v^2 + \frac{\mu K_2}{8 r_p \pi N_p r_w^3} v \tag{8.8}$$

from which the permeability and Forchheimer term characterizing the resistance of the porous medium to fluid flow can be deduced. The permeability is given by:

$$K_p = \frac{12 V_p r_p^2}{K_2} \left(\frac{V_p - V_o}{3 - 3V_o} \right)^{3/2} \tag{8.9}$$

(as in the earlier derivation of [253].), while the Forchheimer (inertial) term is given by:

$$K_f = \frac{9 r_p V_p^2}{K_1} \left(\frac{V_p - V_o}{3 - 3V_o} \right)^2 \tag{8.10}$$

Both expressions underline the importance of porosity and pore size: the permeability is a quadratic function of the pore size and a linear function of the porosity, while the Forchheimer term varies as the square of the porosity, and linearly with the pore size.

Results are presented in *Fig.8.1* and *Fig.8,2*, where model predictions are compared against data collected on several microcellular aluminium samples produced over the course of this project. As seen, a good match between the model predicted and measured permeability is demonstrated for various pore sizes and porosities. The Forchheimer coefficient shows good results for the large cell size samples only (400-450 μm); however, smaller cell sizes do not appear to match as well with theory. A more detailed accountof the same problem, dealing with the above discrepancy has been accepted for publication in Acta Materialia, entitled "Fluid flow through replicated microcellular materials in the Darcy-Forchheimer regime"[258].

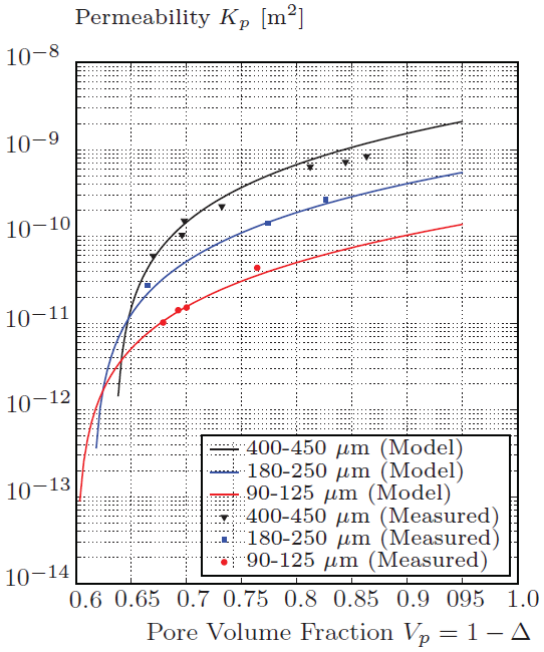

Figure 8.1: Comparison between the experimental and permeability values by the model for different pore sizes and volumetric porosities (Image courtesy of D. Ingram).

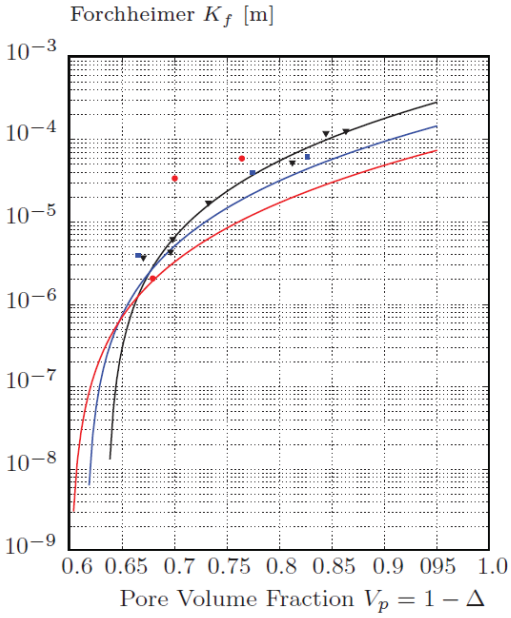

Figure 8.2 Comparison between the experimental and predicted Forchheimer coefficient values by the model for different pore sizes and volumetric porosities. (Image courtesy of D. Ingram).

Appendix B: Electrical Insulating Properties of the IS before and after thermal cycling

We tested the electrical insulating properties of our integrated structure, both before and after thermal cycling; the latter was performed for 3000 cycles from -50 to 250°C. This was done so as to confirm that the ceramic part (AlN here) between the two conductive parts (the aluminum/diamond and aluminium foam phases) remains intact and can hold its insulating capabilities within the structure. The composite structure was tested in the *EPFL School of Electrical Engineering, in the Electromagnetic Compatibility Laboratory*, according to *ASTM D3755-14* and *IEC 60243-2* standards.

For the thermal cycling, a set up was designed, constructed, and tested with success; its goal is to induce thermal fatigue to samples. It consists of (i) a Teflon™ chamber, selected for its low thermal diffusivity, (ii) a resistive heating circuit buried in an aluminium hot plate, and (iii) an air conduct through which nitrogen gas (cooled by liquid nitrogen) is brought to the sample. A cross section of the apparatus can be seen in *Fig. 8.3.*.

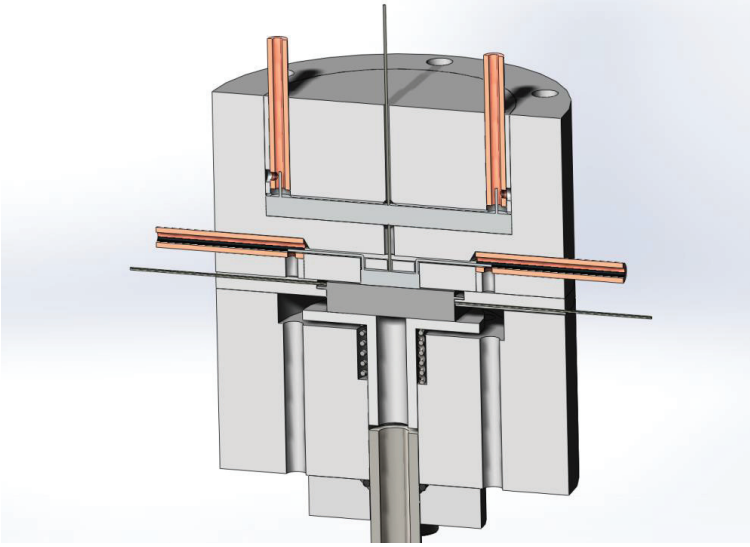

Figure 8.3 Cross section of the setup of the thermal fatigue. The LN_2 dewar in which the nitrogen gas is cooled is not shown.

Every cycle has an average duration of roughly 2 minutes, including a 20 seconds hold at each temperature extreme. A plot of measured temperatures inside the set-up versus time can be seen in *Fig. 8.4.*

The dielectric tests were conducted at room temperature, under SF_6 atmosphere since conducting them in nitrogen gas can lead to corona discharges around the insulating layer. Data showed that our integrated structure remains insulating at 2.5 kV, both before and after the thermal cycling.

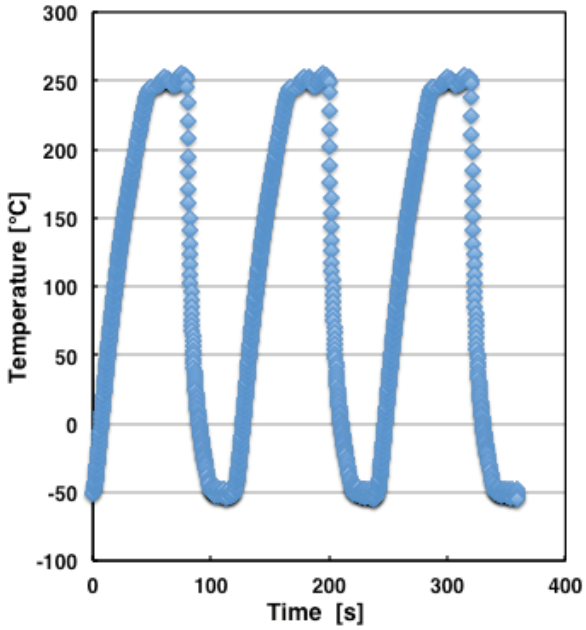

Figure 8.4: Temperature vs. time history obtained for a piece of aluminium foam inserted in the thermal cycle setup. The setup is controlled by a LabView program prepared in house that allows setting the minimum and maximum temperature as well as the hold times as T_{min} and T_{max}.

Appendix C: Thermoelastic bending of the integrated structure

A question that was addressed in the course of the present thesis is the potential importance and consequences of warpage of the composite structures that thermal stresses might induce. We addressed the question by linear elastic analysis of the deformation predicted for structures of this work.

One model found in literature [259], [260] was used in order to estimate how much our integrated structures will be deformed as a consequence of the mismatch in coefficient of thermal expansion (CTE) that exists between the different phases making composite cooling structures of this work. In *Fig. 8.5* the Integrated Structure (IS) is shown with its three distinctive layers. Subscript ***i*** denotes the layer with *s* designating the composite (taken as the substrate of the structure, in keeping with the notation in Ref. [259], [260]), 1 the ceramic and 2 the porous aluminum layer on the other side of the ceramic: t_s is the thickness of the aluminium/diamond composite, t_1 that of the ceramic and t_2 that of the porous aluminum. The coordinate system is defined such that the interface between the aluminium/diamond layer and the ceramic insulation is located at $z=0$, the aluminium diamond layer surface is located at $z=-t_s$, the aluminium foam/ceramic interface is located at $z=h_1=t_1$, and the aluminium foam surface is located at $z=h_2=t_1+t_2$.

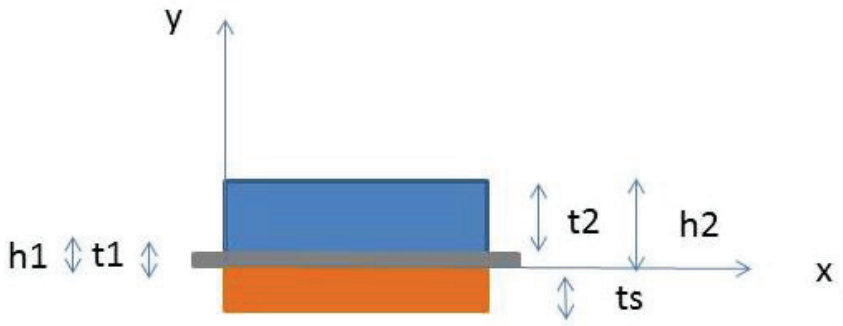

Figure 8.5: Schematic showing the Integrated Structure (IS) and the coordinate system.

The sample is at rest, meaning that there is no external force or momentum applied to it. Calculations differ in how the equations are solved but lead to the same predictions. Namely, the radius of curvature of the structure, r, measured at $z = 0$, is given as:

$$K = \frac{1}{r} = \frac{3[E_S(c - a_s\Delta\mathrm{T})t_s^2 - \sum_{i=1}^{n} E_i t_i (c - a_i\Delta\mathrm{T})(2h_{i-1} + t_i)] + 6M}{E_s t_s^2(2t_s + 3t_b) + \sum_{i=1}^{n} E_i t_i [6h_{i-1}^2 + 6h_{i-1}t_i + 2t_i^2 - 3t_b(2h_{i-1} + t_i)]} \qquad (8.11)$$

where c is a uniform strain across the structure, a_s is the coefficient of thermal expansion for the aluminium/diamond layer, a_i the coefficient of thermal expansion of layer $\boldsymbol{i}$ (=1 or 2) of the integrated structure, ΔT is the temperature excursion of the structure from its initial, strain-free state, M is the applied moment per unit width (taken to be zero here), E_s is Young modulus of the aluminium/diamond layer, E_1 that of the ceramic and E_2 that of the aluminum foam layer. Note that, for this linear elastic problem, changes in curvature caused by a change in temperature are computed similarly (r^{-1} is a linear function of ΔT, as should be).

The radius of curvature r measures the distortion of the structure that is caused by thermal stresses; to give a more easily palatable measure of this we define the "warpage" of the structure as the vertical displacement (lift off) of the center of the structure with respect to the plane defined by its corners when it rests atop a flat surface. With r much larger than the in/plane width of the sample L, the warpage w is approximately equal to:

$$w \approx \frac{L^2}{4r} \qquad (8.12)$$

A plot giving w versus both the thickness of the aluminium-diamond composite layer and the thickness of the aluminium foam layer with $\Delta T = 220^{\circ}$C is in *Fig.*

8.6. As depicted, w is estimated to be on the order of a few micrometers: this is negligibly small. The treatment does not take into account edge effects and a full 3D finite element analysis should be performed to get more precise predictions.

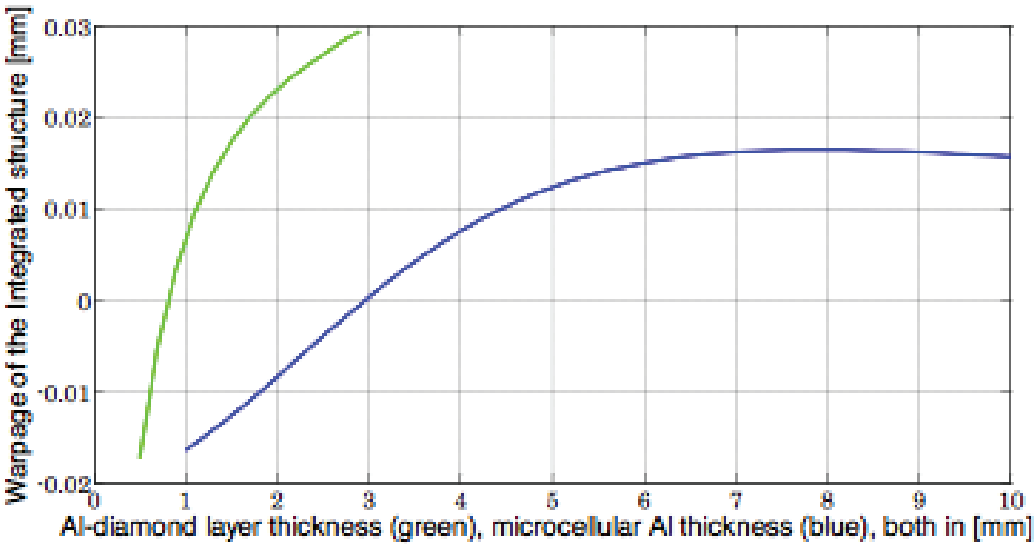

Figure 8.6*:* Influence of the thickness of the first (composite) and the last (porous aluminum) layer of the integrated structure on its warpage : the calculated warpage w is given as a function of the thickness of the aluminum-diamond layer (in blue) or the microcellular aluminum (in green), holding other parameters at the following values: thickness of the Aluminum Nitride t_1 = 500µm, AlN Young's modulus E_1 = 320GPa, diamond/Aluminum composite modulus E_s= 200 GPa (corresponding to roughly 55% diamond by volume) with its thickness t_s fixed at 1100µm when calculating the blue curve, microcellular aluminum modulus E_2=3GPa (corresponding to roughly 88% porosity in closed-pore Al foam or roughly 70% porosity in replicated open-pore microcellular aluminum such as that produced in our experiments) with its thickness t_2 fixed at 4 mm when calculating the green curve.

Appendix D: Thermal Resistance of the Thermal Interface Material

In the course of the thesis, the effect on the amount and method of distribution of the thermal paste on our thermal measurements was studied. Both the mass of the thermal paste and the way the contact surface between the sample and the bronze duct was covered were studied, in order to see how these factors can influence the bottom temperature of our samples.

As depicted in *Fig. 8.7,* the thermal resistance of the thermal paste was found to change during the test sequence. The test followed the modus operandi described in *Section 3.3.6* of the thesis at hand. This alteration of its thermal properties is mainly due to temperature cycling, as it can be seen that under a constant flow (and therefore under a constant temperature), the thermal properties of the paste remain the same. Note that the forced convection apparatus places the ceramic protection ring, surrounding the sample flush with its upper surface, such that that better thermal contact is achieved between the samples and the duct. The

thermal resistances values in forced convection experiments is thus expected to have lower values than the ones depicted in *Fig.8.7*

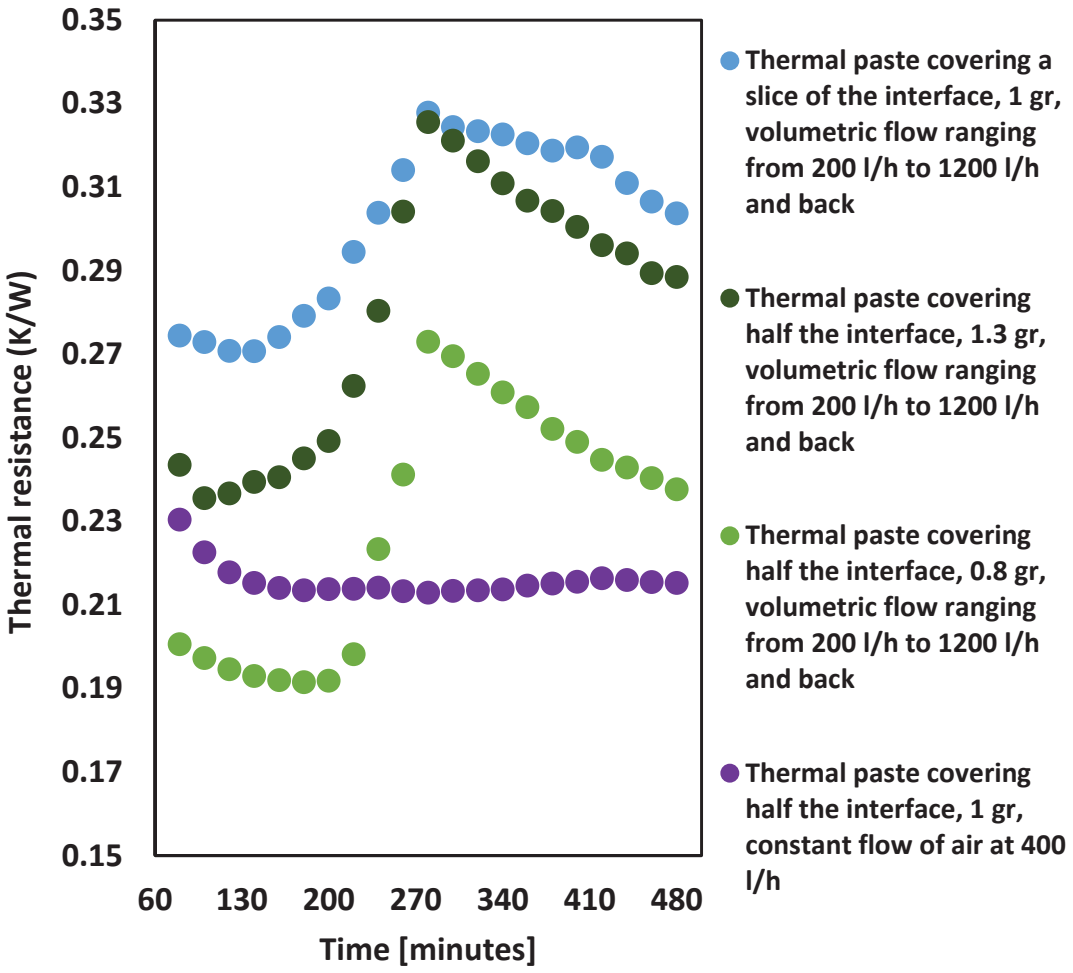

Figure 8.7: Evolution of thermal resistance of the interface material versus time. As seen, the thermal resistance of the paste remains constant under a constant air flow, which keeps also the temperature constant. The amount of thermal paste or the way it is distributed in the contact do not seem to play a key role in this degradation.

Appendix E: Selective compilation of forced convection results

In order to facilitate the juxtaposition between the results of present thesis and other studies, the following table compilates the results of the forced convection tests under three different volumetric flows (around 400, 1400 and 2400 l/h):

Appendix E: Selective compilation of forced convection results

Pore size (µm)	Height (mm)	V_p (%)	Infiltration Pressure, Pinf (bars)	Air flow (l/h)	Heat flux (W/cm^2)	Global Heat Transfer Coefficient, $h_{tot,}$ (W/m^2K)	Ideal Pumping Power per Footprint, W_t/A (W/cm^2)
400-450	28	85	9.7	425.6	2.1	174.8	14.1
400-450	28	85	9.7	1406.5	4.2	389.7	674.5
400-450	28	85	9.7	2394.9	5.4	524.9	3029.5
400-450	28	85	2.7	403.9	2.2	192.6	14.6
400-450	28	85	2.7	1394.9	5.1	501.1	465.1
400-450	28	85	2.7	2402.6	6.9	750.3	2415.3
400-450	28	75	3.3	435.3	2.3	195.5	38.2
400-450	28	75	3.3	1400.2	4.7	458.1	601.7
400-450	28	75	3.3	2407.7	6.5	690.3	2845.7
400-450	10	85	9.7	395.2	2.3	197.1	52.1
400-450	10	85	9.7	1394.3	5.6	559.1	1417.1
400-450	10	85	9.7	2399.5	7.7	853.7	6610.7

Table 5 : Brief selection of key results under forced convection

Appendix E: Selective compilation of forced convection results

Pore size (µm)	Height (mm)	V_p (%)	Infiltration Pressure, Pinf (bars)	Air flow (l/h)	Heat flux (W/cm^2)	Global Heat Transfer Coefficient, $h_{tot,}$ (W/m^2K)	Ideal Pumping Power per Footprint, W_t/A (W/cm^2)
400-450	10	75	3.3	394.1	2.1	183.1	78.1
400-450	10	75	3.3	1415.5	5.6	553.3	2388.3
400-450	10	75	3.3	2410.4	7.7	851.6	10554.2
400-450	10	75	10	420.36	2.2	184.9	145.6
400-450	10	75	10	1396.7	5.2	507.4	2555.7
400-450	10	75	10	2394.6	7.1	779.9	10864.2
125-180	10	85	80	424.3	2.4	202.3	335.6
125-180	10	85	80	1414.4	5.8	572.7	3935.8
125-180	10	85	80	2409.6	7.8	876.8	12485.6
125-180	10	75	80	461.2	2.3	197.5	1020.3
125-180	10	75	80	1202.8	4.6	439.5	6776.5

Table 5 : Brief selection of key results under forced convection

Pore size (µm)	Height (mm)	V_p (%)	Infiltration Pressure, Pinf (bars)	Air flow (l/h)	Heat flux (W/cm^2)	Global Heat Transfer Coefficient, $h_{tot,}$ (W/m^2K)	Ideal Pumping Power per Footprint, W_t/A (W/cm^2)
125-180	28	85	80	420.9	2.4	203.8	324.1
125-180	28	85	80	1407.4	4.6	439.3	3398.4
125-180	28	85	80	2405.4	6.0	605.6	9729.9
900-1100	28	85	3.3	435.3	2.1	177.8	19.3
900-1100	28	85	3.3	1400.2	4.8	470.3	541.3
900-1100	28	85	3.3	2407.7	6.5	687.2	2798.7
900-1100	10	85	3.3	408.8	2.5	216.6	19.3
900-1100	10	85	3.3	1385.9	6.6	667.5	644.7
900-1100	10	85	3.3	2397.5	9.0	1030.0	3209.1

Table 5 : Brief selection of key results under forced convection

Chapter 9 Bibliography

[1] Miguel R.O. Panão, A. M. Correia, A . L. N. Moreira, "High-power electronics thermal management with intermittent multijet sprays," *Appl. Therm. Eng.*, vol. 37, pp. 293–301, May 2012.

[2] I. Mudawar, D. Bharathan, K. Kelly and, "Two-Phase Spray Cooling of Hybrid Vehicle Electronics," *IEEE Trans. Compon. Packag. Technol.*, vol. 32, no. 2, pp. 501–512, Jun. 2009.

[3] X.C. Tong, *Advanced Materials for Thermal Management of Electronic Packaging*. Springer, 2011.

[4] R. Viswanath, V. Wakharkar, A. Watwe and L. Lebonheur, "Thermal performance challenges from silicon to systems," *Intel Technology Journal*, no. Q3, pp. 1–16, 2000.

[5] W. L. Staats Jr, "Active Heat Transfer Enhancement in Integrated Fan Heat Sinks," MIT, 2012.

[6] M. Marz, A. Schletz, B. Eckardt, S. Egelkraut and H. Rauh, "Power electronics system integration for electric and hybrid vehicles," *Integr. Power Electron. Syst. CIPS 2010 6th Int. Conf. On*, pp. 1–10, Mar. 2010.

[7] S. S. Anandan, V. Ramalingam, "Thermal management of electronics: A review of literature," *Therm. Sci.*, vol. 12, no. 2, pp. 5–26, 2008.

[8] C.A. Harper, Ed., "Thermal management," in *Electronic packaging and interconnection handbook*, 4th ed., McGraw-Hill Professional, 2004, p. 1000.

[9] "Market and Technology Study Automotive Power Electronics 2015," Arthur D. Little, Corporate, 2006.

[10] R. Hannemann, "Thermal control of electronics: perspectives and prospects." [Online]. Available: http://web.mit.edu/hmtl/www/papers/HANNEMANN.pdf .

[11] O. Suzuki, Y. Hara and W. Nakayama, "Thermal Management of Electronic and Electrical Devices in Automobile Environment," presented at the Vehicle Power and Propulsion Conference, 2009, pp. 601–608.

[12] A.G. Evans, M.Y. He, J.W Hutchison and M. Shaw, "Temperature distribution in advanced power electronics systems and the effect of phase change materials on temperature suppression during power pulses," *J. Electron. Packag.*, vol. 123, no. 3, pp. 211–217, Sep. 2001.

[13] A. Shakouri, "Nanoscale Thermal Transport and Microrefrigerators on a Chip," *Proc. IEEE*, vol. 94, no. 8, pp. 1613–1638, Aug. 2006.

[14] D. D. L. Chung, C. Zweben, "Composites for Electronic Packaging and Thermal Management", Comprehensive Composite Materials," in *Comprehensive Composite Materials*, vol. 6, A. Kelly and C. Zweben, Ed. Oxford: Pergamon Press, 2000, pp. 701–725.

[15] M. Occhionero, "IGBT Thermal Management," *AlSiC Thermal Management Solutions*, May-2010. [Online]. Available: http://alsicthermalmanagement.blogspot.ch/2010/05/igbt-thermal-management.html.

[16] X.Q. Cao, R. Vassen and D. Stoever, "Ceramic materials for thermal barrier coatings," *J. Eur. Ceram. Soc.*, vol. 24, no. 1, pp. 1–10, 2004.

[17] K. Watari and S.L. Shinde, "High Thermal Conductivity Materials," *MRS Bull.*, vol. 26, pp. 440–444, 2001.

[18] M. de Sorgo, "Thermal Interface Materials," *Electronics Cooling*, 01-Sep-1996. [Online]. Available: http://www.electronics-cooling.com/1996/09/thermal-interface-materials-2/.

[19] "Intel® Core™ 2 Duo Mobile Processors on 45-nm process-Thermal Design Guide," Intel, Jun. 2008.

[20] R.W. Johnson, J.L. Evans, P. Jacobsen, J.R. Thompson and M. Christopher Johnson, "The Changing Automotive Environment: High-Temperature Electronics," *IEEE Trans. Electron. Packag. Manuf.*, vol. 27, no. 3, pp. 164–176, Jul. 2004.

[21] T. Abraham, K .Kellly, K. Bennion and A. Vlahinos, "Advanced Thermal Control Enabling Cost Reduction for Automotive Power Electronics," ANSYS Automotive Conference, Pittsburgh, Pensylvania, USA, 2008.

[22] H. Mahdi, A. Fuentes, P. Lopez and R. Jones, "Thermal performance of aluminium-foam CPU heat exchangers," *Int. J. Energy Res.*, vol. 30, no. 11, pp. 851–860, 2006.

[23] A. Shakouri, "Hot Spot Management and Micro Refrigeration in Integrated Circuits," IEEE CSS and CMPT Santa Clara Valley, 20-Apr-2009.

[24] E. Suhir, "Predictive Analytical Thermal Stress Modeling in Electronics and Photonics," *Appl. Mech. Rev.*, vol. 62, no. 4, pp. 1–20, 2009.

[25] S. Mallik, N. Ekere, C. Best and R. Bhatti, "Investigation of thermal management materials for automotive electronic control units," *Appl. Therm. Eng.*, vol. 31, no. 2–3, pp. 355–362, Feb. 2011.

[26] S. S. Sindu, S. Kumar and A. Batish, "Metal Matrix Composites for Thermal Management: A Review," *Crit. Rev. Solid State Mater. Sci.*, pp. 1–26, Oct. 2015.

[27] M.A. Occhionero, K.P. Fennessy, R.W. Adams and G.J. Sundberg, "AlSiC Baseplates for Power IGBT Modules: Design, Performance, and Reliability," in *IMAPS New England Symposium*, Boxborough MA USA, 2002.

[28] Th. Schütze, J. Biermann, R. Spanke and M. Pfaffenlehner, "High Power IGBT modules with improved mechanical performance and advanced 3.3kV IGBT3 chip technology," in *Power Conversion and Intelligent Motion*, Nuremberg, 2006.

[29] M. Ciappa and A. Castellazzi, "Reliability of High-Power IGBT Modules for Traction Applications," in *45th Reliability Physics Symposium*, Phoenix, 2007.

[30] C. Zweben, "Advances in Composite Materials for Thermal Management in Electronic Packaging," *JOM J. Miner. Met. Mater. Soc.*, vol. 50, no. 6, pp. 47–51, Jun. 1998.

[31] A. Evans, C. San Marchi and A. Mortensen, *Metal Matrix Composites in Industry*. Berlin: Springer, 2003.

[32] N. Chawla and K.K. Chawla, *Metal Matrix Composites*. Berlin: Springer, 2005.

[33] T. W. Clyne and P. J. Withers, *An Introduction to Metal Matrix Composites*. Cambridge: Cambridge University Press, 1993.

[34] J.G. Josenhans, "Diamond as an Insulating Heat Sink for a Series Combination of IMPATT Diodes," *Proc. IEEE*, vol. 56, no. 4, pp. 762–763, Apr. 1968.

[35] R.R. Reeber and K. Wang, "Thermal expansion, molar volume and specific heat of diamond from 0 to 3000k," vol. 25, no. 1, pp. 63–67, 1996.

[36] R. Berman, "Thermal Conductivity of Vapour Deposited and Isotopically Enriched Diamonds," in *The properties of Natural and Synthetic Diamond*, J.E. Field, Ed. Academic Press, 1992, p. 710.

[37] L. Weber and R. Tavangar, "Diamond-based Metal Matrix Composites for Thermal Management made by Liquid Metal Infiltration—Potential and Limits," *Adv. Mater. Res.*, vol. 59, pp. 111–115, 2009.

[38] M. Seal, "High Technology Applications of Diamonds," in *The properties of Natural and Synthetic Diamond*, J.E. Field, Ed. Academic Press, 1992, p. 710.

[39] V. Goyal, S. Subrina, D. L. Nika, and A. Balandin, "Reduced thermal resistance of the silicon-synthetic diamond composite substrates at elevated temperatures," *Appl. Phys. Lett.*, vol. 97, no. 3, pp. 1–3, 2010.

[40] V.T. Goyal, D. Kotchetkov, S. Subrina, M. Rahman and A.A. Balandin, "Thermal conduction through diamond - silicon heterostructures," in *Thermal and Thermomechanical Phenomena in Electronic Systems (Itherm)*, 2010.

[41] N. Govindaraju and R.N. Singh, "Processing of nanocrystalline diamond thin films for thermal management of wide-bandgap semiconductor power electronics," *Mater. Sci. Eng. B*, vol. 176, no. 14, pp. 1058–1072, Aug. 2011.

[42] A. Aleksov, J.M. Gobien, X. Li, J.T. Prater and Z. Sitar, "Silicon-on-Diamond— An engineered substrate for electronic applications," *Diam. Relat. Mater.*, vol. 15, no. 2–3, pp. 248–253, 2005.

[43] R.D. Burnham and R.S.Sussmann, "Diamond composite heat sink for use with semiconductor devices," US 5008737 A, 16-Apr-1991.

[44] N.J. Colella, J.A. Kerns and D. Makowiecki, "Copper-diamond composite substrates for electronic components," in *45th Electronic Components and Technology Conference*, 1995.

[45] Q. Sun and Q.T. Inal, "Fabrication and characterization of diamond/copper composites for thermal management substrate applications," *Mater. Sci. Eng. B*, vol. 41, no. 2, pp. 261–266, 1996.

[46] K. Yoshida and H. Morigami, "Thermal properties of diamond/copper composite material," *Microelectron. Reliab.*, vol. 44, no. 2, pp. 303–308, 2004.

[47] L. Weber and R. Tavangar, "On the influence of active element content on the thermal conductivity and thermal expansion of Cu–X (X = Cr, B) diamond composites diamond composites," *Scr. Mater.*, vol. 57, no. 2007, pp. 988–991.

[48] W.B. Johnson and B. Sonuparlak, "Diamond/Al metal matrix composites formed by the pressureless metal infiltration process," *J. Mater. Res.*, vol. 8, no. 5, pp. 1169–1173, May 1993.

[49] Y.S. Liao and S.Y. Luo, "Effects of matrix characteristics on diamond composites," *Chem. Mater. Sci.*, vol. 28, no. 5, pp. 1245–1251, 1993.

[50] W.A. Ferrando and J.B. Clark, "Diamond/silver composites," US H1358 H, 06-Sep-1994.

[51] R. Tavangar, J.M. Molina and L. Weber, "Assessing predictive schemes for thermal conductivity against diamond-reinforced silver matrix composites at intermediate phase contrast," *Scr. Mater.*, vol. 56, no. 5, pp. 357–360, 2007.

[52] "Metal / Carbon Composites," *Fraunhofer IFAM Dresden*, 05-2016. [Online]. Available: http://www.ifam.fraunhofer.de/en/Dresden/Sintered_and_Composite_Materials/metall-matrix-verbundwerkstoffe/metall_kohlenstoff-verbundwerkstoffe.html.

[53] O. Beffort, S. Vaucher and F.A. Khalid, "On the thermal and chemical stability of diamond during processing of Al/diamond composites by liquid metal infiltration (squeeze casting)," *Diam. Relat. Mater.*, vol. 13, no. 10, pp. 1834–1843, Oct. 2004.

[54] F.A. Khalid, O. Beffort, U.E. Klotz, B.A. Keller and P. Gasser, "Microstructure and interfacial characteristics of aluminium–diamond composite materials," *Diam. Relat. Mater.*, vol. 13, no. 3, pp. 393–400, Mar. 2004.

[55] P.W. Ruch, O. Beffort, S. Kleiner, L. Weber and P.J. Uggowitzer, "Selective interfacial bonding in Al(Si)–diamond composites and its effect on thermal conductivity," *Compos. Sci. Technol.*, vol. 66, no. 15, pp. 2677–2685, Dec. 2006.

[56] J. Flaquer, A. Rios, A. Martin-Meizoso, S. Nogales and H. Bohm, "Effect of diamond shapes and associated thermal boundary resistance on thermal conductivity of diamond-based composites," *Comput. Mater. Sci.*, vol. 41, no. 2, pp. 156–163, Dec. 2007.

[57] N. Chen, X.-F. Pan and M.Y Gu, "Microstructure and physical properties of Al/diamond composite fabricated by pressureless infiltration," *Mater. Sci. Technol.*, vol. 25, no. 3, pp. 400–402, Mar. 2009.

[58] C. Xue, J.K. Yu and X.M. Zhu, "Thermal properties of diamond/SiC/Al composites with high volume fractions," *Mater. Des.*, vol. 32, no. 8–9, pp. 4225–4229, Sep. 2011.

[59] J. Shi, R.C. Che, C.Y. Liang, Y. Cui and S.B. Xu, "Microstructure of diamond/aluminum composites fabricated by pressureless metal infiltration," *Compos. Part BEngineering*, vol. 42, no. 6, pp. 1346–1349, Sep. 2011.

[60] K. Chu ,C. Jia, X. Liang, H. Chen, W. Gao and H. Guo, "Modeling the thermal conductivity of diamond reinforced aluminium matrix composites with inhomogeneous interfacial conductance," *Mater. Des.*, vol. 30, no. 10, pp. 4311–4316, Dec. 2009.

[61] B. Yang, J.K Yu and C. Chen, "Microstructure and thermal expansion of Ti coated diamond/Al composites," *Transcations Nonferrous Met. Soc. China*, vol. 19, no. 5, pp. 1167–1173, Oct. 2009.

[62] Y. Zhang, X.T. Wang, S.B. Jiand and J.J. Wu, "Thermo-Physical Properties of Ti-Coated Diamond/Al Composites Prepared by Pressure Infiltration," *Mater. Sci. Forum*, vol. 654–656, pp. 2572–2575, Jun. 2010.

[63] K. Mizuuchi, K. Inoue, Y. Agari, Y. Morisada, M. Sugioka, M. Tanaka, T. Takeuchi, J. Tani, M. Kawahara and Y. Makino, "Processing of diamond particle dispersed aluminum matrix composites in continuous solid–liquid co-existent state by SPS and their thermal properties," *Compos. Part BEngineering*, vol. 42, no. 2, pp. 825–831, Jun. 2011.

[64] K. Mizuuchi, K. Inoue, Y. Agari, Y. Morisada, M. Sugioka,M. Tanaka,T. Takeuchi,M. Kawahara and Y. Makino, "Thermal conductivity of diamond particle dispersed aluminum matrix composites fabricated in solid–liquid co-existent state by SPS," *Compos. Part BEngineering*, vol. 42, no. 5, pp. 1029–1034, Jul. 2011.

[65] Y. Zhang, J. Li, L. Zhao, H. Zhang and X. Wang, "Effect of metalloid silicon addition on densification, microstructure and thermal–physical properties of Al/diamond composites consolidated by spark plasma sintering," *Mater. Des.*, vol. 63, pp. 838–847, Nov. 2014.

[66] J. Long, X. Li, D. Fang, P. Peng and Q. He, "Fabrication of diamond particles reinforced Al-matrix composites by hot-press sintering," *Int. J. Refract. Met. Hard Mater.*, vol. 41, pp. 85–89, Nov. 2013.

[67] S.V. Kidalov and F. M. Shakhov, "Thermal Conductivity of Diamond Composites," *Materials*, vol. 2, no. 4, pp. 2467–2495, 2009.

[68] Z. Tan, Z. Li, G. Fan, X. Kai, G. Ji, L. Zhang and D. Zhang, "Diamond/aluminum composites processed by vacuum hot pressing: Microstructure characteristics and thermal properties," *Diam. Relat. Mater.*, vol. 31, pp. 1–5, Jan. 2013.

[69] J.M. Molina, M. Rheme, J. Carron and L. Weber., "Thermal conductivity of aluminum matrix composites reinforced with mixtures of diamond and SiC particles," *Scr. Mater.*, vol. 58, no. 5, pp. 393–396, Mar. 2008.

[70] O. Beffort, F.A. Khalid, L. Weber, P. Ruch, U.E. Klotz, S. Meier and S. Kleiner, "Interface formation in infiltrated Al(Si)/diamond composites," *Diam. Relat. Mater.*, vol. 15, no. 9, pp. 1250–1260, Sep. 2006.

[71] H. Feng, J.K. Yu and W. Tan, "Microstructure and thermal properties of diamond/aluminum composites with TiC coating on diamond particles," *Mater. Chem. Phys.*, vol. 124, no. 1, pp. 851–855, Nov. 2010.

[72] J. Shi, R. C. Che, C. Y. Liang, Y. Cui, S. B. Xu and L. Zhang, "Microstructure of diamond/aluminum composites fabricated by pressureless metal infiltration," *Compos. Part B Eng.*, vol. 42, no. 6, pp. 1346–1349, Sep. 2011.

[73] S. Ray, "Synthesis of cast metal matrix particulate composites," *J. Mater. Sci.*, vol. 28, no. 20, pp. 5397–5413, 1993.

[74] Z. Tan, Z. Li, G. Fan, Q. Guo, X. Kai, G. Ji, L. Zhang and D. Zhang, "Enhanced thermal conductivity in diamond/aluminum composites with a tungsten interface nanolayer," *Mater. Des.*, vol. 47, pp. 160–166, May 2013.

[75] Z. Tan, Z. Li, G. Fan, X. Kai, G. Ji, L. Zhang and D. Zhang, "Fabrication of diamond/aluminum composites by vacuum hot pressing: Process optimization and thermal properties," *Compos. Part B Eng.*, vol. 47, pp. 173–180, Apr. 2013.

[76] D.D.L Chung, "Materials for thermal conduction," *Appl. Therm. Eng.*, vol. 21, no. 16, pp. 1593–1605, Nov. 2001.

[77] S. Torquato, *Random Heterogeneous Materials*, 2nd Edition. Berlin: Springer, 2001.

[78] M. Kida, L. Weber, C. Monachon and A. Mortensen, "Thermal conductivity and interfacial conductance of AlN particle reinforced metal matrix composites," *J. Appl. Phys.*, vol. 109, no. 6, pp. 1–8, 2011.

[79] A.N. Norris, A.J. Callegari and P. Sheng, "A generalized differential effective medium theory," *J. Mech. Phys. Solids*, vol. 33, no. 6, pp. 525–543, 1985.

[80] L. Weber, C. Fischer and A. Mortensen, "On the influence of the shape of randomly oriented, non-conducting inclusions in a conducting matrix on the effective electrical conductivity," *Acta Mater.*, vol. 51, no. 22, pp. 495–505, Jan. 2003.

[81] W. Yang, K. Peng, J. Zhu, D. Li and L. Zhou, "Enhanced thermal conductivity and stability of diamond/aluminum composite by introduction of carbide interface layer," *Diam. Relat. Mater.*, vol. 46, pp. 35–41, Jun. 2014.

[82] I.E. Monje, E Louis and J.M. Molina, "On critical aspects of infiltrated Al/diamond composites for thermal management: Diamond quality versus processing conditions," *Compos. Part Appl. Sci. Manuf.*, vol. 67, pp. 70–76, Dec. 2014.

[83] I.E. Monje, E. Louis and J.M. Molina, "Interfacial nano-engineering in Al/diamond composites for thermal management by in situ diamond surface gas desorption," *Scr. Mater.*, vol. 115, pp. 159–163, Apr. 2016.

[84] I.E. Monje, E Louis and J.M. Molina, "Optimizing thermal conductivity in gas-pressure infiltrated aluminum/diamond composites by precise processing control," *Compos. Part Appl. Sci. Manuf.*, vol. 48, pp. 9–14, May 2013.

[85] Y. Zhang, J. Li, L. Zhao, H. Zhang and X. Wang, "Optimisation of high thermal conductivity Al/diamond composites produced by gas pressure infiltration by

controlling infiltration temperature and pressure," *J. Mater. Sci.*, vol. 50, no. 2, pp. 688–696, 2014.

[86] P. Wang, Z. Xiu, L. Jiang, G. Chen, X. Lin and G. Wu, "Enhanced thermal conductivity and flexural properties in squeeze casted diamond/aluminum composites by processing control," *Mater. Des.*, vol. 88, pp. 1347–1352, Dec. 2015.

[87] C. Monachon and L. Weber, "Influence of diamond surface termination on thermal boundary conductance between Al and diamond," *J. Appl. Phys.*, vol. 113, no. 18, 2013.

[88] C. Monachon, G. Schusteritsch, E. Kaxiras and L. Weber, "Qualitative link between work of adhesion and thermal conductance of metal/diamond interfaces," *J. Appl. Phys.*, vol. 115, no. 12, 2014.

[89] C. Monachon and L. Weber, "Effect of diamond surface orientation on the thermal boundary conductance between diamond and aluminum," *Diam. Relat. Mater.*, vol. 39, pp. 8–13, Oct. 2013.

[90] M. Caccia, A. Rodriguez and J. Narciso, "Diamond Surface Modification to Enhance Interfacial Thermal Conductivity in Al/Diamond Composites," *JOM*, vol. 66, no. 6, pp. 920–925, 2014.

[91] J.M. Molina-Jordá, "Design of composites for thermal management: Aluminum reinforced with diamond-containing bimodal particle mixtures," *Compos. Part Appl. Sci. Manuf.*, vol. 70, pp. 45–51, Mar. 2015.

[92] Z. Xiu, X. Wang, M. Hussain, C. Feng and L. Jiang, "Effect of heat treatment on microstructure and thermophysical properties of diamond/2024 Al composites," *Trans. Nonferrous Met. Soc. China*, vol. 23, no. 12, pp. 3584–3591, Dec. 2013.

[93] I.E. Monje, E Louis and J.M. Molina, "Aluminum/diamond composites: A preparative method to characterize reactivity and selectivity at the interface," *Scr. Mater.*, vol. 66, no. 10, pp. 789–792, May 2012.

[94] M.A. De Meller, "Produit métallique pour l'obtention d'objets laminés, moulés ou autres, et procédés pour sa fabrication," 615.147, 03-Dec-1926.

[95] X.-H. Han, Q. Wang, Y-G. Park, C. T'Joen, A. Sommers and A. Jacobi, "A Review of Metal Foam and Metal Matrix Composites for Heat Exchangers and Heat Sinks," *Heat Transf. Eng.*, vol. 33, no. 12, pp. 991–1009, Apr. 2012.

[96] I. Ghosh, "How Good Is Open-Cell Metal Foam as Heat Transfer Surface?," *J. Heat Transf.*, vol. 131, no. 10, pp. 1–8, Jul. 2009.

[97] S. De Schampheleire, P. De Jaeger, K. De Kerpel, B. Armeel, H. Huisseune and M. De Paepe, "How to Study Thermal Applications of Open-Cell Metal Foam: Experiments and Computational Fluid Dynamics," *Materials*, vol. 9, no. 2, p. 94, 2016.

[98] R. Goodall and A. Mortensen, "24 - Porous Metals," in *Physical Metallurgy (Fifth Edition)*, Oxford: Elsevier, 2014, pp. 2399–2595.

[99] C.Y. Zhao, "Review on thermal transport in high porosity cellular metal foams with open cells," *Int. J. Heat Mass Transf.*, vol. 55, no. 13–14, pp. 3618–3632, Jun. 2012.

[100] J.F. Despois, "Replicated aluminium foam: processing and properties," Doctoral Thesis, EPFL, n. 3268, Lausanne, 2005.

[101] R. Goodall and A. Mortensen, "Microcellular Aluminium?-Childs Play!," *Adv. Eng. Mater.*, vol. 9, no. 11, pp. 951–954, Nov. 2007.

[102] Y. Conde, J.F. Despois, R. Goodall, A. Marmottant, L. Salvo, C. San Marchi and A. Mortensen, "Replication Processing of Highly Porous Materials," *Adv. Eng. Mater.*, vol. 8, no. 9, pp. 795–803, Sep. 2006.

[103] P. Ranut, "On the effective thermal conductivity of aluminum metal foams: Review and improvement of the available empirical and analytical models," *Appl. Therm. Eng.*, vol. 101, pp. 496–524, May 2016.

[104] C.Y. Zhao, S.A. Tassou and T.J. Lu, "Analytical considerations of thermal radiation in cellular metal foams with open cells," *Int. J. Heat Mass Transf.*, vol. 51, no. 3–4, pp. 929–940, Feb. 2008.

[105] J.K. Carson, S.J. Lovatt, D.J. Tanner and Andrew C. Cleland, "Thermal conductivity bounds for isotropic, porous materials," *Int. J. Heat Mass Transf.*, vol. 48, no. 11, pp. 2150–2158, May 2005.

[106] L.J. Gibson and M.F. Ashby, *Cellular Solids, Structure and Properties*. Cambridge University Press, 1999.

[107] R. Goodall, L. Weber and A. Mortensen, "The electrical conductivity of microcellular metals," *J. Appl. Phys.*, vol. 100, no. 4, pp. 1–7, 2006.

[108] P. Kumar and F. Topin, "Simultaneous determination of intrinsic solid phase conductivity and effective thermal conductivity of Kelvin like foams," *Appl. Therm. Eng.*, vol. 71, no. 1, pp. 536–547, Oct. 2014.

[109] P. Kumar, F. Topin and J. Vicente, "Determination of effective thermal conductivity from geometrical properties: Application to open cell foams," *Int. J. Therm. Sci.*, vol. 81, pp. 13–28, Jul. 2014.

[110] K. Boomsma and D. Poulikakos, "On the effective thermal conductivity of a three-dimensionally structured fluid-saturated metal foam," *Int. J. Heat Mass Transf.*, vol. 44, no. 4, pp. 827–836, Feb. 2001.

[111] E. Solorzano, J.A. Reglero, M.A. Rogriguez-Perez, D. Lehmhus, M. Wichmann and J.A. de Saja, "An experimental study on the thermal conductivity of aluminium foams by using the transient plane source method," *Int. J. Heat Mass Transf.*, vol. 51, no. 25–26, pp. 6259–6267, Dec. 2008.

[112] F.G. Cuevas, J.M. Montes, J. Cintas and P. Urban, "Electrical conductivity and porosity relationship in metal foams," *J. Porous Mater.*, vol. 16, no. 6, pp. 675–681, 2008.

[113] E. Sadeghi, S. Hsieh and M. Bahrami, "Thermal conductivity and contact resistance of metal foams," *J. Phys. DApplied Phys.*, vol. 44, no. 12, pp. 1–7, 2011.

[114] K. Nawaz, J. Bock, Z. Dai and A. Jacobi, "Experimental Studies to Evaluate the Use of Metal Foams in Highly Compact Air-Cooling Heat Exchangers," in *13th International Refrigeration and Airc Conditioning Conference*, Purdue University, Lafayette, IN, 2010.

[115] A. Mortensen, Y. Conde, A. Rossoll and C. San Marchi, "Scaling of conductivity and Young's modulus in replicated microcellular materials," *J. Mater. Sci.*, vol. 48, no. 23, pp. 8140–8146, décembre 2013.

[116] P. Kumar and F. Topin, "Thermal conductivity correlations of open-cell foams: Extension of Hashin–Shtrikman model and introduction of effective solid phase tortuosity," *Int. J. Heat Mass Transf.*, vol. 92, pp. 539–549, Jan. 2016.

[117] D. A. Nield and A. V. Kuznetsov, "Forced Convection in Porous Media: Transverse Heterogeneity Effects and Thermal Development," in *Handbook of porous media*, 2nd ed., K. Vafai, Ed. 2005, p. 784.

[118] I. Ghosh, "Heat transfer correlation for high-porosity open-cell foam," *Int. J. Heat Mass Transf.*, vol. 52, no. 5–6, pp. 1488–1494, février 2009.

[119] I. Ghosh, "Heat-Transfer Analysis of High Porosity Open-Cell Metal Foam," *J. Heat Transf.*, vol. 130, no. 3, pp. 1–6, Mar. 2008.

[120] M. Kaviany, "Laminar flow through a porous channel bounded by isothermal parallel plates," *Int. J. Heat Mass Transf.*, vol. 28, no. 4, pp. 851–858, Apr. 1985.

[121] T.J. Lu, H.A. Stone and M.F. Ashby, "Heat transfer in open-cell metal foams," *Acta Mater.*, vol. 46, no. 10, pp. 3619–3635, Jun. 1998.

[122] S. Mahjoob and K. Vafai, "A synthesis of fluid and thermal transport models for metal foam heat exchangers," *Int. J. Heat Mass Transf.*, vol. 51, no. 15–16, pp. 3701–3711, Jul. 2008.

[123] A. J. Onstad, C. J. Elkins, F. Medina, R. B. Wicker and J. K. Eaton, "Full-field measurements of flow through a scaled metal foam replica," *Exp. Fluids*, vol. 50, no. 6, pp. 1571–1585, Jun. 2011.

[124] C. Hutter, C. Allemann, S. Kuhn and Ph. Rudolf von Rohr, "Scalar transport in a milli-scale metal foam reactor," *Chem. Eng. Sci.*, vol. 65, no. 10, pp. 3169–3178, May 2010.

[125] S. Mancin, C. Zilio, A. Diani and L. Rosetto, "Air forced convection through metal foams: Experimental results and modeling," *Int. J. Heat Mass Transf.*, vol. 62, no. 0, pp. 112–123, juillet 2013.

[126] S. Mancin, C. Zilio, L. Rosetto and A. Cavallini, "Foam height effects on heat transfer performance of 20 ppi aluminum foams," *Therm. Environ. Issues Energy Syst. ASMEATEUIT*, vol. 49, no. 0, pp. 55–60, Dec. 2012.

[127] S. Mancin, C. Zilio, A. Diani and L. Rosetto, "Experimental air heat transfer and pressure drop through copper foams," *Exp. Therm. Fluid Sci.*, vol. 36, pp. 224–232, Jan. 2012.

[128] S. Mancin, C. Zilio, A. Cavallini and L. Rosetto, "Heat transfer during air flow in aluminum foams," *Int. J. Heat Mass Transf.*, vol. 53, no. 21–22, pp. 4976–4984, Oct. 2010.

[129] P. De Jaeger, C.T'Joen, H. Huisseune, B. Ameel, S. De Schampheleire and M. De Paepe, "Influence of Geometrical Parameters of Open-Cell Aluminum Foam on Thermohydraulic Performance," *Heat Transf. Eng.*, vol. 34, no. 14, pp. 1202–1215, Nov. 2013.

[130] N. Dukhan and K-C. Chen, "Heat transfer measurements in metal foam subjected to constant heat flux," *Exp. Therm. Fluid Sci.*, vol. 32, no. 2, pp. 624–631, Nov. 2007.

[131] V.V. Calmidi and R.L. Mahajan, "Forced Convection in High Porosity Metal Foams," *J. Heat Transf.*, vol. 122, no. 3, pp. 557–565, 2000.

[132] C. Albanakis, D. Missirlis, N. Michailidis, K. Yakinthos, A. Goulas, H. Omar, D. Tsipas and B. Granier, "Experimental analysis of the pressure drop and heat transfer through metal foams used as volumetric receivers under concentrated solar radiation," *Exp. Therm. Fluid Sci.*, vol. 33, no. 2, pp. 246–252, Jan. 2009.

[133] M. Odabaee, S. Mancin and K. Hooman, "Metal foam heat exchangers for thermal management of fuel cell systems – An experimental study," *Exp. Therm. Fluid Sci.*, vol. 51, pp. 214–219, Nov. 2013.

[134] G. Hetsroni, M. Gurevich and R. Rozenblit, "Metal foam heat sink for transmission window," *Int. J. Heat Mass Transf.*, vol. Volume 48, no. 18, pp. 3793–3803, Aug. 2005.

[135] A. Cavallini, S. Macin, L. Rosetto and C. Zilio, "Air Flow in Aluminum Foam: Heat Transfer and Pressure Drops Measurements," *Exp. Heat Transf.*, vol. 23, no. 1, pp. 94–105, décembre 2009.

[136] K. I. Salas and A.M. Waas, "Convective Heat Transfer in Open Cell Metal Foams," *J. Heat Transf.*, vol. 129, no. 9, pp. 1217–1229, Dec. 2006.

[137] S.Y. Kim, B.H. Kang and J-H. Kim, "Forced convection from aluminum foam materials in an asymmetrically heated channel," *Int. J. Heat Mass Transf.*, vol. 44, no. 7, pp. 1451–1454, Apr. 2001.

[138] L. Tadrist, M. Miscevic, O. Rahli and F. Topin, "About the use of fibrous materials in compact heat exchangers," *Int. Symp. Compact Heat Exch.*, vol. 28, no. 2–3, pp. 193–199, Jan. 2004.

[139] A.J. Fuller, T. Kim, H.P. Hodson and T.J. Lu, "Measurement and interpretation of the heat transfer coefficients of metal foams," *Proc. Inst. Mech. Eng. Part C J. Mech. Eng. Sci.*, vol. 219, no. 2, pp. 183–191, Feb. 2005.

[140] S.-C. Tzeng and T.-M. Jeng, "Interstitial Heat Transfer Coefficient and Dispersion Conductivity in Compressed Metal Foam Heat Sinks," *J. Electron. Packag.*, vol. 129, no. 2, pp. 113–119, Aug. 2006.

[141] A. Kopanidis, A. Theodorakakos, E. Gavaises and D. Bouris, "3D numerical simulation of flow and conjugate heat transfer through a pore scale model of high porosity open cell metal foam," *Int. J. Heat Mass Transf.*, vol. 53, no. 11–12, pp. 2539–2550, May 2010.

[142] B. Boyd and K. Hooman, "Air-cooled micro-porous heat exchangers for thermal management of fuel cells," *Int. Commun. Heat Mass Transf.*, vol. 39, no. 3, pp. 363–367, Mar. 2012.

[143] P. Ranut, E. Nobile and L. Mancini, "High resolution microtomography-based CFD simulation of flow and heat transfer in aluminum metal foams," *Appl. Therm. Eng.*, vol. 69, no. 1–2, pp. 230–240, Aug. 2014.

[144] A. Tamayol and K. Hooman, "Thermal Assessment of Forced Convection Through Metal Foam Heat Exchangers," *J. Heat Transf.*, vol. 133, no. 11, p. 111801, 2011.

[145] K. Boomsma and D. Poulikakos, "The Effects of Compression and Pore Size Variations on the Liquid Flow Characteristics in Metal Foams," *J. Fluids Eng.*, vol. 124, no. 1, pp. 263–272, Aug. 2001.

[146] N. Dukhan, "Correlations for the pressure drop for flow through metal foam," *Exp. Fluids*, vol. 41, no. 4, pp. 665–672, 2006.

[147] S. Mancin, C. Zilio, A. Cavallini and L. Rosetto, "Pressure drop during air flow in aluminum foams," *Int. J. Heat Mass Transf.*, vol. 53, no. 15–16, pp. 3121–3130, Jul. 2010.

[148] J.-M. Hugo, E. Brun and F. Topin, "Metal foam effective transport properties," in *Evaporation, Condensation and Heat Transfer*, Dr. Animul Ahsan, Ed. INTECH Open Access Publisher, 2011.

[149] Jean-Michel Hugo and Frédéric Topin, "Metal Foams Design for Heat Exchangers: Structure and Effectives Transport Properties," in *Heat and Mass Transfer in Porous Media*, J.M.P.Q. Delgado, Ed. Berlin, Heidelberg: Springer Berlin Heidelberg, 2012, pp. 219–244.

[150] B. Madani, F. Topin, F. Rigollet and L. Tadrist, "Flow Laws in Metallic Foams: Experimental Determination of Inertial and Viscous Contributions," vol. 10, no. 1, pp. 51–70, 2007.

[151] K. Boomsma, D. Poulikakos and F. Zwick, "Metal foams as compact high performance heat exchangers," *Mech. Mater.*, vol. 35, no. 12, pp. 1161–1176, 2003.

[152] C. Hutter, A. Zenklusen, R. Lang and Ph. Rudolf von Rohr, "Axial dispersion in metal foams and streamwise-periodic porous media," *Chem. Eng. Sci.*, vol. 66, no. 6, pp. 1132–1141, Mar. 2011.

[153] J.W. Paek, B.H. Kang, S.Y. Kim and J.M. Hyun, "Effective Thermal Conductivity and Permeability of Aluminum Foam Materials," *Int. J. Thermophys.*, vol. 21, no. 2, pp. 453–464.

[154] K. Hooman and N. Dukhan, "A Theoretical Model with Experimental Verification to Predict Hydrodynamics of Foams," *Transp. Porous Media*, vol. 100, no. 3, pp. 393–406, Dec. 2013.

[155] K. Boomsma, D. Poulikakos and Y. Ventikos, "Simulations of flow through open cell metal foams using an idealized periodic cell structure," *Int. J. Heat Fluid Flow*, vol. 24, no. 6, pp. 825–834, Dec. 2003.

[156] E. L. Furman, A. B. Finkelstein and M. L. Cherny, "Permeability of Aluminium Foams Produced by Replication Casting," *Metals*, vol. 3, no. 1, pp. 49–57, Dec. 2012.

[157] N. Dukhan and A.S. Suleiman, "Simulation of Entry-Region Flow in Open-Cell Metal Foam and Experimental Validation," *Transp. Porous Media*, vol. 101, no. 2, pp. 229–246, 2013.

[158] G.B. Ribeiro and J.R. Barbosa Jr., "Comparison of metal foam and louvered fins as air-side heat transfer enhancement media for miniaturized condensers," *Appl. Therm. Eng.*, vol. 51, no. 1–2, pp. 334–337, Mar. 2013.

[159] Z. Dai, K. Nawaz, Y. Park, Q. Chen and A.M. Jacobi, "A Comparison of Metal-Foam Heat Exchangers to Compact Multilouver Designs for Air-Side Heat Transfer Applications," *Heat Transf. Eng.*, vol. 33, no. 1, pp. 21–30, Jan. 2012.

[160] S. De Schampheleire, P. De Jaeger, H. Huisseune, B. Armeel, C.T'Joen, K. De Kerpel, and M. De Paepe, "Thermal hydraulic performance of 10 PPI aluminium foam as alternative for louvered fins in an HVAC heat exchanger," *Appl. Therm. Eng.*, vol. 51, no. 1–2, pp. 371–382, Mar. 2013.

[161] M. Bai and J.N. Chung, "Analytical and numerical prediction of heat transfer and pressure drop in open-cell metal foams," *Int. J. Therm. Sci.*, vol. 50, no. 6, pp. 869–880, Jun. 2011.

[162] H. Huisseune, S. De Schampheleire, B. Ameel and M. de Paepe, "Comparison of metal foam heat exchangers to a finned heat exchanger for low Reynolds number applications," *Int. J. Heat Mass Transf.*, vol. 89, pp. 1–9, Oct. 2015.

[163] B.V. Antohe, J.L. Lage, D.C. Price and R.M. Weber, "Experimental Determination of Permeability and Inertia Coefficients of Mechanically Compressed Aluminum Porous Matrices," *J. Fluids Eng.*, vol. 119, no. 2, pp. 404–4012, Jun. 1997.

[164] N. Dukhan, R. Picon-Feliciano, A.R. Alvarez-Hernandez, "Air Flow Through Compressed and Uncompressed Aluminum Foam: Measurements and Correlations," *J. Fluids Eng.*, vol. 128, no. 5, pp. 1004–1012, 2006.

[165] H.R. Seyf and M. Layeghi, "Numerical Analysis of Convective Heat Transfer From an Elliptic Pin Fin Heat Sink With and Without Metal Foam Insert," *J. Heat Transf.*, vol. 132, no. 7, p. 071401, Apr. 2010.

[166] C.T. DeGroot, A.G. Straatman and L.J. Betchen, "Modeling Forced Convection in Finned Metal Foam Heat Sinks," *J. Electron. Packag.*, vol. 131, no. 2, p. 10 pages, Mar. 2009.

[167] S.K. Mohammadian, S.M. Rassoulinejad-Mousavi and Y. Zhang, "Thermal management improvement of an air-cooled high-power lithium-ion battery by embedding metal foam," *J. Power Sources*, vol. 296, pp. 305–313, Nov. 2015.

[168] A. Bhattacharya and R.L. Mahajan, "Finned Metal Foam Heat Sinks for Electronics Cooling in Forced Convection," *J. Electron. Packag.*, vol. 124, no. 3, pp. 1–9.

[169] S.-C. Tzeng, "Spatial thermal regulation of aluminum foam heat sink using a sintered porous conductive pipe," *Int. J. Heat Mass Transf.*, vol. 50, no. 1–2, pp. 117–126, Jan. 2007.

[170] S.Y Kim, J.W. Paek and B.H. Kang, "Flow and Heat Transfer Correlations for Porous Fin in a Plate-Fin Heat Exchanger," *J. Heat Transf.*, vol. 122, no. 3, pp. 572–578, Mar. 2000.

[171] K.P. Carpenter and A.K. da Silva, "A combined hydro-thermal characterization of high-porosity metal foam test sections with discrete pore-size gradients," *Int. J. Heat Mass Transf.*, vol. 77, pp. 770–776, Oct. 2014.

[172] G. Zaragoza and R. Goodall, "Metal Foams with Graded Pore Size for Heat Transfer Applications," *Adv. Eng. Mater.*, vol. 15, no. 3, pp. 123–128, 2013.

[173] S.Y. Kim, J.W. Paek and B.H. Kang, "Thermal performance of aluminum-foam heat sinks by forced air cooling," *Compon. Packag. Technol. IEEE Trans. On*, vol. 26, no. 1, pp. 262–267, Mar. 2003.

[174] T.M. Jeng, S.C. Tzeng and F.Z. Tang, "Fluid flow and heat transfer characteristics of the porous metallic heat sink with a conductive cylinder partially filled in a rectangular channel," *Int. J. Heat Mass Transf.*, vol. 53, no. 19, pp. 4216–4227, 2010.

[175] K.C. Leong and L.W. Jin, "An experimental study of heat transfer in oscillating flow through a channel filled with an aluminum foam," *Int. J. Heat Mass Transf.*, vol. 48, no. 2, pp. 243–253, Jan. 2005.

[176] K.C. Leong and L.W. Jin, "Characteristics of oscillating flow through a channel filled with open-cell metal foam," *Int. J. Heat Fluid Flow*, vol. 27, no. 1, pp. 144–153, Feb. 2006.

[177] K.C. Leong and L.W. Jin, "Effect of oscillatory frequency on heat transfer in metal foam heat sinks of various pore densities," *Int. J. Heat Mass Transf.*, vol. 49, no. 3–4, pp. 671–681, Feb. 2006.

[178] K. C. Leong and L.W. Jin, "Heat Transfer Performance of Metal Foam Heat Sinks Subjected to Oscillating Flow," *IEEE Trans. Compon. Packag. Technol.*, vol. 29, no. 4, pp. 856–863, Dec. 2006.

[179] L. W. Jin and K.C. Leong, "Pressure drop and friction factor of steady and oscillating flows in open-cell porous media," *Transp. Porous Media*, vol. 72, no. 1, pp. 37–52, 2007.

[180] M. Ghafarian. D. Mohebbi-Kalhori and J. Sadegi, "Analysis of heat transfer in oscillating flow through a channel filled with metal foam using computational fluid dynamics," *Int. J. Therm. Sci.*, vol. 66, no. 0, pp. 42–50, Apr. 2013.

[181] Ö. Bağcı, N. Dukhan, M. Özdemir and L.A. Kavurmacıoğlu, "Experimental heat transfer due to oscillating water flow in open-cell metal foam," *Int. J. Therm. Sci.*, vol. 101, pp. 48–58, Mar. 2016.

[182] W. Lu, C.Y. Zhao and S.A. Tassou, "Thermal analysis on metal-foam filled heat exchangers. Part I: Metal-foam filled pipes," *Int. J. Heat Mass Transf.*, vol. 49, no. 15–16, pp. 2751–2761, Jul. 2006.

[183] C. Yang, K. Ando and A. Nakayama, "A Local Thermal Non-Equilibrium Analysis of Fully Developed Forced Convective Flow in a Tube Filled with a Porous Medium," *Transp. Porous Media*, vol. 89, no. 2, pp. 237–249, 2011.

[184] C.Y. Zhao, W. Lu and S.A. Tassou, "Thermal analysis on metal-foam filled heat exchangers. Part II: Tube heat exchangers," *Int. J. Heat Mass Transf.*, vol. 49, no. 15–16, pp. 2762–2770, Jul. 2006.

[185] C. Hutter, D. Büchi, V. Zuber and Ph. Rudolf von Rohr, "Heat transfer in metal foams and designed porous media," *Chem. Eng. Sci.*, vol. 66, no. 17, pp. 3806–3814, Sep. 2011.

[186] G. Zaragoza and R. Goodall, "Development of a device for the measurement of thermal and fluid flow properties of heat exchanger materials," *Measurement*, vol. 56, pp. 37–49, Oct. 2014.

[187] F. Barari, L. Erardo Mario Elizondo, R. Goodall and R. Woolley, "Metal foam regenerators; heat transfer and storage in porous metals," *J. Mater. Res.*, vol. 28, no. 17, pp. 2474–2482, 2013.

[188] L. Giani, G. Groppi and E. Tronconi, "Heat Transfer Characterization of Metallic Foams," *Ind. Eng. Chem. Res.*, vol. 44, no. 24, pp. 9078–9085, Nov. 2005.

[189] J.-J. Hwang, G.-J. Hwang, R.-H. Yeh and C.-H. Chao, "Measurement of Interstitial Convective Heat Transfer and Frictional Drag for Flow Across Metal Foams," *J. Heat Transf.*, vol. 124, no. 1, pp. 120–129, May 2001.

[190] M. Odabaee, K. Hooman and H. Gurgenci, "Metal Foam Heat Exchangers for Heat Transfer Augmentation from a Cylinder in Cross-Flow," *Transp. Porous Media*, vol. 86, no. 3, pp. 911–923, Feb. 2011.

[191] M. Odabaee and K. Hooman, "Metal foam heat exchangers for heat transfer augmentation from a tube bank," *Appl. Therm. Eng.*, vol. 36, pp. 456–463, Apr. 2012.

[192] M. Odabaee and K. Hooman, "Application of metal foams in air-cooled condensers for geothermal power plants: An optimization study," *Int. Commun. Heat Mass Transf.*, vol. 38, no. 7, pp. 838–843, Aug. 2011.

[193] C. T'Joen, P. De Jaeger, H. Huisseune, S. Van Herzeele, N. Vorst and M. De Paepe, "Thermo-hydraulic study of a single row heat exchanger consisting of metal

foam covered round tubes," *Int. J. Heat Mass Transf.*, vol. 53, no. 15–16, pp. 3262–3274, Jul. 2010.

[194] A. Chumpia and K. Hooman, "Performance evaluation of tubular aluminum foam heat exchangers in single row arrays," *Appl. Therm. Eng.*, vol. 83, pp. 121–130, May 2015.

[195] P. De Jaeger, C.T'Joen, H. Huisseune, B. Ameel, S. De Schampheleire and M. De Paepe, "Assessing the influence of four cutting methods on the thermal contact resistance of open-cell aluminum foam," *Int. J. Heat Mass Transf.*, vol. 55, no. 21–22, pp. 6142–6151, Oct. 2012.

[196] A. Chumpia and K. Hooman, "Quantification of Contact Resistance of Metal Foam Heat Exchangers for Improved, Air-cooled Condensers in Geothermal Power Application," presented at the 18th Australasian Fluid Mechanics Conference, Launceston, Tasmania, 2012, pp. 3–7.

[197] T. Fiedler, N. White, M. Dahari and K.Hooman, "On the electrical and thermal contact resistance of metal foam," *Int. J. Heat Mass Transf.*, vol. 72, pp. 565–571, May 2014.

[198] C.T. DeGroot, D. Gateman and A.G. Straatman, "Effect of Thermal Contact Resistance at Porous-Solid Interfaces in Finned Metal Foam Heat Sinks," *J. Electron. Packag.*, vol. 132, no. 4, p. 041007, Nov. 2010.

[199] G. Ledezma and A. Bejan, "Heat sinks with sloped plate fins in natural and forced convection," *Int. J. Heat Mass Transf.*, vol. 39, no. 9, pp. 1773–1783, Jun. 1996.

[200] S.P. Jang and S.J. Kim, "Fluid Flow and Thermal Characteristics of a Microchannel Heat Sink Subject to an Impinging Air Jet," *J. Heat Transf.*, vol. 127, no. 7, pp. 770–779, Dec. 2004.

[201] W.H. Shih, W.C. Chiu and W.H. Hsieh, "Height Effect on Heat-Transfer Characteristics of Aluminum-Foam Heat Sinks," *J. Heat*, vol. 128, no. 6, pp. 530–537, Oct. 2005.

[202] W.H. Hsieh, J.Y. Wu, W.H. Shih and W.C. Chiu, "Experimental investigation of heat-transfer characteristics of aluminum-foam heat sinks," *Int. J. Heat Mass Transf.*, vol. 47, no. 23, pp. 5149–5157, Nov. 2004.

[203] S.S. Feng, J.J. Kuang, T. Wen. T.J. Lu and K. Ichimiya, "An experimental and numerical study of finned metal foam heat sinks under impinging air jet cooling," *Int. J. Heat Mass Transf.*, vol. 77, pp. 1063–1074, Oct. 2014.

[204] W.H. Shih, F.C. Chou and W.H. Hsieh, "Experimental Investigation of the Heat Transfer Characteristics of Aluminum-Foam Heat Sinks With Restricted Flow Outlet," *J. Heat Transf.*, vol. 129, no. 11, pp. 1554–1563, 2007.

[205] S.-C. Tzeng and T.-M. Jeng, "Convective heat transfer in porous channels with 90-deg turned flow," *Int. J. Heat Mass Transf.*, vol. 49, no. 7–8, pp. 1452–1461, Apr. 2006.

[206] T.-M. Jeng and S.-C. Tzeng, "Numerical study of confined slot jet impinging on porous metallic foam heat sink," *Int. J. Heat Mass Transf.*, vol. 48, no. 23–24, pp. 4685–4694, Nov. 2005.

[207] K.-C. Wong and N. H. Saeid, "Numerical study of mixed convection on jet impingement cooling in a horizontal porous layer under local thermal non-equilibrium conditions," *Int. J. Therm. Sci.*, vol. 48, no. 5, pp. 860–870, May 2009.

[208] T.-M. Jeng and S.-C. Tzeng, "Experimental study of forced convection in metallic porous block subject to a confined slot jet," *Int. J. Therm. Sci.*, vol. 46, no. 12, pp. 1242–1250, Dec. 2007.

[209] S.Y Kim, M.H. Lee and K.-S. Lee, "Heat removal by aluminum-foam heat sinks in a multi-air jet impingement," *IEEE Trans. Compon. Packag. Technol.*, vol. 28, no. 1, pp. 142–148, Mar. 2005.

[210] J. J. Kuang, T. Kim, M.L. Xu and T.J. Lu, "Ultralightweight Compact Heat Sinks With Metal Foams Under Axial Fan Flow Impingement," *Heat Transf. Eng.*, vol. 33, no. 7, pp. 642–650, May 2012.

[211] A. Ejlali, A. Ejlali, K. Hooman and H. Gurgenci, "Application of high porosity metal foams as air-cooled heat exchangers to high heat load removal systems," *Int. Commun. Heat Mass Transf.*, vol. 36, no. 7, pp. 674–679, Aug. 2009.

[212] S.S. Feng, J.J. Kuang, T. Wen. T.J. Lu and K. Ichimiya, "Heat Transfer and Pressure Drop Characteristics of Finned Metal Foam Heat Sinks Under Uniform Impinging Flow," *J. Electron. Packag.*, vol. 137, no. 2, p. 021014, Jun. 2015.

[213] C.Y. Zhao, T.J. Lu and H.P. Hodson, "Natural convection in metal foams with open cells," *Int. J. Heat Mass Transf.*, vol. 48, no. 12, pp. 2452–2463, Jun. 2005.

[214] S. De Schampheleire, P. De Jaeger, K. De Kerpel, B. Armeel, C.T'Joen, H. Huisseune, S. Lecompte and M. De Paepe, "Experimental study of buoyancy-driven flow in open-cell aluminium foam heat sinks," *Appl. Therm. Eng.*, vol. 59, no. 1–2, pp. 30–40, Sep. 2013.

[215] G. Hetsroni, M. Gurevich and R. Rozenblit, "Natural convection in metal foam strips with internal heat generation," *Exp. Therm. Fluid Sci.*, vol. 32, no. 8, pp. 1740–1747, Sep. 2008.

[216] M.S. Phanikumar and R.L. Mahajan, "Non-Darcy natural convection in high porosity metal foams," *Int. J. Heat Mass Transf.*, vol. 45, no. 18, pp. 3781–3793, Aug. 2002.

[217] Z. Qu, T. Wang, W. Tao and T. Lu, "Experimental study of air natural convection on metallic foam-sintered plate," *Int. J. Heat Fluid Flow*, vol. 38, pp. 126–132, Dec. 2012.

[218] V. Kathare, F.A. Kulacki and J.H. Davidson, "Buoyant Convection in Superposed Metal Foam and Water Layers," *J. Heat Transf.*, vol. 132, no. 1, p. 014503, Oct. 2009.

[219] A. Bhattacharya and R.L. Mahajan, "Metal Foam and Finned Metal Foam Heat Sinks for Electronics Cooling in Buoyancy-Induced Convection," *J. Electron. Packag.*, vol. 128, no. 3, pp. 1–8, Sep. 2006.

[220] S. Soubielle, "Creep and cyclic behaviour of replicated microcellular aluminium," Institut Polytechnique de Grenoble, 2010INPG0044 ER, Grenoble, 2010.

[221] R. Goodall, J.-F. Despois and A. Mortensen, "Sintering of NaCl powder: Mechanisms and first stage kinetics," *J. Eur. Ceram. Soc.*, vol. 26, no. 16, pp. 3487–3497, 2006.

[222] F. Diologent, R. Goodall and A. Mortensen, "Creep of aluminium–magnesium open cell foam," *Acta Mater.*, vol. 57, no. 3, pp. 830–837, Feb. 2009.

[223] C. J. D. Fell and H. P. Hutchison, "Diffusion coefficients for sodium and potassium chlorides in water at elevated temperatures," *J. Chem. Eng. Data*, vol. 16, no. 4, pp. 427–429, Oct. 1971.

[224] R. Treybal, *Mass Transfer Operation*, 3rd ed. New York: Mc Graw-Hill.

[225] M. C. I. Siu, "National Bureau of Standards line-heat-source guarded-hot-plate apparatus," *Rev. Sci. Instrum.*, vol. 52, pp. 1709–1716, 1981.

[226] R.R. Zarr, "Assessment of Uncertainties for the NIST 1016 mm Guarded-Hot-Plate Apparatus: Extended Analysis for Low-Density Fibrous-Glass Thermal Insulation," *J. Res. Natl. Inst. Stand. Technol.*, vol. 115, no. 1, pp. 23–59, Jan. 2010.

[227] W.M. Healy, "Using Finite Element Analysis to Design a New Guarded Hot Plate Apparatus for Measuring the Thermal Conductivity of Insulating Materials," presented at the ANSYS Users Group Conference, Gaithersburg MD, 2001, vol. 1, pp. 1–9.

[228] "Calibration of Thermocouples," EURAMET, Braunschweig, Calibration Guides 8, Oct. 2011.

[229] H. Alloul, *Introduction to the Physics of Electrons in Solids*, 1st ed. Berlin, Heidelberg: Springer-Verlag, 2011.

[230] R. A. Matula, "Electrical Resistivity of Copper, Gold, Palladium and Silver," *J. Phys. Chem. Ref. Data*, vol. 8, no. 4, p. 1979.

[231] S. Mekid and D. Vaja, "Propagation of uncertainty: Expressions of second and third order uncertainty with third and fourth moments," *Measurement*, vol. 41, no. 6, pp. 600–609, Jul. 2008.

[232] M.A.F. Martins, R. Requião and R.A. Kalid, "Generalized expressions of second and third order for the evaluation of standard measurement uncertainty," *Measurement*, vol. 44, no. 9, pp. 1526–1530, Nov. 2011.

[233] A. D. Kraus, A. Aziz and J. Welty, "Convection Coefficients," in *Extended Surface Heat Transfer*, New York: John Wiley & Sons, Inc., 2007, pp. 160–219.

[234] S. Tavoularis, *Measurement in Fluid Mechanics*. Cambridge: Cambridge University Press, 2005.

[235] E. W. Weisstein, "Vandermonde Matrix." [Online]. Available: http://mathworld.wolfram.com/VandermondeMatrix.html. [Accessed: 05-Aug-2016].

[236] Anna Ploszajski, "Material of the month – cork," *Mater. World*, vol. 23, no. 5, May 2015.

[237] S.P. Silva, M.A. Sabino, E.M. Fernandes, V.M. Correlo, L.F. Boesel and R. L. Reis, "Cork: properties, capabilities and applications," *Int. Mater. Rev.*, vol. 50, no. 6, pp. 345–365, 2005.

[238] M.E. Rosa and M.A. Fortes, "Temperature-induced alterations of the structure and mechanical properties of cork," *Mater. Sci. Eng.*, vol. 100, no. 0, pp. 69–78, avril 1988.

[239] B. McKeon and R. Engler, "Pressure Measurement Systems," in *Springer Handbook of Experimental Fluid Mechanics*, C. Tropea, A.L. Yarin, and J.F. Foss, Eds. Berlin, Heidelberg: Springer Berlin Heidelberg, 2007, pp. 179–214.

[240] J. Krebs, "Cast aluminium microwires: Processing and plastic deformation," Doctoral Thesis, EPFL, n.6472, Lausanne, 2015.

[241] F. P. Incropera, D. P. DeWitt, T. L. Bergman and A. S. Lavine, *Principles of heat and mass transfer*, 7th Edition, International Student Version. New York: John Wiley & Sons, Inc., 2012.

[242] D. A. Nield and A. Bejan, *Convection in Porous Media*, 3rd ed. Berlin: Springer, 2006.

[243] "ERG: Duocel® - Aluminum Foam Properties." [Online]. Available: http://www.ergaerospace.com/Aluminum-properties.htm. [Accessed: 17-Aug-2016].

[244] S. Prétot, B. Zeghmati and Ph. Caminat, "Influence of surface roughness on natural convection above a horizontal plate," *Adv. Eng. Softw.*, vol. 31, no. 10, pp. 793–801, Oct. 2000.

[245] F. Tetsu, F. Motoo and T. Masanori, "Influence of various surface roughness on the natural convection," *Int. J. Heat Mass Transf.*, vol. 16, no. 3, pp. 629–636, Mar. 1973.

[246] F. Barari, "Metal foam regenerators; heat transfer and pressure drop in porous metals," University of Sheffield, Sheffield, 2014.

[247] O. Caggese, G. Gnaegi, G. Hannema, A. Terzis and P. Ott, "Experimental and numerical investigation of a fully confined impingement round jet," *Int. J. Heat Mass Transf.*, vol. 65, pp. 873–882, Oct. 2013.

[248] L.G. Hansen and B.W. Webb, "Air jet impingement heat transfer from modified surfaces," *Int. J. Heat Mass Transf.*, vol. 36, no. 4, pp. 989–997, Mar. 1993.

[249] W.J. Minkowycz, A. Haji-Sheikh and K. Vafai, "On departure from local thermal equilibrium in porous media due to a rapidly changing heat source: the Sparrow number," *Int. J. Heat Mass Transf.*, vol. 42, no. 18, pp. 3373–3385, Sep. 1999.

[250] N. Dukhan, P.D. Quinones-Ramos, E. Cruz-Ruiz, M. Velez-Reyes, E.P. Scott, "One-dimensional heat transfer analysis in open-cell 10-ppi metal foam," *Int. J. Heat Mass Transf.*, vol. 48, no. 25–26, pp. 5112–5120, Dec. 2005.

[251] S. Y. Kim, J.-M. Koo and Andrey V. Kuznetsov, "Effect of anisotropy in permeability and effective thermal conductivity on thermal performance of an aluminium foam heat sink," *Numer. Heat Transf. Part Appl.*, vol. 40, no. 1, pp. 21–36, Jul. 2001.

[252] A. Nakayama, F. Kuwahara, M. Sugiyama and G. Xu, "A two-energy equation model for conduction and convection in porous media," *Int. J. Heat Mass Transf.*, vol. 44, no. 22, pp. 4375–4379, Nov. 2001.

[253] J.-F. Despois, A. Mortensen, "Permeability of open-pore microcellular materials," *Acta Mater.*, vol. 53, no. 5, pp. 1381–1388, Mar. 2005.

[254] A. Ushida, T. Hasegawa and T. Narumi, "Anomalous phenomena in pressure drops of water flows through micro-orifices," *Microfluid. Nanofluidics*, vol. 17, no. 5, pp. 863–870, Nov. 2014.

[255] J. Happel, H. Brenner, *Low Reynolds number hydrodynamics with special applications to particulate media*, 1st ed. The Hague: Springer Netherlands, 1983.

[256] R.A. Sampson, "On Stokes's Current Function," *Philos. Trans. R. Soc. Lond. Math. Phys. Eng. Sci.*, vol. 182, pp. 449–518, Jan. 1891.

[257] E. Arzt, "The influence of an increasing particle coordination on the densification of spherical powders," *Acta Metall.*, vol. 30, no. 10, pp. 1883–1890, Oct. 1982.

[258] L. Weber, D. Ingram, S. Guardia, A. Athanasiou-Ioannou and A. Mortensen, "Fluid flow through replicated microcellular materials in the Darcy-Forchheimer regime," *Acta Mater.*, vol. 126, pp. 280–293, Mar. 2017.

[259] C.H. Hsueh, "Modeling of elastic deformation of multilayers due to residual stresses and external bending," *J. Appl. Phys.*, vol. 91, no. 12, pp. 9652–9656, Jun. 2002.

[260] C.H. Hsueh, "Thermal stresses in elastic multilayer systems," *Thin Solid Films*, vol. 418, no. 2, pp. 182–188, Oct. 2002.

Curriculum Vitae

PERSONAL INFORMATION

Alexandros ATHANASIOU-IOANNOU

Avenue de la gare 38,
Chavannes-près-Renens Vaud, Switzerland.

Born on May 30, 1986.
Greek and Chypriot.

Single, no children.

EDUCATION

PhD in Materials Science and Engineering, École polytechnique fédérale de Lausanne

2011-to present

Master in Nanosciences, École Polytechnique, Palaiseau, France.

2010-2011

Dipl. Ing. Mechanical Engineering, National Technical University of Athens

2004-2010

PRESENTATIONS IN CONFERENCES

1. **Thermal characterization of replicated microcellular aluminium under natural convection,** *A. Athanasiou Ioannou, L. Weber and A. Mortensen*, presented at 8th International Conference on Porous Metals and Metallic Foams, June 23-26, 2013, Raleigh, North Carolina.
2. **Thermal characterization of replicated microcellular aluminium under forced convection,** *A. Athanasiou Ioannou, D. Ingram, L. Weber and A. Mortensen*, presented at 9th International Conference on Porous Metals and Metallic Foams, August 31-September 2, 2015, Barcelona, Spain.